QATAR UNIVERSITY

COLLEGE OF ENGINEERING

APPLICATION OF STEEL REINFORCED COMPOSITES FOR STRENGTHENING OF REINFORCED CONCRETE BEAMS AND COLUMNS: EXPERIMENTAL, ANALYTICAL, NUMERICAL, AND MACHINE LEARNING BASED STUDIES

BY

TADESSE GEMEDA WAKJIRA

A Dissertation Submitted to

the College of Engineering

in Partial Fulfillment of the Requirements for the Degree of

Doctorate of Philosophy in Civil Engineering

June 2022

COMMITTEE PAGE

The members of the Committee approve the Dissertation of
Tadesse Gemeda Wakjira defended on 10/05/2022.

Dr. Usama Ebead
Dissertation Supervisor

Dr. Evangelos Plevris
Committee Member

Dr. Farayi Musharavati
Committee Member

Dr. Adel Elsafty
Committee Member

Approved:

Khalid Kamal Naji, Dean, College of Engineering

ABSTRACT

WAKJIRA, TADESSE G., Doctorate: June: 2022,

Doctorate of Philosophy in Civil Engineering

Title: Application of Steel Reinforced Composites for Strengthening of Reinforced Concrete Beams and Columns: Experimental, Analytical, Numerical, and Machine Learning Based Studies

Supervisor of Dissertation: Usama A. Ebead.

The use of steel reinforced composites (SRC) has emerged as a cost-effective and promising solution for the strengthening of reinforced concrete (RC) structures. The strengthening system in SRC comprises a unidirectional fabric made of ultra-high tensile strength galvanized steel cords embedded within an inorganic matrix or polymeric matrix to form steel reinforce grout (SRG) and steel reinforced polymer (SRP), respectively. The studies to date have focused primarily on the application of SRG to flexural deficient RC beams. Moreover, understanding the shear resistance mechanism of SRG-strengthened RC beams and generally, inorganic composites has always been a challenging task, and thus, has not yet been fully addressed.

Another important application of SRC is for retrofitting of seismically deficient RC columns. To assess the performance of RC columns, and control damages under lateral loads it is critical to properly define the plastic hinge region, which is the region exposed to maximum plastic deformation. However, accurate determination of the plastic hinge length (PHL) remains a challenge.

Accordingly, this dissertation is aimed to examine the application of SRC for strengthening RC beams and columns based on experimental, analytical, numerical, and machine learning (ML) based studies. With this aim, this dissertation comprised seven key studies. The application of SRG for strengthening of shear-deficient RC T-

beams is experimentally and analytically investigated, for the first time, in the first study. The second study investigates the efficacy of SRG for shear strengthening of RC rectangular beams focusing on the effect of shear span-to-depth ratio. In the third study, the use of the near surface mounted technique for the SRG system was experimentally investigated. The fourth and fifth studies present ML-based capacity predictive models and reliability analysis of RC beams strengthened with inorganic composites in shear and flexure, respectively. The sixth study numerically explores the application of SRP for strengthening seismically deficient RC columns and the effects of key design parameters on SRP-confined columns. Finally, the last study proposed a robust ensemble ML-based model to predict the PHL of RC columns. The results of the studies revealed the high potential of SRC for strengthening RC beams and columns. The results of all seven studies have been published in peer-reviewed journals.

DEDICATION

To my mother.

ACKNOWLEDGMENTS

First and foremost, I would like to thank the Almighty God for his unending blessings and mercy. I would like to express my deepest gratitude to my supervisor and great mentor, Prof. Usama Ebead, for his great mentorship, invaluable support, trust, and encouragement that led me to be able to continuously develop my skills and become a better researcher. I am most grateful for the unprecedented amount of time he dedicates to the supervision of his students.

I would like to thank Eng. Siju Joseph, Lab Technician, for his support in carrying out the experimental work. I wish to thank my colleagues and friends in Prof. Ebead's research team.

Finally, I am deeply indebted to my family for their endless love and support. A special thank goes to my hard working and loving mother.

TABLE OF CONTENTS

LIST OF TABLES

LIST OF FIGURES

CHAPTER 1: INTRODUCTION

1.1. Background

Strengthening of civil infrastructures is usually necessary to address deficiencies caused by various factors such as a change in the use of a structure, material degradation, lack of proper maintenance, corrosion of reinforcement bars, and earthquake-induced damage. Several strengthening techniques have been developed to upgrade or restore the load-carrying capacity of deteriorated and/or deficient reinforced concrete (RC) structures and extend their life span. Primarily, composites have been widely used in laboratory and field applications as an effective strengthening and rehabilitation system because of their favorable properties, including excellent resistance to corrosion, high strength-to-weight ratio, and speed and ease of installation, over traditional strengthening techniques [1]. In this context, an external reinforcement with fiber-reinforced polymer (FRP) is a well-established structural strengthening and rehabilitation technique. However, because of the presence of epoxy resin, several drawbacks, including incompatibility with the parent material (e.g., concrete), susceptibility to deterioration when exposed to humidity or moisture, low fire resistance, and difficulty to apply at low temperatures, discourage its use [1,2]. In contrast, fabric reinforced cementitious matrix (FRCM), also identified in the literature as textile reinforced mortar, was introduced into the construction market in lieu of FRP to overcome the limitations associated with the latter [2–7], and it has been shown to be effective for the strengthening of RC structures when used both as externally bonded (EB) [8–15] and near-surface embedded systems (NSE) [16–19]. The latter was introduced as an alternative to the conventional EB-FRCM to delay or suppress the premature FRCM/concrete debonding commonly observed in an EB-FRCM. In addition, the hybrid NSE/EB system has also been shown to be an effective technique

when large numbers of fabric layers are required [18].

From an economical point of view, the fibers and fabrics used in both FRP and FRCM composites are quite expensive. Recently, the increasing interest in the development of cost-effective and efficient strengthening solutions has led to the introduction of an innovative composite referred to as steel reinforced composite (SRC) as an alternative to FRP and FRCM. An SRC makes use of steel in lieu of other composite fibers used in FRP or FRCM (such as glass, carbon, and polyparaphenylene benzobisoxazole (PBO)) [20]. The strengthening system in SRC comprised a unidirectional fabric made of ultra-high tensile strength galvanized steel cords fixed to a fiberglass micromesh to facilitate the installation. The steel fabric can be obtained in different densities based on the number of steel wires distributed in the fabric, and can also be embedded within either a polymeric matrix to form a steel reinforced polymer (SRP) composite or geo-mortar to form a steel reinforced grout (SRG) composite.

A state-of-the-art review of the application of SRP for the strengthening of RC and masonry structures was reported by De Santis et al. [20]. This review indicated that, typically, SRP provided a comparable or even better enhancement than FRP in the structural performance of strengthened beams in bending or confinement of columns [20]. In addition, at the material level, the SRP composite exhibited comparable or better tensile and bond behavior compared to FRP composites [20]. However, Prota et al. [21] compared SRP and carbon FRP for flexural strengthening of RC beams, and reported that SRP exhibited a smaller gain in the ultimate strength (approximately 10%) compared to carbon FRP, but a greater ultimate deflection (approximately 24%).

The use of inorganic matrix in SRG instead of epoxy adhesives in SRP offers advantages such as compatibility with the substrate (e.g., masonry, concrete), ease of application on a wet surface or at low temperature, improved fire resistance, and a

further reduction in cost [2]. Previous experimental results indicated that SRG can be effectively used for the strengthening of RC beams [22–26], confinement of substandard concrete columns and concrete cubes/cylinders [27–29], and masonry structures [30,31]. Regarding SRG-strengthened RC beams, the experimental studies to date have focused primarily on their flexural strengthening both experimentally [24,25] and analytically [32]. Therefore, it is vital to investigate the application of SRG for the strengthening of shear-deficient RC beams.

One of the important factors that influence the shear capacity of RC beams is the shear span-to-depth (*a/d*) ratio. Several studies have reported on the influence of the *a/d* ratio on the behavior of FRP-strengthened RC beams; however, they reported contradicting results. Bousselham and Challal [33] reported that the shear capacity provided by FRP is higher for deep beams than that for slender beams on the basis of test results for RC beams strengthened with carbon FRP in shear. In another study [34], the same authors reported that the increase in the shear capacity of beams attributed to FRP strengthening was substantial in slender beams, whereas it was quite modest in deep beams. Nguyen-minh et al. [35] reported that the efficacy of FRP U-wraps significantly increased with an increase in *a/d* ratio based on the test results of shear-strengthened RC beams with carbon and glass FRPs. In a similar study, Dias and Barros [36] reported that the efficacy of the near-surface mounted FRP increased with increasing beam depth. Li et al. [37] reported that the shear capacity provided by the carbon FRP was highest in strengthened beams with medium *a/d* ratios followed by beams with large *a/d* ratios, while it is the least in strengthened beams with small *a/d* ratios. For FRCM-strengthened beams, Tetta et al. [38] reported that the *a/d* ratio has no effect on the shear contribution of FRCM. These contradicting observations show that further studies are required to fully understand the shear behavior of strengthened

beams with varying *a/d* ratios. Moreover, there is no study devoted to the influence of *a/d* ratio on the behavior of RC beams strengthened in shear with SRG.

The failure of EB-FRCM strengthened beams is mostly attributed to FRCM debonding [8,18,39–41]. This type of failure limits the strength of the composite. In contrast, recent studies have demonstrated that the use of the NSE and hybrid NSE/EB techniques can be an effective approach to improve the concrete/FRCM bond, thereby delaying or precluding the undesired premature debonding observed in the EB technique [16–18,42]. As a result, the use of these techniques yielded better utilization of the FRCM composite [16–18,42]. The NSE technique also provides protection for the strengthening material, unlike the EB technique where the material is exposed to weather conditions and is also susceptible to fire and vandalism. This technique provides similar advantages as that of the near surface mounted technique for FRP in which the FRP reinforcement bars or strips are embedded in a narrow slit of grooves made on the concrete cover [43–45]. Therefore, it is important to investigate the use of the NSE technique for SRG-strengthened beams. Moreover, accurate determination of the shear capacity of the strengthened beams is imperative for achieving a safe and economic design. Thus, it is vital to propose an accurate and reliable predictive model for RC beams strengthened with SRG and inorganic composite in general.

One other important application of SRC is retrofitting of seismically deficient RC columns and bridge piers, which are key structural members resisting the gravity and lateral loads in RC buildings and bridges; thus, dictating the overall performance of the structure. Bridges are important components of the transportation system, sustaining economic growth, social well-being, and logistics of modern communication [46]. The safety and serviceability of bridges are therefore paramount. Yet, most existing RC bridges were built before the 1980s, prior to modern seismic-oriented design philosophies.

Likewise, such bridges were generally designed for gravity loads and their structural performance would be inadequate during seismic events [47,48]. This is often compounded by poor structural detailing and quality control, and the use of low-strength materials [49,50], which makes bridge piers susceptible to deteriorate at relatively low drift levels [51]. The vulnerability of bridge piers has also been found to strictly correlate to unbalanced flexural-shear resistance, particularly for short piers [52]. Previous experimental studies have shown that the seismic performance of bridge piers depends on several factors, including the pier aspect ratio (*H/d*) [53–56], properties of steel reinforcement bars [57], properties of concrete, transverse reinforcement ratio [54,55,58,59], longitudinal reinforcement ratio [55], axial load level [54,55,58–62], and geometry of the pier [63]. However, there is a dearth of studies that explored the combined effects of and interactions between different factors on the bridge pier performance under seismic loads [49,64]. Parghi and Alam [64] reported that the volume fraction of internal transverse reinforcement had an insignificant influence on the lateral load-carrying capacity of the piers [64]. In contrast, Yeh *et al*. [54] reported that the increase in the internal transverse reinforcement ratio increased both the strength and ductility of bridge piers based on experimental results of RC piers with varying *H/d* ratios of 3.0, 3.6, and 4.3. Similar results have been reported by others [58,59]. One other key parameter influencing the performance of bridge piers is the level of concrete confinement [65]. Therefore, there is a need to provide a more detailed analysis of the conditions and reasons for the observations above, while the effects of different design parameters on the seismic performance of rectangular section piers still need concerted research efforts. Moreover, to the best of the author's knowledge, the study on the main effect and interaction effects of different design parameters on the seismic response of SRP-confined RC columns has not been reported.

During extreme loads such as seismic events, RC columns experience

significant plastic deformation [50]. These plastic deformations are localized in the small regions with high moment demand at column ends, commonly known as the plastic hinge zones [66]. The seismic response of critical members is thus highly dependent on its deformation capacity in the plastic hinge zone [66] where the extent of the damage is defined by the plastic hinge length (PHL). The plastic hinge length of RC columns is dependent on various factors including concrete strength [67,68], axial load level [69–72], longitudinal reinforcement ratio [68,73,74], yield strength of reinforcement bars [75], confinement level [68,71,76–78], and aspect ratio [71,73,79]. However, due to several factors including the nonlinearity of material response, strain penetration, and interaction of independent variables, determining the plastic hinge length accurately is still remaining a challenge [80]. In the past decades, several empirical models have been proposed to estimate the PHL of RC members. However, there exists a large scatter and uncertainty in the estimation of the PHL. One of the causes for the discrepancy in the existing models is related to the selection of the significant parameters determining the PHL. There is a lack of consensus on the importance of various factors in determining the PHL. Sheikh and Khoury [81] proposed a simple equation for determining the PHL of RC columns subjected to high axial loads as a function of the cross-sectional depth, ignoring all other factors. Mendis [73] and Park et al. [82] reported that the PHL is insensitive to the axial load level. In contrast, other researchers (e.g. [69,70]) reported an increase in the PHL with an increase in the axial load level. According to Bae and Bayrak [71], the PHL increases with an increase in the axial load level for axial load levels greater than or equal to 0.20; however, it is constant as 0.25 times the section depth ($0.25h$) for low axial load level, less than 0.20. Babazadeh et al. [83] investigated the effect of slenderness on the PHL based on experimental results of three large-scale RC slender bridge piers with aspect

ratios up to 12. They reported that the existing models and design guides underestimate the PHL of slender columns. Ho [68] introduced the effect of transverse reinforcement ratio on the PHL, in addition to the axial load ratio, compressive strength of concrete, reinforcement ratio and yield strength of longitudinal bars, and cross-sectional depth of the member. In addition to the contradictory reports on the significant effect of different factors on the PHL, the existing models are mainly derived empirically based on limited experimental results, which often limits the accuracy of the models [84]. Thus, the use of an alternative and more powerful modelling approach should be considered.

Recently, machine learning (ML) algorithms, a subset of artificial intelligence, have emerged as a powerful technique to solve different civil engineering problems [85–95]. This is attributed to their ability to estimate the relationship between the factors and the response parameter (s) without the requirement for prior assumptions of the underlying mathematical and physical models, contrasting to most empirical models [96]. Some of the applications of ML techniques reported in the literature include the prediction of mechanical properties of concrete [86,88–90], load capacity and failure modes of RC columns and walls [91,97,98], shear [99–104] and torsional [105] capacities of RC beams, and seismic damage assessment of RC buildings and bridges [106–108]. Moreover, successful applications of different ML techniques such as genetic algorithm (GA) and artificial neural network (ANN) have been reported in the literature to estimate the load capacity of FRP-strengthened RC beams [109–112]. Perera et al. [109] applied ANN and GA to estimate the shear capacity of RC beams strengthened with externally bonded (EB) FRP. The predicted shear capacities of the strengthened beams were in acceptable agreement with the corresponding experimental results. They investigated the effects of the beam cross-sectional dimensions, modulus of elasticity of the FRP, yield strength of steel reinforcement, areas of steel

reinforcement and FRP, inclination of the principal FRP fibers, and concrete compressive strength. A dataset comprised of only 46 RC beams strengthened with EB-FRP was considered in the developed models [109]. Tanarslan et al. [110] developed an ANN model based on a larger database of 84 specimens to estimate the shear capacity of RC beams strengthened with EB-FRP. Moreover, they considered the effects of the shear span-to-depth ratio and different strengthening configurations for the first time [110]. It was concluded that the developed model resulted in a higher prediction capability compared to the existing code equations. Similarly, other studies showed the efficacy of ML-based models for estimating the shear capacity of RC beams strengthened with EB-FRP sheets [110,112] and near surface mounted FRP rods [111]. Despite their great capability and promising results, the literature lacks the application of ML techniques to RC beams strengthened with SRG and inorganic composites in general. Moreover, it is vital to investigate the application of ML techniques to estimate the PHL of RC columns and bridge piers.

1.2. Research Objectives and Significance

The use of steel reinforced composites, particularly, SRG has emerged as a promising technique for the strengthening and retrofitting of RC structures, however, the experimental evidence focused primarily on their application to flexural-deficient RC beams. One of the important factors that influence the efficacy of the strengthening system in shear deficient RC beams is the *a/d* ratio. However, no study devoted to the influence of *a/d* ratio on the behavior of RC beams strengthened in shear with SRG has been reported. Moreover, the use of the conventional EB technique limits the utilization of the strengthening system due to the premature debonding failure. Thus, it is important to investigate an alternative technique for the application of the strengthening system.

The other important application of SRC is for retrofitting of seismically deficient RC columns, which are key structural members resisting the gravity and lateral loads in RC buildings and bridges; thus, dictating the overall performance of the structure. However, to the best of the author's knowledge, the study on the main effect and interaction effects of different design parameters on the seismic response of SRP-confined RC columns has not been reported. To assess the performance of RC columns and bridge piers, and control damages under lateral loads it is critical to properly define the plastic hinge region, which is the region exposed to maximum plastic deformation. However, accurate determination of the plastic hinge length remains a challenge.

Accordingly, this dissertation is aimed to examine the application of SRC for strengthening RC beams and RC columns based on experimental, analytical, numerical, and machine learning based studies. The specific objectives of this dissertation are as follows:

a) Investigate the structural performance of SRG-strengthened RC beams critical in shear based on an extensive experimental program that comprised tests on thirty-three (33) shear-deficient RC beams.
b) Investigate the effect of different factors (e.g., fabric density, bond scheme, strengthening configuration, and SRG/stirrups interaction) on the shear strengthening performance of the SRG system.
c) Investigate the influence of the shear span-to-depth ratio on the shear behavior of slender and deep RC beams strengthened with SRG.
d) Propose an analytical procedure for predicting the shear capacity of RC beams strengthened with SRG.
e) Investigate the use of the NSE technique for the SRG system and compare its performance with that of the conventional EB technique.

f) Propose ML-based accurate and reliable models for predicting the shear and flexural capacities of RC beams strengthened with SRG and inorganic composites in general.

g) Explore the effects of key design parameters and their interactions on the performance of seismically deficient rectangular cross-section RC bridge piers strengthened with SRP.

h) Propose an accurate and reliable ML-based model for predicting the PHL of rectangular RC columns and investigate the influence of different factors that influence the PHL.

1.3. Outline of the Dissertation

Considering the objectives of this study discussed above, the dissertation comprised three main parts, as shown in Figure 1.1. The first part deals with the experimental and analytical investigations of the application of SRG for strengthening of RC beams in shear. An extensive experimental program that comprised tests on thirty-three (33) shear-deficient RC beams was used to experimentally investigate the efficacy of SRG for strengthening of RC beams in shear. The second part focused on the application of machine learning for predicting the shear and flexural capacities of RC beams strengthened with SRG and inorganic composites in general. Finally, the third part deals with the application of steel reinforced composite, particularly, SRP for retrofitting RC columns and determining the plastic hinge length of RC columns using machine learning techniques.

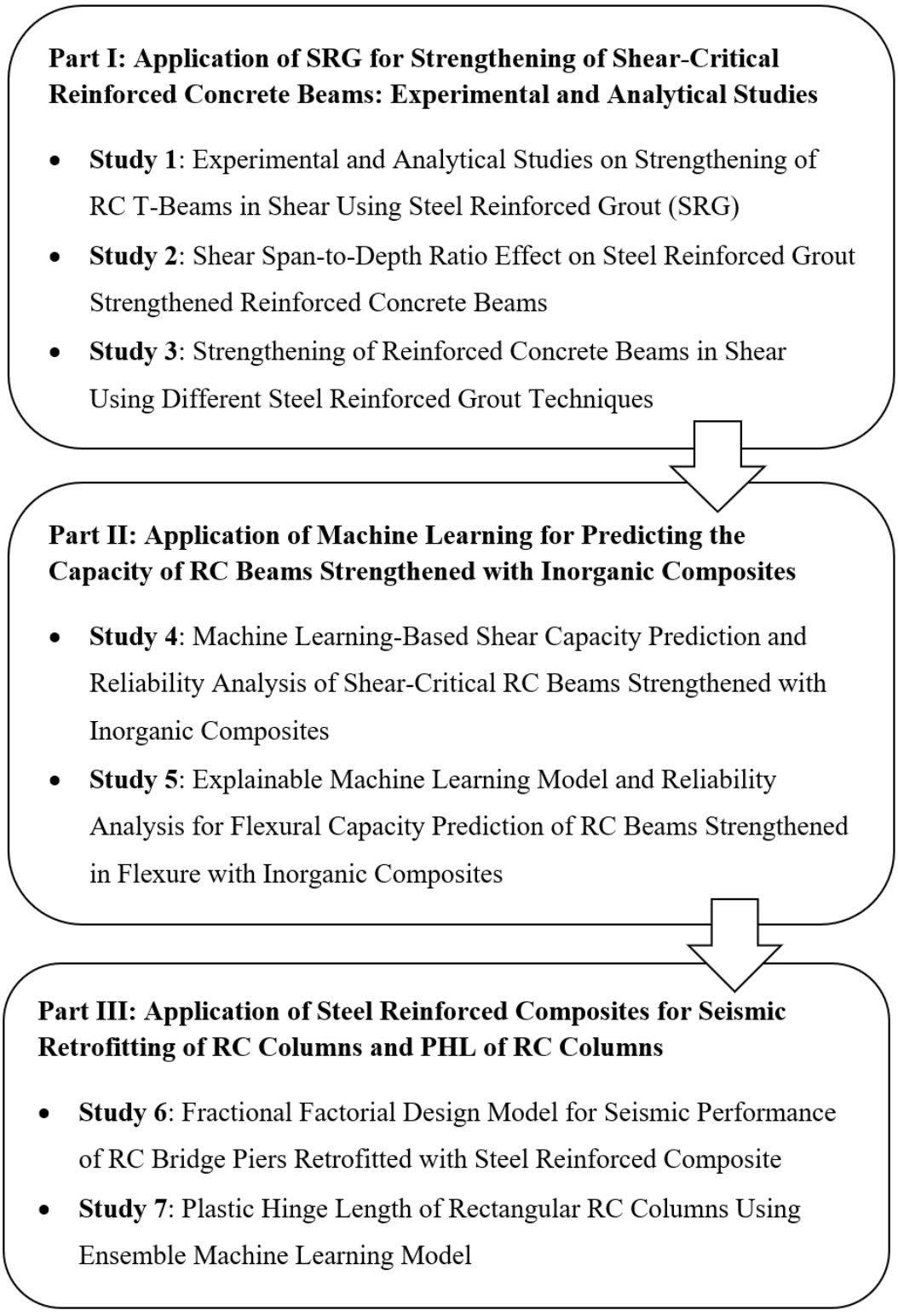

Figure 1.1. Outline of the dissertation body.

Chapter 2 (Study 1, 2, and 3) reports on the experimental and analytical studies on strengthening of RC beams in shear using steel reinforced grout.

Chapter 3 (Study 4 and **5)** proposes machine learning based predictive models and reliability analysis for shear capacity of RC beams strengthened in shear with inorganic composites, and explainable machine learning models and reliability analysis for flexural capacity prediction of RC beams strengthened in flexure with inorganic composites.

Chapter 4 (Study 6) investigates the main and interaction effects of different design parameters on the seismic response of RC bridge piers retrofitted with steel reinforced composite.

Chapter 5 (Study 7) proposes machine learning based predictive models for plastic hinge length of RC columns.

Chapter 6 provides the final conclusions based on the outcomes of this dissertation and recommendations for future studies.

All studies have been published in different journals such as *Composites Part B: Engineering, Engineering Structures, Case Studies in Construction Materials, and Journal of Structural Concrete*, as listed below.

[1] Wakjira TG, Ebead U. Experimental and analytical study on strengthening of reinforced concrete T-beams in shear using steel reinforced grout (SRG). *Composites Part B: Engineering* 2019;177:107368. https://doi.org/10.1016/j.compositesb.2019.107368.

[2] Wakjira TG, Ebead U. Shear span-to-depth ratio effect on steel reinforced grout strengthened reinforced concrete beams. *Engineering Structures* 2020;216:110737. https://doi.org/10.1016/j.engstruct.2020.110737.

[3] Wakjira TG, Ebead U. Strengthening of reinforced concrete beams in shear

using different steel reinforced grout techniques. *Structural Concrete* 2021;22:1113–27. https://doi.org/10.1002/suco.202000354.

[4] Wakjira TG, Ebead U, Alam MS. Machine Learning-Based Shear Capacity Prediction and Reliability Analysis of Shear-Critical RC Beams Strengthened with Inorganic Composites. *Case Studies in Construction Materials* 2022; 16: e01008. https://doi.org/10.1016/j.cscm.2022.e01008.

[5] Wakjira TG, Ibrahim M, Ebead U, Alam MS. Explainable machine learning model and reliability analysis for flexural capacity prediction of RC beams strengthened in flexure with FRCM. *Engineering Structures* 2022;255. https://doi.org/10.1016/j.engstruct.2022.113903.

[6] Wakjira TG, Nehdi ML, Ebead U. Fractional factorial design model for seismic performance of RC bridge piers retrofitted with steel-reinforced polymer composites. *Engineering Structures* 2020;221:111100. https://doi.org/10.1016/j.engstruct.2020.111100.

[7] Wakjira TG, Alam MS, Ebead U. Plastic hinge length of rectangular RC columns using ensemble machine learning model. *Engineering Structures* 2021;244:112808. https://doi.org/10.1016/j.engstruct.2021.112808.

CHAPTER 2: EXPERIMENTAL AND ANALYTICAL STUDY ON STRENGTHENING OF REINFORCED CONCRETE T-BEAMS IN SHEAR USING STEEL REINFORCED GROUT

2.1. Introduction

This chapter aims to investigate the structural performance of steel reinforced grout (SRG)-strengthened reinforced concrete (RC) beams critical in shear based on an extensive experimental program. The experimental campaign comprised a total of thirty-three (33) RC beams deficient in shear. In addition, an analytical procedure based on the simplified modified compression field theory (SMCFT) has been proposed to predict the shear capacity of SRG-strengthened RC beams. A total of three studies have been conducted in this chapter:

Study 1: Experimental and analytical study on strengthening of reinforced concrete T-beams in shear using steel reinforced grout.

[1] Wakjira TG, Ebead U. Experimental and analytical study on strengthening of reinforced concrete T-beams in shear using steel reinforced grout (SRG). *Composites Part B: Engineering* 2019;177:107368. https://doi.org/10.1016/j.compositesb.2019.107368.

Study 2: Shear span-to-depth ratio effect on steel reinforced grout strengthened reinforced concrete beams.

[2] Wakjira TG, Ebead U. Shear span-to-depth ratio effect on steel reinforced grout strengthened reinforced concrete beams. *Engineering Structures* 2020;216:110737. https://doi.org/10.1016/j.engstruct.2020.110737.

Study 3: Strengthening of reinforced concrete beams in shear using different steel reinforced grout techniques.

[3] Wakjira TG, Ebead U. Strengthening of reinforced concrete beams in shear using different steel reinforced grout techniques. *Structural Concrete* 2021;22:1113–27. https://doi.org/10.1002/suco.202000354.

2.2. Description of Experimental Program

The experimental campaign comprised a total of thirty-three (33) RC beams deficient in shear grouped into three sets. In the first set of the experimental program, eleven (11) shear-deficient RC T-section beams are included, while the second and third sets of the experimental program comprised a total of twenty-two (22) shear-deficient rectangular beams. A detailed discussion on the specimen properties, strengthening system, and test setup is presented in this section.

2.2.1. Material characterization

The test beams were cast using a single batch of ready-mixed concrete with a water-to-cement ratio of 0.45. The average compressive strength (f_c') of the concrete was 34 MPa (SD = 1.2 MPa), which was obtained from direct compression tests conducted on eight concrete cylinders (100 mm diameter and 200 mm height) as per ASTM C39/C39M [113] on the day of beam testing. Longitudinal and transverse reinforcement (outside the test region) was provided by BS 4449:2005 [114] Grade 500B steel deformed bars. The test beams were under-reinforced in shear within the test region to promote shear failure prior to flexural failure. Two different sizes of stirrups were used for the T-beams (6 mm diameter bars within the test region for beams reinforced in shear within the test region and 8 mm diameter stirrups outside the test region). The longitudinal compressive and tensile reinforcement bars used in T-section beams were 20 mm and 25 mm diameter deformed bars, respectively. For the rectangular section beams, both longitudinal compressive and tensile reinforcements used 25 mm diameter deformed bars. The average mechanical properties of the

reinforcement bars were determined based on tensile tests conducted on five samples for each bar diameter, and the results are presented in Table 2.1.

Table 2.1. Properties of the steel reinforcement bars

Diameter (mm)	Yield strength (MPa)	Tensile strength (MPa)	Elastic modulus (GPa)	Yield strain (%)
D6	234	420	207	1.17
D8	535	610	207	0.258
D16	562	633	241	0.233
D20	584	659	216	0.269
D25	588	673	244	0.241

The SRG composite used for the shear strengthening was composed of steel fabrics embedded within the associated geo-mortar. The steel fabrics were made of ultra-high tensile strength (UHTS) galvanized steel 3 × 2 cords obtained by assembling five filaments, of which three were held straight and two wrapped with a high torque angle around the straight filaments, as shown in Figure 2.1a. The steel cords were fixed to a fiber glass micro mesh to facilitate the installation as shown in Figure 2.1b and c. Two different types of commercially available steel fabrics were used in the SRG composite known by their commercial names as GeoSteel G600 (Figure 2.1b) and GeoSteel G1200 (Figure 2.1c), indicating the approximate fiber weight in g/m^2. The latter has 3.14 cords/cm, while the former has 1.57 cords/cm. In this study, these fabrics are considered as low-density and high-density fabrics, respectively.

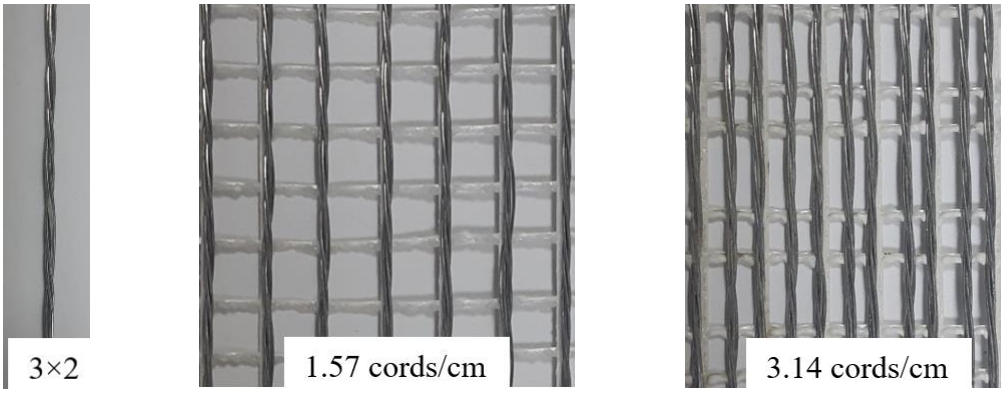

(a) (b) (c)

Figure 2.1. Steel cords (a) and steel fabrics: low-density fabrics, G600, (b) and high-density fabrics, G1200, (c).

Table 2.2 presents the geometric and average mechanical properties of the steel fabrics and the associated geo-mortar. The area of the steel fibers per unit width was 0.084 mm and 0.169 mm for the low- and high-density fabrics, respectively [115], as listed in Table 2.2. The steel fibers had the tensile strength, elastic modulus, and ultimate strain of 3 GPa, 190 GPa, and 2.0%, respectively [115], as listed in Table 2.2. The steel fabrics were embedded within a manufacturer recommended eco-friendly thixotropic mineral mortar, so-called Geolite [115]. The average 28 d tensile strength of the matrix was 8 MPa, while its compressive and bond strengths were 50 MPa and 2 MPa, respectively, as supplied by the manufacturer [115]. The test on the steel fabrics showed an average tensile strength of 3134.4 MPa and an elastic modulus of 183.5 MPa [31]. Moreover, the SRG composite has an average modulus of elasticity of 168 GPa as obtained from the tensile tests on SRG coupons [31].

Table 2.2. Properties of the steel fabrics and the associated mortar

Properties	G600	G1200	Geo-mortar
Equivalent thickness (mm)	0.084	0.169	–
Area of cord (mm^2)	0.538	0.538	–
Fiber weight (g/m^2)	600	1200	–
Density (cords/cm)	1.57	3.14	–
Tensile strength (MPa)	3000	3000	8
Modulus of elasticity (GPa)	190	190	22
Ultimate break wrap (%)	2	2	–
*Compressive strength (MPa)	–	–	50
*Bond strength (MPa)	–	–	2

*Average of 28 days'

2.2.2. Fabrication of test specimens

2.2.2.1. T-section beams

Figure 2.2a–d show the geometric and reinforcement details of the T-section beams. The beams had an overall length of 2550 mm and web and flange cross-sectional dimensions of 180 × 300 mm and 450 × 100 mm, respectively. The test beams were under-reinforced in shear within the test region to promote shear failure prior to flexural failure. The internal transverse reinforcement within the shear span was comprised of either none, 6 mm steel stirrups spaced at 300 mm, or 6 mm steel stirrups spaced at 150 mm, as shown in Figure 2.2a–d.

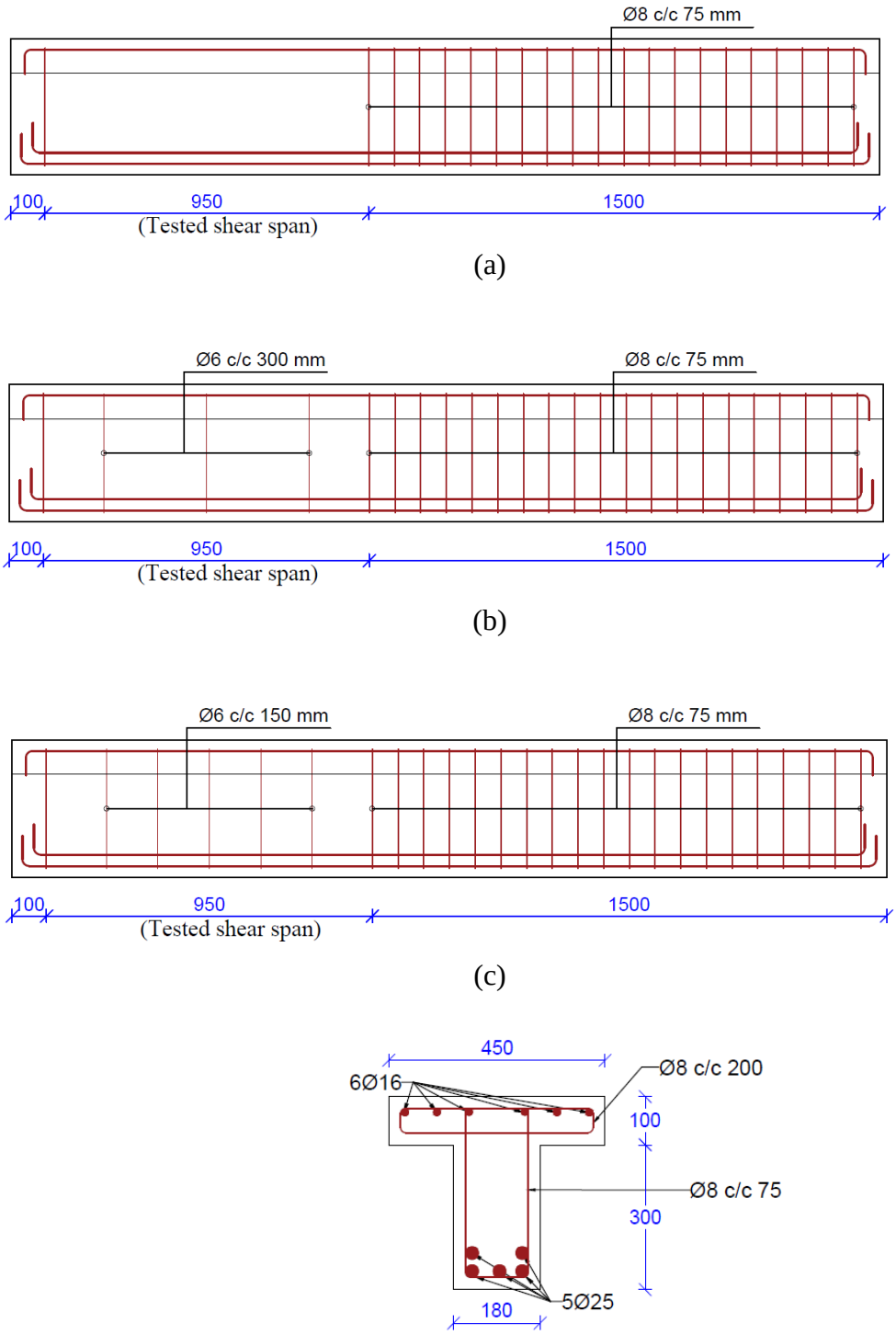

Figure 2.2: Beam longitudinal and transverse reinforcement: (a) Group-1; (b) Group-2; (c) Group-3; and (d) cross-sectional detail outside the test region (units: mm).

2.2.2.2. Rectangular section beams

The rectangular section beams have an overall length of 2550 mm and a rectangular cross-section of 180 mm × 400 mm (width × depth), as shown in Figure 2.3a. The flexural reinforcement comprises five D20 bars at the bottom and two D20 bars at the top of the beam (Figure 2.3a). The internal transverse reinforcement comprises D8 stirrups with 75 mm spacing outside the shear span. The beams were under reinforced in shear; that is, no shear reinforcement was used in the critical shear span. Four different shear span-to-depth (a/d) ratios were considered, specifically, a/d = 3.10 (a = 1035 mm, Figure 2.3a) and a/d = 2.60 (a = 870 mm, Figure 2.3b), both representing slender beams; and a/d = 2.10 (a = 700 mm, Figure 2.3c) and 1.60 (a = 535 mm, Figure 2.3d), both representing deep beams.

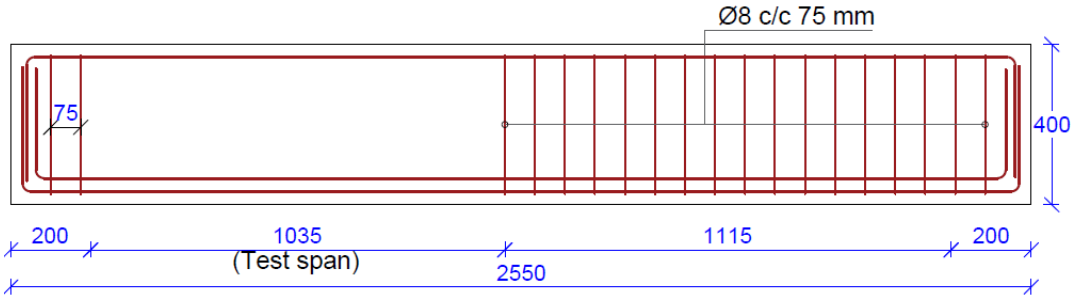

(a) a/d = 3.10

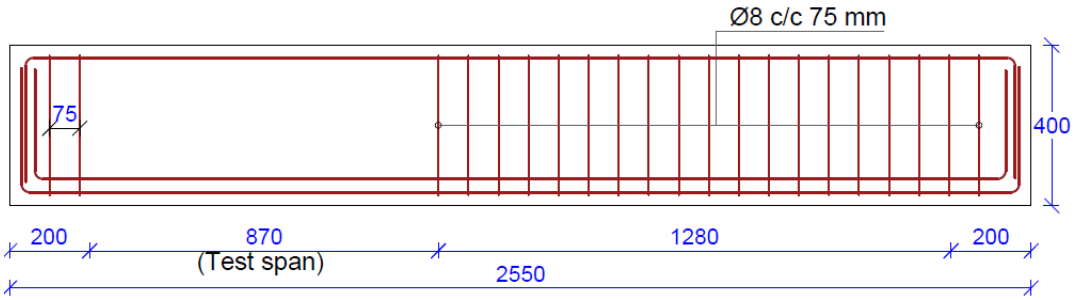

(b) a/d = 2.60

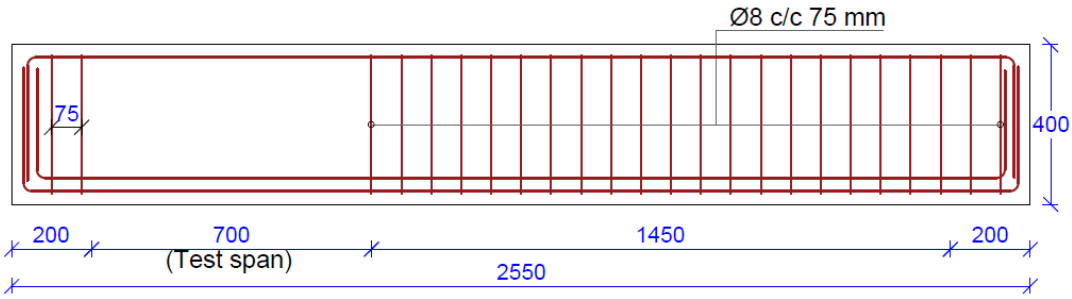

(c) a/d = 2.10

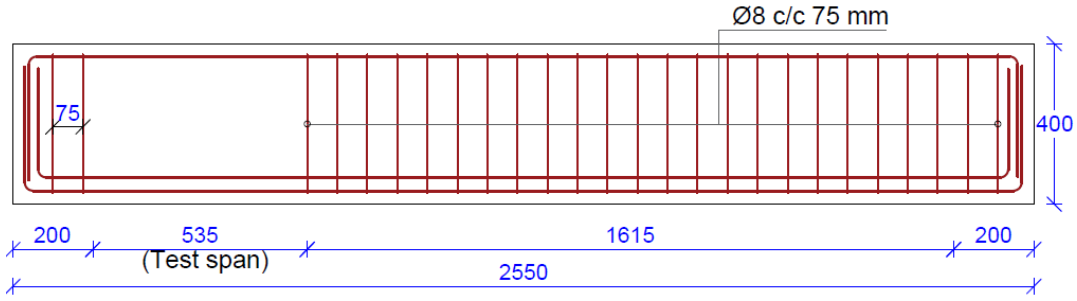

(d) a/d = 1.60

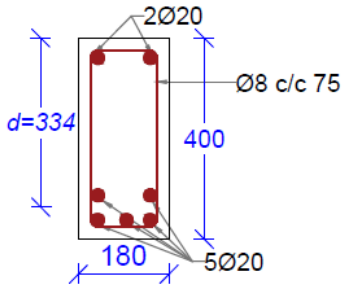

(e)

Figure 2.3: Rectangular beam detail: Longitudinal detail (a)–(d), cross-sectional detail outside the critical shear span (e), (all dimensions are in mm).

2.2.3. Test matrix and investigated parameters

As discussed earlier, a total of thirty-three (33) beam specimens with either a rectangular section or T-section are included in the experimental campaign.

2.2.3.1. Study 1: Experimental and analytical study on strengthening of reinforced concrete T-beams in shear using steel reinforced grout

The first study investigated the structural performance of T-section RC beams

strengthened with externally bonded (EB) SRG, for the first time. The test parameters investigated were as follows: (a) steel fabric density, (b) bond scheme, and (c) amount of internal shear reinforcement within the critical shear span, SRG/stirrups interaction. For this purpose, an experimental investigation has been conducted on eleven RC T cross-section beams. Eight of the beams were strengthened by two layers of EB-SRG system, and three, which were unstrengthened, were used as reference specimens. The test matrix for the first study is presented in. The specimens were categorized into three groups based on the amounts of stirrups within the shear span, as presented in Table 2.3.

Group-1 beams have no stirrup (Figure 2.2a), whereas Group-2 (Figure 2.2b) and Group-3 (Figure 2.2c) specimens are reinforced with 6 mm-diameter double-legged stirrups spaced at 300 mm and 150 mm, respectively. Outside the test region, the internal shear reinforcement comprised 8 mm double-legged stirrups placed at 75 mm center-to-center (c/c), as shown in Figure 2.2a–d. The flexural reinforcement comprised five 25 mm-diameter bars in two layers at the bottom and six 16 mm-diameter bars in one layer in the flange, as shown in Figure 2.2d.

The specimens differed from each other by the test variables as follows:

a) Density of the steel fabrics: Low density (1.57 cords/cm) and high density (3.14 cords/cm) steel fabrics;
b) Bond scheme: Strengthening can be performed in side bonded, U-jacketing, or complete bond schemes. However, the use of a complete/full bond scheme is not feasible in beams because of the presence of concrete slabs [5]. Therefore, the first two types of bond schemes, namely side bonded and U-wrapped schemes were adopted in this study; and

c) Amounts of stirrups within the shear zone: Three different amounts of stirrups (without stirrup, ϕ6 c/c 300, and ϕ6 c/c 150 mm) are used for the specimens strengthened with U-jacketing to study the SRG/stirrups interaction.

Table 2.3. An experimental program for Study 1

Fabric density, Bond scheme	Stirrups within the test region		
	None (Group-1)	ϕ*6 c/c* 300 (Group-2)	ϕ*6 c/c* 150 (Group-3)
Reference (unstrengthen)	B1	B2	B3
L, U	B1-U-L	B2-U-L	B3-U-L
H, U	B1-U-H	B2-U-H	B3-U-H
L, S	B1-S-L	–	–
H, S	B1-S-H	–	–

S for side bonded; U for U-wrap; L for low density; H for high density.

As presented in Table 2.3, the reference beams and the strengthened beams are labeled as BW and BW-X-Y, respectively, where "B"- stands for beam; "W"- refers to the specimen group (1, 2, and 3 in Table 2.3), "X"- denotes the bond scheme ("S"- for side bonded, "U"- for U-jacketing); and "Y"- corresponds to the fabric density ("L"- for low-density fabrics, "H"- for high-density fabrics). Therefore, for instance, Specimen B1-U-H is a Group-1 beam (without stirrup) strengthened with U-wrapped SRG comprising high-density steel fabrics

2.2.3.2. Study 2: Shear span-to-depth ratio effect on steel reinforced grout strengthened reinforced concrete beams

This study further investigated the potential application of SRG as shear strengthening of deficient RC beams and for the first time examined the influence of the critical shear span-to-effective depth (*a/d*) ratio on the shear behavior of both deep and slender beams strengthened with SRG. For this purpose, an experiment was conducted on 12 shear-critical rectangular RC beams, as presented in Table 2.4.

The primary test parameter was the influence of *a/d* ratio on the performance of SRG-strengthened beams in shear. Four different *a/d* ratios were considered, specifically, *a/d* = 3.10 and *a/d* = 2.60, both representing slender beams; and *a/d* = 2.10 and 1.60, both representing deep beams. Thus, the effectiveness of SRG for the shear strengthening of both slender and deep beams was investigated in this study. The second test parameter was the density of the steel fabrics (1.57 and 3.14 cords per centimeter). The test specimens were grouped into four series (S1: *a/d* = 3.10; S2: *a/d* = 2.60, S3: *a/d* = 2.10, and S4: *a/d* = 1.60) on the basis of their span-to-depth ratio, as shown in Figure 2.3a–d and Table 2.4. Each series was composed of one reference beam, without SRG strengthening, and two beams strengthened in shear with SRG.

Table 2.4. An experimental program for Study 2

Beam ID	Beam series	Fabric density
Series 1 (*a/d* = 3.10)		
BS1	S1	–
BS1-L	S1	Low
BS1-H	S1	High
Series 2 (*a/d* = 2.60)		
BS2	S2	–
BS2-L	S2	Low
BS2-H	S2	High
Series 3 (*a/d* = 2.10)		
BS3	S3	–
BS3-L	S3	Low
BS3-H	S3	High
Series 4 (*a/d* = 1.60)		
BS4	S4	–
BS4-L	S4	Low
BS4-H	S4	High

The specimens were identified using the “BSi-Y” label, where BS stands for beam series, the numeral i shows the beam series number, and Y stands for the SRG

fabric density ("L" for low-density fabrics with 1.57 cords per cm density, and "H" for high-density fabrics with 3.14 cords/cm density), as listed in Table 2.4. Only the first two characters with beam series number are used for the reference beams, as presented in Table 2.4. For instance, Specimen BS1-H features a/d = 3.10 and is strengthened with high-density SRG fabrics.

2.2.3.3. Study 3: Strengthening of reinforced concrete beams in shear using different steel reinforced grout techniques

In the third study, the use of the NSE technique for the SRG system was investigated, for the first time, and its performance was compared with that of the conventional EB technique. For this purpose, thirteen full-scale rectangular RC beams with identical geometry and internal reinforcement (Figure 2.3b) were constructed and tested. Twelve beams were strengthened in shear with different SRG systems applied using either the EB or NSE technique, whereas one beam was used as a reference. The beams were under reinforced in shear; that is, no shear reinforcement was used in the critical shear span of 0.87 m, as shown in Figure 2.3b and Figure 2.4a.

The beams were designed to study the effect of the following parameters:

(1) Steel fabric density (1.57 cords/cm and 3.14 cords/cm),

(2) Presence of a U-wrap scheme,

(3) SRG strengthening amounts in a continuous SRG strip (Figure 2.4b) or discontinuous 190 mm wide strips with 100 mm clear spacing (Figure 2.4c), and

(4) Type of strengthening technique (EB versus NSE for discontinuous configuration).

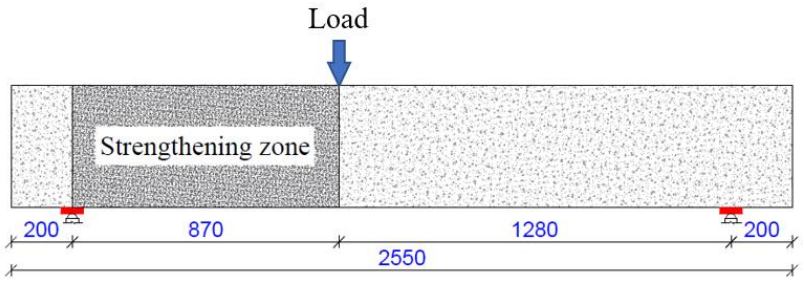

(a) Strengthening zone

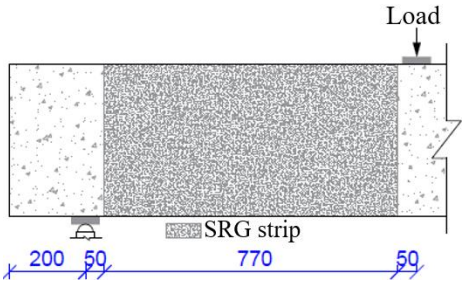

(b) Continuous configuration

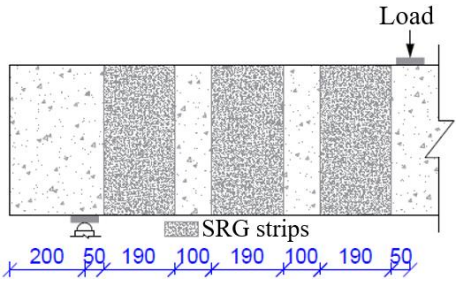

(c) Discontinuous configuration

Figure 2.4: Details of tested beams in Study 3 (dimensions in mm).

The test beams and the test parameters are listed in Table 2.5. The reference beam is labeled as R. The strengthened beams are identified using the notation VWXY: V denotes the strengthening technique, where “E” and “N” represent EB-SRG and NSE-SRG, respectively; W denotes the geometric configuration, where “C” and “D” represent continuous and discontinuous configurations, respectively; X denotes the strengthening scheme, where “U” and “S” represent U-jacket and side bonded, respectively; and Y denotes the density of the steel fabrics, where “H” and “L” represent high-, and low-density fabrics, respectively, as presented in Table 2.5. For instance, ECUH stands for the specimen strengthened with an externally bonded continuous U-jacket of SRG made of high-density steel fabrics. It is worth mentioning here that three of the specimens are taken from Study 2, as listed in Table 2.5.

Table 2.5. Details of the tested beam specimens in Study 3

Beam ID	Technique	Strengthening scheme	SRG configuration, fabric density
[a]R	Reference	–	–
[a]ECUH	EB	U-wrap	C, H
[a]ECUL	EB	U-wrap	C, L
EDUH	EB	U-wrap	D, H
EDUL	EB	U-wrap	D, L
EDSH	EB	Side bonded	D, H
EDSL	EB	Side bonded	D, L
ECSH	EB	Side bonded	C, H
ECSL	EB	Side bonded	C, L
NDUH	NSE	U-wrap	D, H
NDUL	NSE	U-wrap	D, L
NDSH	NSE	Side bonded	D, H
NDSL	NSE	Side bonded	D, L

[a] Specimens included in Study 2.

2.2.4. Strengthening procedures

The beams in Study 1 were strengthened with the EB-SRG either on the lateral sides or applied in the U-shape around the web of the beam. The beams in Study 2 were strengthened with EB-SRG applied in the side bonding scheme, while beams in Study 3 were strengthened with either EB-SRG or NSE-SRG applied in either side bonding scheme or U-wrapped scheme.

The strengthening system for all strengthened beams utilized two layers of unidirectional steel fiber sheets in the SRG composite. In the EB-SRG, the concrete surface was sandblasted and roughened prior to the installation of the SRG, unlike the NSE-SRG that does not require surface preparation owing to the inherited roughened surface due to removing the concrete cover during creating the grooves.

Figure 2.7a–c and Figure 2.6a–c show the relevant steps related to the application of SRG for the EB-SRG and NSE-SRG strengthened rectangular beams,

respectively. The SRG composite in the NSE-SRG system is installed into pre-cut grooves opened on the concrete cover of the lateral faces and/or bottom face of the beam. The strengthening procedure was: 1) the surfaces of the beams were sandblasted and prepared for the EB-SRG strengthened beams; 2) the prepared surface in the EB-SRG and prepared grooves in the NSE-SRG beams are further cleaned and dampened with water; 3) first coat of 4 mm thick geo-mortar is applied on the prepared surface and grooves as per manufacturers' recommendation [115], as shown in Figure 2.5a for the EB-SRG and Figure 2.6a for the NSE-SRG; 4) the steel fabrics are cut as per the desired size, installed and fully impregnated with the matrix, as shown in Figure 2.5b; 5) the second coat of 4 mm thick matrix and second fabric layer installed and fully impregnated with the underlying mortar layer, as shown in Figure 2.6b for the NSE-SRG; 6) the final fabric layer is covered with the mortar (4 mm thick) and finished (Figure 2.5c and Figure 2.6c); 7) the specimens cured for at least 28-days before testing. Similarly, Figure 2.7 shows the strengthening procedure for the T-section beams.

(a) Application of first mortar layer

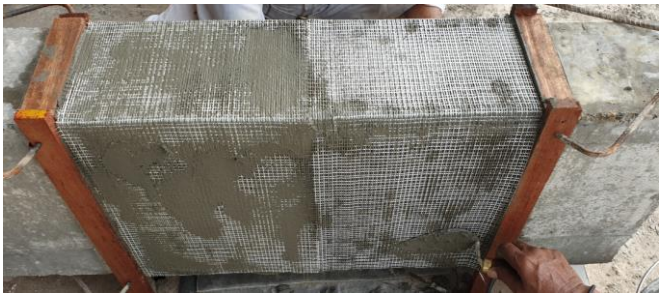

(b) Installation of first fabric layer and impregnation with an underlying mortar layer

(c) Finished surface

Figure 2.5: Application of EB-SRG strengthening for rectangular section beams.

(a) Application of geo-mortar in the prepared groove

(b) Steel fabrics being installed and impregnated with the matrix

(c) Final finished surface

Figure 2.6: Application of the SRG composite for the NSE-SRG.

(a) Bonding the first layer of the steel fabrics and impregnating with the matrix

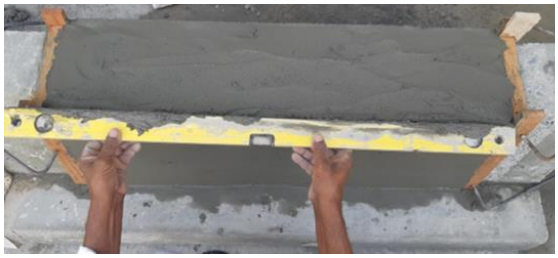

(b) Application of final mortar layer and surface finishing

(c) Final finished surface

Figure 2.7: Strengthening procedures for T-section beams.

2.2.5. Test program and instrumentation

The experimental setup for beam testing and the instrumentation used during the test are shown in Figure 2.8. The test beams were loaded in a three-point bending apparatus using the displacement control protocol at a loading rate of 0.25 mm/minute. The load was applied using an Instron 1500HDX static universal testing machine with a maximum load capacity of 1500 kN and a maximum stroke of 150 mm. The test specimens were instrumented to monitor different parameters. The reaction at each support is measured using load cells installed under the beam at each support. The displacement under the loading point was monitored using two linear variable displacement transducers positioned under the point of load application on both sides of the beam. Strain gauges were used to measure the compressive strains in concrete and tensile strains in the internal reinforcement steel bars.

For the T-section beams reinforced internally with stirrups, Figure 2.9a–c show the location of the strain gauges used to monitor the strains in the stirrups. For Group-2 and Group-3 specimens, the stirrups within the test region were instrumented with strain gauges (S1, S2, S3, S4, and S5) at their mid-height to monitor the strains developed in each stirrup as shown in Figure 2.9b and c. A data acquisition system was used to record the applied load, corresponding deflection, reaction at each support, and strain gauges readings.

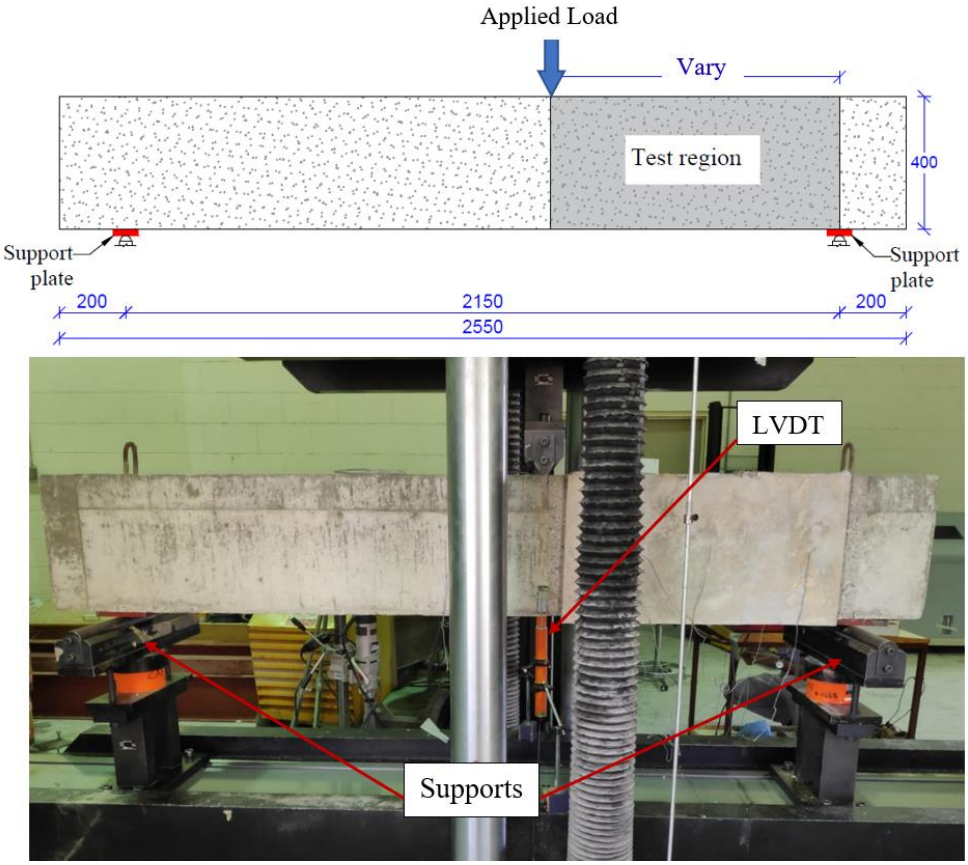

Figure 2.8: Test setup (all dimensions are in mm).

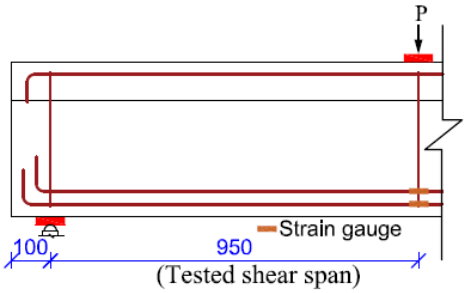

(a) Group-1

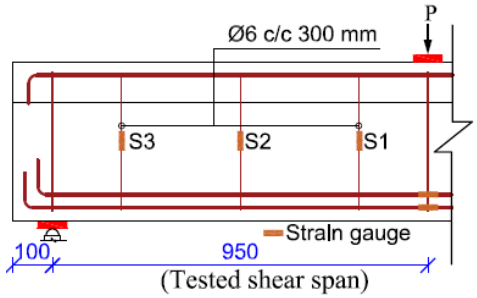

(b) Group-2

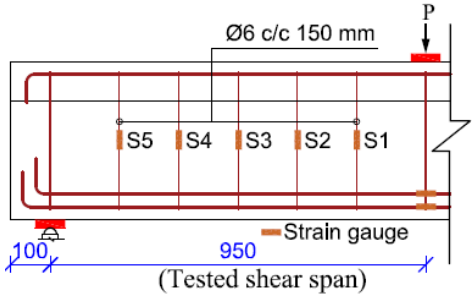

(c) Group-3

Figure 2.9: Positions of strain gauges for internal reinforcements in T-section beams.

2.3. Results and Discussion

This section presents and discusses the experimental results for all three studies.

2.3.1. Discussion of experimental results in Study 1

The test results are presented in Table 2.6 in terms of the ultimate load, P_u; increase in P_u; deflection under the loading point at the ultimate load, δ_u; increase in δ_u relative to the corresponding reference beam; energy absorption ratio; and strains. The experimental results indicate that the SRG system is effective for strengthening of shear-deficient RC T-beams, however, its performance varied with the test parameters.

Table 2.6. Test results from Study 1

Beam ID	P_u (kN)	ΔP_u (%)	δ_u (mm)	$\Delta\delta_u$ (%)	$\varepsilon_{c,u}$ (‰)	$\varepsilon_{t,u}$ (‰)	ψ (kN.mm)	ψ/ψ_r
Group-1								
B1	204	–	2.39	–	0.430	0.789	280.5	–
B1-U-H	349	71	6.17	158	1.124	1.356	1452	5.18
B1-U-L	337	65	5.29	121	1.049	1.103	799.9	2.85
B1-S-H	306	50	4.30	79.9	0.707	1.293	1034	3.68
B1-S-L	290	42	3.99	66.9	0.735	1.282	734.1	2.62
Group-2								
B2	283	–	6.78	–	0.679	1.154	1173	–
B2-U-H	385	36	10.0	47.5	0.817	1.513	2399	2.04
B2-U-L	356	26	8.52	25.6	1.443	1.258	1850	1.58
Group-3								
B3	331	–	8.13	–	2.142	1.312	1812	–
B3-U-H	403	22	11.4	40.7	0.497	1.762	2903	1.60
B3-U-L	364	10	9.26	13.9	1.242	1.727	2222	1.23

2.3.1.1. Load versus deflection response

The responses of the tested specimens are presented in Figure 2.10a–c in the form of load versus deflection curves for the Group-1, -2, and -3 specimens, respectively. As shown in these figures, a linear relationship is observed until failure for all the tested beams. A significant increase in the shear capacity was observed for all strengthened beams, as can be seen in Figure 2.10a–c and Table 2.6. The reference beam of Group-1, B1, failed in shear at an ultimate load of 204 kN after the formation of diagonal shear cracks in the critical shear span. All strengthened specimens failed in shear at an ultimate load considerably greater than that of B1, as shown in Figure 2.10a. The ultimate loads attained by the specimens strengthened with U-wrapped SRG, namely B1-U-H and B1-U-L, were 349 kN and 337 kN, yielding 71% and 65% increases in P_u relative to B1, respectively. Their corresponding specimens strengthened with side bonded SRG, namely B1-S-H and B1-S-L, failed at ultimate

loads of 306 and 290 kN representing 50% and 42% increases in P_u relative to B1, respectively. In all of these specimens, the failure occurred because of premature debonding of the SRG laminate.

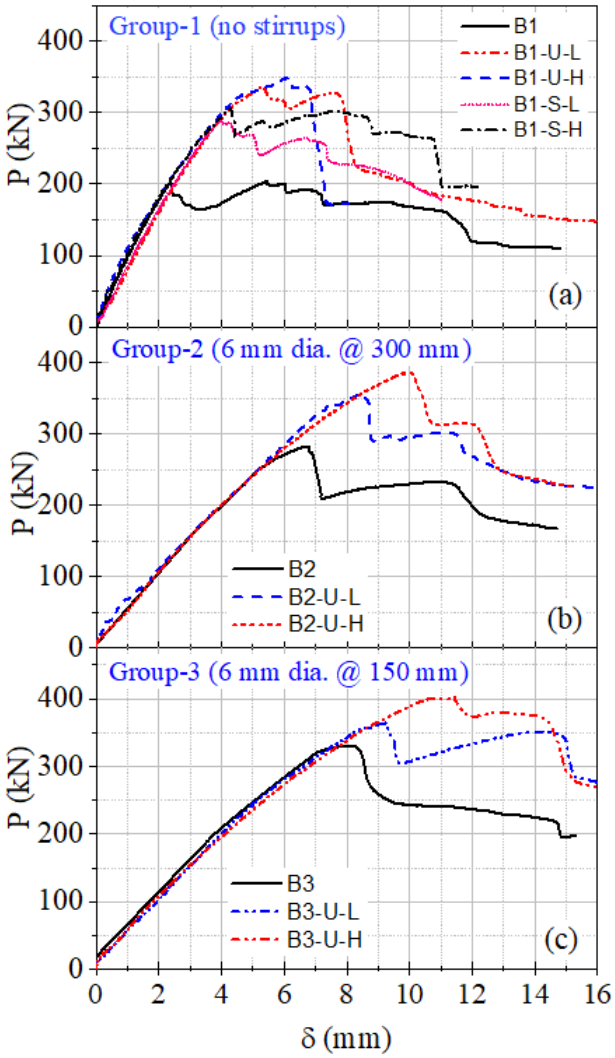

Figure 2.10: Load versus deflection diagrams.

The Group-2 and -3 beams were internally reinforced with 6 mm-diameter double-legged stirrups placed at 300 mm and 150 mm c/c intervals, respectively. The reference specimen, B2, failed at an ultimate load of 283 kN, and the strengthened beams B2-U-H and B2-U-L failed at 385 kN and 356 kN, corresponding to 36% and 26% increases in P_u relative to B2, respectively, as shown in Figure 2.10b and Table

2.6. Specimens B3-U-H and B3-U-L reached peak loads of 403 kN and 364 kN, representing 22% and 10% increases in the load capacity relative to the reference beam, B3 (331 kN), respectively, as shown in Figure 2.10c and Table 2.6. The reference beams B2 and B3 exhibited a typical shear failure, while the failure in the strengthened beams in both groups was attributed to the peeling of SRG laminate off the concrete substrate.

The deflections at P_u under the loading point for the reference specimens B1, B2, and B3 were 2.39 mm, 6.78 mm, and 8.13 mm, respectively, as shown in Figure 2.10a–c and Table 2.6. For the strengthened beams, the maximum deflections, δ_u, at P_u were 6.17 mm, 10.0 mm, and 11.4 mm for Group-1, -2, and -3 beams, which were increases of 158%, 47.5%, and 40.7% compared to the reference beams, respectively, as can be seen in Figure 2.10a–c and Table 2.6. The provision of the internal shear reinforcement within the critical shear span increased the beam deflection at P_u, however, it reduced the increase in δ_u attributed to SRG system. The specimens from Group-1 (140% increase in δ_u on average), without stirrups within the test region, exhibited a greater than 3.8 times increase in the deflection at the ultimate load relative to that for Group-2 specimens (36.6% increase in δ_u on average), as presented in Table 2.6. In addition, an increase in the number of stirrups within the test region in Group-3 specimens further decreased the increase in δ_u to 27.3% attributed to SRG strengthening, as presented in Table 2.6.

2.3.1.2. Effect of investigated parameters on load carrying capacity

Figure 2.11a–c show the effect of the test variables on the load-carrying capacity enhancement. As shown in these figures, the load-carrying capacity of the strengthened beams is significantly affected by the test parameters. Specimens strengthened with U-wrapped SRG exhibited higher gain in P_u compared to those strengthened with side bonded SRG counterparts, as reported from Group-1 specimens, as shown in Figure

2.11a. For instance, Specimen B1-U-L reached a higher ultimate load of 337 kN with respect to specimen B1-S-L (290 kN) resulting in a 23% higher gain in P_u. The effectiveness of the U-wrapped SRG in terms of the increase in P_u was approximately 1.5 times that of the side bonded SRG on average.

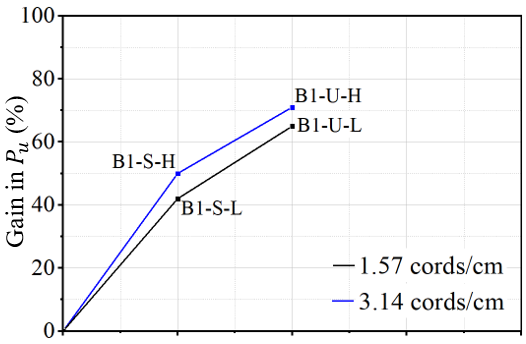

(a) Bond scheme

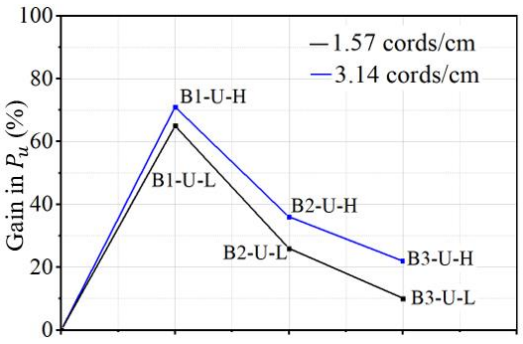

(b) Internal shear reinforcement

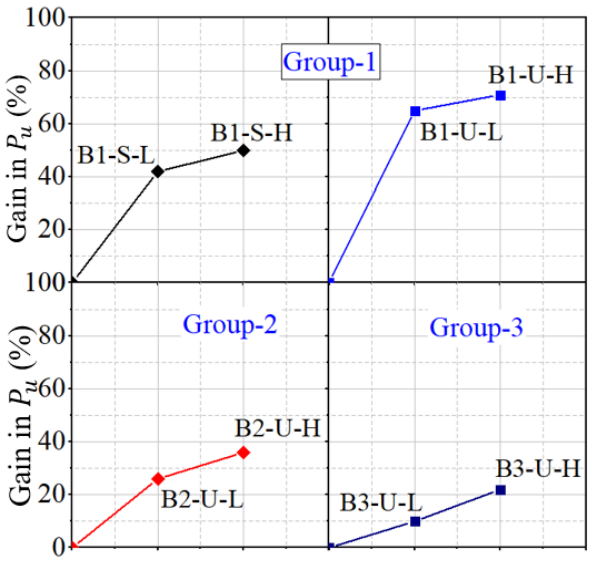

(c) Fabric density

Figure 2.11: Effect of the test parameters on the percentage gain in the load-carrying capacity, Study 1.

The SRG/stirrups interaction was found to have a dominating role in the load-carrying capacity of the strengthened beams. Specimens with the highest internal shear

reinforcement ratio within the critical shear span exhibited a lower contribution of SRG than those with fewer or no stirrup, as shown in Figure 2.11b. For instance, the provision of stirrups within the shear span for beams strengthened with low-density SRG fabrics decreased the increases in the load-carrying capacity to less than half of that in the specimens without stirrups, as can be seen in Figure 2.11b and Table 2.6 (comparing B1-U-L, 65%, and B2-U-L, 26%). In addition, the shear capacity enhancement because of SRG-strengthening was further reduced with an increased number of stirrups within the shear span, as shown in Figure 2.11b (Group-2 versus Group-3 beams). For the fabric density, an increase in the density of the steel fabrics resulted in a greater increase in the load-carrying capacity of the beams, regardless of the wrapping scheme and the internal shear reinforcement ratio, as can be seen in Figure 2.11c.

2.3.1.3. Failure modes and concrete crack behavior

All tested beams failed in shear before flexural bar yielding. This can be observed by the tensile strains in the flexural bars, as shown in Figure 2.12a–c, which show the load versus tensile strains in the longitudinal reinforcement for specimens of Group-1, -2, and -3, respectively. In addition, the compressive strains in the concrete at the ultimate load are below the concrete crushing point (3.5‰), as presented in column 8 of Table 2.6. As shown in Figure 2.12a–c and column 9 of Table 2.6, the SRG system significantly increased the tensile strains developed in the flexural bars of the strengthened beams relative to the corresponding reference beams, which indicates that it was effective in delaying the brittle shear failure.

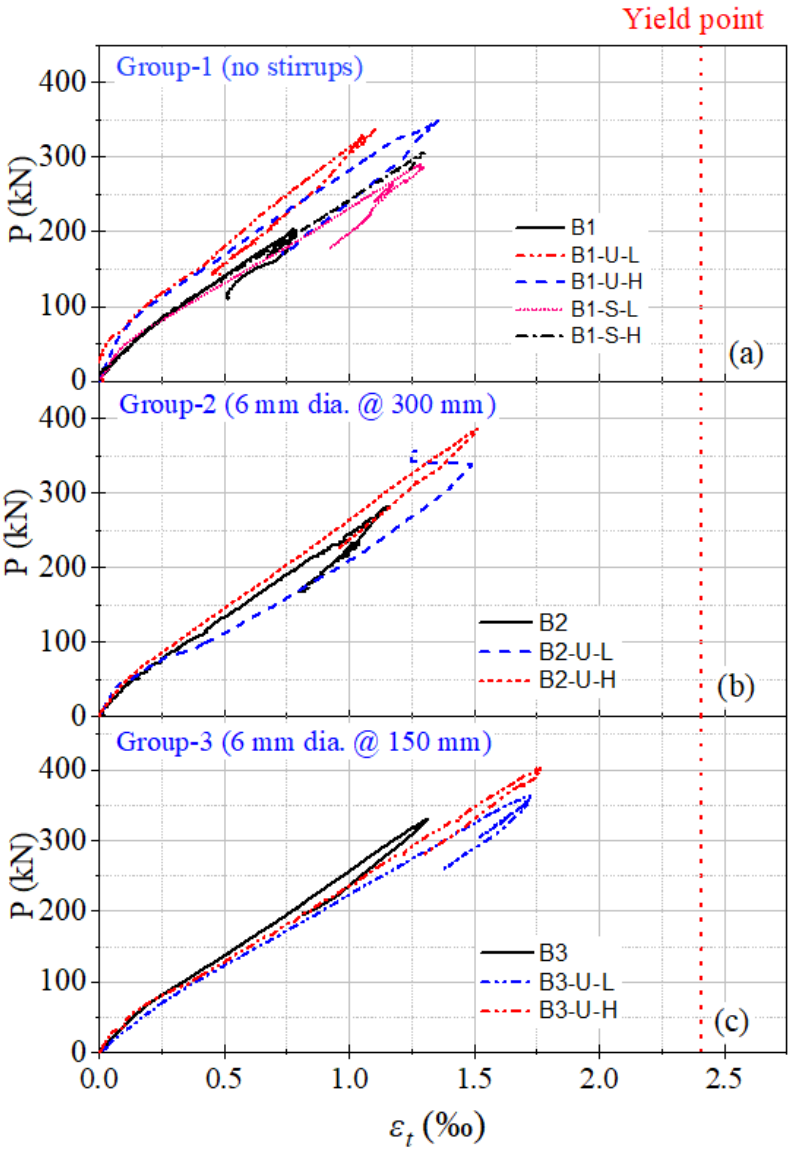

Figure 2.12: Load versus strains in the longitudinal tensile reinforcement bars, Study 1.

The failure patterns of the tested beams are shown in Figure 2.13a–h. The reference beams exhibited a typical shear failure characterized by a main diagonal shear crack within the test region, as shown in Figure 2.13a and b for Specimens B1 and B2, respectively. The failure in all strengthened beams was accompanied by debonding of the SRG laminate from the concrete with or without the concrete cover. The specimens strengthened with the side bonded SRG failed in shear attributed to the detachment of the SRG laminate with the concrete cover, as shown in Figure 2.13c and d for

Specimens B1-S-H and B1-S-L, respectively. Unlike the U-wrapped SRG strengthened beams, cracks were visible on the surface of the specimens strengthened with side bonded SRG laminate, as shown in Figure 2.13c and d. The crack propagation of the specimens strengthened with U-wrapped SRG could not be monitored during the test. These specimens failed because of SRG debonding with no major cracks observed in the SRG laminate, as shown in Figure 2.13e–h, with the exception of Specimen B2-U-H, in which cracks appeared on the surface of SRG that has not increased. The SRG laminate was carefully removed after completion of the test to examine the actual cracking patterns and extent on all the strengthened beams. Following the removal of the SRG laminate, a major diagonal shear crack was observed on the beam surface beneath the SRG, as shown in Figure 2.13h for Specimen B1-U-H. Specimens strengthened with SRG comprising high-density fabrics were associated with fabric slippage, as shown in Figure 2.13g for Specimen B3-U-H, while no fabric slippage was observed in specimens strengthened with low-density fabric SRG. This can be explained in terms of the degree of fiber impregnation with the matrix (geo-mortar). Wider roving spacing in low-density fabrics has a higher degree of fiber-matrix impregnation, resulting in an improved fabric/matrix bond and, therefore, avoiding fabric slippage within the matrix.

(a) B1

(b) B2

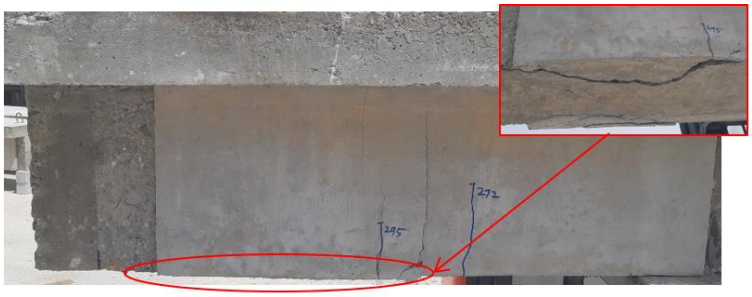

(c) B1-S-H

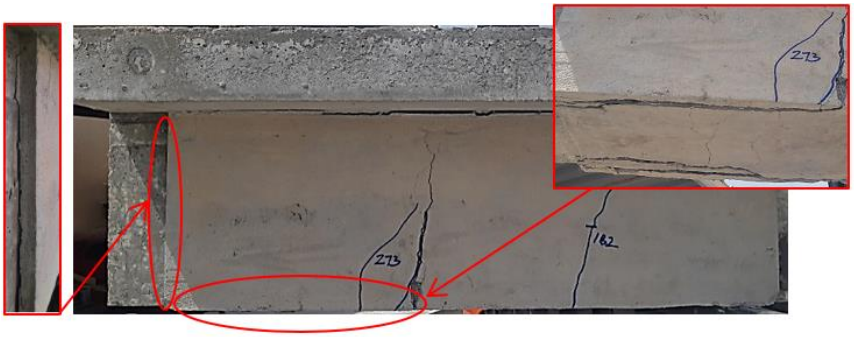

(d) B1-S-L

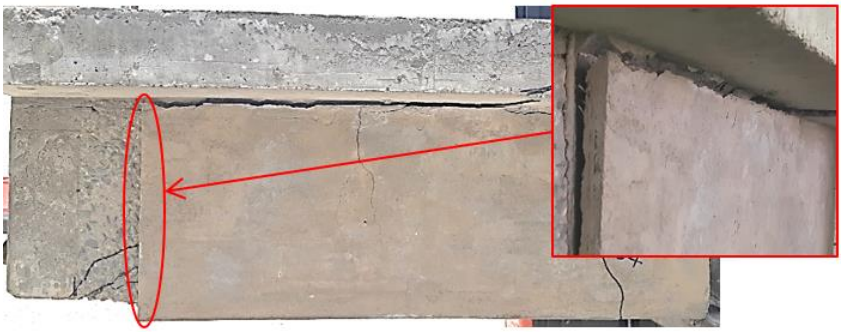

(e) B1-U-L

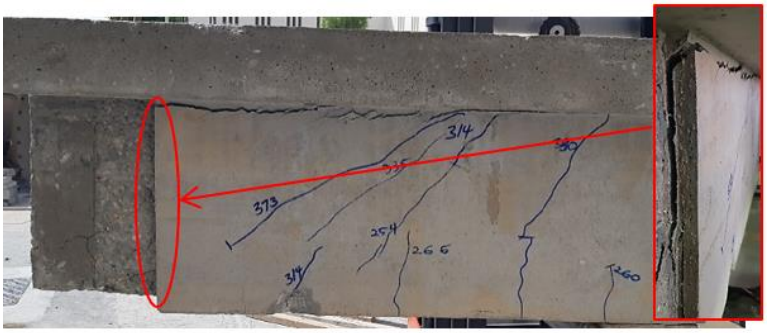

(f) B2-U-H

(g) B3-U-H

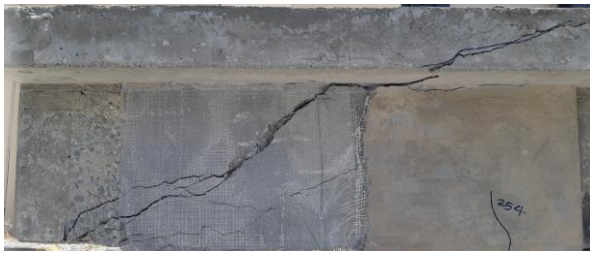

(h) B1-U-H

Figure 2.13: Crack patterns and failure modes of tested beams in Study 1.

2.3.1.4. Strengthening efficacy of SRG system

The strengthening efficacy of the SRG system can also be studied in terms of the energy absorption ratio (ψ_r), which is the ratio of the energy absorption of the strengthened beam to that of its corresponding reference beam, as presented in Table 2.6. The energy absorption (ψ) is defined as the area under the load versus deflection curve up to P_u [116]. The values of ψ for all the tested beams and ψ_r values for the strengthened beams are presented in columns 10 and 11 of Table 2.6. As presented in Table 2.6, the SRG strengthening system exhibited a significant increase in the energy

absorption of the strengthened beams compared to that of the corresponding reference beams. The energy absorptions of reference specimens B1, B2, and B3 were 280.5 kN.mm, 1173 kN.mm, and 1812 kN.mm, respectively. The respective average increases in ψ for Group-1, -2, and -3 specimens were 258%, 81.3%, and 41.5% relative to B1, B2, and B3, respectively. The greatest increase in ψ was reported for Specimen B1-U-H (418%) without internal shear reinforcement within the test region and externally strengthened with U-wrapped SRG composed of high-density fabrics. The corresponding specimen from Group-2, B2-U-H, exhibited an increase in ψ of 104% relative to B2, which is approximately 25% of that for Specimen B1-U-H, while the increase was only 60% for Specimen B3-U-H from Group-3.

Figure 2.14a–c show the effect of the test variables on the strengthening efficacy of SRG in terms of ψ_r. As can be seen in Figure 2.14a, the SRG system is more effective for specimens without steel stirrups within the shear span, the Group-1 specimens. For the specimens internally reinforced with steel stirrups within the test region, an increase in the amount of internal transverse reinforcement reduced the strengthening performance, as shown in Figure 2.14a. The average of ψ_r value for specimens without internal shear reinforcement within the test region was 4.02. The presence of internal shear reinforcement within the test region decreased this value by more than half, as reported for Group-2 beams (ψ_r= 1.81 on average). Further increases in the number of stirrups decreased the average value of ψ_r to 1.42.

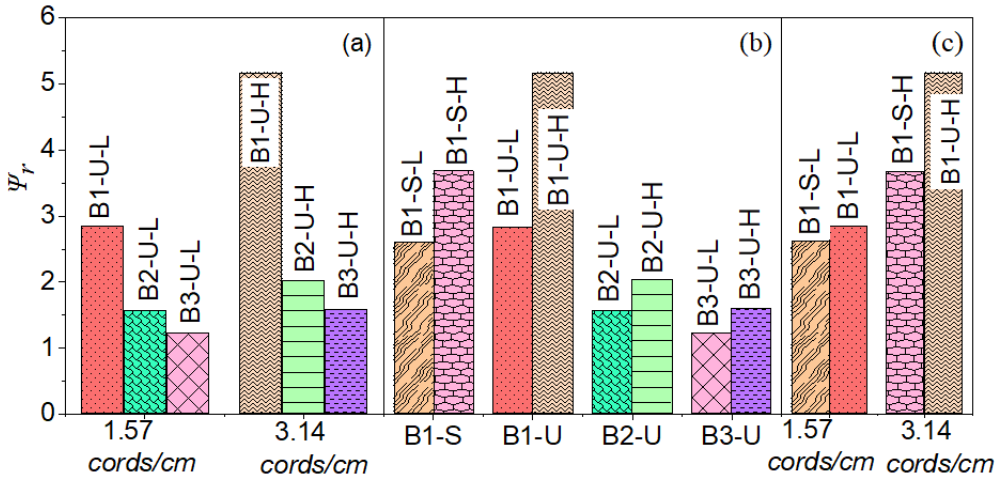

Figure 2.14: Effect of the test variables on the energy absorption ratio of the strengthened beams: (a) SRG/stirrups interaction, (b) fabric density, and (c) bond scheme, Study 1.

Regarding the fabric density, an increase in the fabric density resulted in an increase in the effectiveness of the strengthening system, as shown in Figure 2.14b. In addition, the U-wrapped SRG bond scheme is more effective than its side bonded scheme counterpart, as can be seen in Figure 2.14c. Overall, the average of ψ_r value for specimens strengthened with U-wrapped SRG was 4.02, as opposed to 3.15 for specimens strengthened with side bonded SRG.

2.3.1.5. SRG/stirrups interaction

Figure 2.15 shows the effects of the amount of internal shear reinforcement on the load-carrying capacity of the beams, in addition to Figure 2.11b, which shows the SRG/stirrups interaction effect on the percentage gain in P_u. A reference comparison is first made between the reference specimens B1 (without stirrup), B2 (6 mm stirrups spaced at 300 mm intervals), and B3 (6 mm stirrups spaced at 150 mm intervals). The ultimate load-carrying capacity of Specimen B3 was 331 kN, which is 62% and 29% greater than those of Specimens B1 (204 kN) and B2 (283 kN), respectively, as shown

in Figure 2.15. The contribution of stirrups to the load-carrying capacity of the beams decreased with the provision of an external SRG strengthening system, as can be seen in Figure 2.15, indicating the SRG/stirrups interaction.

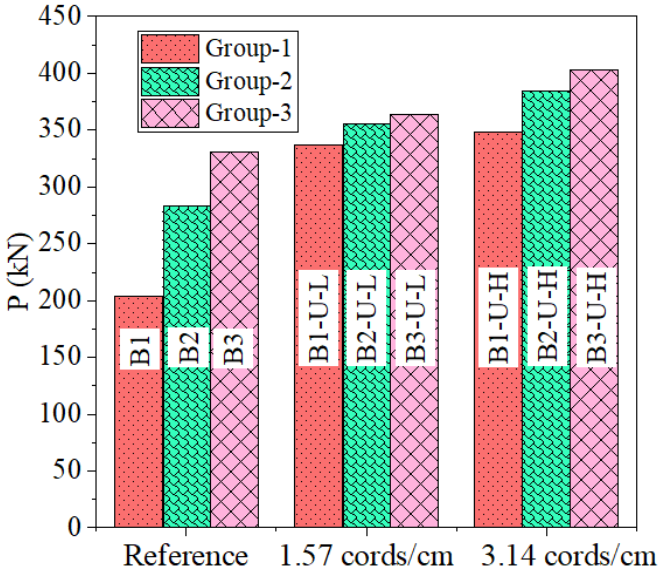

Figure 2.15: Effect of the amount of internal shear reinforcement on the load-carrying capacity, Study 1.

As shown in Figure 2.11b and Figure 2.14a, the SRG system becomes less effective with the provision of stirrups within the test region in Group-2 beams compared to Group-1 beams. The increase in the internal transverse reinforcement ratio in Group-3 beams further decreased the gain in P_u because of the SRG system. In addition, the stirrups became less engaged in the strengthened beams compared to the corresponding reference beams. As discussed in Section 2.4, the strains in each stirrup within the test region were monitored by strain gauges. It is noted that some of the strain gauges were malfunctioning. Figure 2.16a–f show the relationship between the load and strains developed in the stirrups within the test region. As can be seen in these figures, the SRG system significantly decreased the strains developed in the stirrups,

however, this effect was more noticeable in the Group-3 specimens with higher internal shear reinforcement ratios. This observation indicated the interaction between the internal shear reinforcement and SRG, as also reported for FRP [117,118] and FRCM-strengthened beams [17,119–121]. In all cases, with the exception of stirrup S2 in beam B3-U-L, the stirrups yielded before the peak load, as shown in Figure 2.16a–f. Stirrup S2 in Specimen B3-U-L yielded during the post-peak stage.

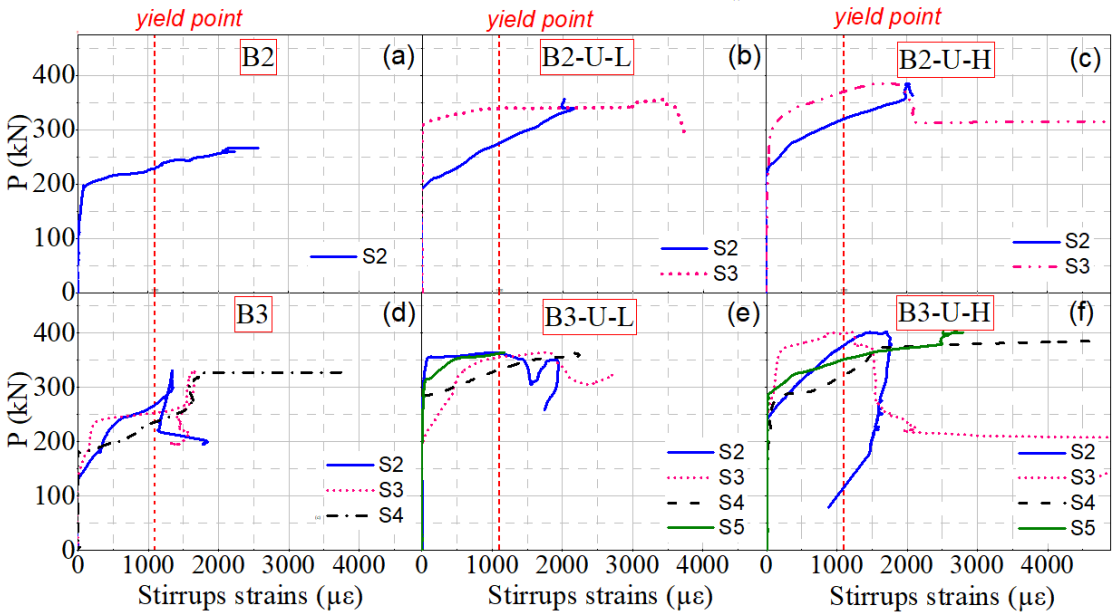

Figure 2.16: Load versus shear strains in stirrups.

2.3.2. Discussion of experimental results in Study 2

2.3.2.1. Overall response

All specimens exhibited shear failure with the formation of a main diagonal shear crack. The reference beams BS1, BS2, BS3, and BS4 failed at the respective ultimate load of 162 kN, 188 kN, 276 kN, and 383 kN as listed in Table 2.7. The strengthened beams failed at P_u significantly higher than that of the reference beam of the same series. The efficacy of SRG can be shown by the ratio of the increased load-

carrying capacity of the strengthened beams (ΔP_u) to that of the reference beam. The average of this ratio was 78% with the highest ratio corresponding to Specimen BS2-H from S2 strengthened with high-density SRG fabrics, which amounted to 133%.

Figure 2.17a shows the variation of P_u with *a/d* ratio for all the tested beams. It indicates that the load-carrying capacity of both strengthened and reference beams decreased with an increase in *a/d* ratio as also reported in the previous study for unstrengthened RC beams [122]. The contribution of the SRG to P_u is highly influenced by the test variables. It is observed that increasing the *a/d* ratio in deep beams increased the value of ΔP_u provided by the shear strengthening system; however, it showed an adverse effect in slender beams in which ΔP_u deteriorated with increased *a/d* ratio, as can be seen in Figure 2.17b. This is highly consistent with the previous experimental results of FRP-strengthened beams [37]. Furthermore, ΔP_u due to SRG strengthening was higher for slender beams compared to that for deep beams. The best performance of the SRG shear strengthening solution was observed for the S2 beam strengthened with high-density SRG fabrics, BS2-H, which showed a 133% increase in P_u. The corresponding beams from S1, S3, and S4, namely, BS1-H, BS3-H, and BS4-H, showed 101%, 75%, and 32% increases in P_u, respectively, as listed in Table 2.7. On average, ΔP_u for slender beams was 108%, whereas this value was only 48% for deep beams.

Table 2.7. Test results from Study 2

Beam ID	Beam series	Fabric density	P_u (kN)	ΔP_u (%)	δ_u (mm)	$\Delta\delta_u$ (%)	ψ (kN.mm)	$\Delta\psi$ (%)	$\varepsilon_{c,u}$ (‰)	V_{ex} (kN)
Series 1 (*a/d* = 3.10)										
BS1	S1	–	162	–	5.62	–	531.3	–		84.0
BS1-L	S1	Low	303	87	8.26	47	1313	147	1.596	157
BS1-H	S1	High	326	101	8.8	57	1503	183	1.867	169
Series 2 (*a/d* = 2.60)										
BS2	S2	–	188	–	3.97	–	375.6	–	0.595	112
BS2-L	S2	Low	399	112	10.2	156	2280	507	1.891	238
BS2-H	S2	High	438	133	11.4	187	2813	649		261
Series 3 (*a/d* = 2.10)										
BS3	S3	–	276	–	5.28	–	779.7	–	0.776	186
BS3-L	S3	Low	458	66	9.26	75.4	2287	193	1.118	309
BS3-H	S3	High	483	75	9.89	87.3	2610	235	1.017	326
Series 4 (*a/d* = 1.60)										
BS4	S4	–	383	–	6.90	–	1427	–		288
BS4-L	S4	Low	462	21	8.09	17.29	1999	40	0.763	347
BS4-H	S4	High	505	32	9.30	34.7	2510	76		379

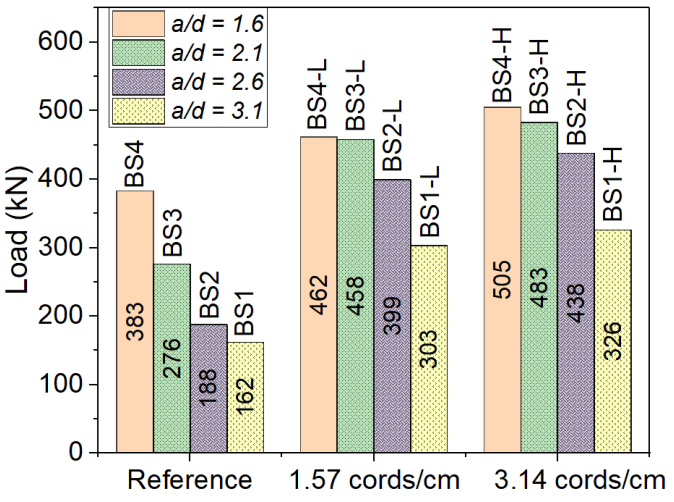

(a)

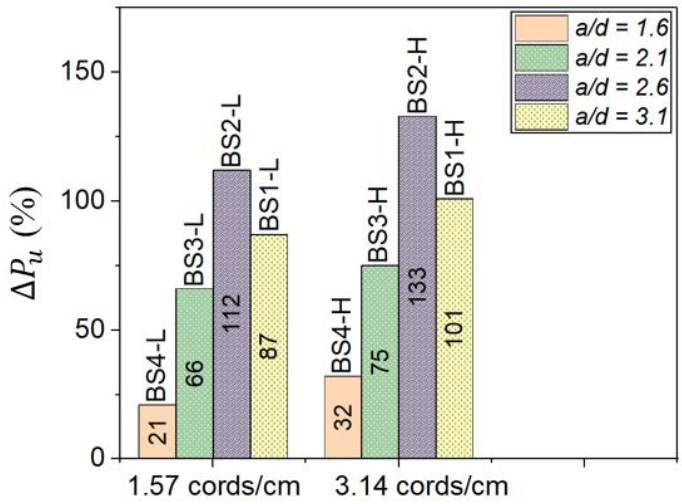

(b)

Figure 2.17: Effect of *a/d* ratio on the load-carrying capacity of the beams (a) and the increase in P_u (b), Study 2.

This trend of the variation in ΔP_u with the change in the *a/d* ratio can be explained in terms of the failure modes observed in the beams. Specifically, for a deep beam, following the formation of the diagonal crack, the arch action dominates, and a substantial portion of the load is transferred directly from the point of the load

application to the support by the diagonal compression strut [123]. Thus, the load is mainly carried by the diagonal compressive strut and SRG reinforcement acts as hoops to control the vertical deformation of the beam. The contribution of SRG reinforcement to P_u is hence moderate. The influence of the arch action reduces with an increase in *a/d* ratio [37], consequently decreasing the contribution of concrete to P_u but increasing the contribution of transverse reinforcement, the SRG system in this case, as also reported in the previous study for unstrengthened RC beams [122].

Increasing the density of the SRG fabric led to an increase in ΔP_u, as presented in Table 2.7. It was also observed that doubling the fabric density from 1.37 cords/cm to 3.14 cords/cm does not lead to an enhancement in P_u in a linear proportion to the increased fabric density as one would expect. For example, for S3 beams, the value of ΔP_u increased from 66% for Specimen BS3-L to 75% for Specimen BS3-H, as presented in Table 2.7. The average increase in P_u was 72% for RC beams strengthened with SRG composed of low-density fabrics, which increased to 85% for high-density SRG fabrics. A similar observation was reported by Thermou et al. [29,124]. This can be explained in terms of the failure modes of the strengthened beams as presented in Section 2.3.2.4.

2.3.2.2. Load versus deflection response

The load versus deflection curves of the tested beams featured linear trends until P_u exhibiting a sharp peak load−deflection curve, which is characteristic of shear failure, as demonstrated in Figure 2.18a−d, which show the load versus deflection (δ) curves at the loaded section for the S1, S2, S3, and S4 specimens, respectively. As shown in these figures, the beams with lower *a/d* ratios showed a sudden failure with a smaller deformation, but a higher P_u, compared to that with a higher *a/d* ratio. The value of δ_u for the reference beams and strengthened beams ranged from 3.79 to 6.90 mm

and from 8.09 to 11.4 mm, respectively, as listed in Table 2.7.

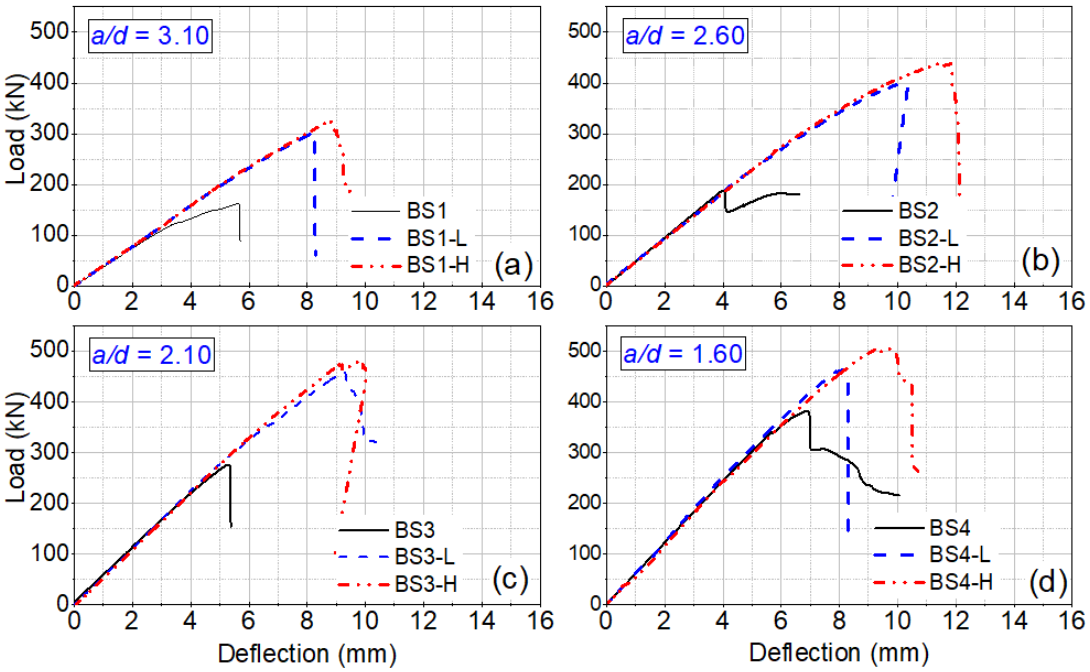

Figure 2.18: Load–deflection curves for beams in Study 2.

Compared with the reference of the same series, the strengthened beams underwent substantially higher deflection at the loaded section, as shown in Figure 2.18a−d and Table 2.7. This result indicates that the SRG system can considerably improve the deformational capacity of the beams. The increase in δ_u is higher for slender beams compared to that for the deep beams, as presented in Table 2.7. Figure 2.19a and b further illustrate the effect of *a/d* ratio on the load−deflection response of the strengthened beams. As shown in these figures, the beams with a higher *a/d* ratio experienced a higher deflection than that with a lower *a/d* ratio, which can be attributed to the increased bending moment with an increasing *a/d* ratio. For instance, for low-density SRG strengthened beams, the deflection at the load value of 300 kN corresponds to 4.82 mm for Specimen BS4-L with the lowest *a/d* ratio. This deflection value increased to 5.46 mm, 6.82 mm, and 8.14 mm for Specimens BS3-L, BS2-L, and

BS1-L, respectively, as shown in Figure 2.19b.

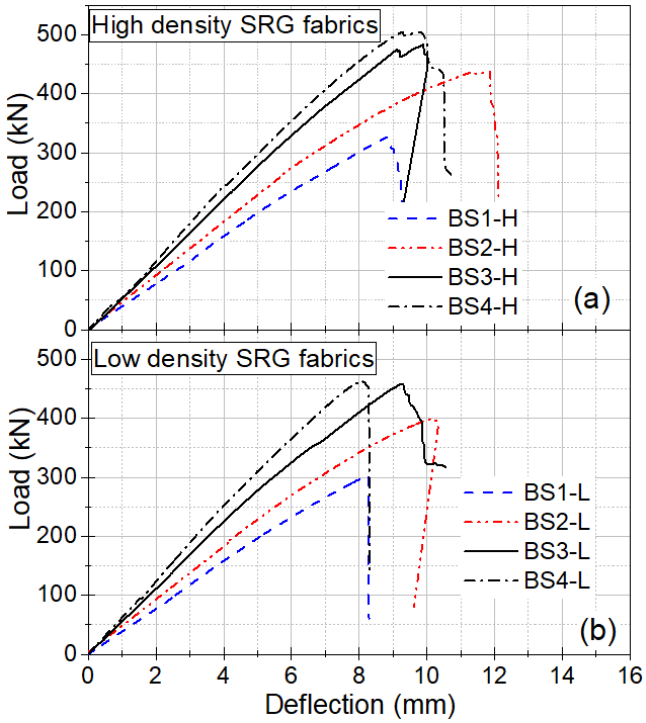

Figure 2.19: Effect of *a/d* ratio on the load–deflection response of beams strengthened with SRG composed of (a) high density and (b) low-density fabrics

2.3.2.3. SRG strengthening efficacy

The values of ψ for both strengthened and reference beams are given in Table 2.7. The reference beams BS1, BS2, BS3, and BS4 showed energy absorption values of 531.3, 375.6, 779.7, and 1427 kN·mm, respectively, as given in Table 2.7. Compared to the reference beam of the same series, the strengthened beams showed substantially higher values of ψ, as listed in Table 2.7. The increase in energy absorption ($\Delta\psi$) attributed to the SRG strengthening relative to the corresponding reference beam ranged from 147 to 649% for slender beams and from 40 to 235% for deep beams. As presented in Figure 2.20, which shows the variation of $\Delta\psi$ with *a/d* ratio, the increase in *a/d* ratio resulted in an increased $\Delta\psi$ value in deep beams, but a reduced value of $\Delta\psi$ in slender

beams. Hence, the efficacy of the SRG system increased with increasing *a/d* ratio in deep beams, but it deteriorated with an increased *a/d* ratio in slender beams. Moreover, in comparing deep and slender beams, the strengthening efficacy of the SRG is higher in slender beams compared to deep beams, as shown in Figure 2.20. Furthermore, increasing the SRG fabric density increased its strengthening efficacy, as presented in Table 2.7.

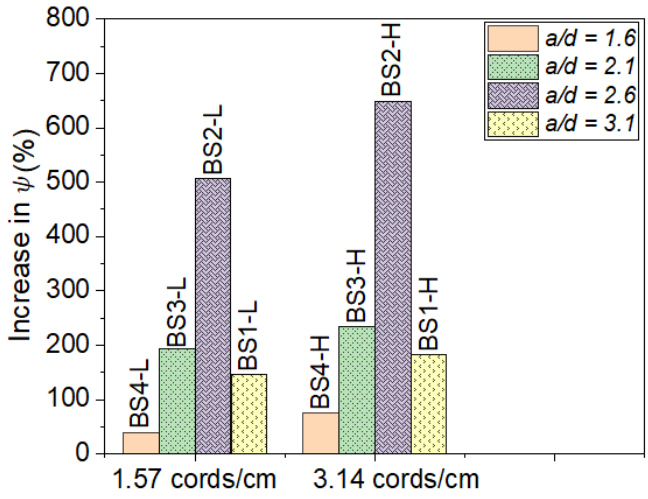

Figure 2.20: Effect of *a/d* ratio on the increase in the energy absorption of the strengthened beams.

2.3.2.4. Failure modes

All tested beams were observed to exhibit shear failure mode in the critical shear span, with the main crack running diagonally, without flexural yielding of longitudinal reinforcement. The reference beams BS1 and BS2 failed in an almost identical manner, namely, a sudden shear failure with the formation of diagonal shear cracks, as shown in Figure 2.21a for Specimen BS2. For the strengthened slender beams S1 and S2, with increasing load, vertical cracks appeared on the lower part of the beam within the test region. When the load increased, a diagonal crack was detected in the critical shear

span. With a further load increase, the beam deflection increased rapidly and resulted in failure. The shear failure of the specimens strengthened with low-density fabrics was attributed to the SRG laminate debonding with concrete cover separation, as depicted in Figure 2.21b for BS2-L beam. The failure in beams strengthened with high-density fabrics was accompanied by debonding at the fiber/matrix interface with delamination of the inner mortar layer, as can be seen in Figure 2.21c and d for Specimens BS1-H and BS2-H, respectively.

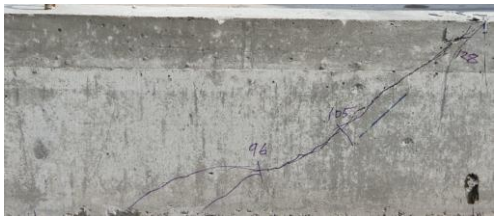

(a) BS2

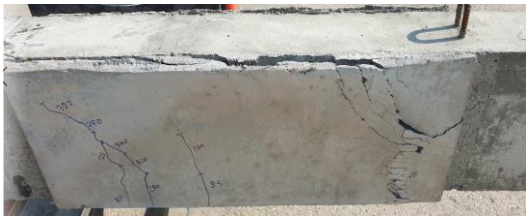

(b) BS2-L

(c) BS1-H

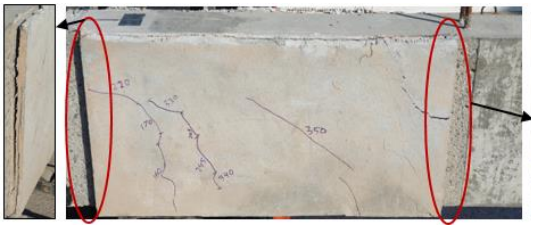

(d) BS2-H

(e) BS4

(f) BS3-L (g) BS4-L

(h) BS3-H (i) BS4-H

Figure 2.21: Failure mode of beams in Study 2.

The reference deep beams BS3 and BS4 were featured with a single principal crack propagating at an average angle of 43° and 39°, respectively, from the support to the load application point, as shown in Figure 2.21e for Specimen BS4. The first crack in Specimens BS3 and BS4 appeared at approximate loads of 118 kN and 205 kN, respectively. For the strengthened beams, the first crack was observed at the load that ranged from 160 to 225 kN. The shear failure in the low-density SRG strengthened beams occurred by debonding of the SRG laminate with the concrete cover separation at a P_u significantly higher than that of the reference beam, as shown in Figure 2.21f and g for Specimens BS3-L and BS4-L, respectively. Similar to S1 and S2 strengthened beams with high-density SRG fabrics, the shear failure in BS3-H (Figure 2.21h) and

BS4-H (Figure 2.21i) strengthened beams was accompanied by fiber/matrix interface debonding with delamination of the inner mortar layer. This phenomenon can be attributed to the improved integrity of the SRG fabrics and cementitious mortar with an increase in the spacing of the fibers in the low-density fabrics resulting in a better bond between the SRG fabrics and mortar. However, the closely spaced fibers in the high-density SRG fabrics reduced the bond between SRG fabrics and mortar, resulting in delamination within the SRG composite in the fiber/matrix interfacial zone.

2.3.2.5. Strains in longitudinal reinforcement and concrete

Figure 2.22a–d show the strain in the longitudinal bar (ε_s) distribution as a function of the applied load for the S1, S2, S3, and S4 beams, respectively. In addition, the compressive strain values of concrete (ε_{cu}) at P_u are given in Table 2.7. As shown by the $\varepsilon_s - P$ curves, the longitudinal bars did not reach the yield strain of 2690 με in all the tested beams. In addition, the measured compressive strain values in concrete were less than 0.35% commonly considered as the crushing strain of concrete, as presented in Table 2.7, confirming the shear failure. The largest longitudinal strain was observed in the strengthened beams as compared to the reference beam of the same series. Furthermore, the concrete in the compressive zone was subjected to higher strains at P_u in the case of strengthened beams, as shown in Table 2.7. Thus, the SRG system delayed the sudden shear failure.

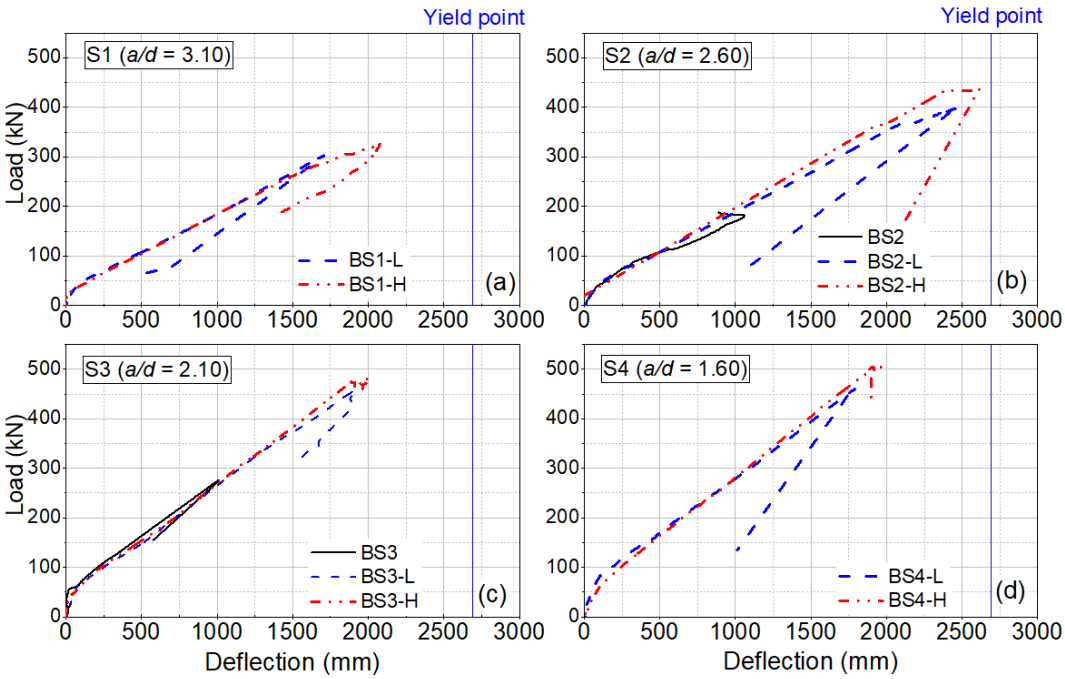

Figure 2.22: Strain distribution in main flexural reinforcement with the applied load for (a) S1, (b) S2, (c) S3, and (d) S4 beams, Study 2.

Figure 2.23a and b show the effect of *a/d* on the tensile strains of the main flexural reinforcement of the strengthened beams. The figures show that the tensile strains in the longitudinal bars at a given load level increased with increasing *a/d* ratio. Moreover, tensile strains developed in the bottom bars at a given load level were higher in slender beams as compared to those in deep beams.

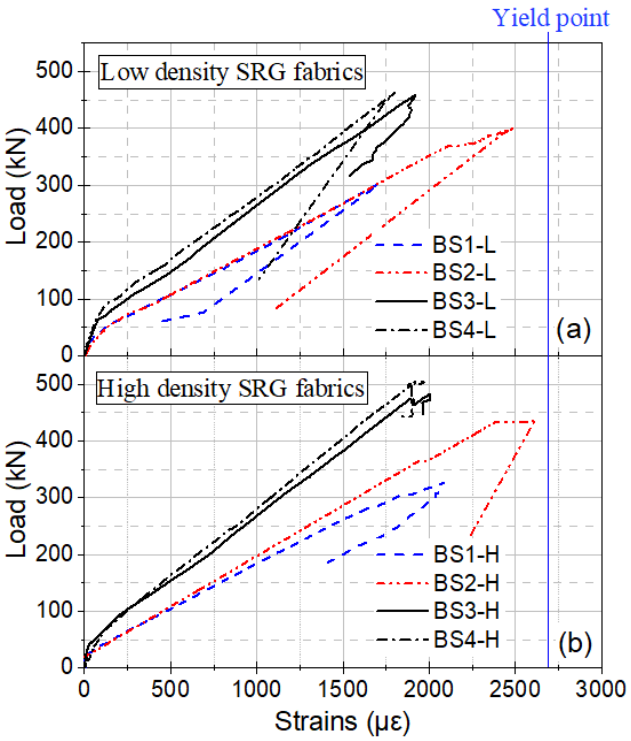

Figure 2.23: Effect of *a/d* ratio on the tensile strains developed in main flexural reinforcement for beams strengthened with SRG composed of (a) low density and (b) high-density fabrics, Study 2.

2.3.3. Discussion of experimental results in Study 3

Table 2.8 presents the results of the experiments, including the shear capacity, V_u, the beam deflection under the loading point, percentage increase in the shear capacity, δ_u corresponding to V_u, and the percentage increase in δ_u compared with the reference beam.

Table 2.8. Test results from Study 3

Beam ID	V_u (kN)	Increase V_u (%)	δ_u (mm)	Increase δ_u(%)	ψ (kN.mm)	Increase in ψ (%)	ε_c (‰)
R	112	–	3.97	–	375.6	–	0.595
ECUH	261	133	11.4	187	2813	649	0.574
ECUL	238	112	10.2	156	2280	507	1.891
EDUH	204	82	8.77	121	1674	346	1.918
EDUL	171	53	6.23	57	917	144	0.709
EDSH	166	48	6.47	63	948	152	0.964
EDSL	147	32	5.96	50	831	121	0.916
ECSH	226	102	9.41	137	1951	419	1.722
ECSL	192	72	6.91	74	1118	198	1.077
NDUH	250	124	10.8	171	2501	566	2.037
NDUL	203	81	8.05	102	1468	291	1.610
NDSH	245	119	10.1	155	2261	502	1.970
NDSL	198	77	7.59	91	1344	258	1.375

2.3.3.1. Shear capacity

All the tested beams exhibited shear failure before flexural failure with the formation of diagonal cracks in the test span. The reference beam failed at a maximum shear load of 112 kN, as presented in Table 2.8, whereas all the strengthened beams failed at a higher shear load than that of the reference specimen; however, the percentage increase in V_u was influenced by the test parameters.

Figure 2.24a–d show the variation in the shear capacity increase with the test parameters for the strengthened beams. It can be observed from Figure 2.24a–d and Table 2.8 that the increase in the shear capacity for the NSE-SRG strengthened beams varied from 77% to 124%, whereas it varied from 32% to 133% for the EB-SRG. As shown in Figure 2.24a, the NSE-SRG strengthened specimens showed a higher increase in V_u compared with the EB-SRG beams regardless of the fabric density and the SRG application method. For instance, Specimen NDSH, which was strengthened with NSE side bonded discontinuous SRG strips comprising high-density steel fabrics, failed at a

shear load of 250 kN representing a 119% increase in V_u relative to R, which is 71% higher than that of the corresponding EB-SRG strengthened beams, namely Specimen EDSH. The average increase in shear capacity was 98% for the side bonded and 102% for the U-wrapped NSE-SRG strengthened beams. The corresponding average values for the EB-SRG strengthened beams were 40% for the side bonded SRG and 68% for the U-wrapped SRG. This result is possibly related to the failure modes of the beams. The NSE technique improved the strengthening performance of the SRG system by delaying and/or precluding premature SRG debonding. Therefore, premature debonding failure can be controlled in the NSE-SRG system, unlike in the EB-SRG where the beams experienced premature SRG debonding. Thus, the SRG strengthening system was more effective when applied as near-surface embedded compared with that of externally bonded SRG.

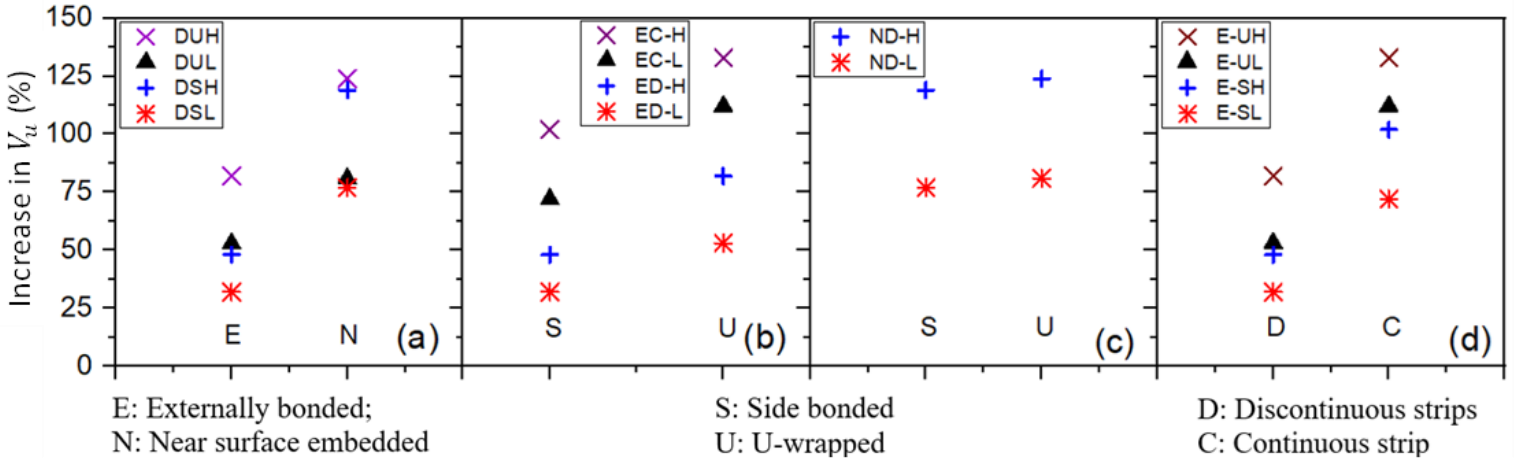

Figure 2.24: Effect the strengthening technique (a), strengthening scheme for EB-SRG (b) and NSE-SRG (C) strengthened beams, and strengthening amount (d) on the percentage increase in V_u, Study 3.

Figure 2.24b and c show the effect of the strengthening scheme on the shear capacity gains of EB-SRG and NSE-SRG strengthened beams, respectively. For the EB-SRG system, the U-wrap SRG resulted in a higher shear capacity gain compared with that of the corresponding side bonded beam, as can be seen in Figure 2.24b. For instance, Specimens EDUL and EDUH, which were strengthened with discontinuous U-jacketed SRG, failed at shear loads of 171 kN and 204 kN corresponding to a 53% and 82% increase in V_u, respectively. The corresponding side bonded SRG-strengthened beams, namely Specimens EDSL and EDSH, failed at lower shear loads of 147 kN and 166 kN representing 32% and 48% increase in V_u, respectively. On average, the U-jacketed EB-SRG showed 36% and 28% higher increase in V_u compared with those of the corresponding side bonded EB-SRG beams for continuous and discontinuous SRG strips, respectively. The strengthening scheme did not significantly influence the strength gain for the NSE-SRG strengthened beams, as shown in Figure 2.24c. The maximum shear load in Specimens NDUH and NDSH were 250 kN and 245 kN, respectively, which are nearly equal. Similarly, the difference in the shear capacity of Specimens NDUL (203 kN) and NDSL (198 kN) was not significant, as presented in Table 2.8. On average, the difference in the gain in V_u was only 4.46% for the beams strengthened with the side bonded and U-wrapped NSE-SRG system. Thus, for the NSE-SRG system, the effect of the wrapping scheme is negligible compared with that of the EB-SRG. This result can be explained using the failure modes of the beams. The use of U-wrap scheme in the EB-SRG allowed it to fail at a later stage compared with the side bonded EB-SRG. However, for the NSE-SRG, both the side bonded SRG and U-wrapped SRG strengthened beams exhibited a similar type of failure.

Regarding the strengthening amount, the increase in the SRG reinforcement in continuous SRG configuration led to a higher increase in V_u, as shown in Figure 2.24d.

The average gain in V_u were 105% and 54% for continuous and discontinuous EB-SRG strips, respectively. In addition, specimens strengthened with SRG made of high-density steel fabrics exhibited higher shear capacity compared with that of low-density fabrics, as shown in Figure 2.24d and Table 2.8. The axial rigidity of the SRG composite (K_{sf}) was used to perform a better comparison of the effect of different steel fabric densities and the amount of SRG reinforcement in the shear span (influenced by the strengthening configuration). The axial rigidity is defined as the product of the geometric reinforcement ratio of the steel fabrics in the SRG composite (ρ_{sf}) and its elastic modulus (E_{sf}), as given in Eq. (2.1).

$$K_{sf} = \rho_{sf} E_{sf} \tag{2.1}$$

The geometric reinforcement ratio of SRG is a function of the amount of the SRG reinforcement, which in turn is influenced by the strengthening configuration, as given below.

$$\rho_{sf} = F \frac{n_{sf}\, t_{sf}}{b_w} \tag{2.2}$$

The reduction factor, *F* in Eq. (2.2) indicates the proportion of the critical shear span (a) strengthened with the SRG system, as given in Eq. (2.3) for discontinuous configuration, whereas *F* is unity for continuous configuration.

$$F = \frac{N_{srg}\, w_{srg}}{a} \tag{2.3}$$

where

w_{srg} and N_{srg} are the width and the number of SRG strips, respectively,

b_w is the beam width,

t_{sf} is the area of the steel fibers per unit width, as defined earlier, and

n_{sf} is the number of steel fabric layers (2 in this study).

Figure 2.25a–c show the effect of the axial rigidity on the percentage increase in V_u for

low- and high-density EB-SRG strengthened beams; Figure 2.25c shows variation in the increase in V_u with K_{sf} for the NSE-SRG strengthened beams. As shown in these figures, an increase in K_{sf} results in an increase in the gain in V_u; however, the result shows a non-proportional relationship between K_{sf} and the gain in V_u. An increase in the SRG amount in the continuous strip leads to an increase in the axial rigidity of SRG compared with the discontinuous strips, which in turn increases the strength gain, as shown in Figure 2.25a–c. An increase in the fabric density results in a higher axial rigidity, which in turn increases the shear contribution of the SRG composite; this result is consistent with those of the FRCM-strengthened beams [12].

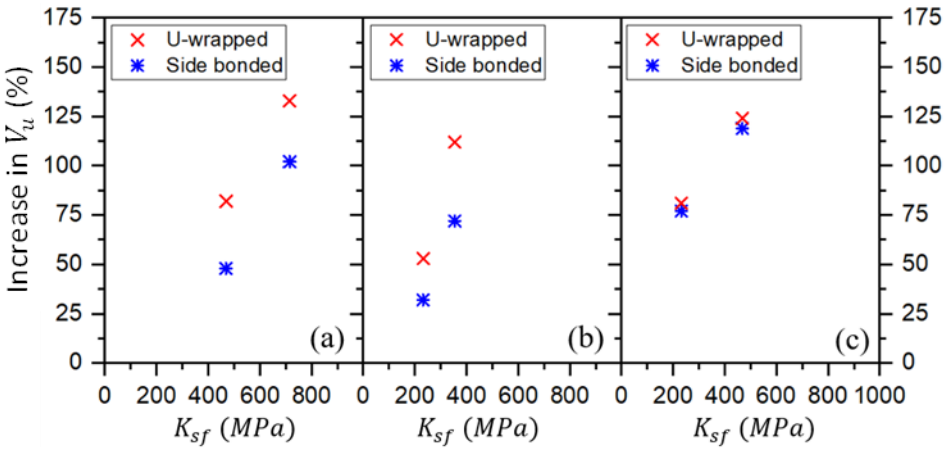

Figure 2.25: Effect of the axial rigidity on the percentage increase in V_{max} for the specimens strengthened with (a) high-density EB-SRG, (b) low-density EB-SRG, and (c) NSE-SRG, Study 3.

2.3.3.2. Observed failure modes

Figure 2.26a–g show the representative failure patterns of the strengthened beams. It should be noted that the values of the load marked on the beams in these figures are the applied load values and not the shear load. The failure mode of the

reference specimen is a typical shear failure pattern with the formation of diagonal shear crack. The failure in the strengthened beams depends on the test parameters, namely the strengthening technique and the type of the SRG application method (for EB-SRG), as shown in Figure 2.26a–g. This is discussed below.

i) SRG debonding: the common failure mode observed in the EB-SRG beams was debonding of the SRG laminate. Debonding occurred at the fiber/matrix interface in the specimens strengthened with high-density SRG fabrics, as shown in Figure 2.26a for Specimen EDUH and Figure 2.26b for Specimen ECUH. However, the failure of the beams strengthened with SRG comprising low-density steel fabrics involved debonding of SRG with cover concrete, as can be seen in Figure 2.26c for Specimen ECUL. In both continuous and discontinuous EB-SRG, the use of a U-wrap strengthening scheme delayed the occurrence of SRG debonding failure by allowing the beam to fail at a later stage compared with the side bonded EB-SRG.

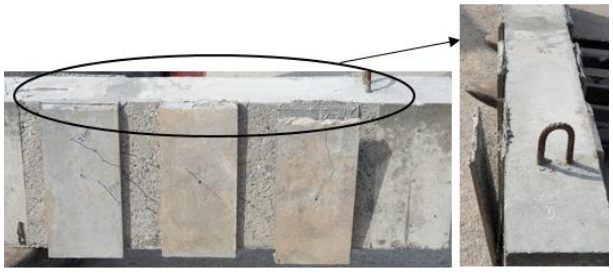

(a) EDUH

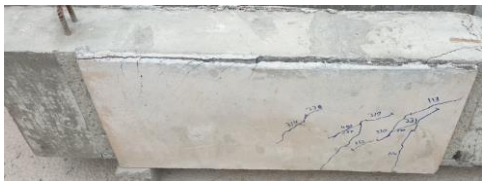

(b) ECUH

(c) ECUL

(d) NDUH

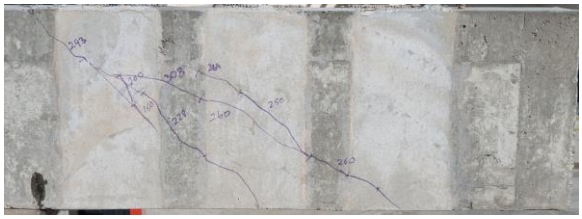

(e) NDUL

(f) NDSL

(g) NDSH

Figure 2.26: Crack pattern and failure modes of beams in Study 3.

ii) Complete/partial rupture of steel fabrics: for the NSE-SRG beams, failure was followed by fabric rupture without any sign of SRG debonding, as can be seen in Figure 2.26d–f for Specimens NDUH, NDUL, and NDSL, except for Specimen NDSH. Failure in Specimen NDSH involved partial debonding of the first two SRG strips, as shown in Figure 2.26g. The application of SRG composite using the NSE technique provided inherent anchorage for the SRG laminate and hence mitigated or delayed the premature debonding failure observed in the EB-SRG strengthened beams. Consequently, the NSE-SRG resulted in better utilization of the composite.

2.3.3.3. Shear load versus deflection response

The shear load versus deflection under the load for the NSE-SRG and EB-SRG strengthened beams is shown in Figure 2.27a and b, respectively. The deflection was linear until the peak shear load in all the tested beams. The maximum deflection corresponding to V_u in all the strengthened beams was larger than that of the reference

(3.97 mm). The values of δ_u were 11.40 mm and 10.8 mm for the EB-SRG and NSE-SRG strengthened beams, respectively. The NSE-SRG strengthened beams had higher values of δ_u compared with the EB-SRG beams, as presented in Table 2.8. The strengthened beams showed considerably higher deflection relative to the reference beam, as can be seen in Figure 2.27a and b and Table 2.8. This result confirms that the SRG strengthening can substantially increase the deformation capacity of the strengthened beams. The specimens strengthened with NSE-SRG showed a higher increase in δ_u compared with the EB-SRG counterparts, as given in Table 2.8. On average, the increase in δ_u was 130% for EB-SRG strengthened beams and 72% for the NSE-SRG strengthened beams.

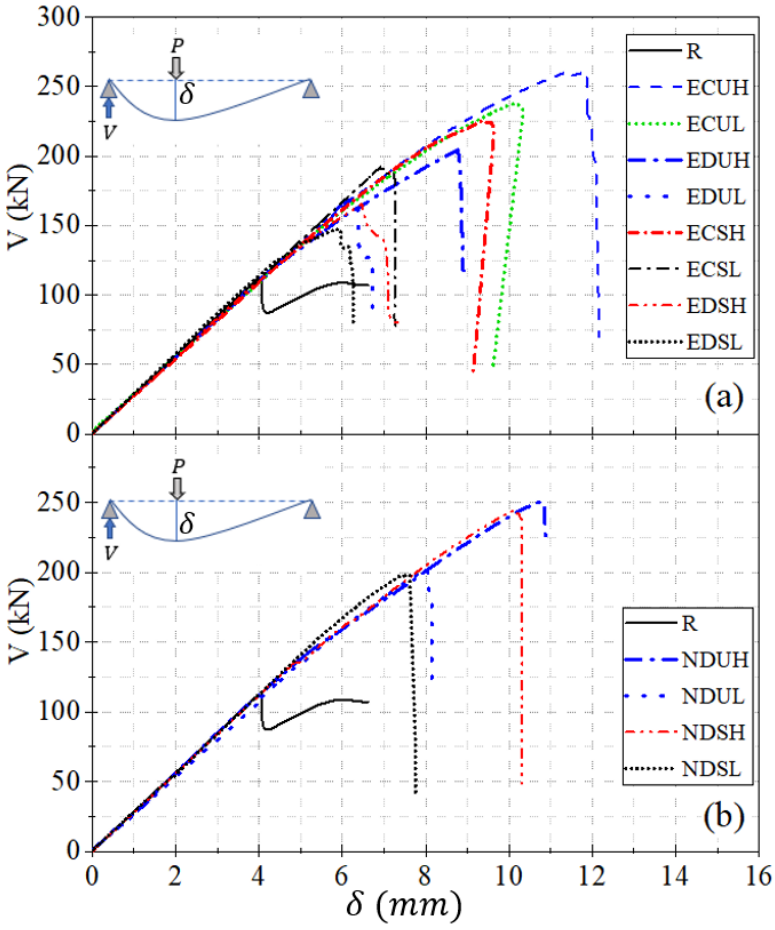

Figure 2.27: Shear load versus deflection under the loading point for (a) EB-SRG and

(b) NSE-SRG strengthened beams.

2.3.3.4. Strains in longitudinal reinforcement and concrete

Figure 2.28a and b show the relationship between the shear load and the strains developed in the flexural tensile bars for beams strengthened with continuous and discontinuous SRG strips. It can be observed from the figures that shear failure in all the beams occurred prior to flexural yielding, except for Specimen NDUH that failed after the yielding of flexural bars. Furthermore, the strains developed in the concrete at V_u were below the concrete crushing strain of 0.35%, as presented in Table 2.8. In addition, NSE-SRG increased the strains developed in the tensile reinforcement compared with the EB-SRG beams.

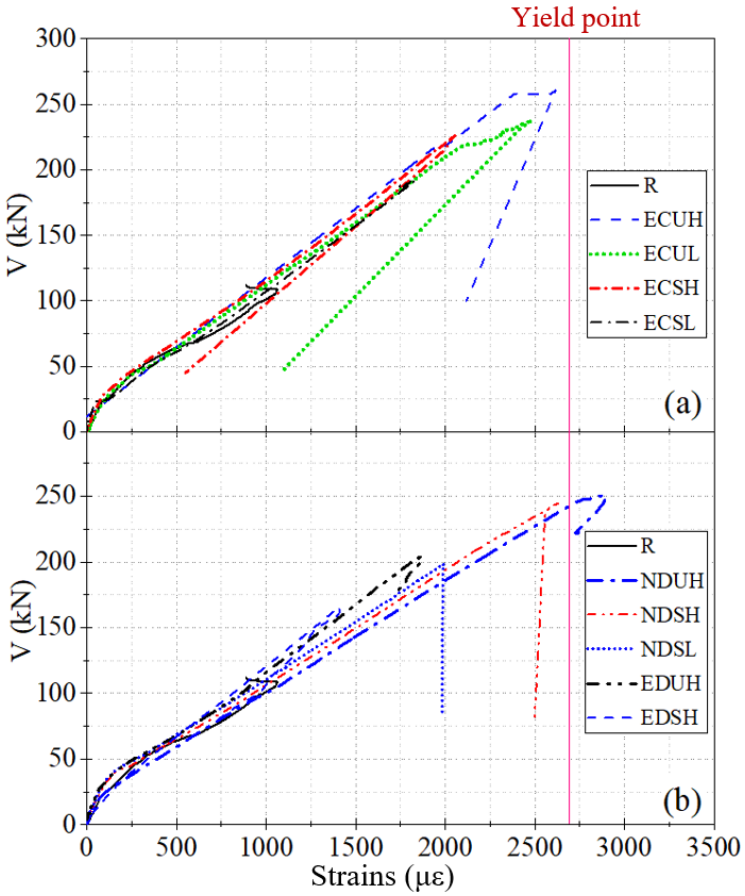

Figure 2.28: Shear load versus tensile strain developed in the flexural bars for beams

strengthened with (a) continuous SRG strip and (b) discontinuous SRG strips, Study 3.

2.3.3.5. SRG strengthening efficacy

The energy absorption for the reference beam is 375.6 kN·mm, as presented in Table 2.8. The strengthened beams exhibited substantially higher values of ψ compared with the reference beam. The increase in ψ ($\Delta\psi$) ranged from 121% to 649% for the EB-SRG strengthened beams and 258% to 566% for the NSE-SRG strengthened beams. Figure 2.29a–d show variations in the increase in ψ with the test parameters. The value of $\Delta\psi$ is higher in the NSE-SRG strengthened beams than in the EB-SRG beams, as shown in Figure 2.29a. Hence, the use of the NSE technique resulted in a higher strengthening efficacy of the SRG. Moreover, the U-wrap scheme in the EB-SRG significantly increased the strengthening capability of the SRG system, except for Specimen EDUL where the difference in $\Delta\psi$ was only 23%, as shown in Figure 2.29b. However, the difference in the increase in ψ was insignificant in the NSE-SRG beams with side-bonded or U-wrap scheme, as shown in Figure 2.29c and Table 2.8. It can be observed from Figure 2.29d that increasing the strengthening amount in continuous EB-SRG increases the gain ψ. Furthermore, as presented in Table 2.8, an increase in the density of the SRG fabrics increased its strengthening efficacy.

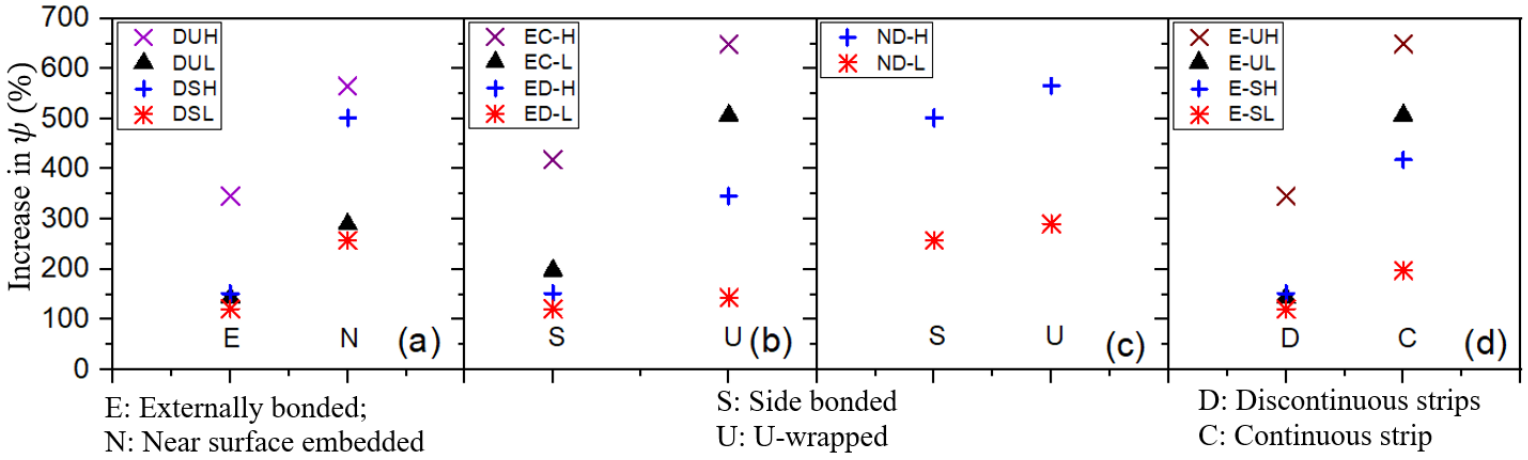

Figure 2.29: Effect the strengthening technique (a), strengthening scheme for EB-SRG (b) and NSE-SRG (C) strengthened beams, and strengthening amount (d) on the percentage increase in the energy absorption of the strengthened beams, Study 3.

2.4. Analytical study

Despite numerous studies into the behavior of RC beams, the assessment of their shear behavior remains a challenging task when compared to that of their flexural behavior [125–132]. The modified compression field theory has demonstrated its capacity to provide a realistic simulation of the shear behavior of RC beams [133]. It uses the principles of equilibrium and compatibility, and the constitutive relations of cracked concrete. Unlike the fixed-angle truss model, the MCFT considers the changes in the shear crack angle with various parameters, as well as the contribution of the concrete tensile stresses. However, it requires solving a number of equations iteratively [134,135]. To decrease the number of required iterations, Bentz et al. [135] developed the simplified MCFT (SMCFT), which is adopted here for predicting the shear capacity of SRG-strengthened RC beams. The MCFT-based models were developed in three stages, as discussed below.

2.4.1. SRG-strengthened T-section RC beams

In the first stage, the MCFT is applied to EB-SRG strengthened T-beams in Study 1. *Figure 2.30*a–d show the MCFT-based model for RC T-section beam strengthened with an externally bonded SRG. As shown in Figure 2.30b, the vertical imbalance between the diagonal tension stress, f_1, and diagonal compression stress, f_2, is carried by the transverse reinforcement, namely stirrups and an externally bonded SRG.

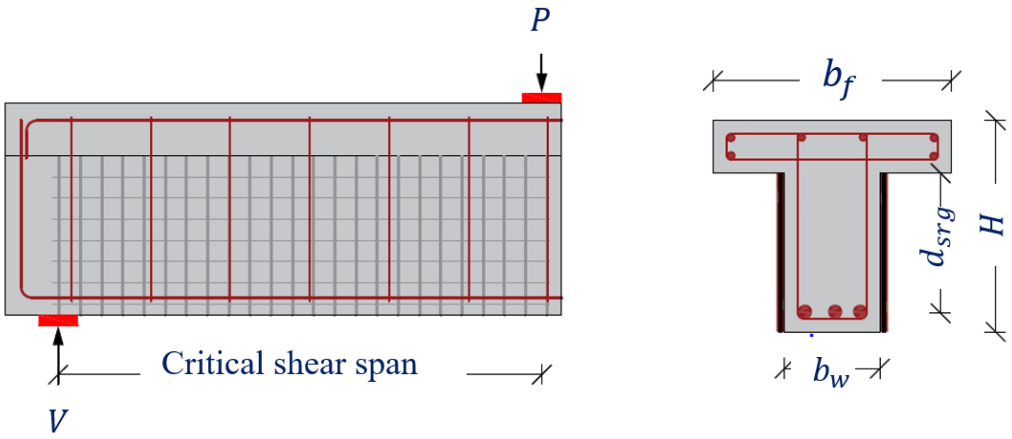

(a) Reinforcement details of SRG-strengthened beam within the critical shear span

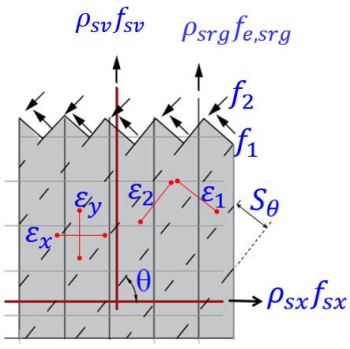

(b) Equilibrium of forces

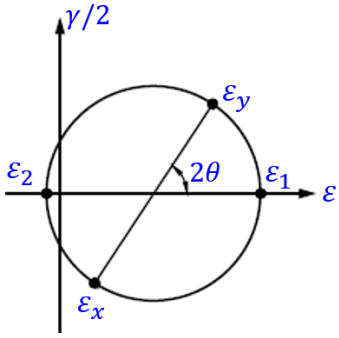

(c) Mohr's circle for average strains

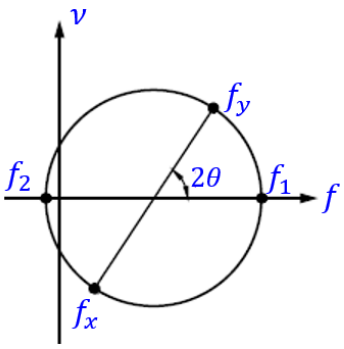

(d) Mohr's circle for average stresses

Figure 2.30: Modified compression field theory-based model for RC beams strengthened with an EB-SRG.

$$\rho_{sy}f_{sy} + \rho_{srg}f_{e,srg} = f_2 \sin^2\theta - f_1 \cos^2\theta \quad (2.4)$$

where,

ρ_{sy} is the reinforcement ratio of the stirrups;

ρ_{srg} is the geometric SRG fabric reinforcement ratio;

f_{sy} is the yield strength of the stirrups within the critical shear span;

$f_{e,srg}$ is the effective stress in the SRG; and

θ is the inclination angle of the principal stress from the horizontal.

Similarly, the longitudinal imbalance (in the horizontal direction in Figure

2.30b) between f_1 and f_2 is carried by the flexural reinforcement as follows:

$$\rho_{sx} f_{sx} = f_2 \cos^2\theta - f_1 \sin^2\theta \tag{2.5}$$

where ρ_{sx} and f_{sx} are the reinforcement ratio and yield strength of the tensile flexural bars, respectively.

From the geometric conditions in Figure 2.30c, the following compatibility equations hold true based on the MCFT:

$$\tan^2\theta = \frac{\varepsilon_x + \varepsilon_2}{\varepsilon_y + \varepsilon_2} \tag{2.6}$$

and

$$\varepsilon_1 = \varepsilon_2 + \varepsilon_x + \varepsilon_x \tag{2.7}$$

Combining Eqs. (2.6) and (2.7), the strains in the transverse direction (ε_y) and longitudinal direction (ε_x) can be determined in terms of the principal tensile strain (ε_1) and principal compressive strain (ε_2) as follows:

$$\varepsilon_x = \frac{\varepsilon_1 \tan^2\theta - \varepsilon_2}{1 + \tan^2\theta} \tag{2.8}$$

$$\varepsilon_y = \frac{\varepsilon_1 - \varepsilon_2 \tan^2\theta}{1 + \tan^2\theta} \tag{2.9}$$

From Mohr's circle for stresses, as shown in Figure 2.30d, Eq. (2.10) can be obtained.

$$v = (f_1 + f_2)\frac{\cot\theta}{1 + \cot^2\theta} \tag{2.10}$$

From Eqs. (2.5) and (2.10), the following equation holds true

$$\rho_{sx} f_{sx} = v/\tan\theta - f_1 \tag{2.11}$$

where v is the shear strength of the beam.

From Eqs. (2.4) and (2.10), the shear strength of the SRG-strengthened beam can be given as follows:

$$v = f_1 \cot\theta + (\rho_{sy} f_{sy} + \rho_{srg} f_{e,srg}) \cot\theta \quad (2.12)$$

The shear strength can also be expressed using the following equation based on the SMCFT [135]:

$$v = \beta\sqrt{f_c'} + (\rho_{sy} f_{sy} + \rho_{srg} f_{e,srg}) \cot\theta \quad (2.13)$$

where f_c' is the compressive strength of concrete, and β is the tensile stress factor of the cracked concrete given by Eq. (2.14) as per the SMCFT [135].

$$\beta = \frac{0.4}{1 + 1500\,\varepsilon_x} \frac{1300}{1000 + S_{xe}} \quad (2.14)$$

where S_{xe} is the crack spacing estimated by Eq. (2.15) in terms of the vertical distance between longitudinal reinforcement (S_x) and the maximum dimension of aggregate (a_g).

$$S_{xe} = \frac{35 S_x}{a_g + 16} \geq 0.85 S_x \quad (2.15)$$

Therefore, the shear strength of RC beams internally reinforced with stirrups and externally strengthened in shear with the SRG system is given as follows:

$$v = \beta\sqrt{f_c'} + (\rho_{sy} f_{sy} + \rho_{srg} f_{e,srg}) \cot\theta \quad (2.16)$$

From Eqs. (2.11), (2.12), and (2.13), the strains in the longitudinal direction is given as follows:

$$\varepsilon_x = \frac{v \cot\theta - \beta\sqrt{f_c'} \tan\theta}{E_s\,\rho_{sx}} \quad (2.17)$$

The inclination of the diagonal compressive stress is given by Eq. (2.16) as per the SMCFT [135]:

$$\theta = (29 + 7000\,\varepsilon_x) \times \left(0.88 + \frac{S_{xe}}{2500}\right) \leq 75° \quad (2.18)$$

where E_s and ρ_{sx} are the elastic modulus and reinforcement ratio of the tensile

flexural reinforcement, respectively.

For determining the effective stress in SRG, the method of Chen and Teng [136] was adopted, which was originally developed for FRP-strengthened beams and recently applied to FRCM-strengthened beams [137,138]. Per the Chen and Teng [136] model, the effective stress in the strengthening system is given by

$$f_{e,srg} = D_{srg} f_{max,srg} \tag{2.19}$$

where $f_{max,srg}$ and D_{srg} are the maximum SRG stress and stress distribution factor, respectively.

The maximum SRG stress at debonding failure is given by Eq. (2.20) but should not exceed the tensile strength of SRG steel fibers ($f_{t,srg}$):

$$f_{max,srg} = 0.427\beta_w\beta_L\sqrt{\frac{E_{srg}\sqrt{f_c'}}{t_{srg}}} \leq f_{t,srg} \ \ (\text{MPa, mm}) \tag{2.20}$$

where β_w is the factor that shows the composite-to-concrete width ratio, which is equal to $1/\sqrt{2}$ for continuous configuration and β_L is the factor that shows the bond length, as given by:

$$\beta_L = \begin{cases} \sin \pi\lambda/2\,, & \lambda < 1 \\ 1, & \lambda \geq 1 \end{cases} \tag{2.21}$$

The stress distribution factor is determined as given in Eq. (2.22) in terms of the normalized maximum bond length parameter ($\lambda = L_{max}/L_e$):

$$D_{srg} = \begin{cases} 1 - \dfrac{\pi - 2}{\pi\lambda}, & \lambda > 1 \\ \dfrac{2}{\pi\lambda}\dfrac{1 - \cos \pi\lambda/2}{\sin \pi\lambda/2}, & \lambda \leq 1 \end{cases} \tag{2.22}$$

where L_{max} is the available bond length, $L_{max} = d_{srg}$ for the U-wrapped bond scheme, and L_e is the effective bond length, as given by

$$L_e = \sqrt{\frac{E_{srg} t_{srg}}{\sqrt{f_c'}}} \tag{2.23}$$

The SMCFT-based analytical procedure is summarized in Figure 2.31, and the MATLAB subroutine is used to determine the shear strength and then the shear capacity of each strengthened beam. The theoretically predicted shear capacity (V_{th}) of the strengthened beams and the ratio of the theoretically predicted shear capacity to its experimental value (V_{th}/V_{ex}) are presented in the last two columns of Table 2.9. The model satisfactory predicted the shear capacity of SRG-strengthened beams with an average ratio of V_{th}/V_{ex} of 0.92 and a standard deviation of 4.07%.

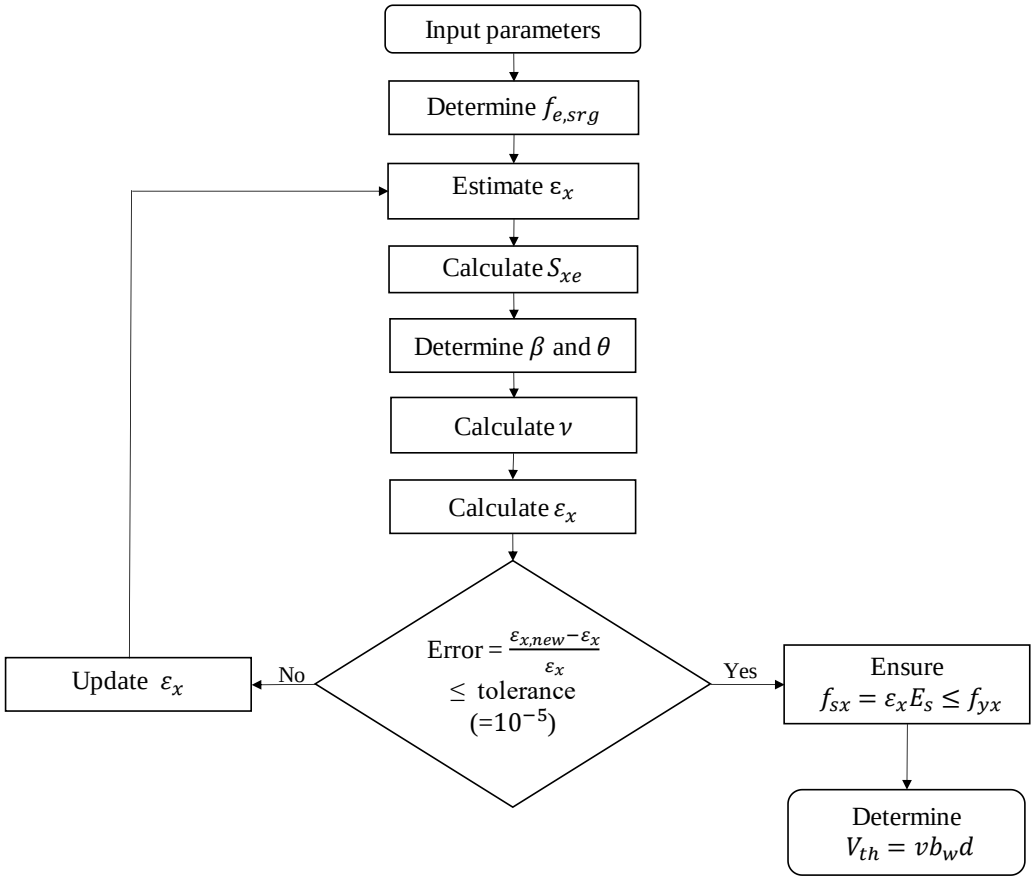

Figure 2.31: Analytical procedure for shear capacity of SRG-strengthened beams based on SMCFT [135].

Table 2.9. Comparison between the experimental and predicted shear capacity of SRG-strengthened T-section beams

Beam ID	V_{ex} (kN)	ρ_{sx} (%)	ρ_{sv} (‰)	ρ_{srg} (‰)	$f_{e,srg}$ (MPa)	V_{srg} (kN)	v (MPa)	V_{th} (kN)	V_{th} $/V_{ex}$
B1-U-H	209	4.113	–	3.76	457	113	3.22	192	0.92
B1-U-L	200	4.113	–	1.87	672	83.9	2.82	168	0.84
B1-S-H	181	4.113	–	3.76	367	91.7	2.93	175	0.97
B1-S-L	173	4.113	–	1.87	583	73.4	2.68	160	0.92
B2-U-H	231	4.113	1.047	3.76	457	111	3.52	210	0.91
B2-U-L	212	4.113	1.047	1.87	672	82.7	3.13	187	0.88
B3-U-H	239	4.113	2.094	3.76	457	110	3.82	228	0.95
B3-U-L	218	4.113	2.094	1.87	672	81.6	3.43	204	0.94

In addition, Figure 2.32 shows the prediction of the model in terms of the V_{th}/V_{ex} ratio, the values of which are classified according to the modified version of the demerit points classification (DPC) [139] proposed by Collins [140]. The DPC is used to evaluate the prediction of the model in terms of the safety, accuracy, and economic aspects. According to the modified version of the DPC, a penalty is assigned to each range of the V_{th}/V_{ex} ratio according to Table 2.10. Therefore, the safety, accuracy, and economic aspects of the proposed model are assessed in this study using the modified DPC strategy [139] as shown in Figure 2.32. As can be seen in this figure, the predictions are safe for all the specimens. None of the predictions are extra conservative or dangerous. The prediction of all the strengthened beams, apart from Specimen B1-U-L, whose prediction was conservative, fell within the appropriate safety range as shown in Figure 2.32. These results indicated that the proposed analytical model resulted in a safe and accurate prediction of the strengthened beams.

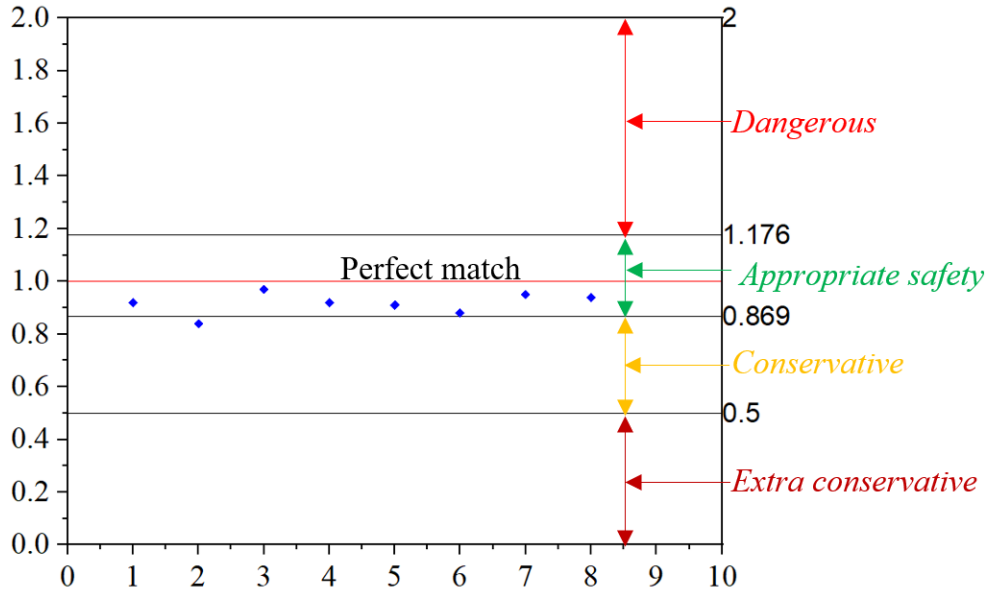

Figure 2.32: Prediction capability of the model based on the modified DPC [139] for strengthened T-beams.

Table 2.10. Criteria for the modified DPC [139]

V_{th}/V_{ex}	Classification	Penalty (PEN)
> 2	Extra dangerous	10
$1.176 \leq V_{th}/V_{ex} \leq 2$	Dangerous	5
$0.869 < V_{th}/V_{ex} \leq 1.176$	Appropriate safety	0
$0.5 < V_{th}/V_{ex} \leq 0.869$	Conservative	1
≤ 0.5	Extra conservative	2

2.4.2. SRG-strengthened rectangular section RC beams: Effect of the strengthening technique

Consider the NSE-SRG strengthened RC beam in Figure 2.33 with no internal shear reinforcement within the critical shear span. Following the same procedure presented in Section 2.4.1, the shear strength is given by:

$$v = \beta\sqrt{f_c'} + \rho_{srg} f_{e,srg} \cot\theta. \quad (2.24)$$

The first part of Eq. (2.24) represents the contribution of concrete to the shear strength, while the second part represents the shear strength contribution of SRG. The

effective stress developed in SRG is determined by adopting the method proposed by Chen and Teng [141], which was originally developed for RC beams strengthened with FRP, as discussed in Section 2.4.1.

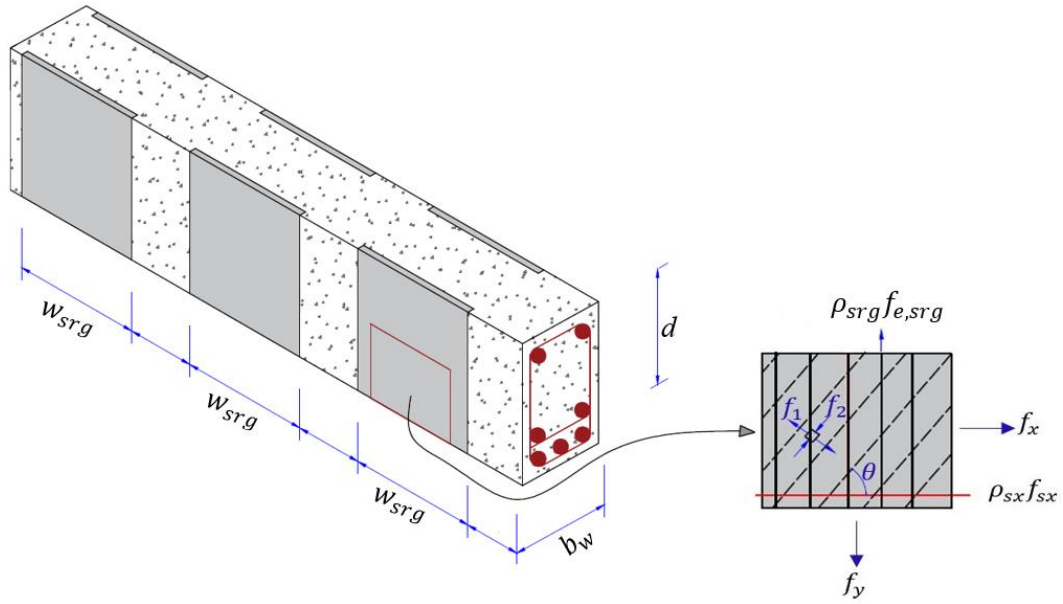

Figure 2.33: SRG-strengthened beam shear model based on the MCFT [133].

This model has been shown to provide a reasonable prediction for the effective stress developed in FRCM [137]. Accordingly, the value of $f_{e,srg}$ is given as follows:

$$f_{e,srg} = D_{srg} f_{u,srg} \tag{2.25}$$

where D_{srg} is the stress distribution factor and $f_{max,srg}$ is the maximum stress in SRG given by Eq. (2.26), which should not exceed the tensile strength of the SRG steel fibers:

$$f_{max,srg} = 0.427\beta_w\beta_L\sqrt{\frac{E_{srg}\sqrt{f_c'}}{t_{srg}}} \leq f_{t,srg}. \ (\text{MPa} \cdot \text{mm}) \tag{2.26}$$

For the NSE-SRG strengthened beam without SRG debonding, the value of $f_{max,srg}$ is given as:

$$f_{max,srg} = 0.724\beta_w\beta_L\sqrt{\frac{E_{srg}\sqrt{f_c'}}{t_{srg}}} \leq f_{t,srg} \ \ (\text{MPa} \cdot \text{mm}) \tag{2.27}$$

The effective depth of the SRG strengthening in rectangular RC beams is taken as $d_{srg} = 0.9d$.

The specimens in Study 3 are used to investigate the prediction capability of the model. The proposed model gives accurate predictions for both EB-SRG and NSE-SRG strengthened beams with an average V_{th}/V_{ex} ratio of 0.98 and a standard deviation of 0.078. The modified DPC [139] was also used to further evaluate the capability of the model, as shown in Figure 2.34. As can be seen in Figure 2.34, the prediction results of all the beams are within an appropriate safety region. Therefore, the model resulted in safe and accurate predictions of the shear capacity of both the NSE-SRG and EB-SRG strengthened beams tested in this study (Study 3).

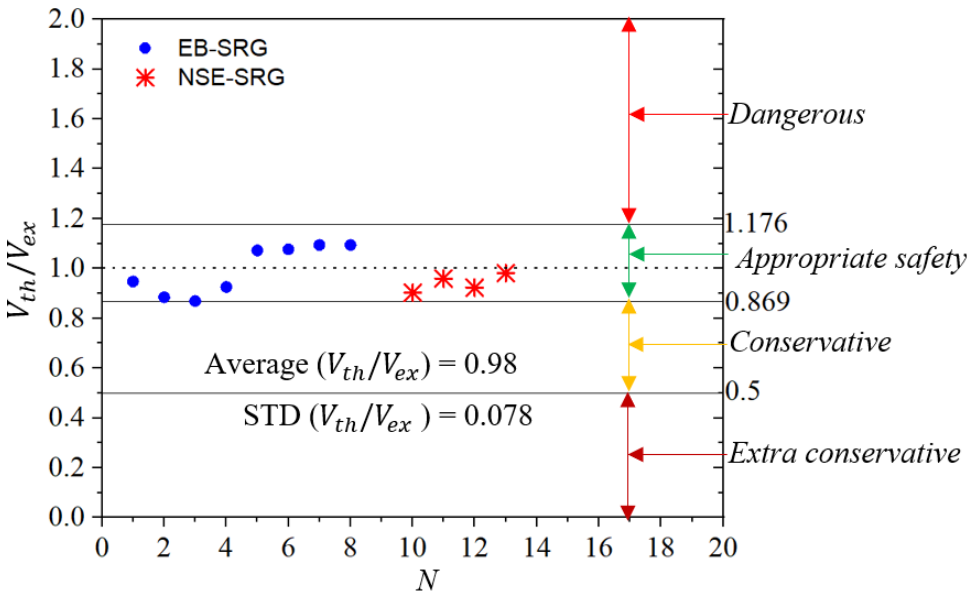

Figure 2.34: Prediction capability of the adopted formulations for rectangular beams in Study 3.

2.4.3. SRG-strengthened rectangular section RC beams: Effect of shear span-to-depth ratio

As discussed previously, variation in *a/d* ratio significantly affects the shear strength of both the reference and strengthened beams. In addition, the contribution of the SRG to the beam capacity varies with *a/d* ratio. Thus, Eq. (2.24) is modified as follows to reflect the influence of *a/d* ratio on the shear capacity of both the reference and strengthened beams:

$$v = R_c \beta \sqrt{f_c'} + R_{srg} \rho_{srg} f_{e,srg} \cot\theta \tag{2.28}$$

where R_c and R_{srg} are given in Eqs. (2.29) and (2.30), respectively:

$$R_c = \begin{cases} (4.6/\chi)^{\eta}, a/d < 2.5 \\ 1.28\eta^{2.1}, a/d > 2.5 \end{cases} \tag{2.29}$$

$$R_{srg} = \begin{cases} 2.025\sqrt{R_c}, a/d < 2.5 \\ {R_c}^{3/4}, a/d > 2.5 \end{cases} \tag{2.30}$$

where $\chi = a/d$ ratio and $\eta = 2.5/\chi$ is the ratio of the boundary for the slender and deep beams (2.50 based on ACI-ASCE Committee 445 [142]) to the *a/d* ratio.

The model is used to predict the shear capacity of RC beams with varying *a/d* ratios included in Study 2. The ratio of the predicted to experimental shear capacities featured an average and standard deviation of 0.99 and 0.068, respectively. The coefficient of correlation between the predicted shear capacity and experimental shear capacity is 97%. The predictions of the model were further assessed on the basis of the modified DPC method, as shown in Figure 2.35. As shown in Figure 2.35, the predictions of all specimens lay within the range of appropriate safety. Thus, the proposed model gives safe and accurate predictions

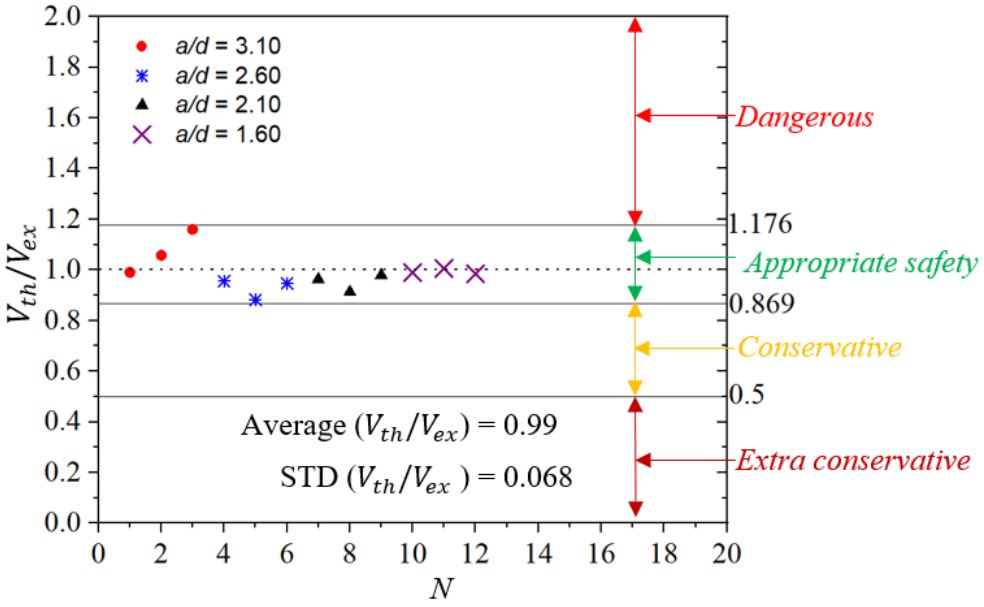

Figure 2.35: Prediction capability of the model based on the modified DPC [139] for beams included in Study 2.

2.5. Conclusion

An extensive experimental program that comprised thirty-three (33) RC beams (11 T-section beams and 22 rectangular section beams) is used to experimentally investigate the shear strengthening performance of SRG composite applied using either EB or NSE technique. Three independent studies were investigated in which the first study focused on the effectiveness of SRG in strengthening of shear-deficient RC T cross-section beams. The parameters of the first study were set as follows: (a) fabric density, (b) amount of internal shear reinforcement in the test span, and (c) bond scheme. In this regard, a total of eleven RC T-beams were designed, fabricated, and tested under monotonically increasing three-point bending until failure. Moreover, an SMCFT-based analytical procedure is proposed to predict the shear capacity of the strengthened beams.

In the second study, the shear behavior of RC beams with varying *a/d* ratio and shear strengthened with EB-SRG was investigated. Twelve rectangular section RC beams with dimensions 180 × 400 × 2550 mm, including four reference beams without SRG and eight shear-strengthened beams were prepared and tested until failure under displacement-controlled three-point bending. The beams were tested as a simply supported system with a clear span between supports of 2150 mm and varying shear span (535, 700, 870, and 1035 mm). The influence of varying *a/d* ratio and the density of the SRG steel fabrics (1.57 cords/cm, 3.14 cords/cm) on the load–deflection curve, load-carrying capacity, deformational characteristics, and failure mode of the strengthened specimens were analyzed. A wide range of *a/d* ratios ranging from 1.60 to 3.10 at 0.5 intervals representing both deep beams (*a/d* = 1.60 and 2.10) and slender beams (*a/d* = 2.60 and 3.10) were considered. Besides, an analytical model that considers the effect of *a/d* ratio was proposed based on the SMCFT.

The third study reported the results of experiments on the shear performance of RC beams strengthened in shear using different techniques for an SRG system. The experiment involved 13 rectangular RC beams with dimensions of 180 mm × 400 mm × 2550 mm subjected to monotonically increasing three-point loading. Two different techniques were used, namely, the NSE and the conventional externally bonded technique. Moreover, the effects of the fabric density, strengthening scheme (side-bonded versus U-wrapped SRG), and strengthening amount in a continuous or discontinuous configuration on the strengthening performance of the SRG system were examined. In addition, an analytical model was proposed to predict the shear capacity of the strengthened beams considering the effect of the strengthening type.

The results of the studies support the following conclusions:

- The use of SRG can significantly increase the shear capacity of RC beams deficient in shear. Enhancements achieved in the shear capacity ranged from 10% to 71% for the T-section beams, while it ranged between 21% and 133% for the rectangular beams.
- Regarding SRG fabric density, the enhancement in P_u increased with increasing SRG fabric density because of increased axial stiffness; however, the increase was not in a linear proportion with the increased fabric density.
- The U-jacketing bond scheme was more effective than the side bonded scheme in increasing the load-carrying capacity of the beams. For the T-beams, on average, the efficacy of the SRG system decreased by 22% because of the change in the bond scheme from U-jacketing to side bonded.
- The SRG strengthening also delayed the formation of the first crack. The first cracks in the SRG-strengthened specimens occurred at a higher load level compared to that in the reference beam.

- The efficacy of the SRG appeared to be dependent on the test parameters.
- As observed from the first study, the presence of internal transverse reinforcement within the critical shear span was observed to increase the shear capacity of the beam comparing the reference beams, however, it decreased the strength gain of the SRG strengthening system. An overall average of the increase in P_u was 68% for specimens without internal transverse reinforcement, and 31% for specimens reinforced with steel stirrups within the test span. This value further decreased to 16% with an increase in the amount of internal transverse reinforcement.
- As observed from Study 1, the experimental results clearly indicated the SRG/stirrups interaction in terms of the strength gain, as well as the strains developed in the internal shear reinforcement. Given the applied load, the strains in the stirrups were significantly greater in unstrengthened specimens. Therefore, it appeared that the presence of the SRG eased the strains in the stirrups.
- The experimental results in Study 2 demonstrated that the behavior of strengthened RC beams is affected by the *a/d* ratio. The increase in P_u attributed to the SRG system increased with an increase in *a/d* ratio for deep beams but decreased with increasing *a/d* ratio for slender beams. The results also showed the higher efficacy of the SRG system in the shear strengthening of slender beams than deep beams. On average, the increase in P_u for slender beams was 108%, whereas this value was only 48% for deep beams, as observed from Study 2.
- As observed from Study 3, the strength properties of the SRG steel fiber can be better utilized by employing the NSE technique. The failure mode of the strengthened beams can be changed from SRG laminate debonding failure to SRG fabric rupture failure using the NSE technique. The failure of the NSE-SRG strengthened beams was mainly characterized by fabric rupture, unlike the EB-SRG

beams where failure was attributed to premature SRG debonding. Thus, the former represents a better utilization of the SRG system. The increase in V_{max} relative to the reference beam ranged from 81% to 124% for the NSE-SRG strengthened beams and 32% to 82% for the corresponding discontinuous EB-SRG strengthened beams, as observed from Study 3.

- Finally, an analytical procedure was proposed to predict the shear strength of T-section as well as rectangular RC beams strengthened with either the NSE-SRG or EB-SRG taking the type of the strengthening technique and *a/d* ratio into consideration. The proposed model resulted in an acceptable prediction capability.

CHAPTER 3: MACHINE LEARNING-BASED CAPACITY PREDICTION AND RELIABILITY ANALYSIS OF RC BEAMS STRENGTHENED WITH INORGANIC COMPOSITES

3.1. Introduction

The use of supervised machine learning (ML) techniques for modeling different civil engineering structures has recently acquired considerable attention owing to its ability to determine the relationship between the input variables and response(s) without prior assumptions of the underlying mathematical and physical models [96] in contrast to most empirical models. It has been successfully applied to solve different problems including damage assessment of bridges [107,143–145] and buildings [146], prediction of the material properties [89,93,147,148], and load-carrying capacity and failure mode of RC members [49,103,111,149–157]. A review of the application of different ML techniques in structural engineering is conducted by Salehi and Burgueño [85].

Previously, single ML models were mainly adopted in the literature including artificial neural network [158–161], decision trees [162], and support vector machine [148,163]. Generally, a single learner might not be sufficient; thus, multiple base learners can be combined to generate a strong model. In this context, ensemble learners combine multiple base learners (aka weak learners) to produce a more stable and accurate prediction. In ensemble models, new predictions are obtained by combining predictions from each base learner. Ensemble models can be formed by training base learners in parallel (e.g., random forest) or sequentially (e.g., gradient boosting and extreme gradient boosting). Successful applications of ensemble learners have been reported in the literature (e.g. [97,103,164–167]). However, the literature lacks the application of ML models for predicting the capacity of RC beams strengthened with SRG and inorganic composites in general.

Therefore, this dissertation presents a pioneer ML-based model for predicting the shear capacity of RC beams strengthened in shear and flexural capacity of

strengthened RC beams in flexure. The dissertation also presents a review of the existing analytical models for RC beams strengthened in shear as well as flexure using inorganic composites. The developed ML models are compared with the existing models and guideline equations. Finally, a reliability analysis is performed to calibrate the resistance reduction factor to achieve a specified target reliability index. Thus, the research presented in this chapter is aimed to address the following aspects:

- Develop accurate and reliable ML models for determining the shear capacity of RC beams strengthened in shear with inorganic composites.
- Develop accurate and reliable ML models for determining the flexural capacity of flexural strengthened RC beams strengthened in flexure with inorganic composites;
- Compare the prediction accuracy of the developed model against that of the existing analytical models; and
- Calibrate a resistance reduction factor to achieve a specified target reliability index of the developed models based on reliability analysis.

The following two studies have been conducted in this chapter:

i. Wakjira TG, Ebead U, Alam MS. Machine Learning-Based Shear Capacity Prediction and Reliability Analysis of Shear-Critical RC Beams Strengthened with Inorganic Composites. Case Studies in Construction Materials 2022; 16: e01008. https://doi.org/10.1016/j.cscm.2022.e01008.

ii. Wakjira TG, Ibrahim M, Ebead U, Alam MS. Explainable machine learning model and reliability analysis for flexural capacity prediction of RC beams strengthened in flexure with FRCM. *Engineering Structures* 2022;255. https://doi.org/10.1016/j.engstruct.2022.113903.

3.2. Overview of ML Models

This section presents an overview of the ML models used in this study.

3.2.1. Single AI models

3.2.1.1. Kernel ridge regression

Kernel ridge regression (KRR) is a nonlinear regression that maps data into different dimensional spaces ($x_i \rightarrow \Phi_i = \Phi(x_i)$) using kernel trick. It addresses the limitations of the well-known least square (LS) method using ridge regression (linear least squares with I2-norm regularization) and kernel function. Thus, it extends the ridge regression to include nonlinear problems using a nonlinear map. For nonlinear regression, KRR transforms the nonlinear regression in the original space into a linear regression in a higher dimensional space using a nonlinear kernel function. The widely used kernels include linear, polynomial, hyperbolic tangent (sigmoid), and radial basis function (RBF) kernels [168].

The KRR regression can be formulated as [169]:

$$y = K\alpha + \varepsilon \tag{3.1}$$

where ε is the error vector and α is the KRR unknown vector determined by minimizing Eq. (3.2).

$$f(\alpha) = 0.5(y - K\alpha)^T(y - K\alpha) + 0.5\lambda\alpha^T K\alpha, \lambda \geq 0 \tag{3.2}$$

where λ is the regularization parameter.

The solution with respect to α can be given by [169]:

$$\alpha = (K + \lambda I_n)^{-1} y \tag{3.3}$$

The KRR solution in Eq. (3.3) can be rewritten as:

$$y = (K + \lambda I_n)\alpha \tag{3.4}$$

The kernel type and parameters α and λ are optimized to find the best model.

3.2.1.2. K-nearest neighbors

The K-nearest neighbors (KNN) is a non-parametric model that can be used for classification as well as regression problems. The KNN regression approximates the relationship between the input features and target variable using the observations of K nearest neighbors. To make a prediction for a query point, the algorithm firstly measures the distance between the training data points and the query data point using Euclidean distance and orders the calculated distance in ascending order. The algorithm then identifies the K training data points closest to the query data point, represented by N_0. Finally, the target value for the query data point is estimated as the weighted mean of all the training responses in N_0. The size of the neighborhood K needs to be optimized.

3.2.1.3. Support vector regression

Support vector machine (SVM) is one of the supervised ML techniques with associated algorithms primarily applied for classification problems using the structural risk minimization principle [170]. It can also be used to efficiently perform non-linear regression by indirectly mapping the original input vectors into a very high-dimensional feature space, using kernel functions [170]. The class of SVM used for regression problems is known as support vector regression (SVR). Given n number of training examples $\{(x_i, y_i)\}_{i=1}^{n} \epsilon\, \mathbb{R}^n \times \mathbb{R}$, SVR estimate the regression function $f(x)$ in Eq. (3.5) by minimizing the regularized risk function in Eq. (3.5(3.5)a) subject to Eqs. (3.5b) and (3.5c) [171].

$$f(x) = w.\phi(x) + b \tag{3.5}$$

$$\tau(w, \xi, \xi^*) = \frac{1}{2}\|w\|^2 + C\frac{1}{n}\sum_{i=1}^{n}(\xi_i + \xi_i^*), i = 1, 2, \dots, n \tag{3.5a}$$

$$(w.\phi(x) + b) - y_i \leq \varepsilon + \xi_i, i = 1, 2, \dots, n \tag{3.5b}$$

$$y_i - (w.\phi(x) + b) \leq \varepsilon + \xi_i^*, i = 1, 2, \ldots, n \quad (3.5c)$$

$$x_i \epsilon X \subseteq R^n \, , y_i \epsilon Y \subseteq R \quad (3.5d)$$

$$\xi_i, \xi_i^* \geq 0 \quad (3.5e)$$

where,

ξ_i and ξ_i^* are slack variables,

w and b are weight vector and the bias, estimated by minimizing Eq. (3.5a) subject to Eqs. (3.5b) and (3.5c) [171],

ε is Vapnik's insensitive loss that serves as a threshold, in which the absolute values of errors less than ε are ignored, and

C is a regularization parameter.

The prediction in SVR is given by [168,172]:

$$f(x) = \sum_{i \epsilon \, SV} (\alpha_i - \alpha_i^*) K(x_i, x) + b \text{ subject to } 0 \leq \alpha_i \leq C, 0 \leq \alpha_i^* \leq C \quad (3.6)$$

where $K(x_i, x)$ is the kernel function, α_i and α_i^* are the Lagrange multipliers, and *SV* denotes support vectors, which are subsets of training data.

The widely used kernels are [173,174]:

- Linear kernel: $k(X_i, X_j) = \langle X_i, X_j \rangle$.
- Polynomial kernel: $k(X_i, X_j) = (\gamma \langle X_i, X_j \rangle + r)^d$, $\gamma > 0$ and d as a polynomial degree.
- Hyperbolic tangent (sigmoid) kernel: $k(X_i, X_j) = \tanh(\gamma \langle X_i, X_j \rangle + r)$, $\gamma > 0$.
- Radial basis function (RBF) kernel: $k(X_i, X_j) = e^{-\frac{1}{2\sigma^2}\|X_i - X_j\|^2}$, where σ is the width of the kernel.

In this study, all the above four kernel functions are considered. The other two hyperparameters that greatly affect the SVM predictive capacity are the regularization

parameter C and ε-insensitive zone [175]. These hyperparameters are also optimized in this study.

3.2.1.4. Decision trees

Decision tree also known as classification and regression tree or CART for short is a non-parametric supervised ML algorithm that resembles a flowchart-like structure. The CART algorithm predicts the response following the decision from the root node to the leaf, in which each internal node or decision node denotes the test, while each leaf or terminal node represents the outcome of the test.

It can be used to solve both classification and regression problems in the form of a tree structure [162]. In regression, given n observations of training dataset $\{(x_1, y_1), (x_2, y_2), \dots, (x_n, y_n)\}$, decision tree iteratively splits the training data into a set of terminal nodes. The algorithm then fits a regression tree in each node using the feature, which produced the highest information gain at each node [162]. The main hyperparameters of the CART; namely, the maximum depth of the tree, minimum number of samples at the internal node, minimum number of samples at the leaf node, and maximum number of input features at each node are optimized to determine the best model.

The decision tree model is easy to interpret and visualize. However, a single tree may not be adequate to effectively learn the model. Furthermore, decision tree suffers from the problem of generalization and high variance and bias. The ensemble of CARTs can be used to overcome these problems.

3.2.2. Ensemble models

Ensemble learners integrate several base learners to enhance the generalization ability over a single model [176]. Bagging and boosting ensembles are widely used techniques for improving prediction performance. They are commonly applied to tree-

based learners although they can be applied to other learners also such as artificial neural networks [176]. The basic idea behind the ensemble model is to combine multiple base learners in computing the final response rather than relying on an individual model.

3.2.2.1. Random forest

Random forest is an ensemble model that constructs several decision trees in parallel as a committee to generate independent outputs, and finally computes their mean to generate the final output in order to ultimately increase the prediction accuracy of the underlying algorithms [177]. In this sense, random forest follows a two-step process: (a) construct T number of decision trees (estimators) and (b) compute the arithmetic mean of the prediction across the estimators to generate the final prediction in the case of regression and a majority vote in the case of classification problems.

Each decision tree predictor in the random forest regression (RFR) algorithm uses bootstrap samples, which are randomly selected samples from the original training dataset with replacement. Moreover, random subsets of input features are considered when splitting nodes in the decision tree on the best split among a random subset of the features selected at every node [178]. The split at each node is performed in two steps. Firstly, a random subset of input features is selected from the bootstrap sample [178]. The best subset feature is then selected to perform the decision split at each node of a decision tree [178]. Figure 3.1 shows a simple schematic of the RFR algorithm. The final prediction of RFR is made by averaging the predictions of each decision tree predictor, as shown in Figure 3.1.

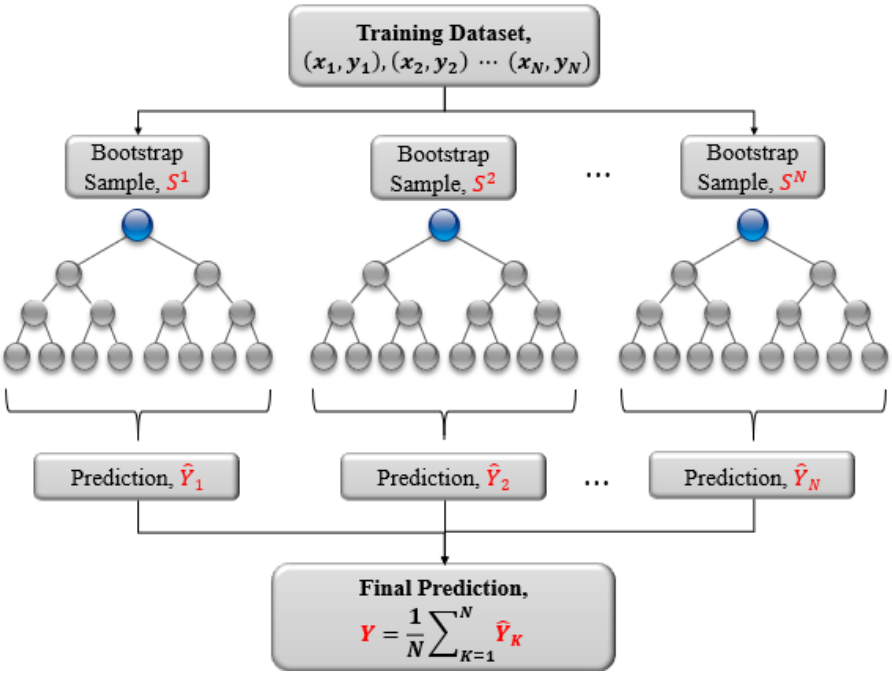

Figure 3.1: Learning process of random forest regression algorithm.

3.2.2.2. Extremely randomized trees

Extremely randomized trees (ERT) algorithm is another type of tree ensemble learners that can be applied to both classification and regression problems [179]. Its main difference with the random forest is that it uses the complete training dataset to grow the trees, unlike random forest that uses bootstrap samples. Besides, ERT adds randomization in selecting the split points of each node [179]. Similar hyperparameters are used for the extremely randomized trees as that of random forest.

3.2.2.3. Gradient boosted trees

Gradient boosted trees (GBT) is one of the powerful boosting algorithms, which combines a sequence of weak learners; particularly classification and regression trees in an additive model. Figure 3.2 illustrates the learning process in the boosting algorithm. The GBT is mathematically expressed as follows:

$$F_T(x) = \sum_{t=0}^{T} f_t(x) \tag{3.7}$$

where T is the number of base learners (CARTs) and f_t is the set of all possible decision trees.

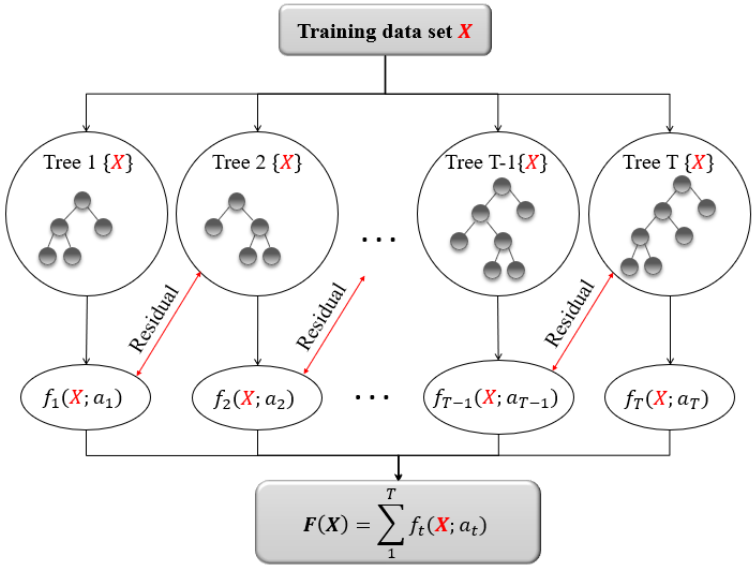

Figure 3.2: Schematic of boosting algorithm.

Given a training dataset $\{(x_1, y_1), (x_2, y_2), \ldots, (x_n, y_n)\}$ with n observations and a differentiable loss function $L(y_i, F(x))$, gradient boosted trees regression (GBTR) performs the following steps [180]:

1) Initialize the model with a constant value that minimizes the loss:

$$F_0(x) = \arg\min_{\rho} \sum_{i=1}^{n} L(y_i, \rho) \tag{3.8}$$

2) For $t = 1$ to T do:

   a. Determine the negative gradient of the loss or pseudo residuals, given the previous ensemble F_{t-1}:

$$r_{it} = -\frac{\partial L[y_i, F_{t-1}(x_i)]}{\partial F_{t-1}(x_i)} \tag{3.9}$$

b. Fit CART to r_{it} values and create terminal regions $R_{jt}, for\ j = 1, 2, \dots, j_t$, where j_t is the number of terminal nodes.

c. For $j = 1, 2, \dots, j_t$ compute the output value for each leaf that minimizes the loss:

$$\rho_{jt} = \arg\min_{\rho} \sum_{x_i \epsilon R_{ij}} L(y_i, F_{t-1}(x_i) + \rho) \tag{3.10}$$

d. Update the estimator of $F(x)$:

$$F_t(x) = F_{t-1}(x) + v \sum_{j=1}^{J_t} \rho_{jt} \mathrm{I}_{x \epsilon R_{jt}}(x) \tag{3.11}$$

where v is the learning rate [180].

3) Output $F_T(x)$.

3.2.2.4. Extreme gradient boosting

The extreme gradient boosting (xgBoost) algorithm developed by Chen and Guestrin [181] is an improved form of gradient boosting algorithm. The xgBoost adds a regularization term in the objective function in order to reduce model complexity and prevent overfitting. The base learners (trees) in the xgBoost are built sequentially by minimizing the objective function [181] in Eq. (3.12), which contains the loss function and regularization term:

$$\sum_{i=1}^{n} L(y_i, \hat{y}_i) + \sum_{t=1}^{T} \Omega(f_t) \tag{3.12}$$

$$\Omega(f) = \gamma T + \frac{1}{2}\lambda \sum_{j=1}^{T} w_j^2 \tag{3.13}$$

where γ is the complexity of each leaf, w_j is the weight of leaf j, and λ is the

penalty parameter.

3.3. Hyperparameter Optimization

The performance of the model is considerably affected by the selection of the model parameters. The optimal hyperparameters are selected with the use of hyperparameter optimization or tuning, which refers to the process of searching for the best values of the hyperparameters. In this study, a grid search optimization technique is adopted to efficiently optimize the hyperparameters. It is an optimization algorithm that exhaustively searches the optimal hyperparameter combinations considering all combinations of the user-defined hyperparameters [182]. In addition, the development of a reliable model requires the validation of the model by external data that was not included as part of the model development to address the problem of overfitting. In this study, a standard technique of detecting overfitting known as the K-fold cross-validation is used to prevent overfitting, where K refers to the number of groups that a given data is to be split into. In this approach, the data is randomly split into K disjoint subsets that have approximately the same number of observations, and then the network is fitted using the $K-1$ folds and validated using the remaining one-fold. Thus, each fold, in turn, serves as a validation set. In this study, a commonly used ten-fold ($K = 10$) cross-validation, which splits the data into ten groups is adopted, as shown in Figure 3.3**.** The 10-fold cross-validation uses the following learning and validation steps:

(a) Split the data into ten subsets of equal sizes $\{D_1,\ D_2,\ ..,D_{10}\}$, as shown in Figure 3.3;

(b) Use nine sets of the data to train the model and the remaining one set of the data to validate the model, as shown in Figure 3.3; and

(c) Repeat steps (a) and (b) with each subset $\{D_i,\ i = 1,2,..,10\}$ used exactly once as the validation set, as shown in Figure 3.3.

The final performance of the model is then computed by averaging the cross-validation performance of the 10 models.

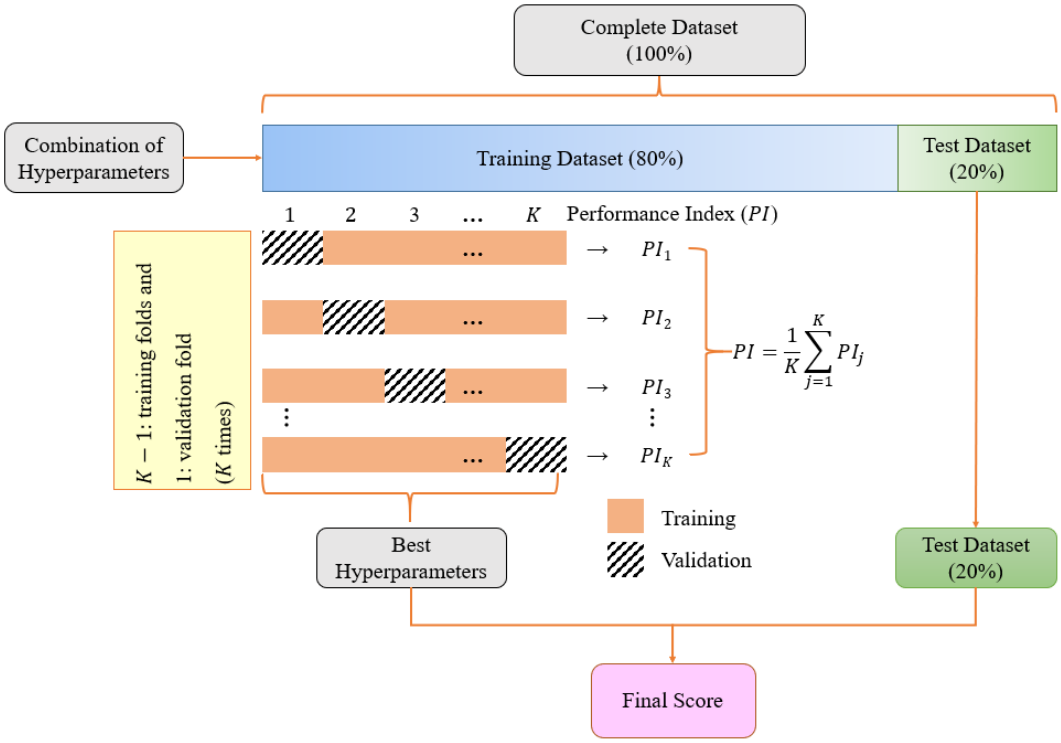

Figure 3.3: Conceptual schematic of 10-fold cross-validation adopted in this study.

3.4. Model Performance Measures

The performance of the ML-based model is usually measured with the use of different statistical indices. Different statistical performance indices; namely, mean absolute percentage error (MAPE), root mean squared error (RMSE), mean absolute error (MAE), and coefficient of determination (R^2) are used in this study, as given below.

$$MAPE = \frac{1}{n}\sum_{i=1}^{n}\left|\frac{y_i - \hat{y}_i}{y_i}\right| \tag{3.14}$$

$$MAE = \frac{1}{N}\sum_{i=1}^{N}|y_i - \hat{y}_i| \tag{3.14a}$$

$$RMSE = \sqrt{\frac{1}{n}\sum_{i=1}^{n}(y_i - \hat{y}_i)^2} \tag{3.14b}$$

$$R^2 = 1 - \frac{\sum_{i=1}^{n}(y_i - \hat{y}_i)^2}{\sum_{i=1}^{n}(y_i - \bar{y})^2} \tag{3.14c}$$

where y is the observed value, $\hat{y}$ is the predicted value, and $\bar{y}$ is the arithmetic mean of y values.

3.5. Model Explainability

Despite their widespread applications, ML models remain mostly black boxes [149]. In this context, explainability is an important step as it is, often, not apparent. To this end, a unified framework referred to as the Shapley Additive exPlanations (SHAP) approach has recently been introduced to interpret the predictions of ML models [183]. However, a limited number of studies have investigated the explainability of such complex ML models in structural engineering applications [149,164,184].

The SHAP approach also enables the identification and prioritization of important factors that determine the response variable using SHAP values that are consistent and individualized to each prediction. Given a prediction from a model $f(x)$ with Q input features, SHAP develops an explanation model $g(x')$ that is a linear function of binary variables in Eq. (3.15) using simplified inputs x' that map the original inputs through the mapping function (h_x) in Eq. (3.16) [183]:

$$g(x') = \phi_0 + \sum_{i=1}^{Q} \phi_i x_i' \tag{3.15}$$

$$x = h_x(x') \tag{3.16}$$

where $\phi_i \epsilon \mathbb{R}$ are the feature attribution values, and ϕ_0 represents a constant value when all inputs are missing.

In Eq. (3.16), $x' \epsilon \{0, 1\}^M$, thus h_x maps 1 or 0 to the original input space, where 0 indicates the input is excluded in the model, while 1 indicates the input is included in

the model.

As described in [183], there exists a single solution to Eq. (3.15) with three desirable properties, namely, local accuracy, missingness, and consistency. The first desirable property, which is local accuracy ensures that the explanation function results in the same values as the original model, $f(x) = g(x')$ whenever $x = h_x(x')$. Missingness ensures that the missing feature has no impact on the model ($x_i' = 0$ implies $\phi_i = 0$). Finally, consistency states that if a given feature has a larger impact in model f' than model f, then the importance measure in the model f' should always be larger than that in model f, as shown in Eq. (3.17).

$$if\ f_x'(z') - f_x'(z'\backslash i) \geq f_x(z') - f_x(z'\backslash i)\ \text{for all inputs}$$
$$z' \epsilon \{0,1\}^M \tag{3.17}$$
$$\text{then } \phi_i(f', x) \geq \phi_i(f, x)$$

where $z'\backslash i$ denotes the setting $z_i' = 0$, and $z' \subseteq x'$ represent all z' vectors.

According to Lundberg and Lee [183], the unique solution that satisfies the three desirable properties is given by:

$$\phi_i(f, x) = \sum_{z' \subseteq x'} \frac{|z'|!\,(M - |z'| - 1)!}{M!} [f_x(z') - f_x(z'\backslash i)] \tag{3.18}$$

where $|z'|$ is the number of non-zero entries in z', $f_x(z') = f_x\big(h_x(z')\big) = E[f(z)\backslash Z_S]$ is the expected value of the model f conditioned on a subset S of the input features, and S is the set of non-zero indices in z'.

3.6. Preparation of the Dataset and Description of Input Parameters

It is well understood that the first step in the ML model involves the collection of a relevant experimental database. The database for RC beams strengthened in shear as well as flexure are discussed below.

3.6.1. RC beams strengthened in shear with inorganic composites

In this study, a database of 173 RC beams strengthened with different types of inorganic composites is developed based on an extensive literature review [2,8,185–194,10,195–198,12,38–40,119,120,124]. The experimental database covers a wide range of beam geometries, concrete strengths, internal shear and flexural reinforcements, fiber types, strengthening configurations, wrapping schemes, and mechanical properties of the fibers. Three types of wrapping schemes are used in the database; namely, side bonded (SB) scheme in which the composite is bonded to the two sides of the beam, U-wrapped (UW) scheme.

The development of an accurate shear model requires the incorporation of all parameters affecting the shear capacity of RC beams strengthened with inorganic composites. Thus, in this research, a comprehensive set of parameters (a total of 17 parameters) are considered, unlike most of the existing models that were developed based on a limited number of parameters. These parameters are the width of the web (b_w), effective depth of the section (d), shear span-to-effective depth ratio (a/d), concrete compressive strength (f_c'), flexural reinforcement ratio (ρ_{sx}), yield strength of reinforcing flexural bars (f_{yx}), reinforcement ratio of stirrups (ρ_{sy}), yield strength of stirrups (f_{sy}), and characteristics of the strengthening system including the fabric type, tensile strength of the fibers (f_{fu}), elastic modulus of the fibers (E_f), effective depth (h_{fe}) (Figure 3.7), thickness of the composite (t_f), number of strips (N_f) and width of each strip (W_f) (for discontinuous configuration), number of fabric layer(s) (n_f), and wrapping scheme. The variables W_f, N_f, n_f, and t_f are used in the model in terms of the FRCM reinforcement ratio (ρ_f) as given by:

$$\rho_f = 2\frac{N_f\, W_f}{a}\ \frac{n_f\, t_f}{b_w} \tag{3.19}$$

where a is the shear span.

Thus, fourteen (14) parameters are used as the final input vectors of the ML model. Five different types of fabrics are included in the collected experimental database; namely, carbon (C), basalt (B), glass (G), polyparaphenylene benzobisoxazole (PBO), and steel (S). The G, C, PBO, B, and S fabrics are identified with values 1, 2, 3, 4, and 5 in the ML model. Similarly, all the three wrapping schemes; viz., FW, UW, and SB schemes are included in the database and assigned values of 1 for the SB and 2 for the UW/FW schemes.

Table 3.1 presents a summary of the geometry and internal reinforcement properties of the experimental tests included in the database along with the descriptive statistics of each parameter, while Table 3.2 provides a summary of the characteristics of the strengthening system. Besides, Figure 3.4 illustrates the statistical distribution of the database in terms of the input parameters versus experimental shear capacity (V_{ex}) plots.

Table 3.1. Geometry and material characteristics of RC beams strengthened in shear

References	Geometry			Concrete	Internal reinforcement			
	b_w (mm)	d (mm)	a/d	f_c' (MPa)	ρ_{sx} (%)	f_{sx} (MPa)	ρ_{sy} (%)	f_{sy} (MPa)
[185]	180	419	2.98	46.2	3.20	555	–	–
[186]	150	159	2.52	20	1.30	578	–	–
[187]	150	307.5	3.25	37.5	2.17	480	–	–
[40]	102	177	2.60	21.6–23.8	2.23	547	–	–
[188]	300	254	2.76	28–28.3	0.79	517.2	–	–
[119]	150	250	3.00	36	5.03	520	0.0–0.50	0.0–294
[120]	150	225	2.78–3.0	29.2–38.3	1.86–2.79	457	0.23–0.32	446
[189]	200	385	2.63	14–15.2	3.26	571	–	–
[190]	150	256	3.91	23.2	3.20	500	–	–
[191]	250	317	3.15	61	3.72	494	0.0–0.75	0.0–365

[38]	102	177	2.6–3.6	20–23.8	2.20	547	–	–

References	Geometry			Concrete	Internal reinforcement			
	b_w (mm)	d (mm)	a/d	f_c' (MPa)	ρ_{sx} (%)	f_{sx} (MPa)	ρ_{sy} (%)	f_{sy} (MPa)
[2]	150	272	2.85	25.3	1.50	575	0.14	275
[192]	120	372	2.69	25.5–34	4.20	500	0.42	500
[39]	152	248	3.00	29.1–42.9	3.04	690	0.27	276
[193]	120	204	3.18	25.6–35.2	2.60	570	–	–
[194]	150	320	2.50	10.1–20.8	1.60	545	–	–
[195]	150	270	2.22	28	1.50	515	–	–
[12]	150	230	3.00	21.3–24.7	6.16	545	0.22–0.34	527
[8]	150	289	1.90	30	1.39	595	–	–
[10]	150	242	3.31	45.95	4.33	526	0.27	526
[124]	200	273	2.20	23.3–28	0.75–1.60	500	–	–
[196]	180	329.5	2.88	34	4.14	588	0.10–0.21	234
[197]	180	334	1.6–3.1	34	2.61	584	–	–
[198]	180	334	2.60	34	2.61	584	–	–
Mean	160	276	2.72	30.5	2.69	543.8	0.09	129.0
STD	41	66	0.46	10.1	1.32	44.3	0.16	203.5
Minimum	102	159	1.60	10.1	0.75	457.2	0	0
Maximum	300	419	4.90	61	6.16	690	0.75	527

Table 3.2. Summary of the strengthening system included in the database for RC beams strengthened in shear

References	Fabric type	E_f (GPa)	f_{fu} (GPa)	Wrapping scheme	ρ_f (‰)	h_{fe} (mm)
[185]	C	201–262	2.950–3.8	SB	0.20	377.1
[186]	B	31.9	0.623	SB	1.20–3.40	143.1
[187]	G, C	75–230	2.3–3.8	SB, UW	0.49–1.18	276.75
[40]	C	225	3.8	SB, FW	1.86–5.59	159.3
[188]	B, G, C,	90–270	2.61–5.8	FW	0.28–0.35	228.6

	PBO					
[119]	C	230	3.8	SB	1.92–3.84	225
[120]	PBO	270	5.8	UW	0.30–1.20	202.5
[189]	C	74–225	1.4–4.8	UW	1.86–3.80	238.5
References	Fabric type	E_f (GPa)	f_{fu} $(\mathrm{G}Pa)$	Wrapping scheme	ρ_f (‰)	h_{fe} (mm)
[190]	G	75	0.574	FW	1.50–2.20	230.4
[191]	C	230	3.8	SB	0.70–1.41	285.3
[38]	C	225	3.8–4.8	UW	1.22–6.80	159.3
[2]	C	225	3.35	FW	0.60–1.30	244.8
[192]	G	75	0.574	UW	1.80–5.50	252
[39]	PBO	127	1.664	UW	0.61–2.42	223.2
[193]	G	74	1.102	SB, UW	0.20–1.20	183.6
[194]	C	225	3.375	UW	0.60–2.60	220
[195]	C	240	4.3	SB, UW	0.40–2.90	243
[12]	C, S	190–240	3.8	UW	0.63–3.60	207
[8]	C, G, PBO	80–270	2.6–5.8	SB	0.40–0.63	260.1
[10]	PBO	270	5.8	UW	0.34	300
[124]	S	190	2.8	UW, FW	0.84–2.54	245.5
[196]	S	190	3.0	SB, UW	1.87–3.76	229.5
[197]	S	190	3.0	UW	1.87–3.76	300.6
[198]	S	190	3.0	SB, UW	1.22–3.76	300.6

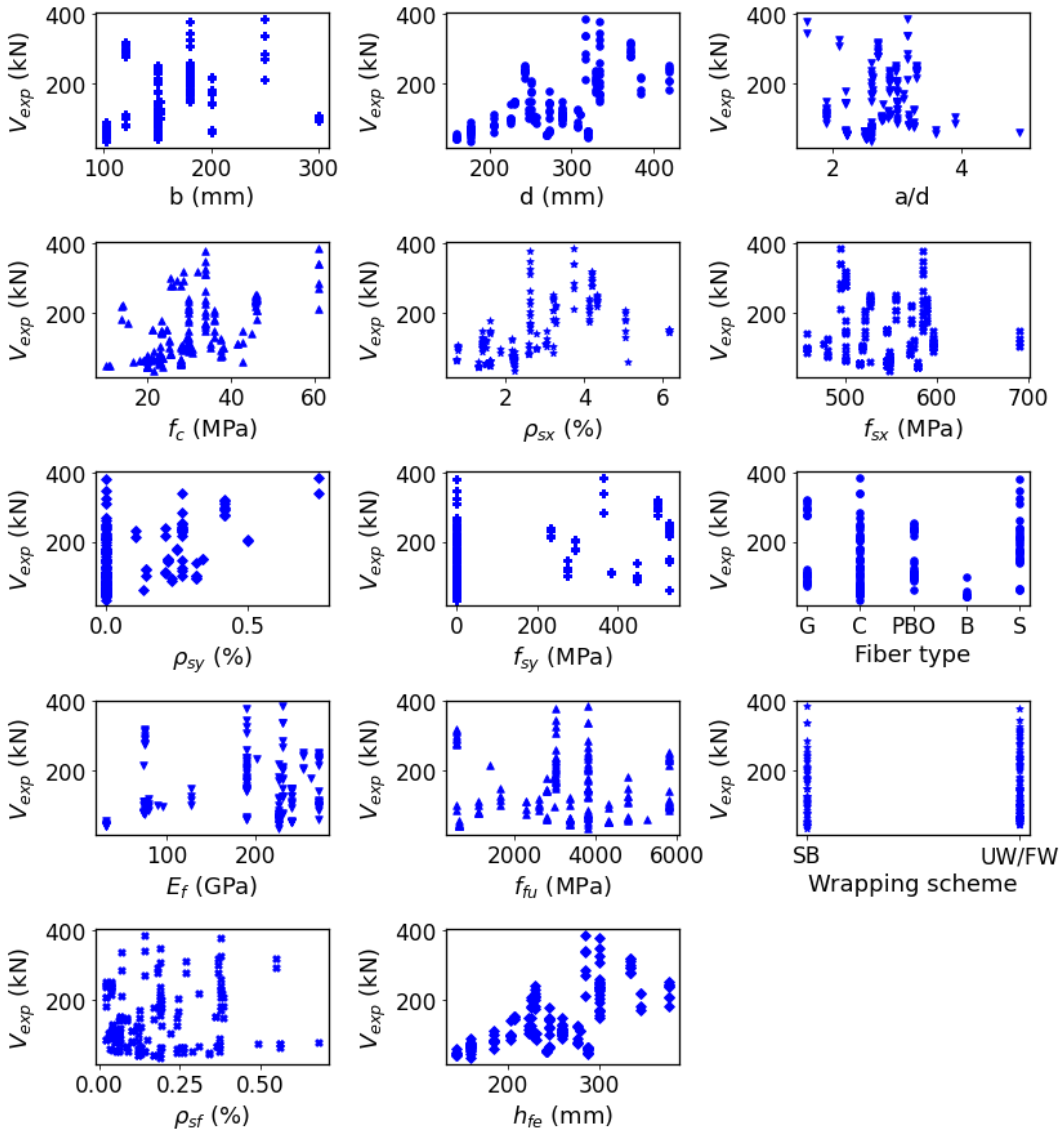

Figure 3.4: Correlation between the input parameters and the shear capacity.

3.6.2. RC beams strengthened in flexure with inorganic composites

A database of flexural strengthened rectangular RC beams in flexure with inorganic composites collected from the literature [9,11,22,24,26,199–208] is used in this study. A total of 132 RC beams strengthened in flexural are included in the developed database. A wide range of beam geometries, mechanical characteristics of materials (concrete, steel, and strengthening composite), fabric types (carbon, PBO, and steel), and reinforcement areas for both internal steel reinforcement and external strengthening reinforcement are considered in the database, as shown in Figure 3.5.

However, the mechanical characteristics of strengthening mortar are not reported in most of the studies, thus, its effect on the flexural capacity of the strengthened beam is not considered herein. Different input variables including the width of the web (b_w), effective cross-sectional depth (d), concrete compressive strength (f_c), yield strength of steel bars (f_y), area of steel reinforcement in the tension (A_{st}) and compression (A_{sc}) zones, elastic modulus of fibers (E_f), number of fabric layers (n_f), width of the composite plate (b_f), and thickness of the fabrics (t_f) are considered in this study. The width of the composite plate, the thickness of the fabrics, and the number of fabric layers are represented in terms of the area of composite reinforcement, $A_f = b_f n_f t_f$. Thus, the final input vector comprises a total of nine parameters. It is worth mentioning here that the response of two beams strengthened with an equivalent A_f, but different numbers of fabric layers in the composite may vary due to the difference in the behavior of the strengthening system with the change in the number of fabric layers. However, the current model does not consider such an effect on the flexural response of the strengthened beams. Table 3.3 presents the statistical distribution of the input parameters of the experimental database used in this study, while the range of each input variable is clearly illustrated in Figure 3.5. In addition, Figure 3.6 shows an 8 × 8 matrix in which the diagonal of the matrix shows the histogram for the distribution of each variable, whereas the lower and upper triangular matrices show the scatter plot and Pearson correlation coefficient (r) between the input variables, respectively.

Table 3.3. Distribution of input parameters for RC beams strengthened in flexure

Description	Input parameter	Mean	STD	Min	Max	Q1	Q2	Q3
Geometry	b_w (mm)	250.2	115.9	120	400	150	176	400
	d (mm)	218.7	66.24	129	450	210	210	217
Concrete	f_c (MPa)	40.86	14.44	15.1	67.5	29.13	42.38	49.0
Internal reinforcement	f_y (MPa)	496.4	85.13	267	604.2	468.3	517.2	537
	A_{st} (mm^2)	331.3	134.1	157	602.9	212.5	339.1	461.6
	A_{sc} (mm^2)	159.3	165.3	0.00	602.9	0.00	100.5	157.1
FRCM reinforcement	A_f (mm^2)	26.39	18.71	6.75	108	13.80	23.0	31.96
	E_f (GPa)	234.7	48.45	73.5	271	206	270	270
	Fabric type	Carbon, PBO, Steel						

STD: standard deviation; Max: maximum; Min: minimum; and Q1, Q2, Q3: 25th, 50th, and 75th percentiles

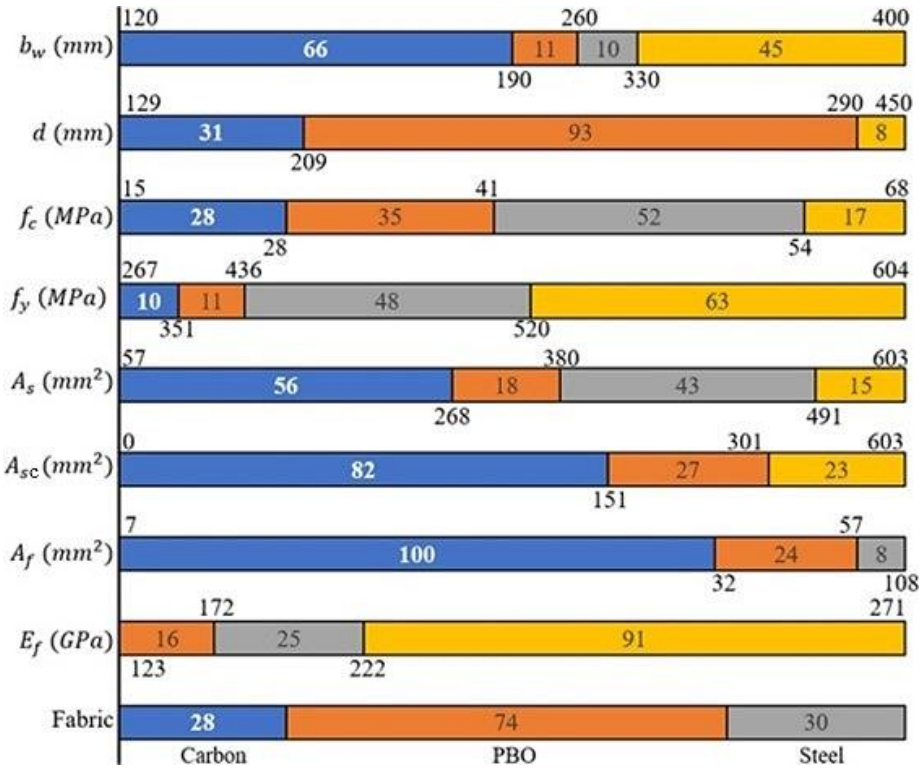

Figure 3.5: Distribution of the input variables.

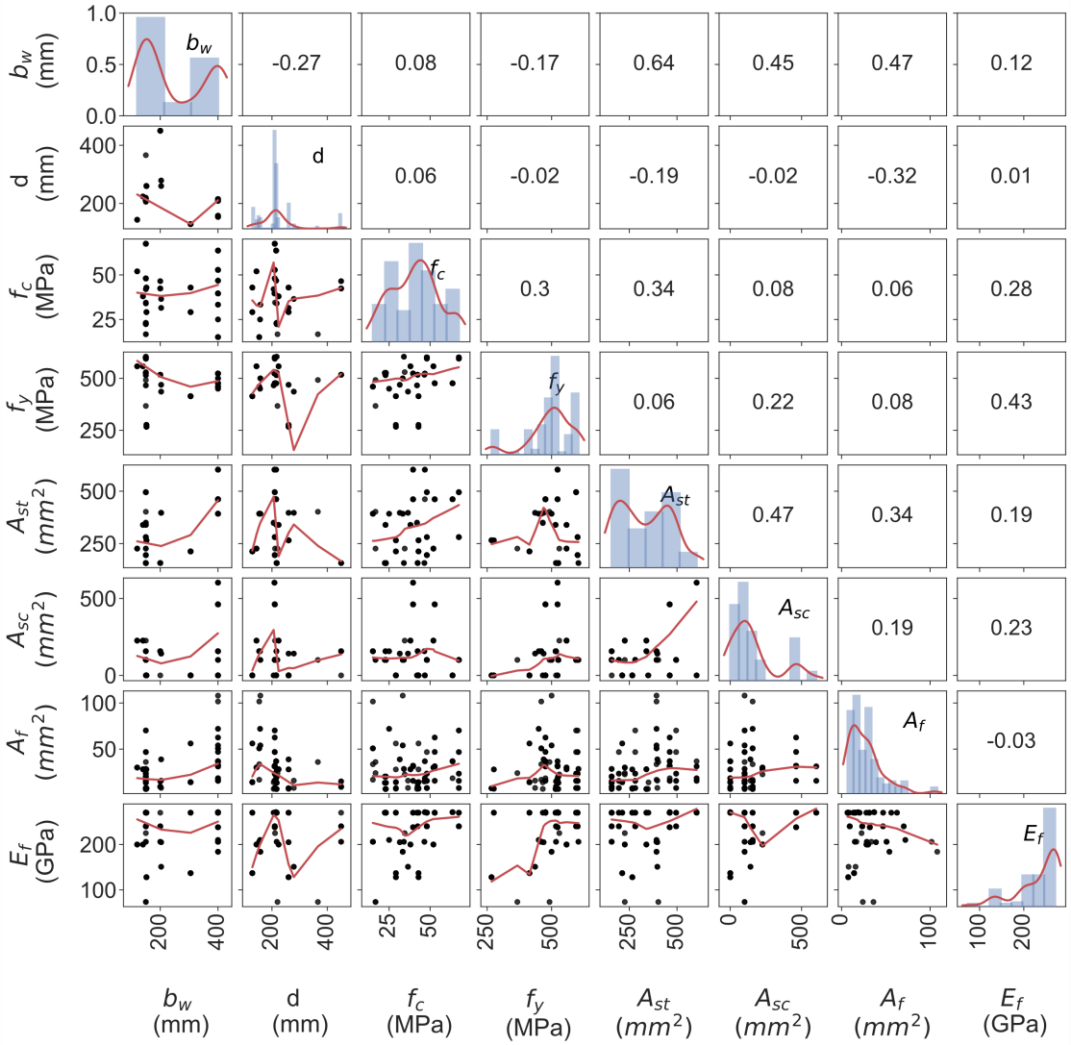

Figure 3.6: Details of the dataset used for RC beams strengthened in.

To mitigate the problems associated with low learning rates of the network at the extreme values, the database is normalized into a range within [0, 1], as follows:

$$x_n = \frac{x_{orig} - x_{min}}{x_{max} - x_{min}} \tag{3.20}$$

where,

x_{orig} and x_n are the original and normalized value of the variable, respectively, and

x_{max} and x_{min} are the maximum value and minimum value of the variable.

3.7. Review of Existing Models and Design Guideline

3.7.1. RC beams strengthened in shear with inorganic composites

Figure 3.7 shows the details of RC beam strengthened in shear. In most of the existing design models [2,120,188,209], the shear capacity of the FRCM-strengthened RC beam is evaluated as a simple superposition of the capacity provided by concrete, stirrups, and FRCM system, as follows:

$$V = V_c + V_S + V_f \tag{3.21}$$

where V_c, V_S, and V_f denote concrete, stirrups, and FRCM contributions to shear resistance, respectively.

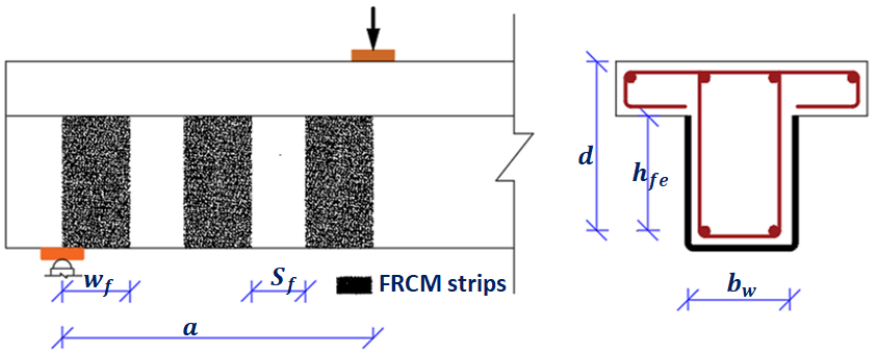

Figure 3.7: Details of RC beams strengthened in shear within the shear span with UW FRCM.

Seven existing models for the shear capacity of RC beams strengthened in shear with inorganic composites, particularly, FRCM are considered in this study. The first four models [2,120,188,209] generally differ in the evaluation of the FRCM contribution. In two of the models; namely, Triantafillou and Papanicolaou [2] and Escrig et al. [188] models, the shear capacity provided by the FRCM system is determined as a function of the FRCM fiber properties, while ACI 549 [209] and Ombres [120] models are based on the properties of FRCM composite. Model-1

through Model-4 fail to consider FRCM/stirrups interaction. Moreover, the models do not account for the variation of the shear crack with both applied load and axial tensile strain in the flexural reinforcement bars. As a result, Wakjira and Ebead [138] proposed an analytical procedure based on the MCFT [135], in which the shear capacity of the FRCM-strengthened beams is determined in an iterative procedure considering the effect of FRCM/stirrups interaction and change in the shear crack angle. In another study [210], the same authors used a simplified compression field theory combined with probability and statistical techniques to develop a non-iterative simplified shear design equation for FRCM-strengthened beam.

3.7.1.1. Model-1: Triantafillou and Papanicolaou [2]

According to Triantafillou and Papanicolaou [2], the shear capacity provided by the FRCM is given as follows, assuming that the FRCM fibers are made of continuous rovings parallel and perpendicular to the beam axis:

$$V_f = \rho_f \varepsilon_{eff} E_f b_w h_{fe} \tag{3.22}$$

$$h_{fe} = 0.9d \tag{3.22a}$$

$$\varepsilon_{eff} = 0.5\varepsilon_{fu} \tag{3.22b}$$

where ρ_f is the reinforcement ratio of FRCM, h_{fe} is the effective depth of the jacket (Figure 3.7), d is the effective depth of the beam section, and ε_{eff}, ε_{fu}, and E_f are the effective strain, ultimate strain, and the elastic modulus of FRCM fibers, respectively.

3.7.1.2. Model-2: Escrig et al. [188]

Escrig et al. [188] proposed the following equation for determining the shear capacity provided by the FRCM:

$$V_f = 2n_f \varepsilon_{eff} E_f t_f h_{fe} (\cot\alpha + \cot\theta) \sin^2\alpha \tag{3.23}$$

$$\varepsilon_{eff} = k_1 \left(\frac{{f_c'}^{2/3}}{\rho_f E_f} \right)^{k_2} \varepsilon_{fu} \qquad (f_c' \text{ in MPa}, E_f \text{ in GPa}) \tag{3.23a}$$

$$k_1 = \begin{cases} 0.020; & \text{SB or UW} \\ 0.035; & \text{FW} \end{cases} \tag{3.23b}$$

$$k_2 = \begin{cases} 0.550; & \text{SB or UW} \\ 0.650; & \text{FW} \end{cases} \tag{3.23c}$$

$$\theta = 45^0 \tag{3.23d}$$

where n_f is the number of fabric layers, and α is the inclination of the fiber with respect to the longitudinal axis of the beam. In Eqs. (3.23b) and (3.23c), FW, UW, and SB indicate the wrapping scheme; particularly, full, U-, and side bonded wrapping, respectively.

3.7.1.3. Model-3: Ombres [120]

Ombres [120] proposed a formula to predict the contribution of FRCM, which is given by:

$$V_f = k_e \varepsilon_{eff} E_{frcm} \rho_f b_w d(\cot\alpha + \cot\theta) \sin\alpha \tag{3.24}$$

$$\varepsilon_{eff} = \frac{f_{fdd}}{E_{frcm}} \left[1 - \frac{1}{3} \frac{l_e \sin\alpha}{\min(0.9d;\ h_w)} \right]; \tag{3.24a}$$

$$f_{fdd} = \frac{0.24}{\gamma_{fd}\sqrt{\gamma_c}} \sqrt{\frac{E_{frcm} k_b \sqrt{f_{ck} f_{ctm}}}{t_f}}; \tag{3.24b}$$

$$f_{ctm} = 0.30 {f_{ck}}^{2/3}; \tag{3.24c}$$

$$l_e = \left[\frac{E_{frcm} t_f}{2 f_{ctm}} \right]^{0.5}; \tag{3.24d}$$

$$k_b = \left[\frac{2 - w_f/b}{1 + w_f/400} \right]^{0.5}; \tag{3.24e}$$

$$k_e = 0.5; \tag{3.24f}$$

$$b \tag{3.24g}$$

$$= \begin{cases} s_f; & \text{discontinuous FRCM configuration;} \\ 0.9d \sin(\alpha+\theta)/\sin\alpha\,; & \text{continuous FRCM configuration} \end{cases}$$

$$w_f/b \leq 0.33 \tag{3.24h}$$

where θ is assumed to be 45º, k_e is the effectiveness coefficient, l_e is the optimal bond length, k_b is the geometric coefficient, w_f is the width of FRCM strips, and s_f is the spacing of FRCM strips for discontinuous FRCM configuration.

3.7.1.4. Model-4: ACI 549 [209]

According to ACI 549 [209] guideline, V_f is given by:

$$V_f = n_f A_f \sigma_{eff} d \tag{3.25}$$

$$\sigma_{eff} = \varepsilon_{eff,FRCM} E_{FRCM} \tag{3.25a}$$

$$\varepsilon_{eff,FRCM} = \varepsilon_{FRCM,u} \leq 0.004 \tag{3.25b}$$

In the above equations, σ_{eff}, $\varepsilon_{eff,FRCM}$, $\varepsilon_{FRCM,u}$, and E_{FRCM} are the design tensile strength, effective strain, ultimate strain, and elastic modulus of the FRCM composite.

3.7.1.5. Model-5: Wakjira and Ebead [138]

The above models [2,120,188,209] fail to consider FRCM/stirrups interaction. Moreover, the models do not account for the variation of the shear crack with both applied load and axial tensile strain in the flexural reinforcement bars. As a result, Wakjira and Ebead [138] proposed an analytical procedure based on the modified compression field theory [135], in which the shear capacity of the FRCM-strengthened beams is determined in an iterative procedure considering the effect of FRCM/stirrups interaction and change in the shear crack angle. Based on this model, the shear capacity of FRCM-strengthened RC beams is given by:

$$V = \beta\sqrt{f_c'}b_w d + (R_s\rho_{sy}f_{sy} + \rho_f f_f)bd\cot\theta \tag{3.26}$$

where R_s is the FRCM/stirrups interaction factor, β is the tensile stress factor of the cracked concrete, f_f is the effective stress in FRCM, and θ is the shear crack angle from the longitudinal axis of the beam determined based on the simplified compression field theory (SCFT) [135].

3.7.1.6. Model-6: Wakjira and Ebead [210]

Despite its accuracy, Model-5 [138] above involves an iterative procedure to determine the shear capacity of FRCM-strengthened beams. Thus, in another study, the authors [210] used an SCFT combined with probability and statistical techniques to develop a non-iterative simplified shear design equation for FRCM-strengthened beams. Accordingly, the shear capacity of FRCM-strengthened beams is given by:

$$v = 0.855(f_c')^{0.38}\sqrt[4]{\rho_{sx}} + 1.286\left(\rho_{sy}f_{sy}\right)^{0.84} + 3.608{K_f}^{0.97}\ (in\ \text{MPa}) \tag{3.27}$$

$$V = vb_w d \tag{3.27a}$$

where v is the shear strength of FRCM-strengthened beam and $K_f = \rho_f E_f$ is the axial stiffness of the FRCM system [210].

3.7.2. RC beams strengthened in flexure with inorganic composites

In existing formulae, a cross-sectional model was adopted to estimate the flexural capacity (M) of FRCM-strengthened RC beams [211]. From the equilibrium of stresses in Figure 3.8, the flexural capacity of the FRCM-strengthened RC beam can be given by:

$$M_n = A_{st}f_y\left(d - \frac{\beta_1 c_u}{2}\right) + A_{sc}E_{sc}\varepsilon_{sc}\left(\frac{\beta_1 c_u}{2} - d_c\right) + A_f E_f \varepsilon_{fe}\left(d_f - \frac{\beta_1 c_u}{2}\right) \tag{3.28}$$

where,

A_{sc} and A_{st} are the reinforcement area of compressive and tensile steel bars, respectively,

β_1 is the concrete stress block parameter (Figure 3.8),

d and d_c are the distance between the extreme fiber of the beam and the center of the tensile and compressive steel bars, respectively, (Figure 3.8),

c_u is the neutral axis depth (Figure 3.8),

f_y is the yield strength of internal steel reinforcement bars,

E_{sc} and ε_{sc} are the elastic modulus and tensile strain of the compressive reinforcement bars, and

d_f, A_f, E_f, and ε_{fe} are the effective depth, reinforcement area, elastic modulus, and effective strain of the FRCM reinforcement.

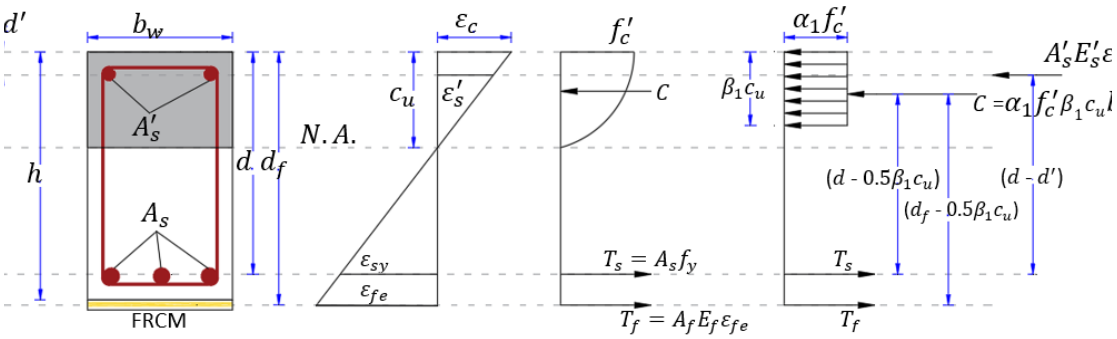

Figure 3.8: Cross-section and internal stress and strain distribution of RC beams strengthened with FRCM in flexure.

According to Bencardino et al. [212], Eq. (3.28) can be approximated as shown in Eq. (3.29) with the following three assumptions: (a) the tensile reinforcement bars reached their yielding point at the ultimate load, (b) the strains in the FRCM is equal to

the debonding strain ($\varepsilon_{fe} = \varepsilon_{deb}$), and the moment arms of the steel reinforcement and FRCM are equal to 90% of the effective depth and height of the beam, respectively.

$$M_n = 0.9dA_{st}f_y + 0.9hE_fA_f\varepsilon_{deb} \tag{3.29}$$

where h is the cross-sectional height of the beam. The load capacity of the FRCM-strengthened beams can then be determined based on the loading configuration. It is worth mentioning here that this simplified equation that does not consider the contribution of compressive reinforcement bars.

The available models for the flexural capacity of RC beams strengthened with FRCM vary mainly in the formulations for estimating the values of debonding strains, ε_{deb}. Five models adopted in the literature for determining the effective/debonding strain in the FRCM reinforcement are discussed below.

3.7.2.1. Model-1: Jung et al. [211]

Jung et al. [211] suggested the following expression for the debonding strain of FRCM composite based on the Teng et al. [213], originally proposed for FRP system:

$$\varepsilon_{deb} = \alpha_p\beta_w\beta_L\sqrt{\frac{E_f\sqrt{f_c}}{t_p\sqrt{n_f}}} \tag{3.30}$$

$$t_p = t_f \times \sqrt{n_f} \tag{3.30a}$$

$$\beta_W = \sqrt{\frac{2 - b_f/b_w}{1 + b_f/b_w}} \tag{3.30b}$$

$$\beta_L = \begin{cases} 1, & L_f \geq L_e \\ \sin\dfrac{\pi L_f}{2L_e}, & L_f < L_e \end{cases} \tag{3.30c}$$

$$L_e = \sqrt{\frac{E_f t_P}{\sqrt{f_c}}} \tag{3.30d}$$

where α_p is a coefficient that is experimentally calibrated to be 0.729 and L_f is the bond length.

3.7.2.2. *Model-2: Bencardino et al.* [212]

Bencardino et al. [212] suggested the following empirical equation for determining ε_{deb} based on the results of a nonlinear regression analysis for steel FRCM strengthened beams.

$$\varepsilon_{deb} = 2.24\left(E_f t_f\right)^{-0.52} \tag{3.31}$$

They also used the fracture mechanics approach to come up with another formula as shown in Eq. (3.32).

$$\varepsilon_{deb} = K\sqrt{2G_f}\sqrt{\frac{1}{t_f E_f}} \tag{3.32}$$

where G_f is the fracture energy at the debonding surface. It is required to perform flexural tests on RC beams in addition to single/double shear test for the FRCM to determine the coefficient K, which limits the application of this equation in determining ε_{deb}. Thus, only Eq. (3.31) is adopted in this study.

3.7.2.3. *Model-3: Ceroni and Salzano* [214]

Ceroni and Salzano [214] examined the influence of different factors on the debonding strains of FRCM systems based on the results of 856 single and double shear tests on concrete (347) and masonry (509) elements bonded externally with FRCM. Based on the results of a non-linear regression analysis on the collected data, the authors suggested the following equation to determine the debonding strain in the FRCM system bonded to concrete elements.

$$\varepsilon_{deb} = 0.008\frac{(f_c')^{1.15}}{\left(E_f A_f\right)^{0.3}} \tag{3.33}$$

3.7.2.4. *Model-4: Mandor and El Refai* [215]

Mandor and El Refai [215] have recently investigated the debonding strains in the FRCM strengthening system used for flexural members. Based on the results of the

sensitivity analysis, axial stiffness of FRCM ($E_f A_f$), compressive strength of the concrete substrate, and tensile strength (f_{ct}) of the concrete substrate were identified as the three most important factors that influence debonding strains in FRCM. Finally, the authors proposed three simple optimized models for determining the debonding strains in FRCM, as follows:

$$\varepsilon_{deb} = 0.77 \frac{{f_{ct}}^{1.191} {f_{cm}}^{0.056} e^{(0.032 f_c')}}{\left(E_f A_f\right)^{0.091}} \tag{3.34}$$

$$\varepsilon_{deb} = 0.77 \frac{{f_{ct}}^{1.232} e^{(0.035 f_c')}}{\left(E_f A_f\right)^{0.083}} \tag{3.35}$$

$$\varepsilon_{deb} = 0.95 \frac{{f_{cm}}^{0.28} e^{(0.056 f_c')}}{\left(E_f A_f\right)^{0.153}} \tag{3.36}$$

where f_{cm} is the compressive strength of FRCM mortar.

In the first equation, the debonding strain is given as the function of the compressive and tensile strengths of concrete, compressive strength of FRCM mortar, and axial stiffness of FRCM. Based on the results of the analysis, the authors concluded that the exclusion of the compressive strength of FRCM mortar has no significant effect on the predicted debonding strains. Among the proposed equations, the first two equations were reported as the best predictive equations, while the third equation showed the least predictive performance. Moreover, the second equation showed the least coefficient of variation (0.26). Hence, the second equation is considered in this study.

3.7.2.5. Model-5: ACI549.4-20 Model [216]

The ACI 549.4-20 [216] guideline suggests the following expression for determining the value of ε_{deb} interms of the design tensile strain (ε_{fd}) and ultimate tensile strain (ε_{fu}) of the FRCM composite:

$$\varepsilon_{deb} = \varepsilon_{fd} = \varepsilon_{fu} \leq 0.012 \quad (3.37)$$

The design tensile strain and tensile modulus of the FRCM composite are obtained by testing FRCM coupons. Thus, it is required to perform a test on the FRCM coupons to use this equation. Therefore, this model has been excluded from the current study.

3.8. Results and Discussion

3.8.1. RC beams strengthened in shear with inorganic composites

For RC beams strengthened in shear, six ML models; namely, SVR, CART, RFR, ERT, GBT, and xgBoost are investigated. The optimized hypermeters for each ML model are presented in Table 3.4.

3.8.1.1. Performance of ML models

The performance of ML models is presented in Table 3.5 in terms of the MAPE, MAE, RMSE, and R^2. In addition, Figure 3.9a–f compare the predicted (V_{pred}) and experimental (V_{exp}) shear capacities based on the proposed ML models in which the solid line shows the perfect match between V_{exp} and V_{pred}, while the hidden lines denote the 20% overestimation or underestimation of the shear capacity. As can be seen in these figures, the predictions provided by all models are in good agreement with the corresponding experimental values ($R^2 \geq 0.943$ for all models). It can also be observed from the same figures that the xgBoost model produced the best prediction for the shear capacity compared to all other models. A strong correlation exists between the experimental and predicted shear capacities based on the xgBoost model as evidenced by the value of R^2 of 0.995 and 0.984 for the training and test datasets, respectively, as can be seen in *Figure 3.9*f and Table 3.5. The GBT model was the second best model in predicting the shear capacity of the strengthened beams, as shown in Figure 3.9e and Table 3.5.

Table 3.4. Optimized hyperparameters

Models	Parameters
SVR	Kernel = RBF, C = 50, ε = 0.00001, gamma = 'auto'
CART	Maximum depth = 7, maximum features = 8, minimum sample leaf = 1, minimum sample split = 3
RFR	Number of estimators = 6, maximum features = 6, maximum depth = 10, minimum sample leaf = 1, minimum sample split = 3
ERT	Number of estimators = 12, maximum features = 13, maximum depth = 8, minimum sample leaf = 1, minimum sample split = 2
GBT	Number of estimators = 138, maximum features = 8, learning rate = 0.15, maximum depth = 5, subsample = 0.3, minimum sample split = 2, minimum sample leaf = 1
xgBoost	Number of estimators = 440, learning rate = 0.5, subsample = 0.4, maximum depth = 8, reg lambda = 1, reg alpha = 0, γ = 0, colsample by node = 1.0, colsample by level = 0.9, colsample by tree = 1

Table 3.5. Performance indices for the proposed models

Models	Training dataset				Test dataset			
	MAPE (%)	MAE (kN)	RMSE (kN)	R^2	MAPE (%)	MAE (kN)	RMSE (kN)	R^2
SVR	6.69	7.97	14.55	0.968	10.01	13.76	19.29	0.952
CART	4.58	6.86	12.23	0.978	9.36	14.56	20.98	0.943
RFR	7.09	8.60	12.21	0.978	7.96	12.82	19.48	0.951
ERT	3.83	4.35	7.03	0.993	7.37	11.44	16.61	0.964
GBT	3.50	4.30	6.78	0.993	8.48	10.50	13.55	0.976
xgBoost	1.84	2.62	5.94	0.995	6.16	8.23	10.96	0.984

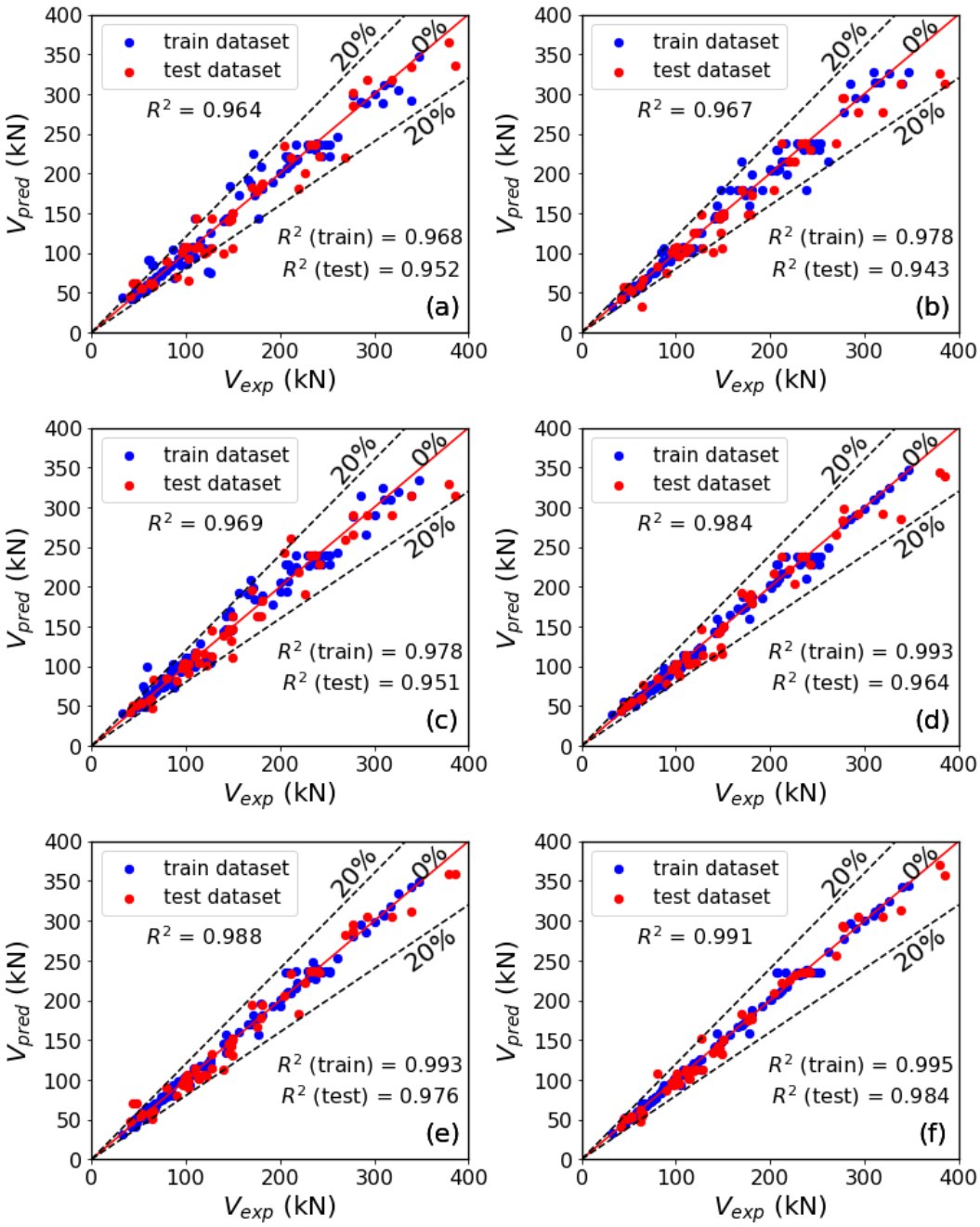

Figure 3.9: Comparison of experimental and predicted shear capacities of the strengthened beams based on (a) SVR, (b) CART, (c) random forest, (d) extremely randomized trees, (e) gradient tree boosting, and (f) xgBoost.

3.8.1.2. Comparison of the proposed and existing models

Moreover, performance evaluation of the ML models showed a very small difference between the experimental shear capacities and the corresponding predicted values using the xgBoost model in the training and test phases as indicated by the RMSE of 5.94 kN and 10.96 kN, respectively. For the SVR, CART, RFR, ERT, and GBT models, these values were 14.55 kN, 12.23 kN, 12.21 kN, 7.03 kN, and 6.78 kN, respectively, for the training dataset and 19.29 kN, 20.98 kN, 19.48 kN, 16.61 kN, and 13.55 kN, respectively, for the test dataset (Table 3.5). Thus, the xgBoost model showed the highest predictive capability with the highest R^2 and least MAE, MAPE, and RMSE followed by the GBT model (Table 3.5). The superior predictive performance of xgBoost, as an improved version of gradient tree boosting, is associated with the enhanced aspects of the loss function and loss optimization. On the contrary, the CART model showed the least predictive performance on the test dataset with the lowest R^2 ($R^2 = 0.943$) and highest RMSE (20.98 kN), as shown in Figure 3.9a–f and Table 3.5.

The prediction performance of the proposed xgBoost model is compared with that of the existing models and design guideline formulae discussed in Section 3.7. As discussed earlier, Ombres [120] and ACI 549.4R [209] models are based on the properties of the FRCM composite, while Triantafillou and Papanicolaou [2], Escrig et al. [188], and Wakjira and Ebead [138,210] models are based on the fiber properties. Out of the total number of beams included in the database, E_{FRCM} is not reported for 78 beams. As a result, the Ombres [120] and ACI 549.4R [209] models are validated against 95 beams only. Moreover, Wakjira and Ebead [138,210] models are proposed for FRCM-strengthened RC beams with $a/d > 2.5$, thus they are evaluated against 128 beams out of 173 beams. *Figure 3.10*a–f show the scatter plots of the experimental versus predicted shear capacities based on the existing models. As can be observed in

these figures, Model-1 overpredicted the shear capacity for large number of beams, while the shear capacity for most of the beams are underestimated by Model-2, -3, and -4, as shown in *Figure 3.10*a–d. However, the predictions provided by Model-5 and Model-6 are scattered around the equity line that shows the perfect match between the predicted and experimental shear capacities, as shown in *Figure 3.10*e and f. As shown in *Figure 3.10*a–f, Model-5, which is based on the modified compression field theory provided the best predictions among the existing models followed by Model-6.

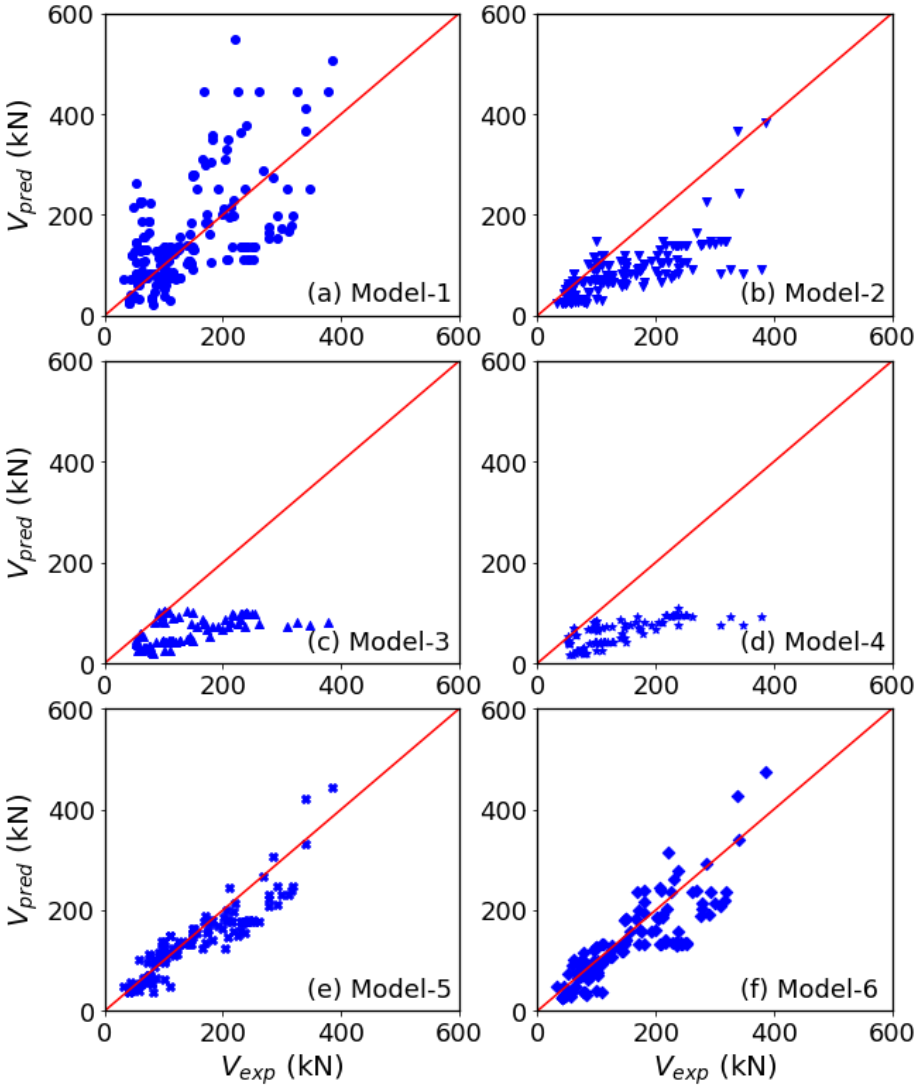

Figure 3.10: Predictions of the shear capacity based on the existing models.

Figure 3.11 compares the experimental shear capacity and the corresponding predicted values based on the existing and proposed xgBoost models. As can be observed in this figure, the predictions provided by the proposed model lied within ±20% error margins for all beams except two, while most of the predictions are highly overestimated or underestimated for the existing models. Besides, the statistical performance indices for the existing and proposed xgBoost models are listed in Table 3.6 and further illustrated in Figure 3.12 in terms of the MAE and RMSE.

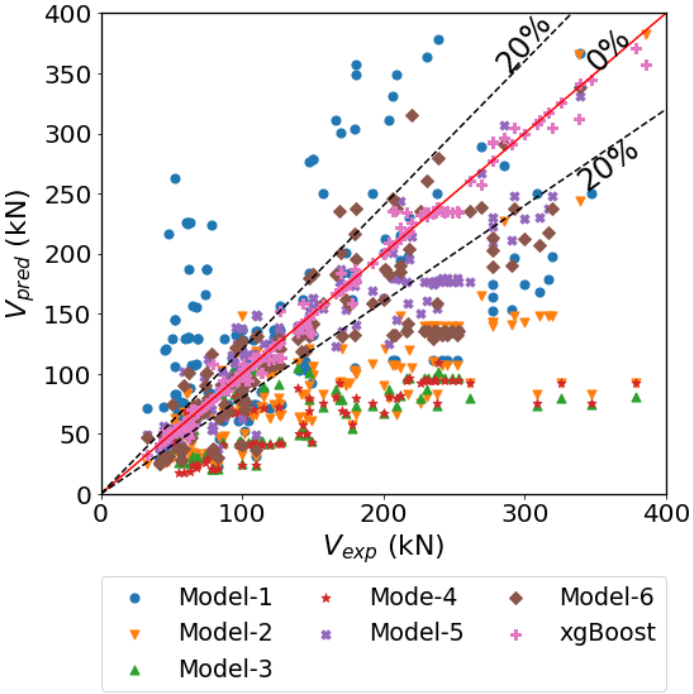

Figure 3.11: Comparisons of shear capacity predictions based on existing and proposed xgBoost models with ±20% error bounds.

Table 3.6. Performance of different shear models

Model	Model ID	Sample size	RMSE (kN)	MAE (kN)	Mean of V_{pred}/V_{exp}	STD of V_{pred}/V_{exp}
Triantafillou and Papanicolaou [2]	Model-1	173	87.02	65.30	1.28	0.81
Escrig et al. [188]	Model-2	173	81.60	60.66	0.66	0.26
Ombres [120]	Model-3	95	97.17	73.86	0.53	0.25
ACI 549.4R [209]	Model-4	95	97.21	77.83	0.49	0.21
Wakjira and Ebead [138]	Model-5	128	37.84	27.97	0.94	0.22
Wakjira and Ebead [210]	Model-6	128	50.29	37.60	0.90	0.28
xgBoost	–	173	7.80	4.30	0.99	0.06

The proposed xgBoost model substantially reduced the RSME by 91%, 90%, 92%, 92%, 79%, and 85% compared to Model-1, -2, -3, -4, -5, and -6, respectively, as shown in Figure 3.12 and Table 3.6. Similarly, the proposed model provided a significantly lower MAE compared to others, as shown in Figure 3.12 and Table 3.6. The mean of the V_{pred}/V_{exp} ratio is 0.99 for the proposed xgBoost model compared with mean values of 1.28, 0.66, 0.53, 0.49, 0.94, and 0.9 for Model-1 through Model-6, respectively, as listed in Table 3.6. The predictions provided by the proposed xgBoost model was less scattered as evidenced by the standard deviation (STD) for the V_{pred}/V_{exp} ratio value of 0.06 compared to STD values of 0.81, 0.26, 0.25, 0.21, 0.22, and 0.28 for Model-1, -2, -3, -4, -5, and -6, respectively, as listed in Table 3.6.

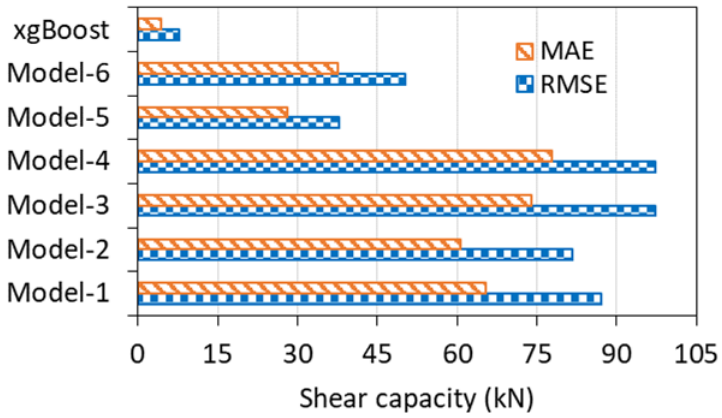

Figure 3.12: Comparison of the predictions of the shear models in terms of the RMSE and MAE.

The prediction capability of the proposed xgBoost model and existing models was also evaluated in terms of the MDPC method [139]. *Figure 3.13*a–g compare the prediction capability of the proposed and existing models based on the MDPC method in which 'AS', 'C', 'EC', 'D', and 'ED', donate the appropriate safety, conservative, extra conservative, dangerous, and extra dangerous regions, respectively. As can be seen in these figures, the predictions provided by Model-1 [2] are most scattered and biased with the least predictive capacity, while the predictions of Model-4 [209] mainly lie in the conservative and extra conservative regions. Among the existing models, Model-5 [138], which is based on the modified compression field theory provided the best predictions followed by Model-6, as can be seen in *Figure 3.13*a–g. Table 3.7 presents the number of beams in each range and the total penalty as per the MDPC method [139] for all models. As can be seen in *Figure 3.13*a–g and Table 3.7, the predictions for 98% of the beams, based on the proposed xgBoost model lie in the appropriate safety region compared to only 22%, 18%, 16%, 3%, 51%, and 34% of the beams for Model-1, -2, -3, -4, -5, and -6, respectively. Thus, the proposed xgBoost model exhibited superior predictions with a total penalty of 12 compared to the total

penalty of 559, 220, 125, and 190 for Model-1, -2, -5, and -6, respectively, as listed in Table 3.7. Model-3 and Model-4 are evaluated against 95 beams only and are associated with total penalties of 144 and 157, respectively, as listed in Table 3.7. This observation evidenced that the proposed xgBoost model is capable to yield accurate and safe predictions with superior prediction capability compared to the existing models.

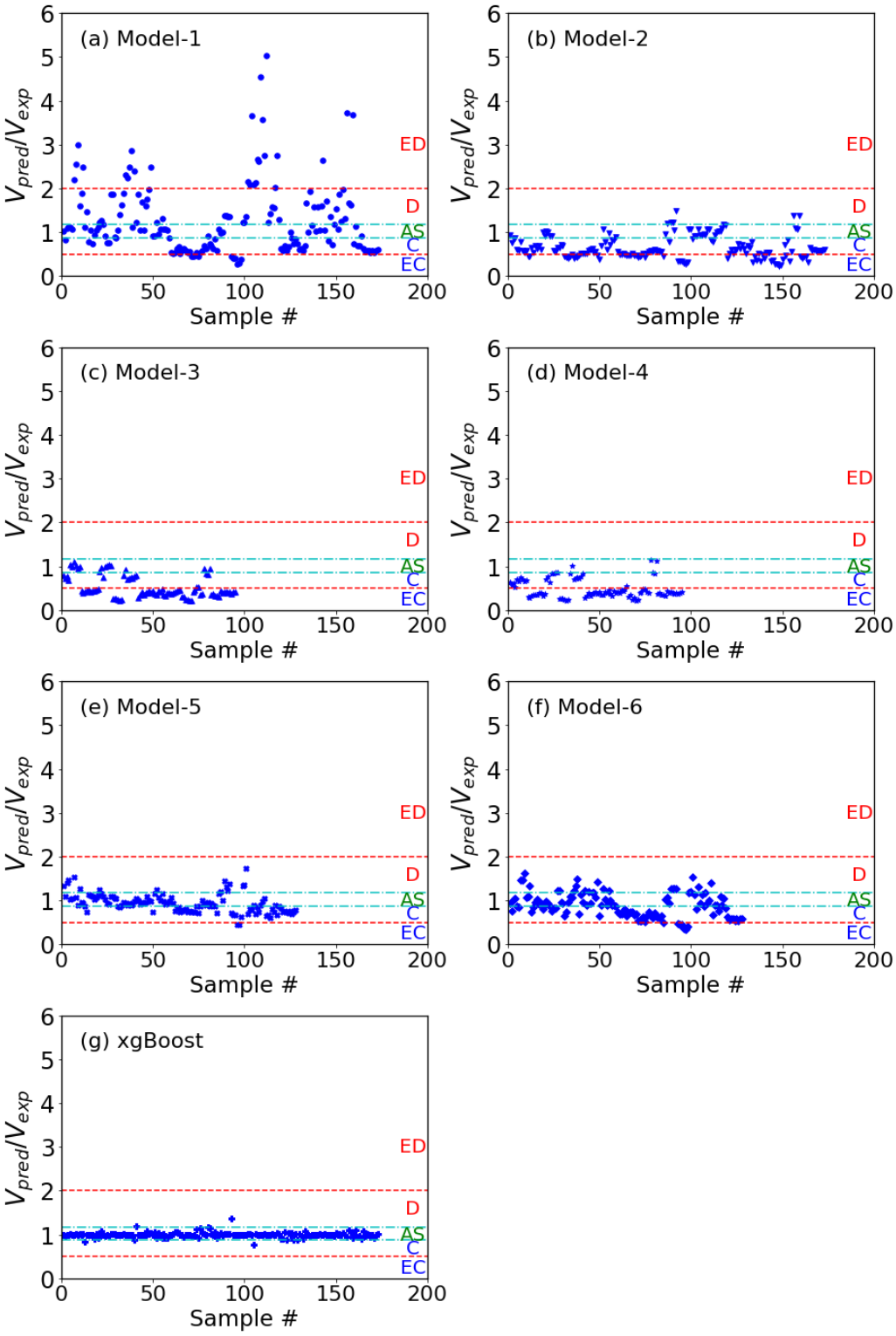

Figure 3.13: Prediction capability of the proposed and existing models based on the MDPC method [139].

Table 3.7. Predictive performance of the models based on the Modified Demerits Points Classification [139]

Shear model	Sample size	V_{th}/V_{ex}	> 2	[1.176 – 2]	[0.869 – 1.176]	[0.5 – 0.869]	≤ 0.5	Total penalty
		Criteria	Extra dangerous	Dangerous	Appropriate safety	Conservative	Extra conservative	
		Penalty	10	5	0	1	2	
Triantafillou and Papanicolaou [2]	173	N	26	45	38	54	10	559
		Penalty	260	225	–	54	20	
Escrig et al. [188]	173	N	–	7	32	83	51	220
		Penalty	–	35	–	83	102	
Ombres [120]	95	N	–	–	15	16	64	144
		Penalty	–	–	–	16	128	
ACI 549.4R [209]	95	N	–	–	3	27	65	157
		Penalty	–	–	–	27	130	
Wakjira and Ebead [138]	128	N	–	15	65	46	2	125
		Penalty	–	75	–	46	4	
Wakjira and Ebead [210]	128	N	–	25	44	53	6	190
		Penalty	–	125	–	53	12	
xgBoost	173	N	–	2	169	2	–	12
		Penalty	–	10	–	2	–	

N: number of samples in the specified range

3.8.2. RC beams strengthened in flexure with inorganic composites

Seven different types of data-driven ML models are evaluated to determine the final best predictive model for the flexural capacity of RC beams strengthened in flexure. In the proposed ML models, the flexural capacity of the strengthened beams is directly determined from the properties of the composite fibers without the need for the estimation of debonding strains and experimental results of the strengthening composite.

3.8.2.1. Performance of ML models

Figure 3.14a–d show the scatter plots for the predicted (M_{pred}) versus experimental (M_{exp}) flexural capacities using the single ML models, while Figure 3.15a–c compare the experimental and predicted flexural capacities of the strengthened beams based on the ensemble ML models. Generally, all developed ML models showed a good correlation between the experimental and predicted flexural capacities with $R^2 \geq 93.1\%$. Among the single models, KNN showed the least predictive performance on both the training and test sets, while SVR showed the highest predictive performance followed by CART, as can be observed in Figure 3.14a–d.

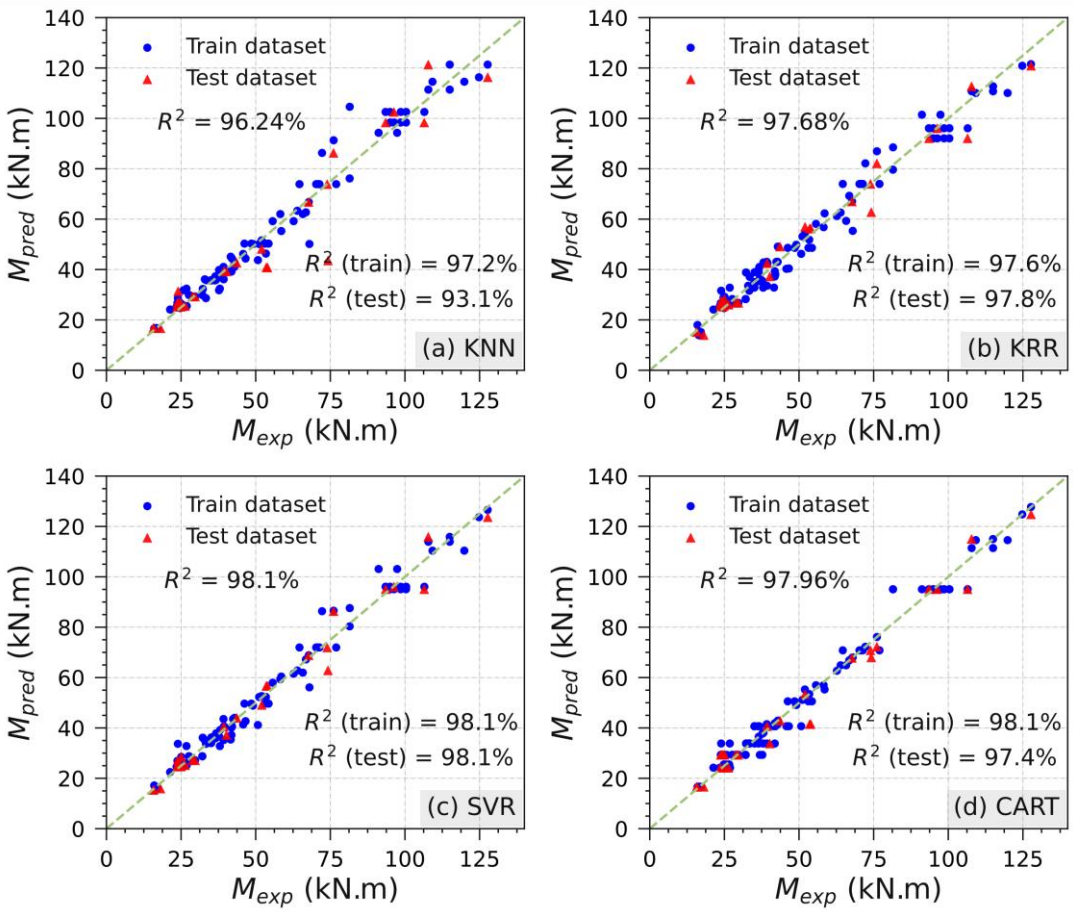

Figure 3.14: Experimental versus predicted load capacity of flexural-strengthened beams based on single models.

For all the ensemble models, as illustrated in Figure 3.15a–c, the predicted flexural capacities are well concentrated closely around the 45-degree diagonal line that represents a perfect match between the predicted flexural capacities and the corresponding experimental values. This can also be observed in Figure 3.16a–c which show the residual of the predicted flexural capacity of the beams, which is the difference between M_{exp} and M_{pred} on the normalized training and test datasets. The figures also provide the coefficient of determination for both the training and test datasets. The residuals for all ensemble models are distributed around zero, as can be seen in Figure

3.16a–c. In addition, the proposed ensemble models resulted in a strong correlation between the predicted and experimental flexural capacities as can be evidenced from the values of coefficient of determination, $R^2 \geq 98.2\%$, as can be seen in Figure 3.15a–c and Figure 3.16a–c. This observation showed that the proposed ensemble models are effective in predicting the flexural capacity of FRCM-strengthened RC beams.

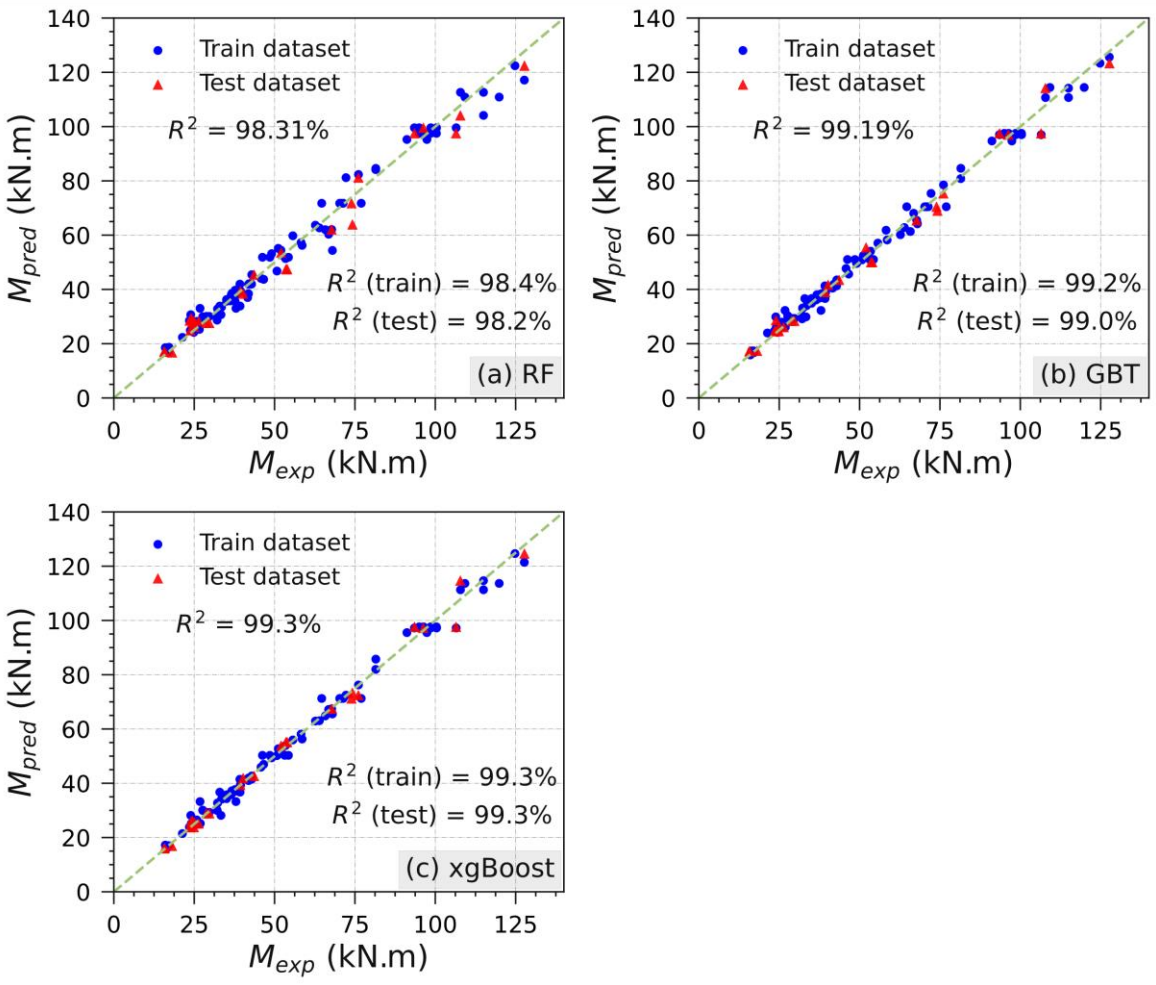

Figure 3.15: Experimental versus predicted load capacity of FRCM-strengthened beams based on ensemble models.

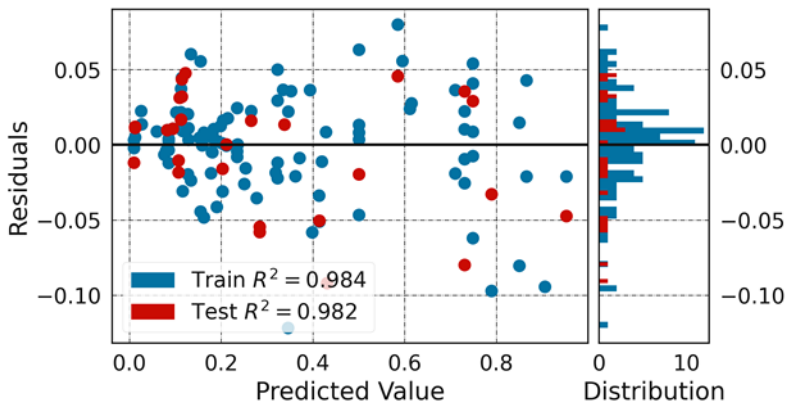

(a) Random forest

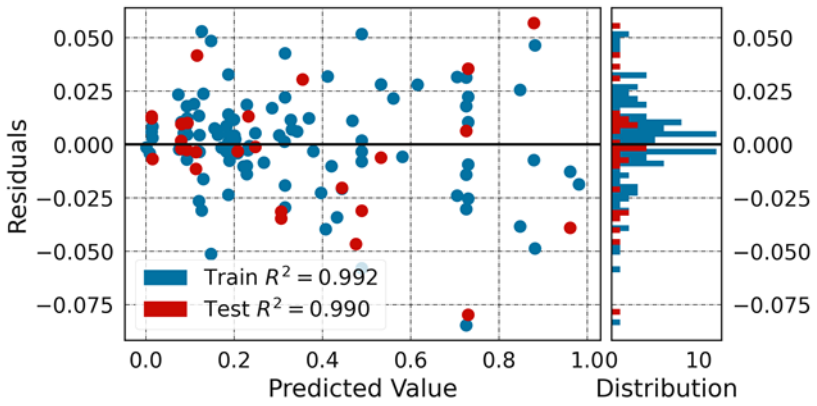

(b) Gradient Boosted trees

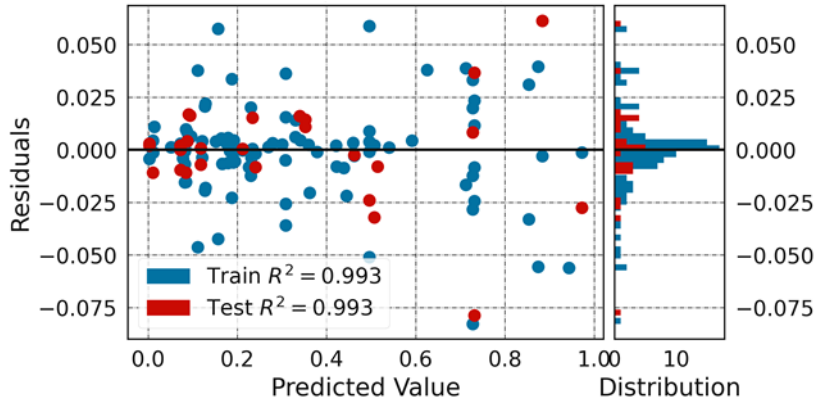

(c) xgBoost

Figure 3.16: Residual of the predicted load capacity on the normalized training and test datasets for ensemble models.

The performance metrics discussed earlier are computed and listed in Table 3.8 for all models. The results in Table 3.8 suggested that the predictive performance of all ensemble models is higher than that of the single models (KRR, KNN, SVR, and CART). The CART and SVR models showed a comparable prediction performance on the training set, while the latter performed better on the test set, as listed in Table 3.8. The KNN resulted in the lowest coefficient of determination (97.2% and 93.1% on the train and test sets, respectively) and the highest RMSE (4.80 kN and 8.43 kN on the train and test sets, respectively), as listed in Table 3.8.

Table 3.8. Performance indices of different ML models

Model	Training dataset				Test dataset			
	RMSE (kN.m)	MAE (kN.m)	MAPE (%)	R^2 (%)	RMSE (kN.m)	MAE (kN.m)	MAPE (%)	R^2 (%)
KNN	4.80	3.10	5.87	97.2	8.43	5.15	9.30	93.1
KRR	4.45	3.56	7.86	97.6	4.71	3.37	7.32	97.8
SVR	3.97	2.72	5.77	98.1	4.44	3.04	6.01	98.1
CART	3.95	2.58	5.86	98.1	5.14	3.68	8.44	97.4
RF	3.71	2.67	5.52	98.4	4.30	3.51	7.92	98.2
GBT	2.52	1.84	3.91	99.2	3.19	2.33	4.73	99.0
xgBoost	2.41	1.55	3.17	99.3	2.70	1.77	3.25	99.3

Among the investigated ML models, the xgBoost model outperformed all other models on both the train and test sets as suggested by the performance metrics in Table 3.8. The statistical metrics for the xgBoost model are 99.3% (R^2), 2.70 kN.m (RMSE), 1.77 kN.m (MAE), and 3.25% (MAPE) on the test set, as listed in Table 3.8. The value of the coefficient of determination for the GBT, RF, CART, SVR, KRR, and KNN models was 99.0%, 98.2%, 97.4%, 98.1%, 97.8%, and 93.1%, respectively, compared to R^2 value of 99.3% for the xgBoost model on the test set, as presented in Table 3.8. Among the ensemble models, the RF model showed the least performance on both the

train and test sets. The following section compares the performance of the proposed xgBoost model with that of the existing models in predicting the flexural and load capacities of flexural deficient RC beam strengthened with FRCM.

3.8.2.2. Comparison of the proposed and existing models

The predictive performance of the proposed model; particularly, the xgBoost model and the existing models for the FRCM-strengthened RC beams are compared herein. A total of four models proposed by Jung et al. [211], Bencardino et al. [212], Ceroni and Salzano [214], and Mandor and El Refai [215] are used for the comparison purpose, as discussed in Section 3.7.2. Model-1 [211] is the most general model developed based on the Teng et al. [213], originally proposed for the FRP system. Hence, it is validated against the complete database. Model-2 [212] is developed for steel FRCM; thus, it is applied to RC beams strengthened with steel FRCM only (a total of 30 beams). The ACI 549.4-20 guideline [216] is based on the elastic modulus and strains in FRCM composites obtained from the test results of FRCM coupons; however, these values are not reported in the majority of the specimens included in the database. Thus, this model [216] is excluded from the comparative study.

Figure 3.17a–e illustrate the experimental versus predicted flexural and load capacities based on the existing models [211,212,216–219] and the proposed xgBoost.

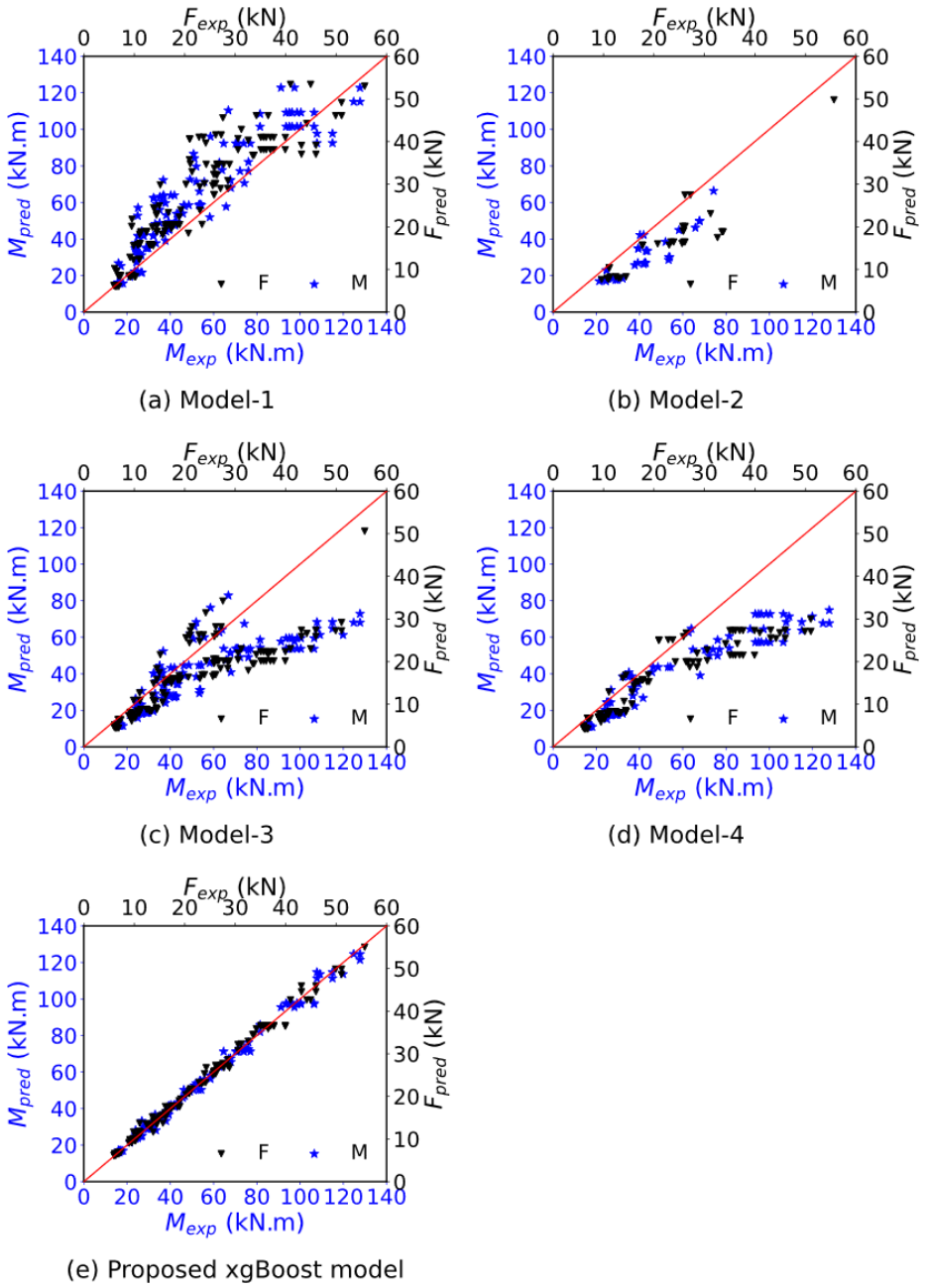

Figure 3.17: Experimental versus predicted load capacity of FRCM-strengthened beams based on the existing models.

The flexural capacity of the strengthened beams is determined using the existing and proposed models, while the load capacity is determined based on the loading and boundary conditions of the beams. The equity solid line in these figures represents the

perfect match between the experimental and predicted responses. Besides, Table 3.9 presents the evaluation of the existing and proposed models in terms of the average, STD, and coefficient of variation (COV) of M_{pred}/M_{exp} ratio. Among the existing models, Model-4 [215] showed the best predictive performance with an average of M_{pred}/M_{exp} ratio of 0.799 ± 0.162 and COV of 0.203, as listed in Table 3.9. As discussed earlier, Model-2 [212] was applied to only 30 specimens strengthened with steel FRCM in the collected database. The average of M_{pred}/M_{exp} ratio based on Model-2 [212] was 0.738 ± 0.134 with COV of 0.182. As can be observed in Figure 3.17a–d and Table 3.9, Model-1 [211] tends to highly overestimate the flexural capacity of the strengthened beams with an average of M_{pred}/M_{exp} ratio of 1.257 ± 0.286 and COV of 0.228. The proposed model showed superior prediction ability compared to the existing models, as can be seen in Figure 3.17a–e and Table 3.9.

Table 3.9. Evaluation of existing and proposed models based on M_{pred}/M_{exp} ratio

Model	Mean	STD	COV
Model-1 [211]	1.257	0.286	0.228
Model-2 [212]	0.738	0.134	0.182
Model-3 [214]	0.755	0.205	0.272
Model-4 [215]	0.799	0.162	0.203
Proposed xgBoost	1.002	0.048	0.048

STD: Standard deviation; COV: Coefficient of variation

3.8.2.3. Model exPlainability using SHAP approach

A unified SHAP approach is used to explain the outputs of the xgBoost model and highlight the most significant factors and their interactions in determining the flexural capacity of RC beams strengthened in flexure. In this approach, the SHAP value, which is the average marginal contribution of each factor is assigned to each

factor. The factor with large absolute SHAP values is deemed most significant. A typical single prediction plot using the xgBoost model is shown in Figure 3.18 (in a natural logarithmic scale), in which the base value denotes the average of the observed response values ($\frac{1}{132}\sum_{i=1}^{132} \ln M_{exp}$). The length and color of the bar in Figure 3.18 show the degree of significance and direction (negative or positive) of the effect of each factor. As can be observed in Figure 3.18, the internal reinforcement ratios (A_{st}) showed the highest effect followed by FRCM reinforcement area and width of the beam section. All factors in Figure 3.18 showed positive influences; thus, contributing to the increase in the base value.

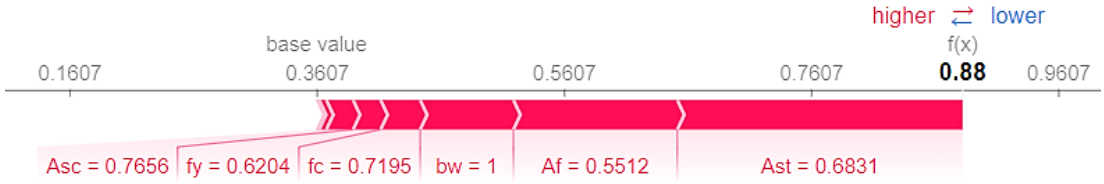

Figure 3.18: Explanation of flexural capacity of RC beams strengthened with FRCM in flexure for Specimen CC1 strengthened with PBO-FRCM in [201].

The distribution of the Shapley values for each factor across the entire dataset is shown in Figure 3.19a. In this figure, each point represents a Shapley value for a feature and an individual observation in the dataset. The position of each dot on the *x*-axis represents a Shapley value for each factor, which shows the influence of each factor on the flexural capacity of the strengthened beams, while the y-axis provides the factors in their order of importance. The color in Figure 3.19a shows the value of the factors. For instance, the high value of the internal steel reinforcement area and FRCM area increase the predicted flexural capacity of the strengthened beams.

The global significance of the factors is determined as the average of the absolute Shapley values across the entire dataset (in Figure 3.19a) for each factor and plotted in descending order of their importance in Figure 3.19b. As can be observed in this figure, the four most influential features are the area of the internal tensile steel reinforcement (A_{st}), width of the beam section (b_w), area of the composite, and effective depth of the beam section. On the contrary, A_{sc} is the least influential feature compared to all other factors for the flexural capacity prediction using the proposed xgBoost model. Moreover, the direction of the effect of each factor is shown in the same figure. All factors showed positive effects on the flexural capacity of the strengthened beams, as shown in Figure 3.19b. Furthermore, Figure 3.20 shows the effect of the internal/external reinforcement interaction on the flexural capacity of the strengthened beams based on the results of SHAP feature dependence analysis. As can be observed in Figure 3.20, a negative interaction is observed between the internal/external flexural reinforcement.

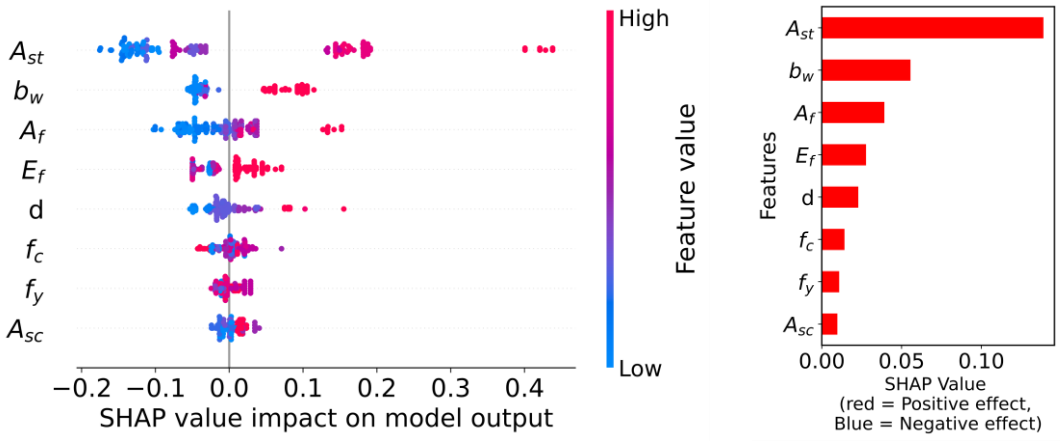

(a) (b)

Figure 3.19: Summary plot for elucidating the global feature influences of the input features (the color represents the value of the factor varying from low (blue) to high

(red)) (a) and global importance of the input features (b).

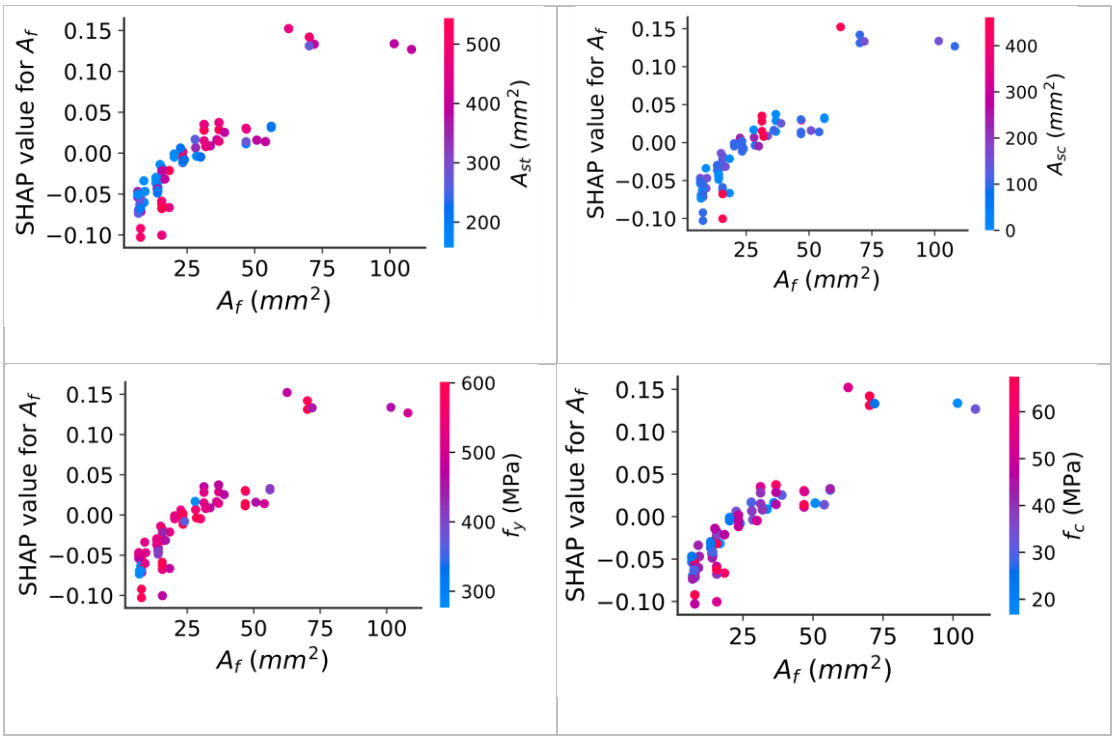

Figure 3.20: SHAP dependency and interaction plots.

3.9. Reliability Evaluation

Reliability analysis is used to estimate the level of safety of a system in terms of its failure probability. Accordingly, structural reliability analysis measures the performance of structures. In this study, the structural reliability analysis is performed for the proposed xgBoost model to calibrate the resistance (strength) reduction factors to achieve specified target reliability indices.

The reliability index (β) can be given by Eq. (3.38), while Eq. (3.39) defines the safety margin (g) in terms of the resistance (R) and load effect (Q):

$$\beta = \varphi^{-1}(1 - P_F) \tag{3.38}$$

$$g = R - Q \tag{3.39}$$

where P_F is the probability of failure and φ^{-1} is the inverse of standard normal cumulative distribution.

Thus, the probability of failure is the probability that a particular combination of R and Q will result in a failure state which corresponds to a negative value of g. The ultimate limit state load cases as per ACI 318 [220] is used in this study considering only dead load (P_{DL}) and live load (P_{LL}):

$$\phi R_n \geq 1.4P_{DL} \tag{3.40a}$$

$$\phi R_n \geq 1.2P_{DL} + 1.6P_{LL} \tag{3.40b}$$

The following steps are followed in this study to determine the reliability index:

- Load distribution: both dead load and live load are assumed to follow a normal distribution [221]. According to Szerszen and Nowak [221], the bias factor for dead load is taken as 1.05 with a coefficient of variation (COV) of 10% for cast-in-place concrete, whereas the bias and COV for a 50 year live load are taken as 1.0 and 18%, respectively. To determine the nominal live load, dead load to total load ratios ($\alpha = P_{DL}/(P_{DL} + P_{LL})$) of 0 to 1.0 at 0.1 intervals are considered in this study. A total of 250 million simulations was generated using Monte Carlo simulation for each α. The actual mean is determined as the product of the nominal mean and bias.
- Resistance distribution: the experimental data is used to determine the bias factor and COV of the resistance distribution, while the nominal resistance distribution is determined based on the governing load combination in Eqs. (3.40a) and (3.40b).

- The reliability index is then determined in terms of the failure probability in Eq. (3.38) where P_F is determined based on the ultimate limit state in Eq. (3.39), where Q is the sum of dead load and live load.

The selection of the target reliability index depends on the consequences of failure [222]. According to [222], the target reliability index is taken between 3.5 and 4.0 for brittle/sudden failure, while it is taken between 3.0 and 3.5 for flexural members.. Thus, two levels of target reliability ($\beta_T = 3.5$ and $\beta_T = 4.0$) are considered in this study in order to represent the range of target reliability indices in design manuals for shear failure. A target reliability index of 3.5 is considered for the flexural capacity of RC beams strengthened in flexure with FRCM.

The resistance reduction factor is calibrated using the least square method:

$$LSM = \frac{1}{n}\sum_{i=1}^{n}(\beta_i - \beta_T)^2 \tag{3.41}$$

where LSM is the least square mean, β_i is the reliability at a particular ϕ and β_T is the target reliability, as defined earlier.

3.9.1. RC beams strengthened in shear with inorganic composites

Several values of resistance (strength) reduction factor (ϕ) ranging from 0.80 to 0.95 at 0.01 intervals were considered. Similarly, the load ratio ranged between 0.0 to 1.0 at 0.1 intervals. The results of the reliability analysis for the proposed xgBoost model are illustrated in *Figure 3.21*a and b in terms of reliability indices versus resistance reduction factor and load ratio, respectively. As can be seen in these figures, the reliability index varies with the load ratio and ϕ. Most of the reliability indices are greater or equal to 3.0, as shown in Figure 3.21a and b.

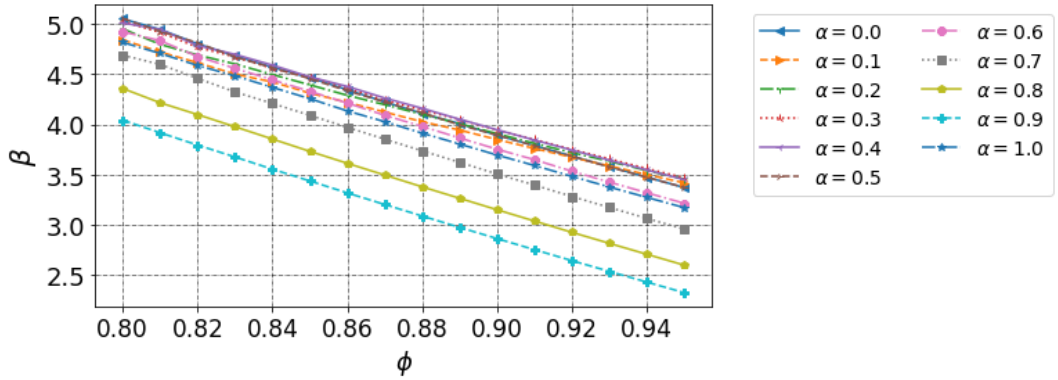

(a) resistance reduction factor (ϕ) versus reliability index (β)

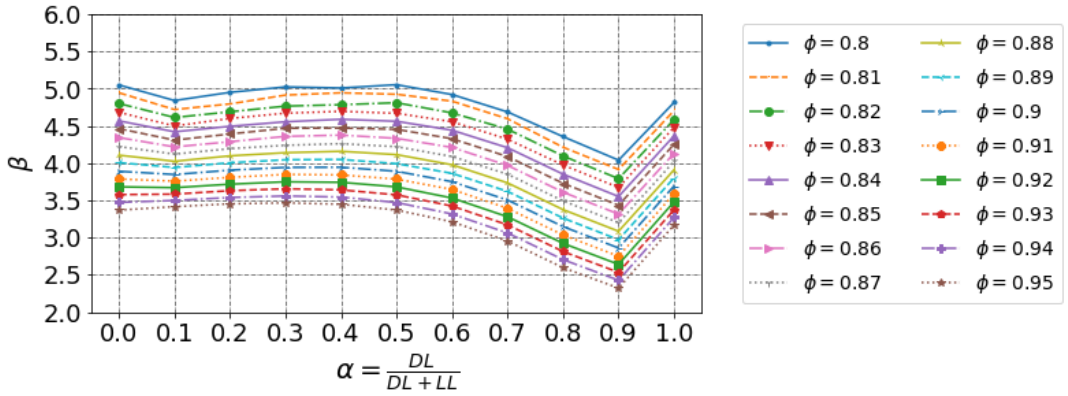

(b) load ratio (α) versus reliability index (β)

Figure 3.21: Reliability index for the proposed xgBoost model.

Moreover, Figure 3.22 illustrates the LSM_ϕ versus ϕ responses for target reliability indices of 3.5 and 4.0. As can be observed in these figures, LSM_ϕ initially decreased with an increase in ϕ and subsequently increased with an increase in ϕ. The minimum LSM_ϕ corresponds to resistance reduction factors of 0.91 and 0.87 for target reliability levels of 3.5 and 4.0, respectively, as shown in Figure 3.22. Thus, the calibrated resistance reduction factor is 0.91 to achieve a target reliability index of 3.5, while a reduction factor of 0.87 is selected to yield $\beta_T = 4.0$ for the developed xgBoost

model. A lower strength reduction factor of 0.75 is used in the ACI 318 [220] for the shear failure of pristine RC beams compared to $\phi = 0.91$ for xgBoost model proposed in this study for FRCM-strengthened RC beams to achieve the same target reliability level of 3.5. A design example is presented in the following section using the calibrated resistance reduction factor ($\phi = 0.91$) for $\beta_T = 3.5$.

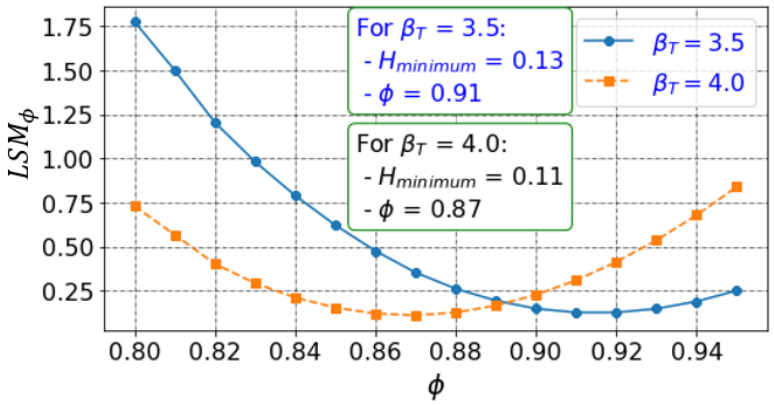

Figure 3.22: Calibration of strength reduction factors to achieve target reliability index of $\beta_T = 3.5$ and $\beta_T = 4.0$ for the proposed xgBoost model.

3.9.2. RC beams strengthened in flexure with inorganic composites

A range of capacity reduction factor $\phi = 0.750: 0.01: 0.95$ was analyzed and the value of β corresponding to each ϕ is determined and results plotted in Figure 3.23a. As expected, the value of β increases with a decrease in ϕ, as shown in Figure 3.23a. The larger safety margin corresponds to a smaller value of the resistance reduction factor. Figure 3.23b shows the variation of LSM_ϕ with the change in ϕ for a target reliability index of 3.5. As shown in this figure, the minimum LSM corresponds to a capacity reduction factor of 0.92. Hence, a reduction factor of 0.92 is recommended to achieve a target reliability index of 3.5 for RC beams strengthened in flexure with

FRCM based on the proposed xgBoost mode. A design example is provided in Appendix A to illustrate the design of the FRCM system for flexural strengthening of RC beams based on the calibrated ϕ using the proposed xgBoost model.

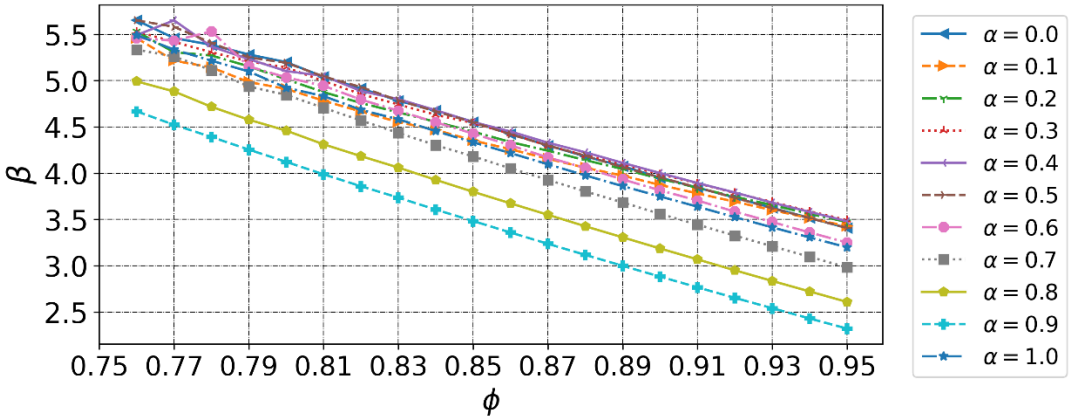

(a) α versus β response

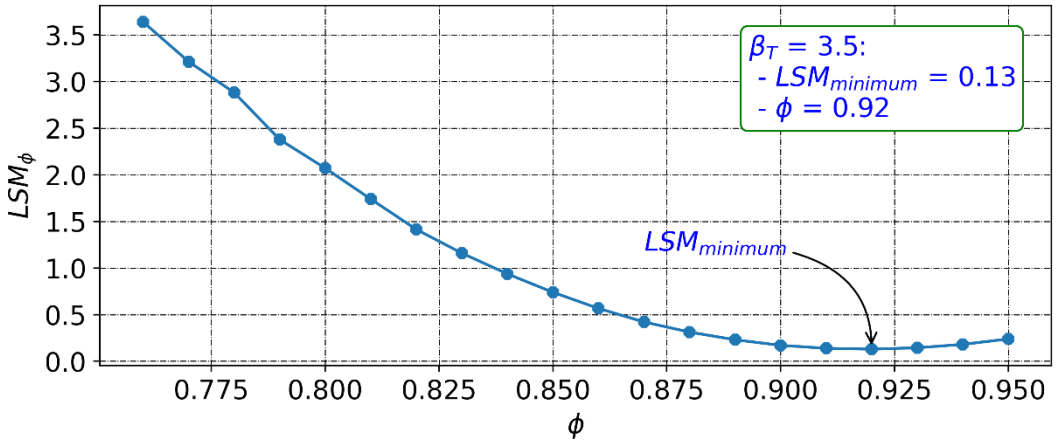

(b) calibration of the strength reduction factor

Figure 3.23: Reliability index and calibration of strength reduction factor for the proposed xgBoost model.

3.10. Design Example

3.10.1. Shear deficient RC beam

Consider a simply supported shear deficient rectangular RC beam of dimensions

180×400 mm ($b \times h$) and a clear span of 1000 mm subjected to two factored point loads of 200 kN on each clear span. Figure 3.24 shows the cross-sectional dimensions and reinforcement details of the beam in the shear span. Assuming the following material properties and internal reinforcement, the FRCM strengthening amount needs to be designed.

Material properties and internal reinforcement details:

- Concrete: $f_c' = 30$ MPa,
- Yield strength of longitudinal bars: $f_{sx} = 550$ MPa,
- Yield strength of transverse bars: $f_{sy} = 350$ MPa,
- Flexural reinforcement: 6 bars with 20 mm diameter arranged in two layers (Figure 3.24),
- Internal transverse reinforcement: 8 mm stirrups spaced at $d/2 = 165$ mm (Figure 3.24), and
- FRCM properties: uni-directional steel fabrics with elastic modulus and tensile strength of 190 GPa and 3000 MPa, respectively [223].

The factored load (V_Q) at the supports is 200 kN. The shear capacity of the unstrengthened beam is 169 kN using the SCFT. The design is carried out as follows:

i. Provide one layer of externally bonded U-wrapped steel FRCM reinforcement with nominal fiber thickness of 0.084 mm (Table 3.10) and determine the shear capacity of the beam using the proposed xgBoost model, which is available at: https://github.com/twakjira/FRCM-shear-strengthened-beam. Based on this design, the predicted nominal shear capacity of the beam is 197 kN. Considering the resistance reduction factor of 0.91 calibrated to achieve a reliability level of 3.5 as in ACI 318 [220], the factored resistance (V_r) $= \phi V_n = 0.91 \times 197$ kN $= 179$ kN, which

is less than the applied factored load (200 kN).

ii. Increase the FRCM reinforcement: by increasing the FRCM fabric layers to two, the nominal shear capacity of the beam is increased to 248 kN, as listed in Table 3.10. Thus, $V_r = \phi V_n = 0.91 \times 248\ kN = 225\ kN > V_Q$, which implies that the provided strengthening system is adequate to resist the applied shear.

iii. Check for ductile failure: using section analysis the flexural capacity of the beam is determined to be 256 kN.mm, which corresponds to a load capacity of 256 kN.

iv. Comparing the results in steps (ii) and (iii), it can be observed that the flexural capacity is larger than the shear leading to shear failure, which is not ductile; hence, increase the FRCM reinforcement by increasing the nominal thickness of the fabric. Using two layers of steel fabrics with a nominal thickness of 0.169 mm, the nominal shear capacity is increased to 290 kN (Table 3.10), which corresponds to $V_r = \phi V_n = 0.91 \times 290\ kN = 263\ kN$, which is greater than the load capacity for flexural failure (256 kN).

Therefore, use two layers of steel FRCM fabrics with a nominal thickness of 0.169 mm, tensile strength of 3000 MPa, and elastic modulus of 190 GPa. The designed steel fabric is known by its commercial name as GeoSteel G1200 [223].

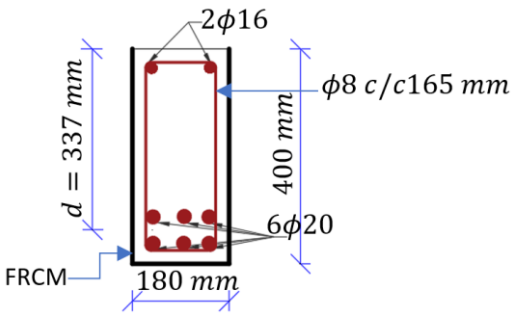

Figure 3.24: FRCM-strengthened beam section.

Table 3.10. Design example for FRCM-strengthened beam

Internal reinforcement				FRCM properties						Resistance	
ρ_{sx} (%)	f_{sx} (MPa)	ρ_{sy} (%)	f_{sy} (MPa)	Fabric type	Wrapping scheme	t_f (mm)	n_f	ρ_f (‰)	h_{fe} (mm)	V_n (kN)	ϕV_n (kN)
3.17	550	0.34	350	Steel	UW	0.084	1	0.933	297	197	179
3.17	550	0.34	350	Steel	UW	0.084	2	1.867	297	248	225
3.17	550	0.34	350	Steel	UW	0.169	2	3.756	297	290	263

3.10.1. Flexural deficient RC beam

A simply supported RC bridge beam is seriously damaged due to corrosion on its bottom face (Figure 3.25). The beam is estimated to have lost 20% of its flexural reinforcement due to corrosion. Design the required strengthening reinforcement for strengthening of the beam and recovering its flexural capacity.

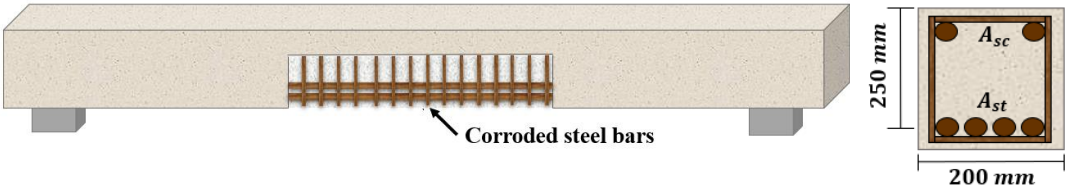

Figure 3.25: Schematic of the beam and cross-sectional detail.

Details of the existing beam:

- Cross-sectional dimension: 200 × 250 mm ($b_w \times d$).
- Concrete strength: $f_c' = 30$ MPa,
- Yield strength of steel bars: $f_{sx} = 420$ MPa,
- Longitudinal tension reinforcement: 4 bars with 14 mm diameter, and

- Longitudinal compression reinforcement: 2 bars with 14 mm diameter.
- Flexural capacity of the beam before strengthening:
- Nominal flexural capacity before damage: $M_n = 58.1$ kN. m
- Nominal flexural capacity after damage: $M_{nd} = 46.48$ kN. m

Try two layers of carbon fabric based inorganic composite:

Selected fabrics: bi-directional carbon fabrics with the following properties:

- Grid spacing: 10 × 10 mm,
- Area of fiber per unit width in both the weft and warp directions: 047 mm^2/mm, and
- Elastic modulus: $E_f = 240$ GPa.

Flexural capacity of the strengthened beam:

$A_f = n_f t_f b_f = 18.8\ \text{mm}^2$, $A_{st} = 523.39\ \text{mm}^2$, $A_{sc} = 307.88\ \text{mm}^2$

- Determine the nominal flexural capacity using the proposed xgBoost model. A web-based application, which is under development using the proposed xgBoost model is available at https://beamcapacity.herokuapp.com/. The predicted nominal flexural capacity of the strengthened beam ($M_{n,new}$) is determined to be:

  $$M_{n,new} = 65.75\ \text{kN. m}$$

- Check the flexural capacity of the strengthened beam against that of the original beam before damage:

  $$M_{n,new} = 65.75\ \text{kN. m} \geq M_n = 58.1\ \text{kN. m, OK}$$

- Determine the design flexural capacity:

$$M_{r,new} = \phi M_{n,new} = 0.92 \times 65.75 \text{ kN.m} = 60.49 \text{ kN.m}$$

3.11. Conclusions

Despite several experimental studies aimed to understand the structural response of RC beams strengthened with inorganic composites, there are limited analytical or numerical studies. Moreover, there exists a large discrepancy in the predictions of the shear capacity and flexural capacity of shear/flexural-strengthened RC beams using the existing models.

To this end, data-driven ML-based models to predict the shear capacity of RC beams strengthened in shear as well as flexural and load capacities of RC beams strengthened in flexure with inorganic composites are presented in this chapter for the first time. The developed ML models account for several input parameters that characterize the beam geometry, concrete strength, internal shear and flexural reinforcements, and strengthening system. The findings of the studies in this chapter showed the successful implementation of machine learning techniques to predict the shear capacity and flexural capacity of RC beams strengthened with inorganic composites in shear and flexure, respectively.

The following conclusions can be drawn for RC beams strengthened in shear with inorganic composite:

- The developed ML-based models are shown to be effective in predicting the shear capacity of the strengthened beams. Among the ML models, xgBoost is the most efficient algorithm in predicting the shear capacity with stable and accurate predictions. The experimental shear capacity and predicted values based on the xgBoost model showed the least margins of error and strongest

correlation with a coefficient of determination (R^2) of 0.995 and 0.984, for the training and test datasets, respectively.

- Among the existing models, Model-5, which is based on the modified compression field theory resulted in the highest predictive accuracy. The comparisons of the proposed models with the existing formulae confirmed the superiority of the xgBoost model over other models. Moreover, the proposed xgBoost model resulted in the most stable, accurate, and safe predictions.
- Furthermore, the safety, accuracy, and economical aspects of the predictions provided by the proposed and existing models were compared using the Modified Demerits Point Classification method. The proposed xgBoost model provided safe and accurate predictions compared to all other models. Model-1 highly overpredicted the shear capacity of the strengthened beams with more scatter, while Model-4 highly underpredicted the shear capacity of the strengthened beams. The predictions provided by the proposed xgBoost model lie in the appropriate safety region for 98% of the beams compared to only 22%, 18%, 16%, 3%, 51%, and 34% of the beams for Model-1, -2, -3, -4, -5, and -6, respectively.
- Finally, the reliability analysis was performed to calibrate the resistance reduction factors that meet two different levels of target reliability indices ($\beta_T = 3.5$ and 4.0) for shear capacity prediction of shear-strengthened beams using the proposed xgBoost model. Based on the results of the analysis, resistance reduction factors of 0.91 and 0.87 are calibrated to achieve target reliability levels of 3.5 and 4.0, respectively, for RC beams strengthened in shear. A design example is provided using $\phi = 0.91$ for $\beta_T = 3.5$.

The following conclusions can be drawn for RC beams strengthened in flexure:

- Among the existing models, Model-4 [215] resulted in the most accurate predictions with an average of M_{pred}/M_{exp} ratio of 0.799 ± 0.162 and COV of 0.203. Model-1 [211], which is the most general model developed based on Teng et al. [213] model for the FRP system, provided unsafe predictions for most of the strengthened beams with an average of M_{pred}/M_{exp} ratio of 1.257 ± 0.286 and COV of 0.228.
- Generally, all the developed ML models showed good prediction accuracy. The xgBoost model achieved the best predictive ability with the least RMSE, MAE, and MAPE values and the highest R^2 on both the training and test datasets. The value of R^2 using the xgBoost model was 99.3% and 99.2% for the training and test datasets, respectively.
- A comparative study between the proposed and existing models revealed the superior predictive capability and robustness of the proposed model. The predicted flexural and load capacities of the strengthened beams based on the existing models are highly scattered and unsafe.
- Based on the results of SHAP, it is noted that the area of internal tensile steel reinforcement, area of strengthening reinforcement, and width and depth of the beam section have the most significant influences on the flexural capacity of the strengthened beams.
- A capacity reduction factor $\phi = 0.92$ is calibrated to achieve a reliability index $\beta_T = 3.5$. A design example is provided to illustrate

the design of the strengthening system for flexural deficient RC beams based on the proposed xgBoost model and calibrated reduction factor.

The present study can contribute to the state-of-the-art for design and shear/flexural strengthening of RC beams. However, the results of this study are limited to the parameters investigated. Therefore, future research is recommended to investigate the application of data-driven ML models to predict the failure mode of RC beams strengthened in shear/flexure.

CHAPTER 4: FRACTIONAL FACTORIAL DESIGN MODEL FOR SEISMIC PERFORMANCE OF RC BRIDGE PIERS RETROFITTED WITH STEEL-REINFORCED POLYMER COMPOSITES

This chapter reports the following study:

Wakjira TG, Nehdi ML, Ebead U. Fractional factorial design model for seismic performance of RC bridge piers retrofitted with steel-reinforced polymer composites. *Engineering Structures* 2020;221:111100. https://doi.org/10.1016/j.engstruct.2020.111100.

4.1. Introduction

Bridges are important components of the transportation system, sustaining economic growth, social well-being, and logistics of modern communication [46]. The safety and serviceability of bridges are therefore paramount. Yet most existing reinforced concrete (RC) bridges were built before the 1980s, prior to modern seismic-oriented design philosophies. Likewise, such bridges were generally designed for gravity loads and their structural performance would be inadequate during seismic events [47,48]. This is often compounded by poor structural detailing and quality control, and the use of low-strength materials [49,50], which makes bridge piers susceptible to deteriorate at relatively low drift levels [51]. The vulnerability of bridge piers has also been found to strictly correlate to unbalanced flexural-shear resistance, particularly for short piers [52]. Previous experimental studies have shown that the seismic performance of bridge piers depends on several factors, including the pier aspect ratio (*H/d*) [53–56], properties of steel reinforcement bars [57], properties of concrete, transverse reinforcement ratio [54,55,58,59], longitudinal reinforcement ratio [55], axial load level [54,55,58–62] and geometry of the pier [63].

The influence of the aspect ratio (assumed as the ratio of the height of the pier to

its diameter) was investigated by Mostafa *et al.* [53] who studied the seismic performance of two-column bridge bents with hinged bases considering three different aspect ratios of 2.5, 4.5, and 6.64. They found that the bridge piers with *H/d* ratios of 4.5 and 6.64 exhibited flexural controlled failure mode, with large levels of ductility and drift prior to failure. In contrast, the pier with the lowest *H/d* ratio (2.5) experienced a combined shear-flexural failure and reached lower ductility and drift levels. This specimen also did not reach maximum flexural capacity due to high shear demand at the pier base caused by the smaller aspect ratio [53]. In a similar study by Cassese *et al*. [48], piers with an *H/d* ratio of greater than or equal to 2.5 experienced flexural failure with damage involving mainly concrete crushing and longitudinal bar buckling, whereas specimens with low aspect ratios of *H/d* = 1.5 and *H/d* = 2.25 exhibited shear failure after yielding of the flexural reinforcement bars.

Mo and Nien [58] investigated the effect of the axial load, aspect ratio (*H/d* = 3.0 to 3.6), and internal shear reinforcement spacing on the seismic performance of high-strength concrete (50 to 70 MPa) bridge piers. Based on test results of six pier specimens, they reported that an increase in the axial load resulted in higher flexural capacity, but reduced the ductility of the pier [58]. In a similar study, Shao *et al.* [59] reported that excessive axial compression could deteriorate the ductility of the pier because of premature concrete crushing. Similar results were reported by Esmaeily and Xiao [60], Holub [61], and Yeh *et al*. [54,56].

However, there is a dearth of studies that explored the combined effects of and interactions between different factors on the bridge pier performance under seismic loads. Reza *et al.* [49] performed a parametric study to examine the influence of the mechanical properties of concrete and reinforcement bars, spacing between internal ties, and the longitudinal reinforcement ratio on the load-carrying capacity of rectangular bridge piers under shear and flexure loads. Similarly, Parghi and Alam [64] examined the effect of different variables on the seismic behavior of flexural dominated fiber-reinforced polymer

(FRP)-confined circular piers. Based on numerical analysis carried out on 81 piers, they concluded that the pier seismic performance was mainly affected by the *H/d* ratio. The authors also reported that the volume fraction of internal transverse reinforcement had an insignificant influence on the lateral load-carrying capacity of the piers [64]. In contrast, Yeh *et al*. [54] reported that the increase in the internal transverse reinforcement ratio increased both the strength and ductility of bridge piers based on experimental results of RC piers with varying *H/d* ratios of 3.0, 3.6, and 4.3. Similar results have been reported by others [58,59].

The performance of piers also depends on their geometric shape. Based on experimental results of hollow RC columns confined with FRP, Kusumawardaningsih and Hadi [63] reported that circular columns performed better than rectangular section columns. Moreover, Su *et al*. [224] reported that the effect of the mechanical properties of concrete and longitudinal reinforcement bars on the performance of piers was more pronounced for piers with rectangular section than that in piers with circular section. Therefore, there is a need to provide a more detailed analysis of the conditions and reasons for the observations above, while the effects of different design parameters on the seismic performance of rectangular section piers still need concerted research efforts.

One other key parameter influencing the performance of bridge piers is the level of concrete confinement [65]. Inadequately confined RC columns possess insufficient ductility to dissipate seismic energy during earthquake events [225]. RC bridge piers could also become deficient due to corrosion of reinforcement bars and changes in service loads [226]. Different confinement and retrofitting techniques have been reported in the literature to improve the performance of seismically vulnerable bridge piers, including steel [227], CFRP [65,226,228–231] and GFRP [232] jackets. Steel jackets have been observed to increase the size and weight of the pier and reduce clearance, and are susceptible to corrosion [65]. In contrast, FRPs have excellent corrosion resistance and a high strength-

to-weight ratio. Elgawady *et al*. [65] tested deficient rectangular bridge piers with aspect ratios of 2.0 and 1.5, confined with CFRP and steel jackets. The test parameters were the amount of CFRP reinforcement, configuration of CFRP jacketing, and type of retrofitting material (CFRP and steel jackets). The retrofitted specimens exhibited higher displacement ductility and energy dissipation, which increased with an increase in the amount of CFRP reinforcement.

Yet FRPs tend to be more costly, have low impact resistance, and can be vulnerable to fire events and high temperatures. This motivated the development of cost-effective retrofitting materials without compromising the mechanical strength. For instance, steel-reinforced polymer (SRP) composites, with research dating back to 2005 [31, 33], utilize high-strength steel fabrics, have been introduced as a cost-effective and promising alternative strengthening solution [20,22,197,233,234].

The present study deploys numerical analysis and factorial design of experiments (DOE) to investigate the effects of key parameters and their interactions on the seismic performance of deficient rectangular section RC bridge piers confined with SRP. The independent variables investigated include concrete compressive strength (f_c'), longitudinal reinforcement ratio (ρ_{sl}), aspect ratio, internal transverse reinforcement spacing (S_{st}), yield strength of reinforcement bars (f_y), and number of SRP layers (n). The study should provide guidance to practitioners on using SRP for retrofitting a large portfolio of ageing RC bridge piers that are deficient in terms of seismic performance.

4.2. Bridge Pier Geometry and Model

4.2.1. Geometry of bridge pier

A rectangular bridge pier with deficient design simulating bridge piers built before the 1970s was selected from the literature [65,228]. Figure 4.1 shows the pier geometry and its reinforcement detailing. A rigid foundation was assumed at pier-footing, similar to

previous studies (e.g. [49,64,235]). The piers were subjected to lateral displacement applied at its top with a constant axial compression load, and restrained in the out-of-plane motion, allowing for movement in one horizontal direction only. The bridge pier specimens were 635 mm × 1000 mm in cross-section with varying height. The pier specimens were internally reinforced with transverse reinforcement of D10 (10 mm diameter) and varying longitudinal bar diameter (19 mm, 25 mm, and 30 mm), as shown in Figure 4.1. The height of the pier was adjusted to investigate the effect of aspect ratios of 4 to 7, implying flexural dominated piers [236]. Similarly, the longitudinal reinforcement ratio was explored by adjusting the area of longitudinal reinforcement (A_{sl}), as shown in Table 4.1. The spacing of internal transverse reinforcement of the pier was also varied, as shown in Figure 4.1 and Table 4.1, to study its effect on seismic performance. The pier specimens were retrofitted with steel-reinforced polymer. Retrofitting of RC columns can be performed in full confinement covering the entire height of the column (e.g. [237–240]) or partial confinement (e.g. [241–243]). In this study, the full confinement method was consistently employed with the SRP fiber direction perpendicular to the pier axis, as shown in Figure 4.1. Details of the steel fabrics will be discussed in Section 4.3. A constant axial compression load of 2,540 kN, corresponding to an axial load level $P/(f_c' A_g)$, which ranges from 10% (f_c' = 40 MPa) to 16% (f_c' = 25 MPa), was applied on top of the pier, as shown in *Figure 4.1*.

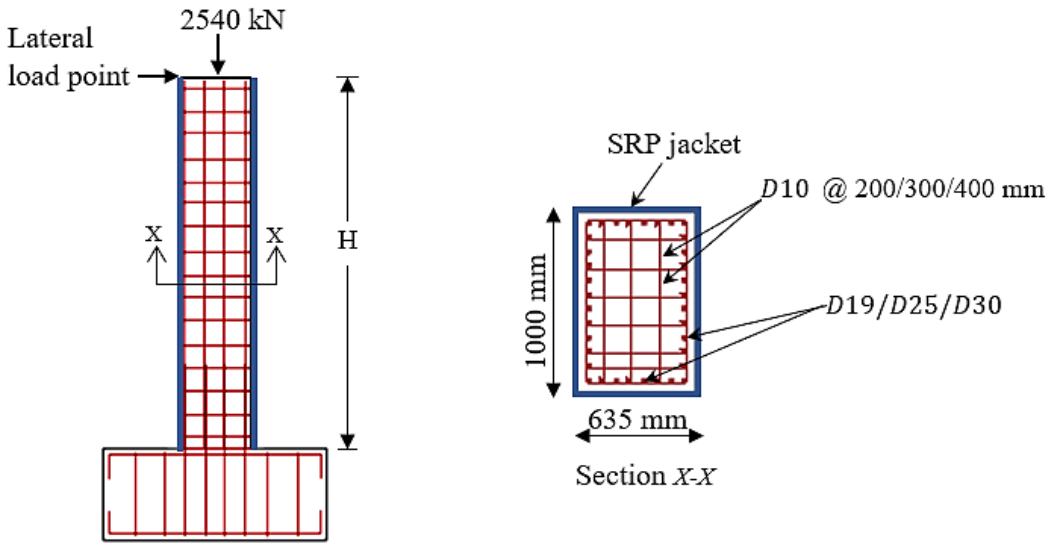

Figure 4.1: Pier geometry and reinforcement details.

Table 4.1. Factor levels used in a three-level fractional factorial design

S.N.	Factors		Lower level (-)	Intermediate level (0)	Upper level (+)
1	Concrete compressive strength, f_c' (MPa)	A	25	32.5	40
2	Yield strength of steel, f_y (MPa)	B	250	400	550
3	Reinforcement ratio of longitudinal bars, ρ_{sl} (%)	C	1.45	2.75	4
4	Tie spacing, S_{st} (mm)	D	200	300	400
5	Aspect ratio, H/d	E	4	5.5	7
6	SRP layers number, n	F	2	3	4

4.2.2. Fiber element section model

Recent advances in computational tools permitted sophisticated modeling of the nonlinear behavior of bridges subjected to seismic excitation, enabling researchers to use refined analysis. Fiber-based modeling is the most recent and widely used method to simulate the nonlinear inelastic behavior of structural components [244–248]. This approach was therefore utilized for simulating the piers in this study. The pier specimens

were modeled in the SeismoStruct program [249] using displacement-based non-linear fiber beam-column elements. This program has been demonstrated to accurately predict the performance of bridge structures under seismic loading, accounting for geometric nonlinearities and material inelasticity [250–252]. The fiber beam-column elements are discretized into nine finite frame elements, as shown in Figure 4.2a. The first element was assumed to have a length equal to that of the plastic hinge (L_p), given by the following equation according to Berry and Eberhard [67]:

$$L_p = 0.05L + 0.1\frac{f_y d_b}{\sqrt{f_c'}} \leq 0.25L \tag{4.1}$$

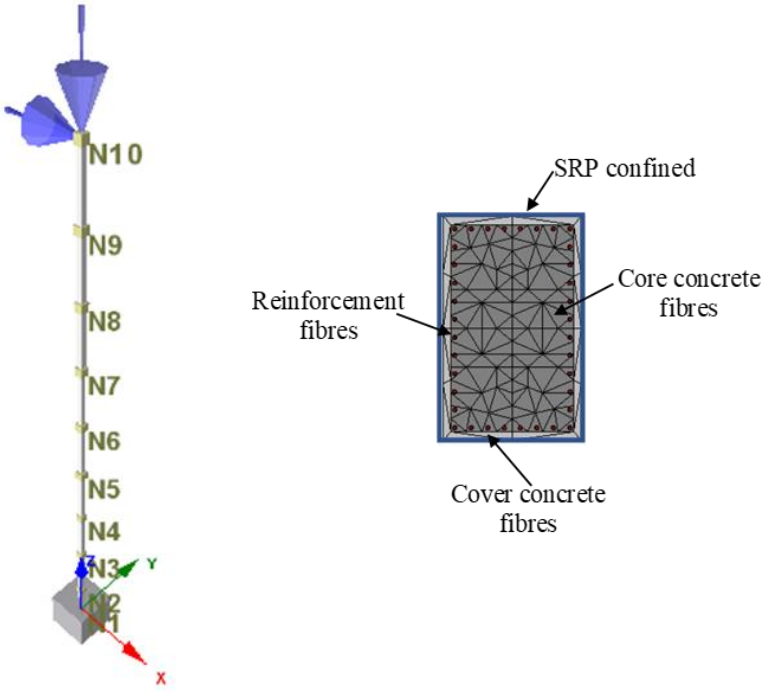

(a) Pier model (b) Fiber representation (200 fibers)

Figure 4.2: Finite element model for bridge pier.

As shown in Figure 4.2b, the section used for the bridge pier was discretized into concrete fibers and longitudinal steel fibers. The concrete fibers were further discretized

into core fiber for concrete confined with SRP and internal transverse reinforcement, and cover fiber for concrete confined with SRP only (Figure 4.2b). The section was divided into 200 fibers. The total weight of the superstructure was assumed lumped at the pier top; as commonly used in modeling bridges [251].

4.2.3. Constitutive material models

The constitutive behavior of concrete was simulated after the Mander *et al.* [253] model, further augmented by [254]. The confining effect of transverse reinforcement was accounted for using a confinement factor of the section core based on Mander *et al*. [253]. The confinement pressure provided by the SRP jacket was determined based on the formulations proposed by Ferracuti and Savoia [255]. This model is based on the constitutive relationship proposed by Mander et al. [253] and Spoelstra and Monti [256] for concrete in compression and Yankelevsky and Reinhardt [257] model for confined concrete in tension. A three-dimensional displacement-based inelastic frame element type was used to account for the material non-linearity. The sectional stress-strain state was determined by integrating the response of the individual fibers, accounting for the inelasticity along the member length and its cross-section. Moreover, the constitutive behavior of reinforcement bars was simulated after Menegotto and Pinto's [258] nonlinear model, as modified by Filippou *et al.* [259].

4.3. Parameters Studied and Design of Experiment

This study considered six key design parameters that influence the seismic performance of SRP-confined deficient rectangular section piers, namely: a) concrete compressive strength (f_c'); b) yield strength of steel bars (f_y); c) internal transverse reinforcement spacing (S_{st}); d) longitudinal reinforcement ratio ($\rho_l = A_{sl}/bh$); e) aspect ratio (H/d); and f) number of SRP layers; where d is the depth to centerline of the outermost tensile bars, H is the pier height, b and h are the cross-sectional width and depth of the pier,

respectively.

To investigate the significance of the main effects and interactions of the six parameters on the seismic performance of the bridge pier, a 3^k fractional factorial DOE was performed on the six factors, with the superscript *k* being the factors and 3 the levels of each factor employed [260]. Factorial designs are widely used to identify the important factors affecting the response in multi-variable studies [260]. Moreover, this is considered the most efficient design method to investigate the significance of the combined effect of two or more factors on the response [260]. The fractional factorial design was used in this study to examine the main effects of the factors and two-way interactions, thus requiring 78 factor combinations. The factorial design was conducted at a 95% confidence level and a significance level of 5%, using a two-sided confidence interval.

Table 4.1 presents the levels applied in the factorial design, which were selected based on a literature survey [49,65,228,229,236]. The effect of the longitudinal reinforcement ratio (from 1.45 to 4%), yield strength of steel bars (250 MPa to 550 MPa), concrete compressive strength (25 MPa to 40 MPa), internal transverse reinforcement spacing (200 to 400 mm), aspect ratio (4 to 7), number of SRP layers (2 to 4), and their interactions on the seismic performance of rectangular cross-section SRP-retrofitted piers were investigated. ACI 318-11 [261] limits the yield strength of the reinforcement bars to be used as concrete confinement to 550 MPa; accordingly, this study varied the yield strength between 250 MPa and 550 MPa. The SRP retrofit was composed of commercially available unidirectional steel fabrics embedded within an eco-friendly epoxy mineral adhesive [115]. The properties of the steel fabrics are presented in Table 4.2. The steel fabrics are made of UHTS galvanized 3×2 (5 wires) steel micro-cords containing 3.14 cords per centimeter [115]. As listed in Table 4.2, the fabrics have an approximate fiber weight (γ_f) of 1200 g/m^2, an equivalent thickness per unit width (t_f) of 0.169 mm, an actual cord

area (A_f) of 0.538 mm^2, tensile strength ($f_{f,u}$) of 3000 MPa, ultimate elongation ($\varepsilon_{f,uf}$) of 2%, and elastic modulus (E_f) of 190 GPa [115].

Table 4.2. Properties of the steel fabrics

Material	t_f (mm)	A_f (mm2)	γ (g/m2)	Density (cords/cm)	$f_{f,u}$ (MPa)	E_f (GPa)	$\varepsilon_{f,u}$ (%)
G1200	0.169	0.538	1200	3.14	3000	190	2

t_f = equivalent thickness; A_f = area of cord; γ_{sf} = net fibre weight; $f_{f,u}$ = tensile strength; E_f = modulus of elasticity; $\varepsilon_{f,u}$ = ultimate elongation.

4.4. Pushover Analysis

Generally, pushover analysis is an effective method for performance-based seismic design. In a performance-based approach, a structure is designed to achieve different performance levels under different levels of ground motion [55,262]. The extent of the damage and repair effort are quantified with engineering limit states that can be reflected in terms of strain limits of the steel bars and concrete [55,248,263,264]. This study uses pushover analyses to examine the main effects and interactions of different parameters on the seismic performance of SRP-jacketed rectangular section piers at different limit states. Three strain limits were considered as three performance criteria. These limits include the initiation of a) crushing of core concrete, b) longitudinal bar yielding, and c) longitudinal bar buckling.

Concrete core crushing was considered to occur at the ultimate concrete compressive strain (ε_{cu}), which is reached when the confining reinforcement fractures [75,253]. Lam and Teng [265] proposed a model to predict the ultimate compressive strain of concrete confined with FRP, which was modified by Teng et al. [266]. This model was further refined by Jiang and Teng [267] to eliminate the deficiency of the Teng et al. [266] model in predicting the response of weekly confined specimens. Based

on the Jiang and Teng [267] model, Teng et al. [268] proposed an equation to predict the ultimate compressive strain of FRP-steel confined concrete accounting for the effect of both transverse steel reinforcement and retrofitting composite, which was further modified by Lin et al. [269]. According to Lin et al. [269] model, the ultimate compressive strain of concrete confined by FRP-steel is given by:

$$\varepsilon_{cu} = \varepsilon_{co}\left(1.75 + 6.5{\rho_K}^{0.80}{\rho_\epsilon}^{1.45} + 0.85\alpha\frac{f'_{ls}}{f'_{co}}(1 + 0.465\rho_\epsilon)\right) \quad (4.2)$$

where,

f'_{ls} is the effective lateral confining pressure provided by the transverse steel reinforcement,

$\rho_\epsilon = \varepsilon_{f,rup}/\varepsilon_{co}$ is the strain ratio [270],

$\varepsilon_{f,rup} = f_{f,u}/E_f$ is the rupture strain of the composite,

ε_{co} is the unconfined concrete compressive strain,

f'_{co} is the unconfined concrete compressive strength,

ρ_K is the confinement stiffness ratio of FRP as defined by Teng et al. [270]:

$$\rho_K = \frac{E_f\rho_f}{f'_{co}/\varepsilon_{co}} \geq 0.01 \quad (4.3)$$

where,

ρ_f is the jacket volumetric ratio, which is given by $\rho_f = 2nt_f(b + h)/bh$ for rectangular or square column [271],

The coefficient α in Eq. (4.2) is given by [268]:

$$\alpha = 1.59 + 15.1(K_f/K_{steel}) \quad (4.4)$$

where,

$K_f = \rho_f E_f$ and $K_{steel} = 2k_e E_s \rho_{st}$ are the confinement stiffness of FRP

and transverse steel following Mander et al. [253] and Teng et al. [268],

E_s elastic modulus of the steel bar,

ρ_{st} is the ratio of the volume of transverse confining steel to the volume of confined concrete core.

The effective lateral confining stress of transverse steel reinforcement in the *x* and *y* directions are given by [253].

$$f'_{ls,x} = k_e \rho_{st,x} f_{yt} \tag{4.5}$$

$$f'_{ls,y} = k_e \rho_{st,y} f_{yt} \tag{4.6}$$

where,

f_{yt} is the yield strength of transverse steel reinforcement,

$\rho_{st,x}$ and $\rho_{st,y}$ are the volumetric reinforcement ratio of transverse steel reinforcement in the *x* and *y* directions, respectively,

k_e is the confinement effectiveness coefficient as defined by Mander et al. [253]. For rectangular columns, k_e is given by [253]:

$$k_e = \frac{\left(1 - \sum_{i=1}^{j} \frac{(w'_i)^2}{6 b_c d_c}\right)\left(1 - \frac{s'}{2b_c}\right)\left(1 - \frac{s'}{2d_c}\right)}{1 - \rho_{cc}} \geq 0 \tag{4.7}$$

where,

b_c and d_c are core dimensions to centerlines of transverse bars in the x and y directions, respectively, where $b_c \geq d_c$,

w'_i is the *i*th clear distance between adjacent longitudinal bars,

j is number of longitudinal bars,

s' is vertical clear spacing of transverse steel bars,

$\rho_{cc} = A_{sl}/b_c d_c$ is the ratio of the volume of the longitudinal steel to the volume of confined concrete core,

A_{sl} is the total area of longitudinal reinforcement.

The steel strain at yielding of the longitudinal bar (ε_{by}) was taken as the ratio of the yielding stress to the elastic modulus of the steel bar. Different formulations were proposed for determining the strain at buckling limit state [62,67,272,273]. According to Berry and Eberhard [272], the strain in the longitudinal bar at the onset of longitudinal bar buckling (ε_{bb}) is given as a function of the effective confinement ratio ($\rho_{eff} = \rho_{st} f_{yt}/f_c'$), Eq. (4.8).

$$\varepsilon_{bb} = \chi_0 + \chi_1 \rho_{eff} \leq 0.15 \tag{4.8}$$

where χ_0 and χ_1 are constants.

In another study, Berry and Eberhard [67] calibrated the values of $\chi_0 = 0.045$ and $\chi_1 = 0.25$ empirically based on experimental results of RC columns. Goodnight et al. [62] developed a more refined estimate for determining the value of ε_{bb} based on the experimental results of large scale RC bridge columns. This equation considers the effect of axial load level on the strain at the onset of longitudinal bar buckling as given below:

$$\varepsilon_{bb} = 0.03 + 700\rho_{st}\frac{f_{yt}}{E_s} - 0.1\frac{P}{f_c' A_g} \tag{4.9}$$

Studies on the performance limit states at longitudinal bar buckling of retrofitted columns are rather scarce [274]. Bournas and Triantafillou [274] studied the onset and evolution of longitudinal bar buckling of RC columns confined with FRP and textile reinforced mortar (TRM). They concluded that the confining composite had no effect on the strain at the onset of longitudinal bar buckling. Thus, Eq. (4.9) was used in this study to determine the value of ε_{bb} for each specimen.

4.4.1. Effect of key design parameters on base shear

A pushover analysis was performed for each combination of three levels of the six factors, for a total of 78 pier specimens. Typical pushover analysis result for a high level of each factor is shown in Figure 4.3. This figure also indicates the three limit states, namely yielding of the longitudinal bar, concrete core crushing, and buckling of longitudinal bar. The main effect and possible interactions of input parameters on the response variable can be examined using analysis of variance (ANOVA) [260]. This method allows to determine which factors have a significant influence on the response [260] and distinguishes the prevailing factors and interactions that influence the response variable from the less important factors and interactions. Thus, ANOVA analysis was used to investigate the main influence and possible interactions of the six factors at a significance level (α) of 5% using a two-sided confidence interval. Accordingly, the conclusions were made based on the *P*-value, in which each effect with a *P*-value less than α was considered as a significant effect on the response at 95% confidence. The *P*-value is the smallest level α at which the data are significant [260]. Table 4.3 presents the results of ANOVA analysis for the lateral bearing capacity at different limit states. In addition, the degree and direction of significant effect were evaluated by a normal probability plot of standardized effect at 95% confidence.

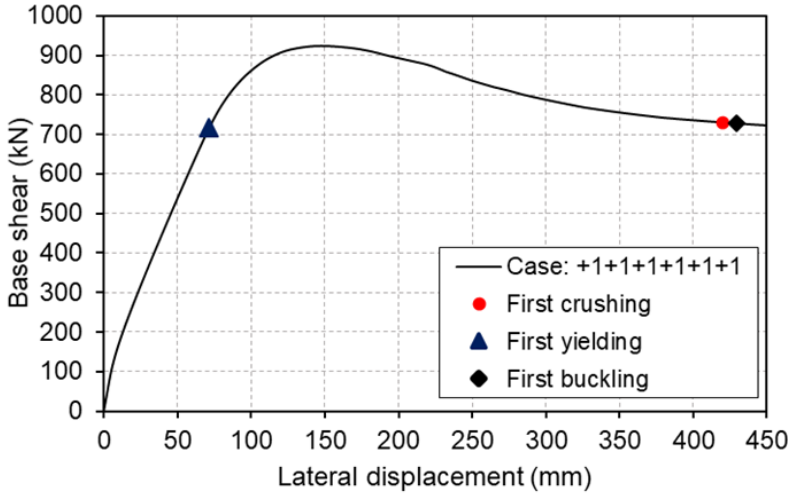

Figure 4.3: Typical pushover response curve.

Table 4.3. Effect of key design parameters on base shear at different limit states based on ANOVA

S.N.	Design parameters		*P*-values at different limit states		
			Yielding	Crushing	Buckling
Main parameters effect					
1	f_c'	Concrete compressive strength	**0.0057**	**0.0015**	0.1464
2	f_y	Yield strength of steel	**< 0.0001**	**< 0.0001**	**< 0.0001**
3	ρ_{sl}	Longitudinal reinforcement ratio	**< 0.0001**	**< 0.0001**	**< 0.0001**
4	S_{st}	Tie spacing	0.9647	**0.0356**	0.0798
5	H/d	Aspect ratio	**< 0.0001**	**< 0.0001**	**< 0.0001**
6	n	SRP layers number	0.8456	0.722	**0.043**
Two-way interaction					
7		$f_c' \times f_y$	0.8154	0.3962	0.4046
8		$f_c' \times \rho_{sl}$	0.9733	0.7731	0.332
9		$f_c' \times S_{st}$	0.6575	0.9679	0.4775
10		$f_c' \times$ H/d	0.8505	0.546	0.7911
11		$f_c' \times$ n	0.7678	0.5531	0.3388
12		$f_y \times \rho_{sl}$	**0.0002**	**0.0015**	**0.0014**
13		$f_y \times S_{st}$	0.7807	0.5819	0.3844
14		$f_y \times$ H/d	**0.0013**	**0.0042**	**0.0056**
15		$f_y \times$ n	0.9839	0.9616	0.7242
16		$\rho_{sl} \times S_{st}$	0.7444	0.832	0.6762
17		$\rho_{sl} \times$ H/d	**0.0013**	**0.0027**	**0.0036**
18		$\rho_{sl} \times$ n	0.8318	0.9093	0.3088
19		$S_{st} \times$ H/d	0.8552	0.436	0.4788
20		$S_{st} \times$ n	0.895	0.3384	0.4739
21		H/d × n	0.7397	0.7596	0.702

4.4.4.1. Factorial design at first yielding of longitudinal reinforcement

As presented in Table 4.3, the main effects of f_c', f_y, ρ_{sl}, and *H/d* have *P*-values of less than the significance level of 5%. Therefore, these factors produce significant effects on the yielding base shear, which is the base shear at the first yielding of longitudinal bars. However, both the internal transverse reinforcement and SRP jacket exhibited insignificant effects on the yielding base shear. Previous research [49] also observed that internal transverse reinforcement did not influence the yielding base shear. The normal probability plot of the yielding base shear in Figure 4.4 shows the standardized effects of the design parameters relative to a distribution fit line. The standardized effects test the null hypothesis that the effect is zero. In the normal probability plot, the factors with no significant effect on the response were fitted to a line, whereas the significant factors fell some distance away from the fitted line. In addition, the normal probability plot shows whether the response increased or decreased with an increase in each factor and the interaction between factors. Positive effects, which are on the right side of the fitted line in the normal probability plot, increase the response with an increase in the value of the factor, while negative effects decrease the response with an increase in the value of the factor. It can be observed in Figure 4.4 that the main effects of f_c', ρ_{sl}, and f_y have a positive standardized effect on the yielding base shear, meaning that the base shear increased with an increase in these factors. However, the base shear decreased with an increase in the value of *H/d* as the main effect of *H/d* had a negative standardized effect on the base shear. Moreover, the distance from the fitted line shows the degree of the importance of the factor. For instance, the aspect ratio was located farthest from the fitted line with a negative effect, signifying the highest effect on the base shear and therefore causing a sharp decrease in the yielding base shear. Concrete compressive strength had a slightly smaller effect and is thus closer to the fitted line on the positive side, meaning that an increase in f_c' slightly increased the yielding base

shear.

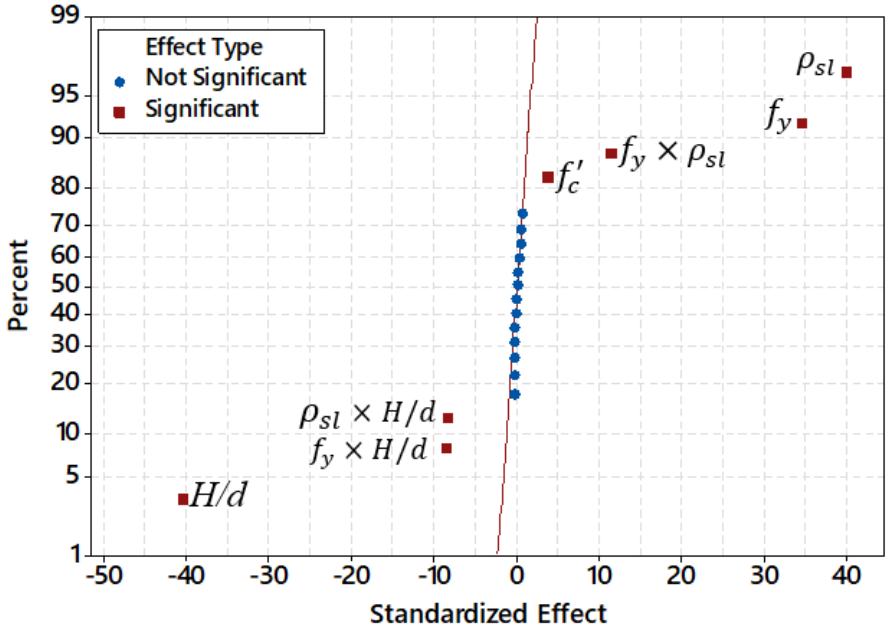

Figure 4.4: Normal plot of the standardized effects for the design parameters for base shear at yielding of longitudinal reinforcement, $\alpha = 0.05$.

Interactions between different design parameters are complex relationships among those parameters' effects and thus are not independent in their effects on the response. The ANOVA results suggest the $f_y \times \rho_{sl}$, $H/d \times f_y$, and $H/d \times \rho_{sl}$ interactions significantly affect the base shear at yielding. Moreover, as can be observed in Figure 4.4, the combined effect of $f_y \times \rho_{sl}$ showed positive standardized effect on base shear. The influence of aspect ratio was so high that the combined effects of $H/d \times f_y$ and $H/d \times \rho_{sl}$ were skewed to the negative side of the fitted line. Thus, $H/d \times f_y$ and $H/d \times \rho_{sl}$ interactions decreased the base shear at the initiation of yielding.

Figure 4.5a shows the percentage contribution of the design parameters to the yielding base shear. It can be observed that the aspect ratio had the highest influence on the yielding base shear, followed by the yield strength and reinforcement ratio of longitudinal

steel bars. The contributions of the main effect of f_c' and $f_y \times \rho_{sl}$, $H/d \times f_y$, and $H/d \times \rho_{sl}$ interaction effects were less than 5%. The variation of yielding base shear with the change in the aspect ratio of the pier is shown in Figure 4.5b. The variation in base shear was less pronounced in piers with a high H/d ratio (Figure 4.5b). Figure 4.6a–c show the contour plots of H/d versus ρ_{sl}, H/d versus f_y, and ρ_{sl} versus f_y, respectively, to predict the yielding base shear.

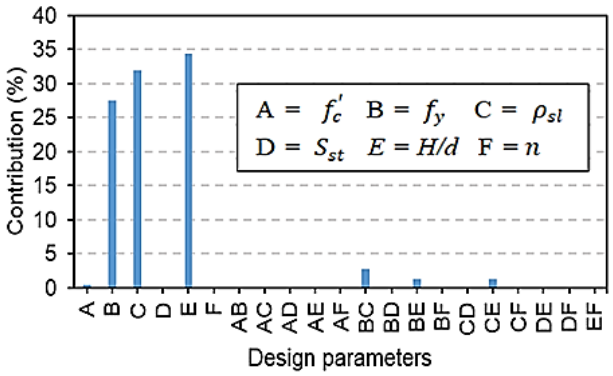

(a) Percentage contribution of each parameter

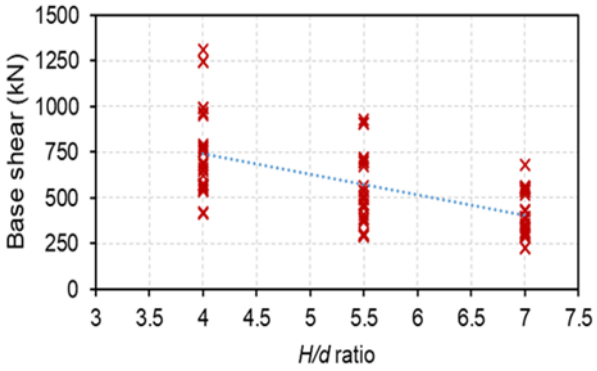

(b) Effect of variation in H/d on base shear

Figure 4.5: Base shear at yielding of longitudinal reinforcement.

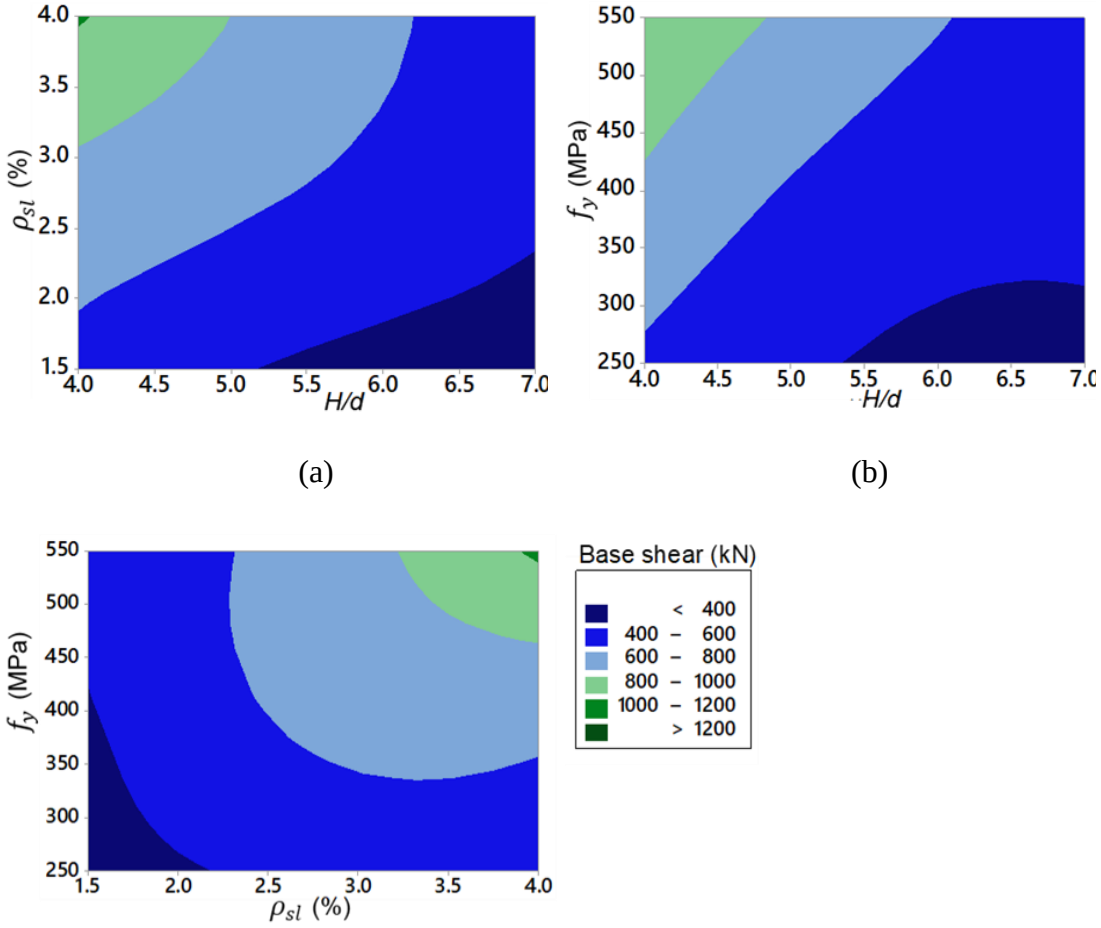

Figure 4.6: Contour diagram of (a) *H/d* versus ρ_{sl}, (b) *H/d* versus f_y, and (c) ρ_{sl} versus f_y for predicting base shear at yielding of longitudinal reinforcement.

4.4.4.2. Factorial design at the initiation of concrete core crushing

The base shear at concrete core crushing was mostly affected by the longitudinal reinforcement ratio, aspect ratio, compressive strength of concrete, spacing of internal transverse reinforcement, and yield strength of reinforcing steel (Figure 4.7). This figure also shows that the aspect ratio was farthest from the fitted line and had the strongest negative effect. Moreover, the interaction effects of $f_y \times \rho_{sl}$, $H/d \times f_y$, and $H/d \times \rho_{sl}$ were significant, as can be observed from the *P*-values in Table 4.3 and Figure 4.7.

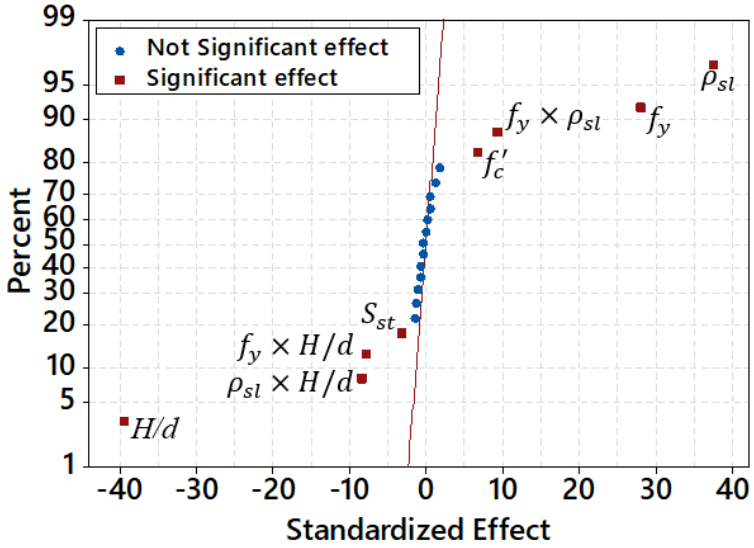

Figure 4.7: Normal plot of the standardized effects for the design parameters for base shear at the concrete core crushing, $\alpha = 0.05$.

The crushing base shear increased with an increase in ρ_{sl}, f_y, f_c', and $f_y \times \rho_{sl}$, which all had positive effect on base shear, as shown in the normal probability plot of Figure 4.7. However, the aspect ratio and its interaction with f_y and ρ_{sl} showed negative influence on the crushing base shear. Similarly, spacing of internal transverse reinforcement showed a negative effect on crushing base shear, as shown in *Figure 4.7*. The enhancement in base shear due to an increase in ρ_{sl} and f_y can be further observed from the contour plots of base shear in Figure 4.8a–c, where the crushing base shear decreased with the increasing aspect ratio of the pier. The effects of parameter interactions on the crushing base shear were less significant than the main effects, as shown in Figure 4.9a. The longitudinal reinforcement ratio had the highest contribution of 36%, while the contributions of *H/d* and f_y were 35.4% and 22.6%, respectively. The effects of the design parameters were more pronounced in piers with a smaller aspect ratio (Figure 4.9b).

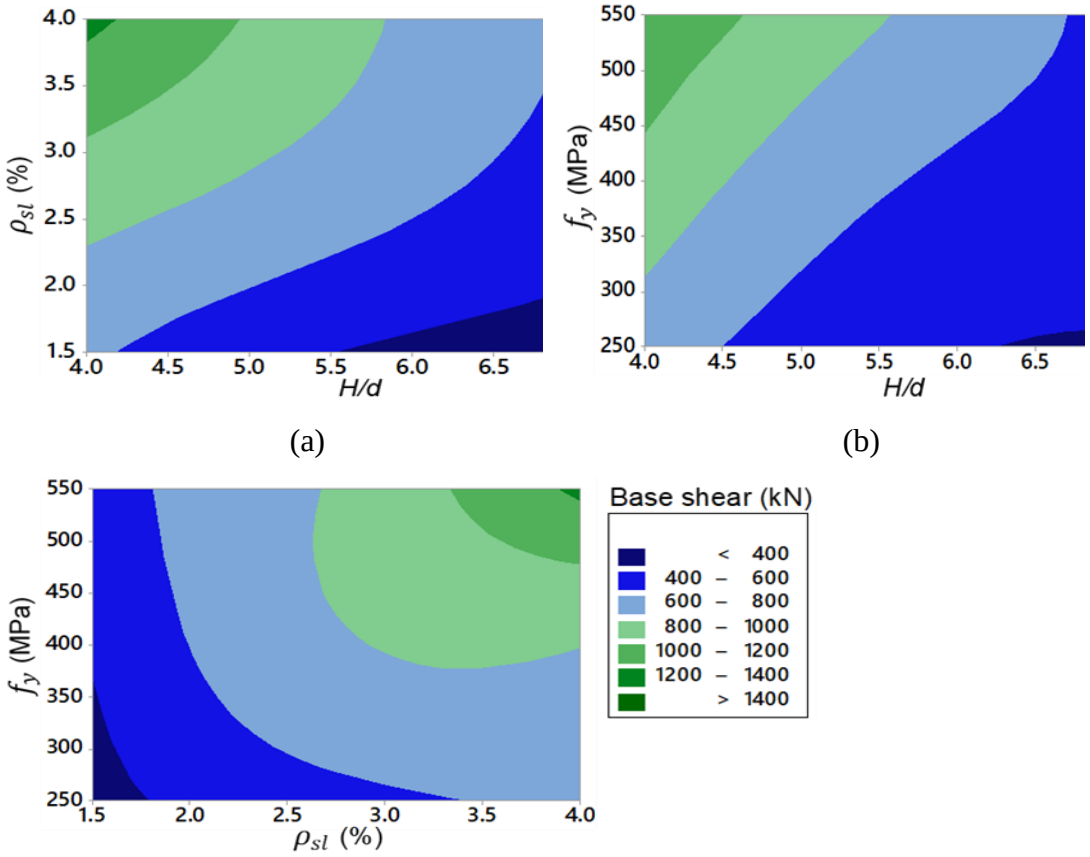

Figure 4.8: Contour diagram of (a) *H/d* versus ρ_{sl}, (b) *H/d* versus f_y, and (c) ρ_{sl} versus f_y for predicting base shear at concrete core crushing.

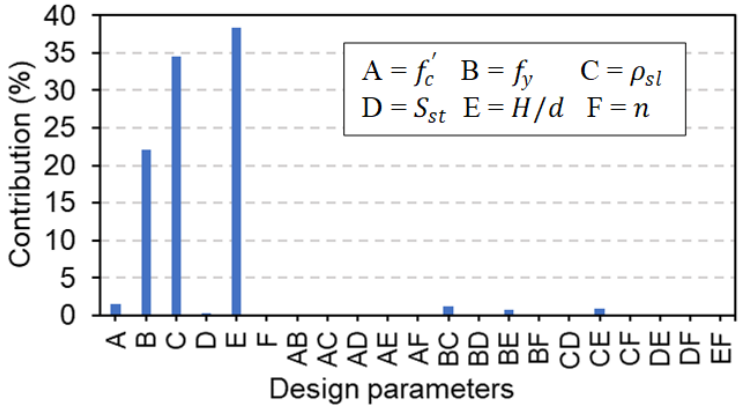

(a) Percentage contribution of each parameter

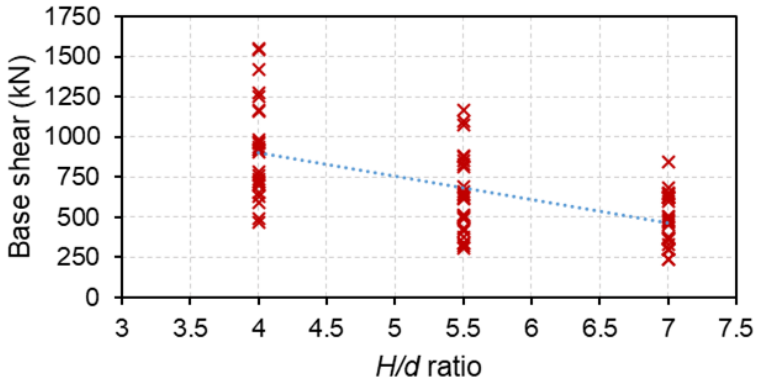

(b) Effect of variation in *H/d* on base shear

Figure 4.9: Base shear at concrete core crushing.

4.4.4.3. Factorial design at the initiation of longitudinal reinforcement buckling

The ANOVA analysis provided in Table 4.3 shows that all main factors, except concrete compressive strength and spacing of internal transverse reinforcement, had a significant influence on the buckling base shear. Moreover, ANOVA results suggest that interactions of $H/d \times f_y$, $f_y \times \rho_{sl}$, and $H/d \times \rho_{sl}$ play vital roles in the buckling base shear. The influence of f_c' on the buckling base shear was not significant.

The normal probability plot in Figure 4.10 shows that the aspect ratio farthest from the fitted line in the negative direction affected the buckling base shear the most. The contribution of *H/d* to the buckling base shear was 37.99% (Figure 4.11a). Moreover, f_y and ρ_{sl} were the most critical parameters with positive effect on the buckling base shear (Figure 4.10 and Figure 4.11a). The contribution of $f_y \times \rho_{sl}$ was the highest of the interaction effects (Figure 4.11a). Specimens with lower *H/d* ratio exhibited more variation in buckling base shear with a change in design parameters (Figure 4.11b). The interaction effects of $H/d \times \rho_{sl}$, $H/d \times f_y$, and $f_y \times \rho_{sl}$ can also be clearly observed in Figure 4.12a–c.

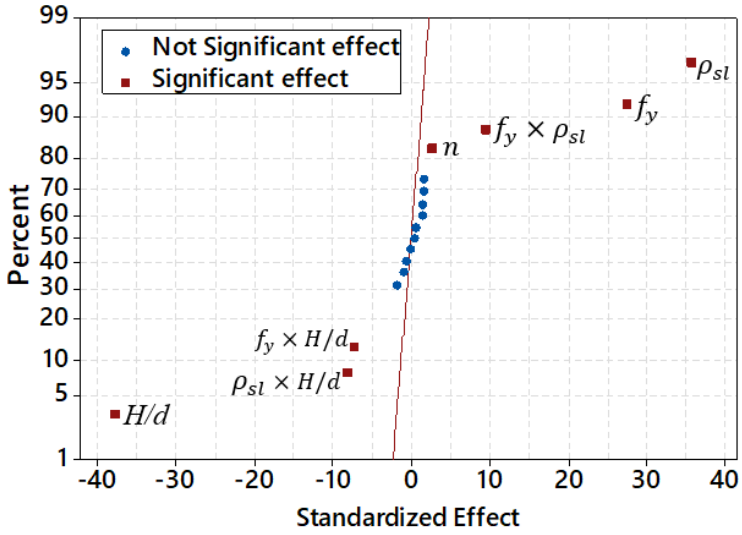

Figure 4.10: Normal plot of the standardized effects for the design parameters for base shear at longitudinal bar buckling, $\alpha = 0.05$.

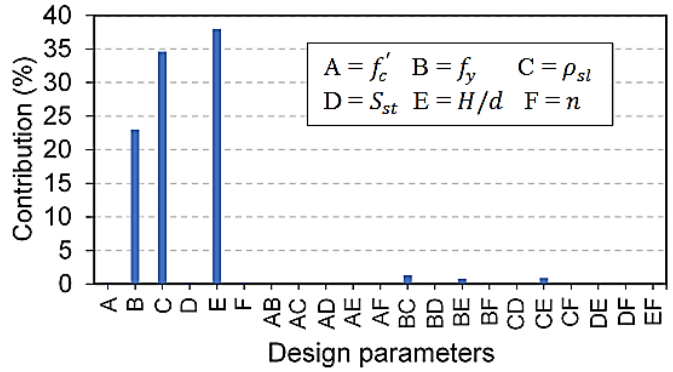

(a) Percentage contribution of each parameter

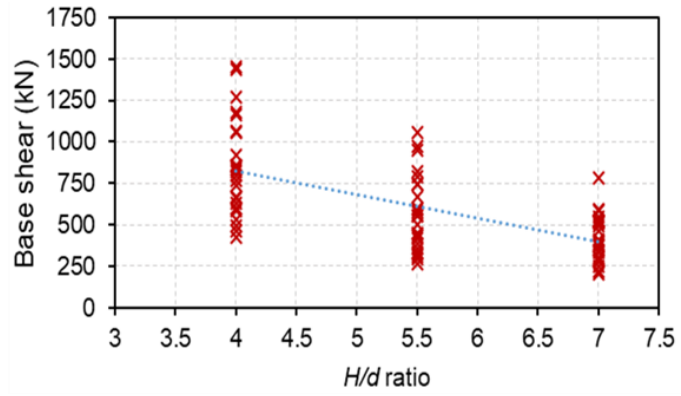

(b) Effect of variation in *H/d* on base shear

Figure 4.11: Base shear at longitudinal bar buckling.

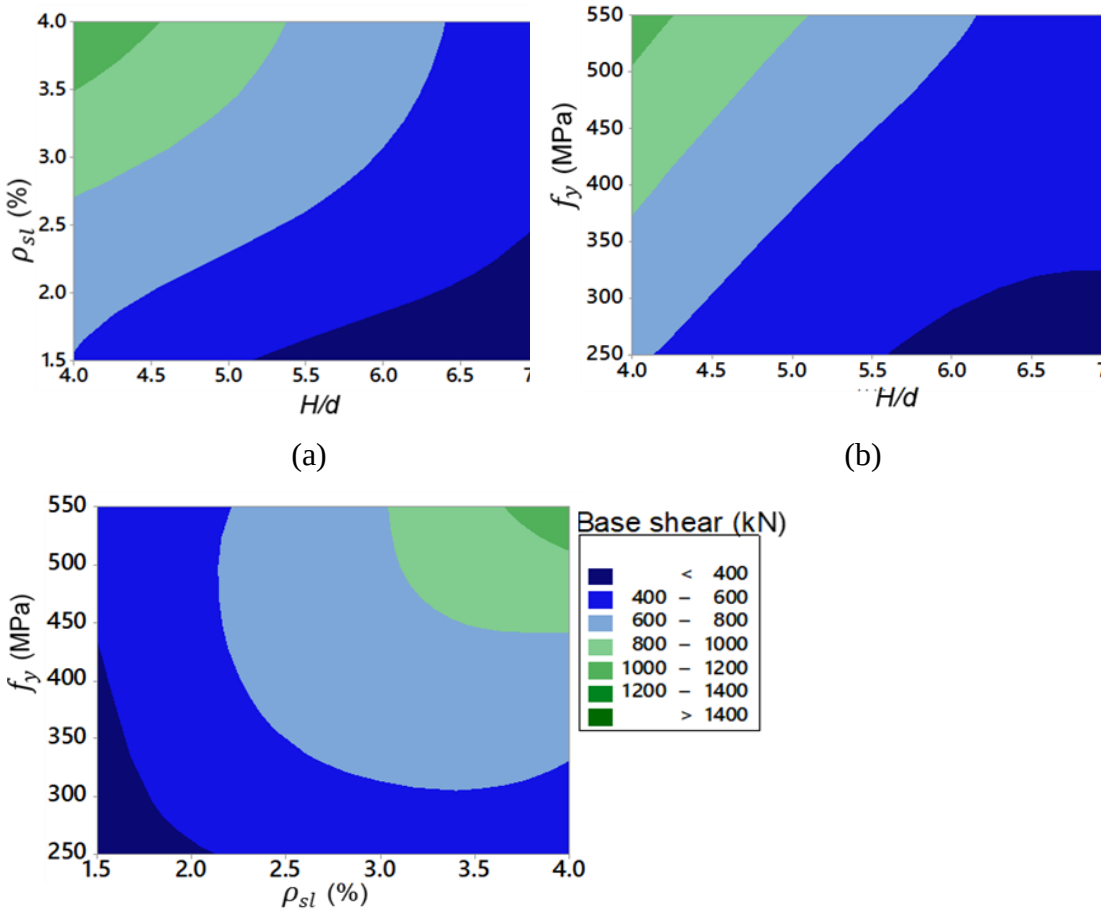

Figure 4.12: Contour diagram of (a) *H/d* versus ρ_{sl}, (b) *H/d* versus f_y, and (c) ρ_{sl} versus f_y for predicting base shear at buckling of longitudinal reinforcement.

4.4.2. Factorial design of lateral displacement at different limit states

Table 4.4 presents the influence of design parameters and interactions at different limit states. The yielding displacement was most significantly influenced by f_c', ρ_{sl}, f_y, and the aspect ratio, while the effect of transverse reinforcement (internal ties and SRP) was negligible. Moreover, the interaction effects of f_c'× *H/d*, f_y × ρ_{sl}, f_y × *H/d*, and ρ_{sl} × *H/d* had an important effect on yielding displacement. Figure 4.13 illustrates the normal probability plot of the standardized effects. The aspect ratio had the highest positive effect

on the yielding displacement, which also increased with an increase in ρ_{sl} and f_y. Similarly, the ρ_{sl} × *H/d*, f_y × *H/d*, and f_y × ρ_{sl} interactions had significant positive effect on the yielding displacement. In contrast, concrete compressive strength and its interaction with the aspect ratio had a negative effect on the yielding displacement. As presented in Table 4.4, the crushing displacement was affected by all factors. Moreover, the interactions of effects of interactions of f_c' × f_y, f_c'× *H/d*, f_c' × *n*, f_y × *H/d*, and *H/d* × *n* significantly influence the crushing displacement, as listed in Table 4.4.

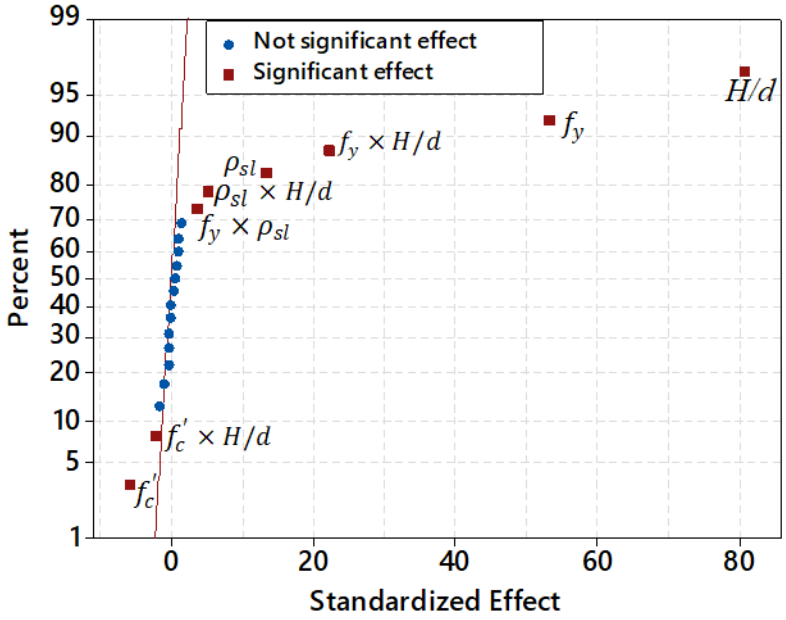

Figure 4.13: Normal plot of the standardized effects for the design parameters for yielding displacement, $\alpha = 0.05$.

Table 4.4. Effect of key design parameters on lateral displacement at different limit states based on ANOVA

S.N.	Design parameters		*P*-values at different limit states		
			Yielding	Crushing	Buckling
Main parameters effect					
1	f_c'	Concrete compressive strength	**< 0.0001**	**< 0.0001**	**< 0.0001**
2	f_y	Yield strength of steel	**< 0.0001**	**< 0.0001**	**< 0.0001**
3	ρ_{sl}	Longitudinal reinforcement ratio	**< 0.0001**	**0.0001**	**< 0.0001**
4	S_{st}	Tie spacing	0.8648	**0.0041**	**< 0.0001**
5	*H/d*	Aspect ratio	**< 0.0001**	**< 0.0001**	**< 0.0001**
6	*n*	SRP layers number	0.8548	**< 0.0001**	**0.0032**
Two-way interaction					
7	$f_c' \times f_y$		0.4029	**0.0084**	0.5155
8	$f_c' \times \rho_{sl}$		0.9166	0.5203	0.2279
9	$f_c' \times S_{st}$		0.9542	0.2494	0.4654
10	$f_c' \times H/d$		**0.023**	**0.002**	**0.0241**
11	$f_c' \times n$		0.8572	**0.0106**	0.2235
12	$f_y \times \rho_{sl}$		**0.0051**	0.1824	**0.0197**
13	$f_y \times S_{st}$		0.8831	0.0755	**0.0106**
14	$f_y \times H/d$		**< 0.0001**	**0.0003**	**0.0001**
15	$f_y \times n$		0.9505	0.1282	0.5561
16	$\rho_{sl} \times S_{st}$		0.5557	0.5725	0.1706
17	$\rho_{sl} \times H/d$		**0.0013**	0.9354	0.0523
18	$\rho_{sl} \times n$		0.8382	0.4778	0.2045
19	$S_{st} \times H/d$		0.7952	0.8933	0.3295
20	$S_{st} \times n$		0.8766	0.4137	0.2671
21	$H/d \times n$		0.6283	**0.0005**	0.082

ANOVA analysis also suggests that the effects of all factors on the buckling displacement were significant, as can be observed from the *P*-values in Table 4.4. Moreover, the $f_c' \times H/d$ interaction and interactions of yield strength of steel with ρ_{sl}, S_{st}, and the aspect ratio significantly influenced the displacement at the initiation of longitudinal bar buckling.

Figure 4.14a–c show contributions of the parameters to the lateral displacement at different limit states. It can be observed that the aspect ratio had the highest contribution at all limit states, which was more than 80% and 65% for the buckling and crushing

displacements, respectively. The contribution of *H/d* to the yielding displacement was 57.4%, while f_y had 35.5% contribution (Figure 4.14a). The effect of f_y on the lateral displacement was higher in the yielding limit state compared to the other limit states. In the crushing and buckling limit state, the contributions of f_c', f_y, ρ_{sl}, and S_{st} ranged from 0.21 to 13.1% (Figure 4.14b and c). The number of SRP layers had the least significant effect on the buckling displacement. The range of displacement was broader with increasing *H/d* ratio (Figure 4.15a–c).

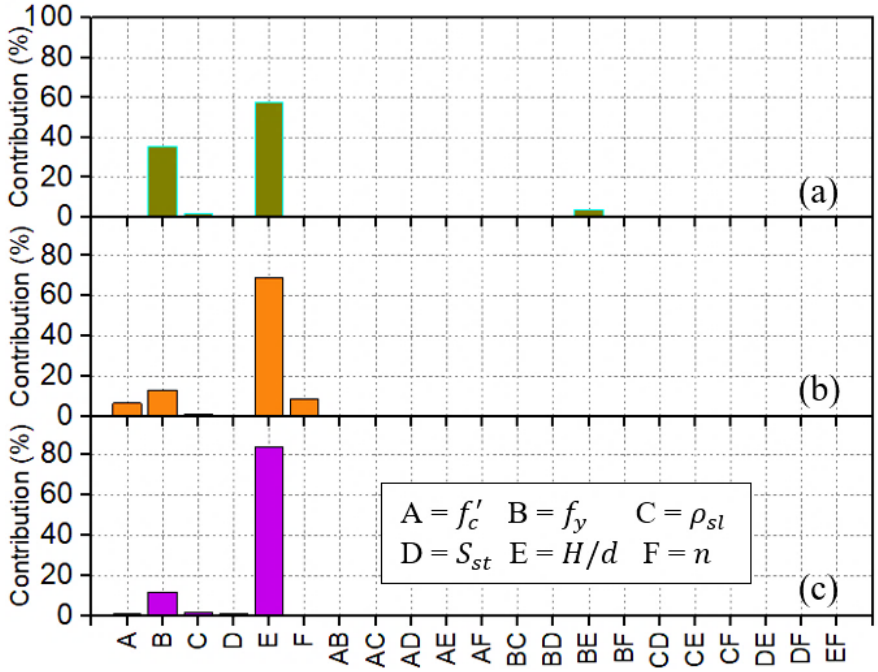

Figure 4.14: Percentage contribution of each parameter to (a) yielding, (b) crushing, and (c) buckling displacements.

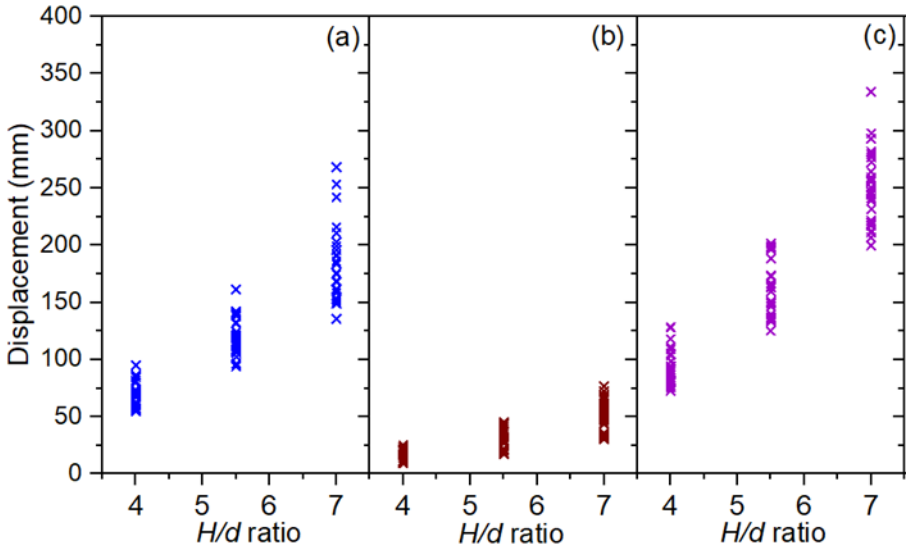

Figure 4.15: Variation of lateral displacement with *H/d* for (a) yielding, (b) crushing, and (c) buckling limit states, $\alpha = 0.05$.

4.4.3. Factorial design of displacement ductility factor

The displacement ductility factor (μ_δ) is a vital performance indicator in performance-based seismic design. The displacement ductility factor can be defined as the ratio of the concrete core crushing displacement (δ_{cc}) to the yielding displacement (δ_y) [49].

$$\mu_\delta = \frac{\delta_{cc}}{\delta_y} \tag{4.10}$$

Figure 4.16 shows the range of displacement ductility factors for different *H/d* ratios. It can be observed that the range of ductility factor was less for piers with the highest *H/d* ratio. ANOVA results in Table 4.5 suggest that the main effects of all factors significantly influenced the ductility factor. Moreover, Figure 4.17 shows the degree and direction of the effects of each factor and its possible interactions. The compressive strength of concrete and number of SRP layers had positive effects on the ductility factor, whereas

the spacing between internal transverse reinforcement, f_y, ρ_{sl}, and the aspect ratio had negative effect on the ductility factor. This is consistent with previous test results in which the ductility of the pier increased with an increase in the number of CFRP strengthening layers [58] and a reduction in the internal transverse reinforcement spacing [54,58,59]. Similarly, interactions of $f_y \times n$, $f_c' \times f_y$, and $f_c' \times \rho_{sl}$ decreased the ductility factor of the pier. However, the interaction of $f_y \times \rho_{sl}$ had a positive effect on the ductility factor (Figure 4.17). The yield strength of reinforcing rebar had the highest contribution to displacement ductility, followed by the longitudinal reinforcement ratio (Figure 4.18).

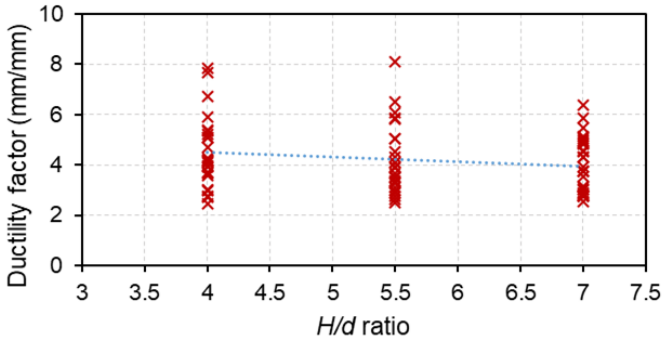

Figure 4.16: Range of displacement ductility factors for different *H/d* ratios.

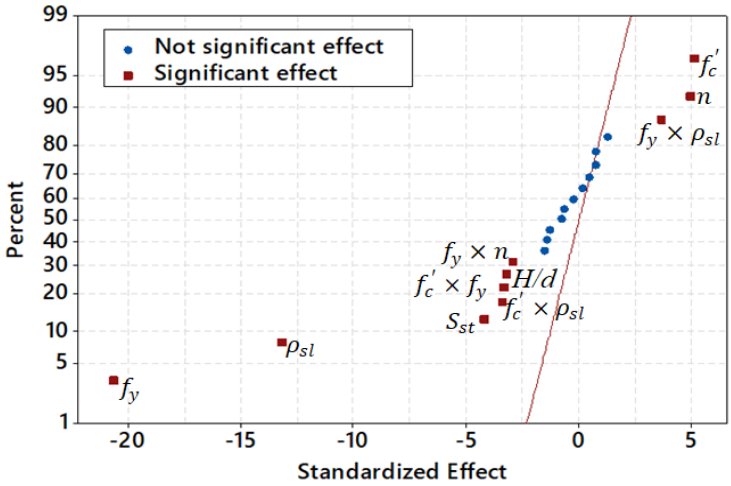

Figure 4.17: Normal plot of the standardized effects for the design parameters for displacement ductility, $\alpha = 0.05$.

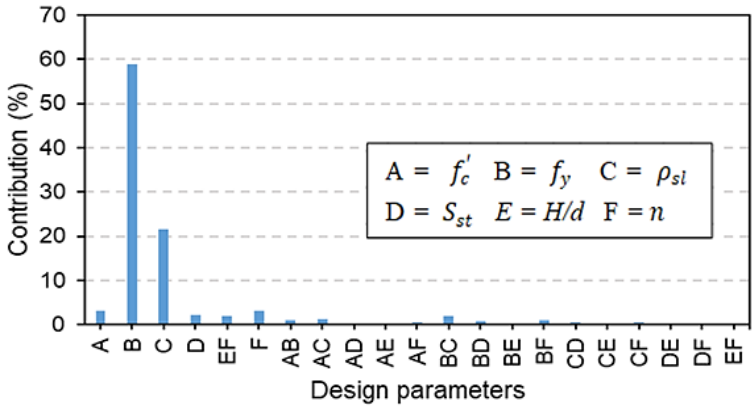

Figure 4.18: Percentage contribution of each parameter to the displacement ductility of the pier.

Table 4.5. Effect of key design parameters on the displacement ductility factor

S.N.		Design parameters	*P*-values
Main parameters effect			
1	f_c'	Concrete compressive strength	< **0.0001**
2	f_y	Yield strength of steel	< **0.0001**
3	ρ_{sl}	Longitudinal reinforcement ratio	< **0.0001**
4	S_{st}	Tie spacing	< **0.0001**
5	H/d	Aspect ratio	< **0.0001**
6	n	SRP layers number	< **0.0001**
Two-way interaction			
7	$f_c' \times f_y$		**0.0009**
8	$f_c' \times \rho_{sl}$		**0.0094**
9	$f_c' \times S_{st}$		0.2033
10	$f_c' \times$ H/d		0.2405
11	$f_c' \times$ n		0.3552
12	$f_y \times \rho_{sl}$		0.412
13	$f_y \times S_{st}$		**0.0039**
14	$f_y \times$ H/d		**0.0057**
15	$f_y \times$ n		**0.0038**
16	$\rho_{sl} \times S_{st}$		0.0797
17	$\rho_{sl} \times$ H/d		**0.0066**
18	$\rho_{sl} \times$ n		0.1425
19	$S_{st} \times$ H/d		0.194
20	$S_{st} \times$ n		**0.014**
21	H/d × n		0.9115

4.4.4. Factorial design of drift ratio

The total drift ratio is used to study the effect of the design parameters on the deformational capacity of SRP-jacketed piers. The influence of key design parameters on the total drift ratio at different limit states is listed in Table 4.6. ANOVA suggests that the effects of f_c', ρ_{sl}, f_y, and *H/d* were significant on yielding drift ratio, while the spacing of internal transverse reinforcement and number of SRP layers showed insignificant effect, as listed in Table 4.6. As shown in Figure 4.19a, the yielding drift ratio increased with an increase in ρ_{sl}, f_y, and *H/d*. Similarly, the $f_y \times H/d$, and $\rho_{sl} \times H/d$, and $f_y \times \rho_{sl}$ interactions had positive significant effect on yielding drift ratio, as shown in Figure 4.19a. However, the yielding drift ratio decreased with an increase in concrete compressive strength. The interaction of f_c' with *H/d* and f_y also had a negative effect on the yielding drift ratio, as shown in Figure 4.19a.

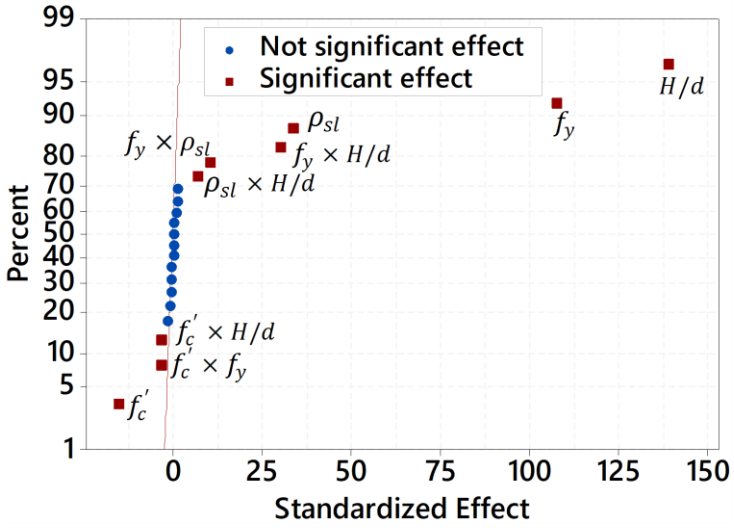

(a)

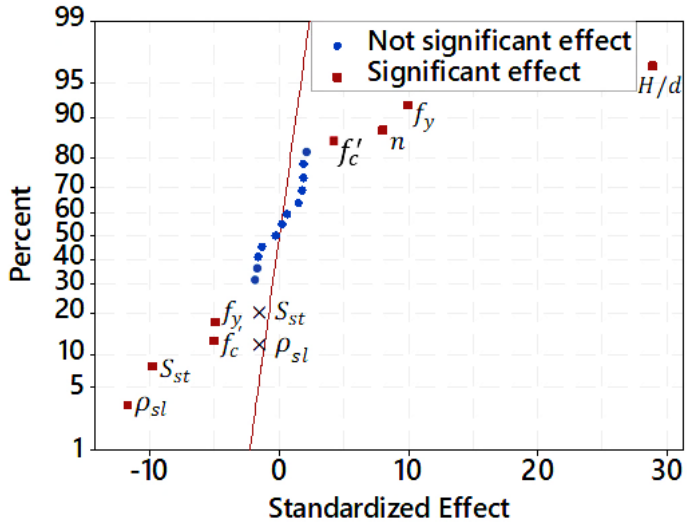

(b)

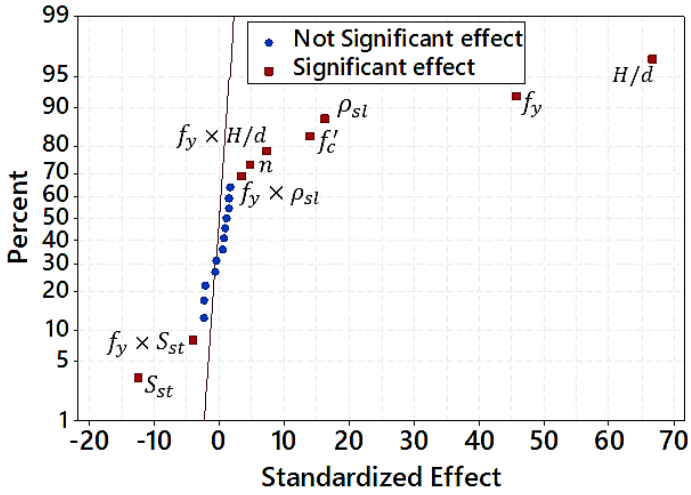

(c)

Figure 4.19: Normal plot of standardized effects for drift ratio at (a) yielding, (b) crushing, and (c) buckling limit states.

Table 4.6. Effect of key design parameters on drift ratio at different limit states based on ANOVA

S.N.	Design parameters		*P*-values at different limit states		
			Yielding	Crushing	Buckling
Main parameters effect					
1	f_c'	Concrete compressive strength	**< 0.0001**	**< 0.0001**	**< 0.0001**
2	f_y	Yield strength of steel	**< 0.0001**	**< 0.0001**	**< 0.0001**
3	ρ_{sl}	Longitudinal reinforcement ratio	**< 0.0001**	**< 0.0001**	**< 0.0001**
4	S_{st}	Tie spacing	0.5272	**< 0.0001**	**< 0.0001**
5	*H/d*	Aspect ratio	**< 0.0001**	**< 0.0001**	**< 0.0001**
6	*n*	SRP layers number	0.4619	**< 0.0001**	**0.0006**
Two-way interaction					
7	$f_c' \times f_y$		**0.034**	0.3213	0.2367
8	$f_c' \times \rho_{sl}$		0.7396	**0.0439**	0.0739
9	$f_c' \times S_{st}$		0.9872	0.62	0.2494
10	$f_c' \times H/d$		**0.0137**	0.7367	0.2075
11	$f_c' \times n$		0.8066	0.6613	0.0963
12	$f_y \times \rho_{sl}$		**0.0001**	0.6635	**0.0073**
13	$f_y \times S_{st}$		0.6151	**0.0351**	**0.0024**
14	$f_y \times H/d$		**< 0.0001**	0.5207	**0.0012**
15	$f_y \times n$		0.882	0.1694	0.5577
16	$\rho_{sl} \times S_{st}$		0.5008	0.2531	0.0856
17	$\rho_{sl} \times H/d$		**0.0007**	0.1924	0.3198
18	$\rho_{sl} \times n$		0.8415	0.2838	0.1028
19	$S_{st} \times H/d$		0.6591	0.7618	0.48
20	$S_{st} \times n$		0.69	0.5663	0.12
21	$H/d \times n$		0.2942	0.6099	0.1203

All factors had a significant effect on the crushing drift ratio (Figure 4.19b and Table 4.6). The crushing drift ratio increased with an increase in f_y, n, f_c', and *H/d*, as shown in Figure 4.19b. In contrast, the spacing between internal transverse reinforcement, ρ_{sl}, and interaction of $f_c' \times \rho_{sl}$ and $f_y \times S_{st}$ had a negative effect of the crushing drift ratio, as shown in Figure 4.19b.

ANOVA analysis also suggests that the effects of all factors on the buckling drift ratio were significant (Table 4.6). As shown in Figure 4.19c, the buckling drift ratio increased with an increase in *H/d*, f_y, ρ_{sl}, f_c', and number of SRP layers. Similarly, the

interactions of f_y × *H/d* and f_y × ρ_{sl} showed a positive significant effect (Figure 4.19c). However, the spacing between internal transverse reinforcement and its interaction with f_y had a negative effect on buckling drift ratio (Figure 4.19c). As shown in Figure 4.19c, the aspect ratio had the highest effect on the drift ratio at all limit states.

4.5. Conclusions

This study explores the behavior of seismically deficient rectangular section RC bridge piers retrofitted with external steel-reinforced polymer composites. The seismic performance of the piers was numerically investigated. A six-factor, three-level fractional factorial design of experiments at 95% confidence was used to perform a parametric study to investigate the main effects and possible interactions on the seismic performance of the SRP-confined rectangular section piers. The main finds of this study are summarized below.

- The effects of longitudinal reinforcement ratio, yield strength of steel, concrete compressive strength, and aspect ratio on the yielding base shear were found to be highly significant. However, the effects of spacing of internal transverse reinforcement and number of SRP layers on the yielding base shear were found insignificant.
- The results of the factorial analysis showed that only three of the factor interactions, namely f_y × ρ_{sl}, *H/d* × f_y, and *H/d* × ρ_{sl} had significant effect on the base shear.
- The effect of the spacing of internal transverse reinforcement on the crushing base shear was significant. However, it had no significant influence on the base shear at the onset of longitudinal bar yielding and buckling.
- The parametric study showed that the ductility of the pier was enhanced with increased f_c' and higher number of SRP layers, whereas the spacing between

internal transverse reinforcement, *H/d* ratio, f_y, and ρ_{sl} had a negative effect on the ductility factor.

- The interactions of $f_y \times n$, $f_c' \times f_y$, and $f_c' \times \rho_{sl}$ decreased the ductility factor of the pier, while the interaction of $f_y \times \rho_{sl}$ increased the ductility.
- The pier aspect ratio had the highest contribution to the base shear under all limit states. Moreover, the range of variation in base shear with the change in the value of the design parameters was higher in piers with a lower *H/d* ratio.
- The lateral displacement at all limit states was mostly affected by the aspect ratio of the pier, whereby bridge piers with a higher *H/d* ratio showed wider scatter of displacement compared to those with a lower *H/d* ratio.
- The aspect ratio of the pier showed the highest positive effect on the total drift ratio followed by f_y at all limit states. The interactions of $f_y \times$ *H/d* and $f_y \times \rho_{sl}$ showed a positive significant effect on the total drift ratio at the onset of longitudinal bar yielding and buckling.

The crushing and buckling drift ratio increased with an increase in the number of SRP layers, but it decreased with an increase in the spacing between internal transverse reinforcement.

CHAPTER 5: PLASTIC HINGE LENGTH OF RECTANGULAR RC COLUMNS USING ENSEMBLE MACHINE LEARNING MODEL

This chapter is based on the following study:

Wakjira TG, Alam MS, Ebead U. Plastic hinge length of rectangular RC columns using ensemble machine learning model. *Engineering Structures* 2021;244:112808. https://doi.org/10.1016/j.engstruct.2021.112808.

5.1. Introduction

During extreme loads such as seismic events, RC columns experience significant plastic deformation [50]. These plastic deformations are localized in the small regions with high moment demand at column ends, commonly known as the plastic hinge zones [66]. The seismic response of critical members is thus highly dependent on its deformation capacity in the plastic hinge zone [66] where the extent of the damage is defined by the plastic hinge length (PHL). The plastic hinge length of RC columns is dependent on various factors including concrete strength [67,68], axial load level [69–72], longitudinal reinforcement ratio [68,73,74], yield strength of reinforcement bars [75], confinement level [68,71,76–78], and aspect ratio [71,73,79]. However, due to several factors including the nonlinearity of material response, strain penetration, and interaction of independent variables, determining the plastic hinge length accurately is still remaining a challenge [80].

In the past decades, several empirical models have been proposed to estimate the PHL of RC members. However, there exists a large scatter and uncertainty in the estimation of the PHL. One of the causes for the discrepancy in the existing models is related to the selection of the significant parameters determining the PHL. There is a lack of consensus on the importance of various factors in determining the PHL. Sheikh

and Khoury [81] proposed a simple equation for determining the PHL of RC columns subjected to high axial loads as a function of the cross-sectional depth, ignoring all other factors. Mendis [73] and Park et al. [82] reported that the PHL is insensitive to the axial load level. In contrast, other researchers (e.g. [69,70]) reported an increase in the PHL with an increase in the axial load level. According to Bae and Bayrak [71], the PHL increases with an increase in the axial load level for axial load levels greater than or equal to 0.20; however, it is constant as 0.25 times the section depth ($0.25h$) for low axial load level, less than 0.20. Babazadeh et al. [83] investigated the effect of slenderness on the PHL based on experimental results of three large-scale RC slender bridge piers with aspect ratios up to 12. They reported that the existing models and design guides underestimate the PHL of slender columns. Ho [68] introduced the effect of transverse reinforcement ratio on the PHL, in addition to the axial load ratio, compressive strength of concrete, reinforcement ratio and yield strength of longitudinal bars, and cross-sectional depth of the member.

In addition to the contradictory reports on the significant effect of different factors on the PHL, the existing models are mainly derived empirically based on limited experimental results, which often limits the accuracy of the models [84]. Thus, the use of an alternative and more powerful modelling approach should be considered. Accordingly, this study leveraged the capacity of ensemble learners by combining the performance of various base learners in an attempt to propose an accurate and reliable model for predicting the PHL of rectangular RC columns. Furthermore, this study used the SHAP approach to interpret the predictions of the ML model, rank the input factors in their importance, and identify the most important factors and interactions on the prediction of the PHL of RC columns for the first time. In addition, the proposed ML-based model is compared with twelve existing models and guideline equations and

provided higher accuracy in predicting the PHL.

5.2. Overview of Existing Formulations and Design Codes

The plastic hinge deformation involves a complex mechanism and various uncertainties [275]. The most commonly used formulations for the PHL are presented in Table 5.1 and discussed in this section. Sheikh and Khoury [81] proposed a simple equation for determining the PHL of RC columns subjected to high axial loads as a function of the cross-sectional depth, ignoring all other factors, as given in Eq. (5.1). In most of the other formulations [50,67,75,79,275–277], the PHL has the following form, as listed in Table 5.1:

$$L_p = k_1 L + k_2 d_b \tag{5.1}$$

where L is the shear span, d_b is the diameter of the longitudinal bars, and k_1 and k_2 are the model coefficients.

In the above expression for the PHL, the first term accounts for the bending along the length of the column, while the second term reflects additional fixed-end rotation and deflection due to tensile strain-penetration of longitudinal reinforcement into the joint or footing.

Table 5.1. Existing expressions for plastic hinge length of ordinary RC members

S.N.	Reference	Plastic hinge length, L_p	Eq.
1	Sheikh and Khoury [81]	$L_p = 1.0h$	(5.2)
2	Priestley and Park [79]	$L_p = 0.08L + 6d_b$	(5.3)
3	Paulay and Priestley [75]	$L_p = 0.08L + 0.022f_y d_b$	(5.4)
4	Priestley et al. [50]	$L_p = 0.08L + 0.022f_y d_b \leq 0.044f_y d_b$	(5.5)
5	Panagiotakos and Fardis [276]	$L_p = 0.12L + 0.014a_{sl}f_y d_b$	(5.6)
6	Lu et al. [275]	$L_p = 0.077L + 8.16d_b$	(5.7)
7	Berry and Eberhard [67]	$L_p = 0.05L + 0.1d_b \frac{f_y}{\sqrt{f_c'}}\ (mm, MPa) \leq 0.25L$	(5.8)
8	EN 1998-3 (2005) EC8 [277]	$L_p = \frac{L}{30} + 0.2h + 0.11d_b \frac{f_y}{\sqrt{f_c'}}\ (mm, MPa)$	(5.9)
9	Bae and Bayrak [71]	$L_p = \left(0.3\frac{P}{P_0} + 3\rho_s - 0.1\right)L + 0.25h \geq 0.25h$ where $P_0 = 0.85f_c'(A_g - A_s) + A_s f_y$ and $\rho_s = A_s/A_g$	(5.10)
10	Ning and Li [80]	$L_p = \left(0.042 + 0.072\frac{P}{P_0}\right)L + 0.298h + 6.407d_b$	(5.11)
11	Ho [68]	$L_p = \left(20\sqrt{P/P_0}\left(\frac{f_c'}{f_y}\right)^{1.5}\left(\frac{\rho_s}{\rho_{st}}\right)^{0.5} + 0.6\right)h$	(5.12)
12	Biskinis and Fardis [278]	$L_p = 0.2h\left(1 + \frac{1}{3}minimum\left(9, \frac{L}{h}\right)\right)$	(5.13)

Priestley and Park [79] proposed an expression for the PHL in which the values of k_1 and k_2 are 0.08 and 6, respectively, as given in Eq. (5.2). Paulay and Priestley [75] incorporated the effect of yield strength of the longitudinal bars (f_y) on the deflection due to strain penetration, in which $k_2 = 0.022f_y$, as given by Eq. (5.3). In addition, they reported that the PHL of a typical column can be taken as half of its section depth, $L_p = 0.5h$. Priestley et al. [50] suggested an upper limit for the PHL proposed by Paulay and Priestley [75], as given in Eq. (5.4). Panagiotakos and Fardis [276] proposed a new expression for the PHL for RC columns subjected to cyclic loads in which $k_1 = 0.12$ and $k_2 = 0.014a_{sl}$, where constant a_{sl} represents the fixed-end rotation due to slippage of longitudinal bars, Eq. (5.5). The value of a_{sl} is unity if the slippage of longitudinal reinforcement bars from its anchorage zone is possible and zero otherwise [276], as listed in Table 5.1. Lu et al. [275] proposed a modified version of the Priestley and Park [79] model for the PHL based on a survey on large experimental data of RC columns and regression analysis. According to Lu et al. [275], the modified values of k_1 and k_2 are 0.077 and 8.16, respectively, as given in Eq. (5.6). In Eq. (5.7), Berry and Eberhard [67] incorporated the effect of the concrete strength (f_c') on the deformation caused by tensile-strain penetration in which $k_1 = 0.05$ and $k_2 = 0.1f_y/\sqrt{f_c'}$. Moreover, Berry and Eberhard [67] provided an upper limit for the PHL, $L_p \leq 0.25L$, as listed in Table 5.1.

In Eurocode 8 [277], a term is added to the expression for PHL given in Eq. (5.1), to account for the effect of cross-sectional depth for seismic resistant members without longitudinal bars lapping in the plastic hinge region, as given in Eq. (5.8). Bae and Bayrak [71] studied the effect of axial load level (P/P_0) and longitudinal reinforcement ratio on PHL and proposed a new expression for PHL as a function of

P/P_0, reinforcement ratio of longitudinal bars, shear span, and cross-sectional depth of the column, as given in Eq. (5.9). Ning and Li [80] used a probabilistic approach to estimate the PHL of RC columns and suggested a new expression for PHL in terms of axial load level, shear span, cross-sectional depth, and diameter of longitudinal bars, as given in Eq. (5.11). Ho [68] introduced the effect of transverse reinforcement on the PHL, as given in Eq. (5.12). In the equation proposed by Biskinis and Fardis [278], the PHL is given as a function of the cross-sectional depth and aspect ratio only, as given by Eq. (5.13) in Table 5.1. This model has been adopted in the fib Model Code [279].

5.3. Data Preprocessing

For this study, the experimental database of RC columns (a total of 133 RC columns) was obtained from [80]. Twelve (12) variables that characterize the geometry of the column, aspect ratio, mechanical properties of concrete and internal steel reinforcements, diameter of longitudinal bars, and axial load level are considered as input parameters, as listed in Table 5.2 along with their descriptive statistics. These variables include cross-sectional width (b) and depth (h) of the column, shear span (L), aspect ratio (L/h), compressive strength of concrete (f_c'), diameter of longitudinal bars (d_b), reinforcement ratio (ρ_s) and yield strength (f_y) of longitudinal bars, spacing (S_{st}) and yield strength of transverse reinforcement bars (f_{st}), reinforcement ratio of transverse bars (ρ_{st}), and axial load ratio (P/P_0). The range of each parameter can be clearly observed in Table 5.2. For instance, f_c', f_y, d_b, and aspect ratio were in the range of 24.8–175 MPa, 339–572 MPa, 8–32 mm, and 1.8–10.71, respectively. In addition, Figure 5.1 shows the relationship between the independent variables and the experimental plastic hinge length ($L_{p,exp}$) of the RC columns included in the database.

Table 5.2. Description of input and output variables in the experimental database of RC columns and their distribution

Parameter			Unit	μ	σ	Min	Q1	Q2	Q3	Max
Input parameters	b	Cross-sectional width	mm	274	107	150	150	300	305	610
	h	Cross-sectional depth	mm	288	107	140	200	305	350	610
	L	Shear span	mm	1713	408	630	1500	1800	2010	3050
	L/h	Aspect ratio	–	6.70	2.49	1.8	5.74	6.56	7.50	10.71
	f_c'	Concrete compressive strength	MPa	70.3	30.9	24.8	41.0	72.6	91.3	175
	d_b	Longitudinal bar diameter	mm	16.8	5.07	8.00	12.00	19.0	20.0	32.0
	ρ_s	Longitudinal reinforcement ratio	%	2.31	0.91	0.82	2.06	2.3	2.74	6.1
	f_y	Yield strength of longitudinal bars	MPa	498	44.7	339	469	508	537	572
	S_{st}	Spacing of transverse bars	mm	93.6	28.9	50.0	75	100	100	220
	ρ_{st}	Transverse reinforcement ratio	%	2.11	1.26	0.32	1.00	1.90	3.00	6.72
	f_{st}	Yield strength of transverse bars	MPa	531	159	325	463	530	531	952
	P/P_0	Axial load ratio	–	0.35	0.19	0.00	0.20	0.35	0.50	0.77
Output parameter	L_p	Plastic hinge length	mm	307	123	70.0	248	299	381	741

μ: mean; σ: standard deviation; Min: minimum; Max: maximum; and Q1, Q2, Q3: 25^{th}, 50^{th}, and 75^{th} percentiles

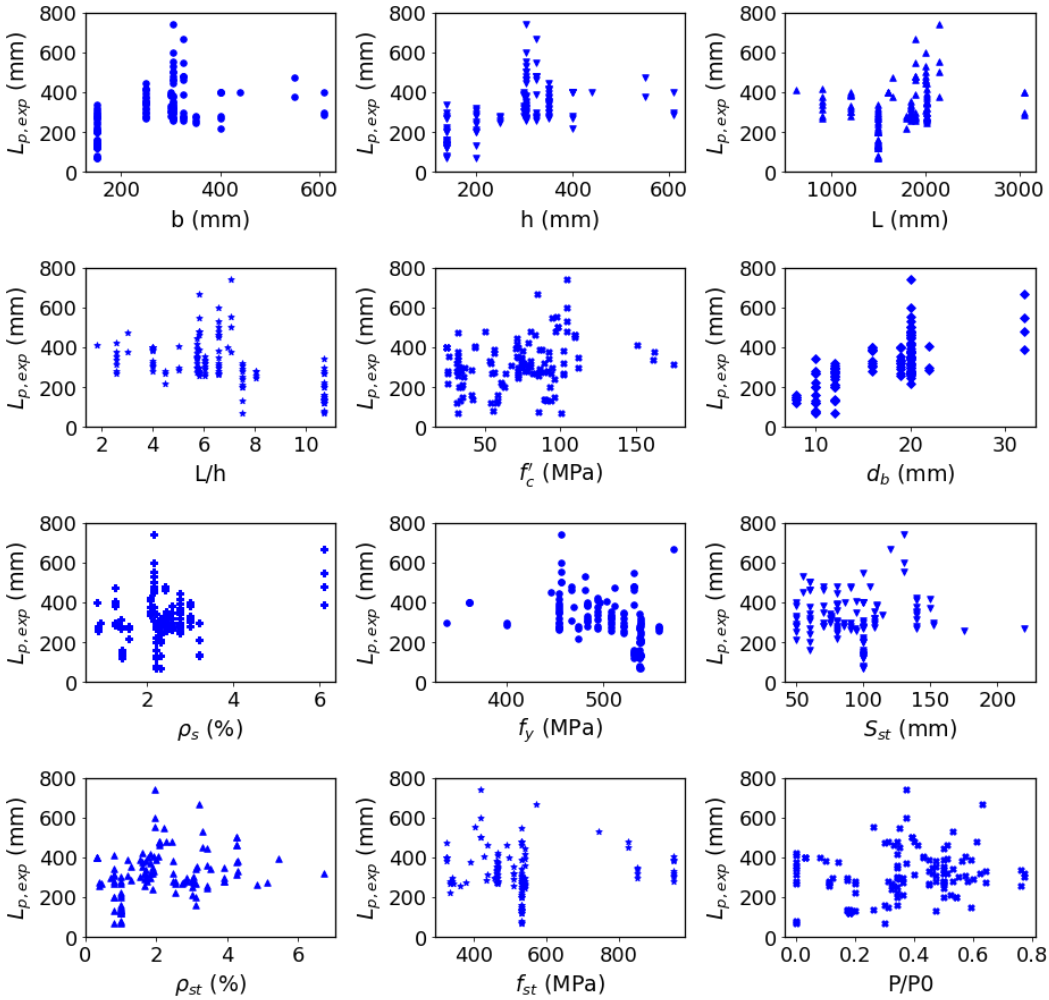

Figure 5.1: Variation of the PHL with the input parameters.

5.4. ML models

In addition to the ML Models discussed in Section 3.2, stacking ensemble is used in this study. Stacking (also known as stacked generalization) is another technique of ensemble learners, which combines multiple base learners (often heterogeneous learners) via a meta-model and combines the result of all base learners to produce the final prediction with better accuracy than the single model [280,281]. According to Wolpert [280], stacking can be considered as a more sophisticated version of cross-validation. It has been successfully implemented for regression problems [282].

Stacking ensemble model can also be used to compare and select the best models among the base learners. Here, the base learners are trained in parallel based on the complete training dataset. The cross-validated predictions (10-fold cross-validated prediction of the base model, in this study) returned by the base models are then combined by training a meta-model based on the outputs of individual base learner features. In this context, stacking requires two things; namely, multiple base learners and a meta-model that combines the base learners. In this study, the three best models are stacked using linear SVR as a meta-model to improve the predictions obtained from the models, as shown in Figure 5.2.

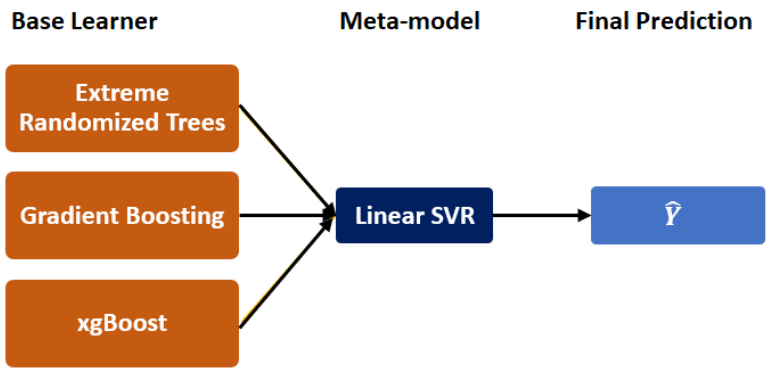

Figure 5.2: Structure of a stacking ensemble learner used in this study.

5.5. Model Performance

In this study, the following four performance indices are considered; namely, RMSE, MAE, Nash-Sutcliffe model efficiency coefficient (NSE), and index of agreement (*d*) [283]. The NSE and index of agreement are presented mathematically by Eq. (5.14) and Eq. (5.15), respectively.

$$NSE = 1 - \frac{\sum_{i=1}^{n}(y_i - \hat{y}_i)^2}{\sum_{i=1}^{n}(y_i - \bar{y})^2}, \qquad -\infty < NSE \leq 1 \tag{5.14}$$

$$d = 1 - \frac{\sum_{i=1}^{n}(y_i - \hat{y}_i)^2}{\sum_{i=1}^{n}(|y_i - \bar{y}| + |\hat{y}_i - \bar{y}|)^2}, \qquad 0 < d \leq 1 \tag{5.15}$$

where y and $\hat{y}$ are the target values and the corresponding predictions, respectively and $\bar{y}$ is the average of y values.

The Nash-Sutcliffe model efficiency coefficient represents the goodness-of-fitness of the model, where $NSE = 1$ represents a perfect agreement between the predicted and observed values. Similarly, the value of the index of agreement ranges between 0 and 1, with 0 and 1 representing no correlation and perfect fitness, respectively.

5.6. Results and Discussion

5.5.1. Evaluation of existing models

Firstly, the predictions of the PHL using the existing equations (discussed in Section 5.2) are investigated. The prediction capability of the existing models is summarized in Table 5.3 in terms of the statistical distribution for the predicted ($L_{p,pre}$) to experimental ($L_{p,exp}$) PHL. Moreover, the factors considered in each model are included in the same table. Large discrepancies in the significant parameters considered in the existing models can be observed in this table. In addition, the relationships between the predicted and experimental PHL are shown in Figure 5.3a–l. In this figure, the solid equity lines represent a perfect match between the predicted and experimental PHL. As can be seen in Figure 5.3a–l and Table 5.3, the existing models are unable to capture the actual or observed PHL. The models proposed by Panagiotakos and Fardis [276] and Biskinis and Fardis [278] showed the least standard deviation for the $L_{p,pre}/L_{p,exp}$ ratio, as listed in Table 5.3. However, both models have significantly

underestimated the experimentally observed PHL, as shown in Figure 5.3a–l. Even at the third quartile, the average of $L_{p,pre}/L_{p,exp}$ was only 0.47 for the Panagiotakos and Fardis [276] model, as listed in Table 5.3. Similarly, the predictions of the PHL based on the Priestley and Park [79] and Berry and Eberhard [67] models are significantly underestimated, as shown in Figure 5.3b and g, respectively. Conversely, most of the predictions by the Ho [68] model are overestimated compared to the experimental PHL, as can be seen in Figure 5.3k and Table 5.3. Although the Lu et al. [275] model resulted in the average $L_{p,pre}/L_{p,exp}$ close to one, as listed in Table 5.3, its accuracy was greatly hindered by a large standard deviation value for the $L_{p,pre}/L_{p,exp}$ ratio.

Table 5.3. Predicted to experimental PHL of RC column ($L_{p,pre}/L_{p,exp}$) based on existing models

S.N.	Reference	Design parameters											Statistical parameter on $L_{p,pre}/L_{p,exp}$						
		b	h	L	L/h	f_c'	d_b	ρ_s	f_y	S_{st}	ρ_{st}	f_{st}	P/P_0	μ	σ	Min	Q1	Q2	Q3	Max
1	Sheikh and Khoury [81]		x											0.99	0.36	0.41	0.77	0.97	1.11	2.86
2	Priestley and Park [79]			x			x							0.87	0.40	0.39	0.61	0.80	0.99	2.74
3	Paulay and Priestley [75]			x			x		x					1.17	0.52	0.50	0.83	1.07	1.32	3.74
4	Priestley et al. [50]			x			x		x					1.15	0.51	0.50	0.83	1.06	1.31	3.74
5	Panagiotakos and Fardis [276]			x			x		x					0.42	0.17	0.17	0.31	0.39	0.47	1.30
6	Lu et al. [275]			x			x							0.98	0.43	0.44	0.70	0.89	1.13	3.05
7	Berry and Eberhard [67]			x		x	x		x					0.71	0.34	0.27	0.48	0.64	0.82	2.42
8	EN 1998-3 (2005) EC8 [277]		x	x		x	x		x					0.83	0.36	0.31	0.58	0.78	0.98	2.60
9	Bae and Bayrak [71]		x	x				x					x	0.73	0.37	0.21	0.46	0.69	0.91	1.98
20	Ning and Li [80]		x	x			x						x	1.10	0.39	0.49	0.80	1.01	1.27	3.31
11	Ho [68]		x		x	x	x		x		x		x	1.19	0.61	0.48	0.88	1.10	1.35	5.99
12	Biskinis and Fardis [278]		x	x										0.61	0.26	0.27	0.43	0.56	0.71	2.00

μ: mean; σ: standard deviation; Min: minimum; Max: maximum; and Q1, Q2, Q3: 25^{th}, 50^{th}, and 75^{th} percentiles

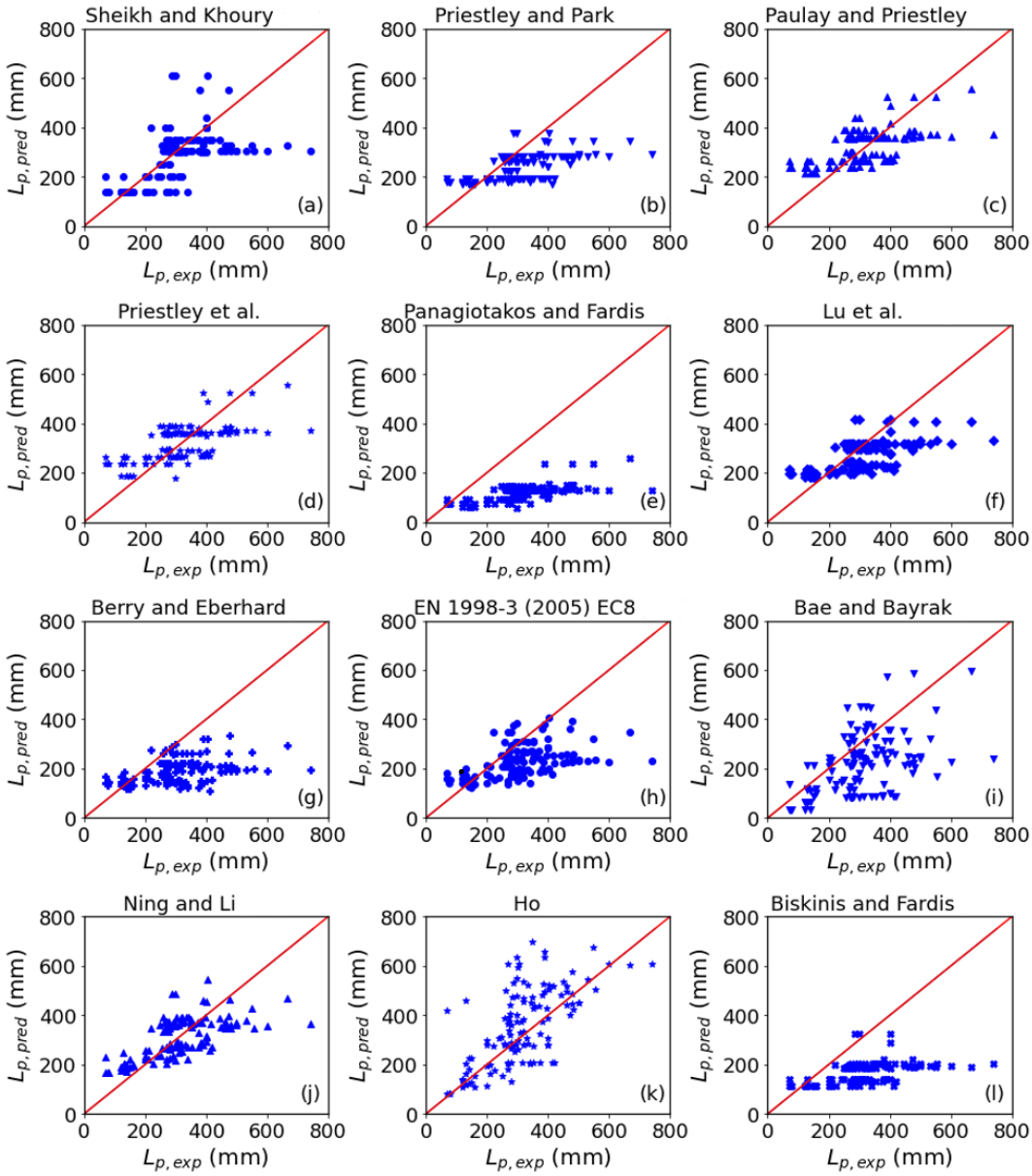

Figure 5.3: Experimental versus predicted PHL based on existing models.

Table 5.4 summarizes the statistical performance indicators for the existing models. In addition, Figure 5.4a and b compare the predictions of the existing models in terms of MAE, RMSE, NSE coefficient, and *d*. Among the existing models, Ning and Li [80] model provided the least RMSE and MAE, followed by Priestley et al. [50] model for the RMSE, as shown in Figure 5.4a and Table 5.4. Ho [68] showed the highest

agreement index of 0.77, as shown in Figure 5.4b and Table 5.4. However, it has a lower NSE coefficient compared to many of the existing models. Ning and Li [80] showed better performance accuracy in terms of both NSE coefficient (NSE = 0.42) and agreement index (d = 0.76), as shown in Figure 5.4b and Table 5.4. Thus, it is observed that Ning and Li [80] outperformed the other models in predicting the PHL, as can be seen in Figure 5.4a, Figure 5.4b, and Table 5.4. Priestley et al. [50] model provided the second best performance among the existing models, as can be observed in Figure 5.4a, Figure 5.4b, and Table 5.4. The predictions of the existing models are compared with that of the proposed ensemble model in the following section.

Table 5.4. Performance measures for existing models

S.N.	Reference	Model performance indices			
		MAE	RMSE	NSE	d
1	Sheikh and Khoury [81]	77.15	114.2	0.16	0.71
2	Priestley and Park [79]	94.73	122.5	-0.07	0.59
3	Paulay and Priestley [75]	80.80	97.83	0.37	0.72
4	Priestley et al. [50]	79.30	96.52	0.39	0.74
5	Panagiotakos and Fardis [276]	190.1	216.6	-2.34	0.46
6	Lu et al. [275]	81.11	104.1	0.24	0.66
7	Berry and Eberhard [67]	128.3	161.5	-0.86	0.51
8	EN 1998-3 (2005) EC8 [277]	101.6	133.6	-0.25	0.59
9	Bae and Bayrak [71]	123.1	156.4	-0.71	0.62
20	Ning and Li [80]	74.89	93.56	0.42	0.76
11	Ho [68]	93.65	124.9	-0.08	0.77
12	Biskinis and Fardis [278]	143.6	174.9	-1.20	0.51

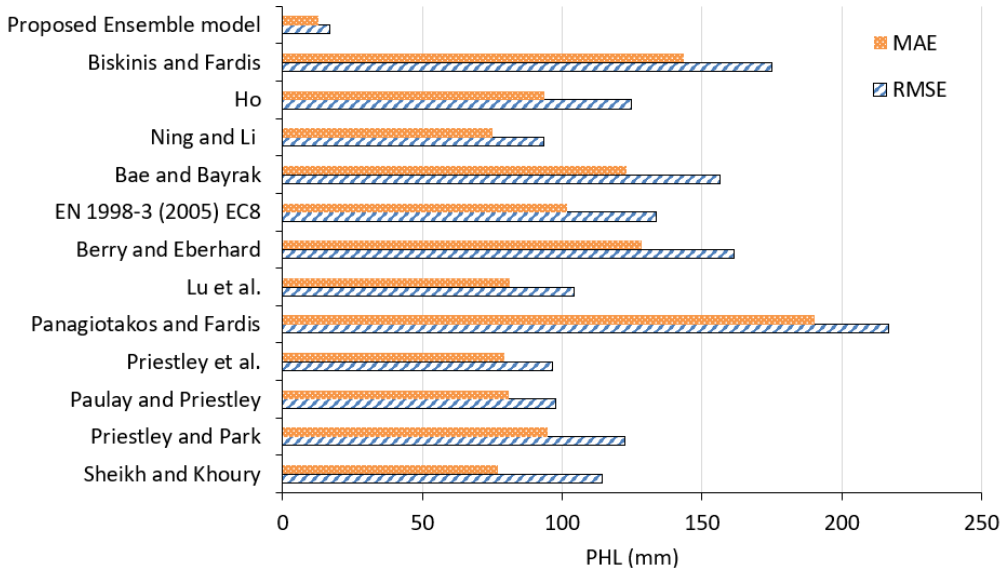

(a) MAE and RMSE

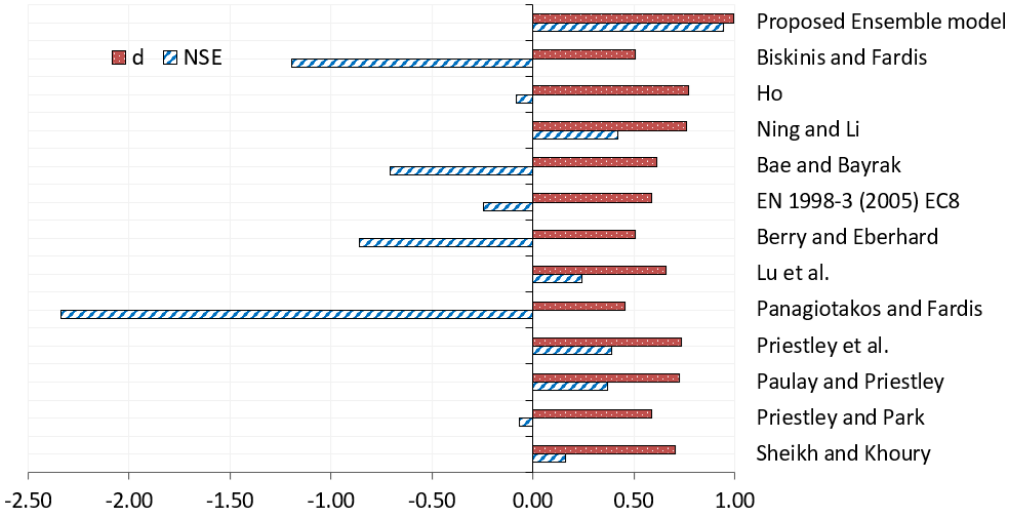

(b) NSE cefficient and *d*

Figure 5.4: Comparison of proposed and existing models.

5.5.2. Predictions of the proposed model

The input and output vectors in the database are randomly split into the training dataset and test dataset, which contains 80% and 20% of the database, respectively. The hyperparameters for each model are optimized and validated through grid search with 10-fold cross-validation using scikit package in python [284], as discussed in Section

3.3, and the result is presented in Table 5.5. The predictions of the SVR, RFR, ETR, GBR, and xGBoost are compared with the experimental results in Figure 5.5a–e. In these figures, the solid line represents a perfect match between the predicted and actual value of the PHL, while the hidden lines represent 20% underestimation/overestimation of the PHL. Moreover, Table 5.6 lists the performance of the models in terms of the RMSE and MAE for both the training and test datasets. It can be observed that the xgBoost model provided the best predictions for PHL compared to other models, as shown in Figure 5.5a–e and Table 5.6. Support vector regression showed the least performance with the highest RMSE and MAE of 64.79 mm and 41.27 mm, respectively, for the training dataset and 64.39 and 48.47, respectively, for the test dataset, as listed in Table 5.6. The three best models; namely, xgBoost, GBR, and ETR are stacked via a linear SVR meta-model to obtain better accuracy.

Table 5.5. Hyperparameters for each model

Model	Tuned hyperparameters
SVR	Kernel = ‘rbf’, C = 35, ε = 0.00005, γ = 'auto'
RFR	Number of estimators = 10, minimum sample split = 3, minimum sample leaf = 1, maximum depth = 7, maximum features = 6
ETR	Number of estimators = 15, maximum depth = 8, minimum sample split = 2, minimum sample leaf = 1, maximum features = 5
GBR	Number of estimators = 170, maximum depth = 4, learning rate = 0.085 subsample = 0.3, minimum sample split = 2, minimum sample leaf = 1, maximum features = 7
xgBoost	Number of estimators = 436, maximum depth = 5, learning rate = 0.057, reg alpha = 0, reg lambda = 1, γ = 0, colsample by level = 0.9, colsample by node = 0.9, colsample by tree = 1, booster = 'gbtree', subsample = 0.3

Table 5.6. Performance measures for different ML models

Model	Train dataset		Testing dataset	
	RMSE	MAE	RMSE	MAE
SVM	64.79	41.27	64.39	48.47
RFR	33.06	26.14	37.50	32.48
ETR	18.48	13.28	32.97	26.91
GBR	14.95	12.16	30.82	25.76
xgBoost	8.69	6.25	29.39	23.35
Stacking Ensemble	13.94	10.98	24.95	19.21

Figure 5.6 shows the scatterplot for experimental versus predicted PHL based on the stacking ensemble model. It can be observed that the proposed stacking ensemble model accurately predicted the PHL with a high coefficient of determination (R^2) value of 0.98, as shown in Figure 5.6. Moreover, as listed in Table 5.6, the stacking ensemble model showed the least RMSE and MAE for the test dataset compared to all other models. To show the accuracy of the proposed stacking ensemble model, the obtained PHL predictions were compared with those predicted by the existing models discussed in Section 5.2. Figure 5.7 compares the predictions for the PHL based on the proposed and existing models. As can be seen in this figure, the proposed stacking ensemble model was superior to all existing models in predicting the PHL. Moreover, Figure 5.8a–m show the distribution of the predicted to experimental PHL ratio based on the proposed and existing models. The proposed stacking ensemble model provided the most stable, safe, and accurate predictions, as shown in Figure 5.8a–m. It can also be observed in Figure 5.4a and b that the proposed model resulted in superior predictive performance with the least RMSE and MAE and highest agreement index and NSE coefficient compared to all other models.

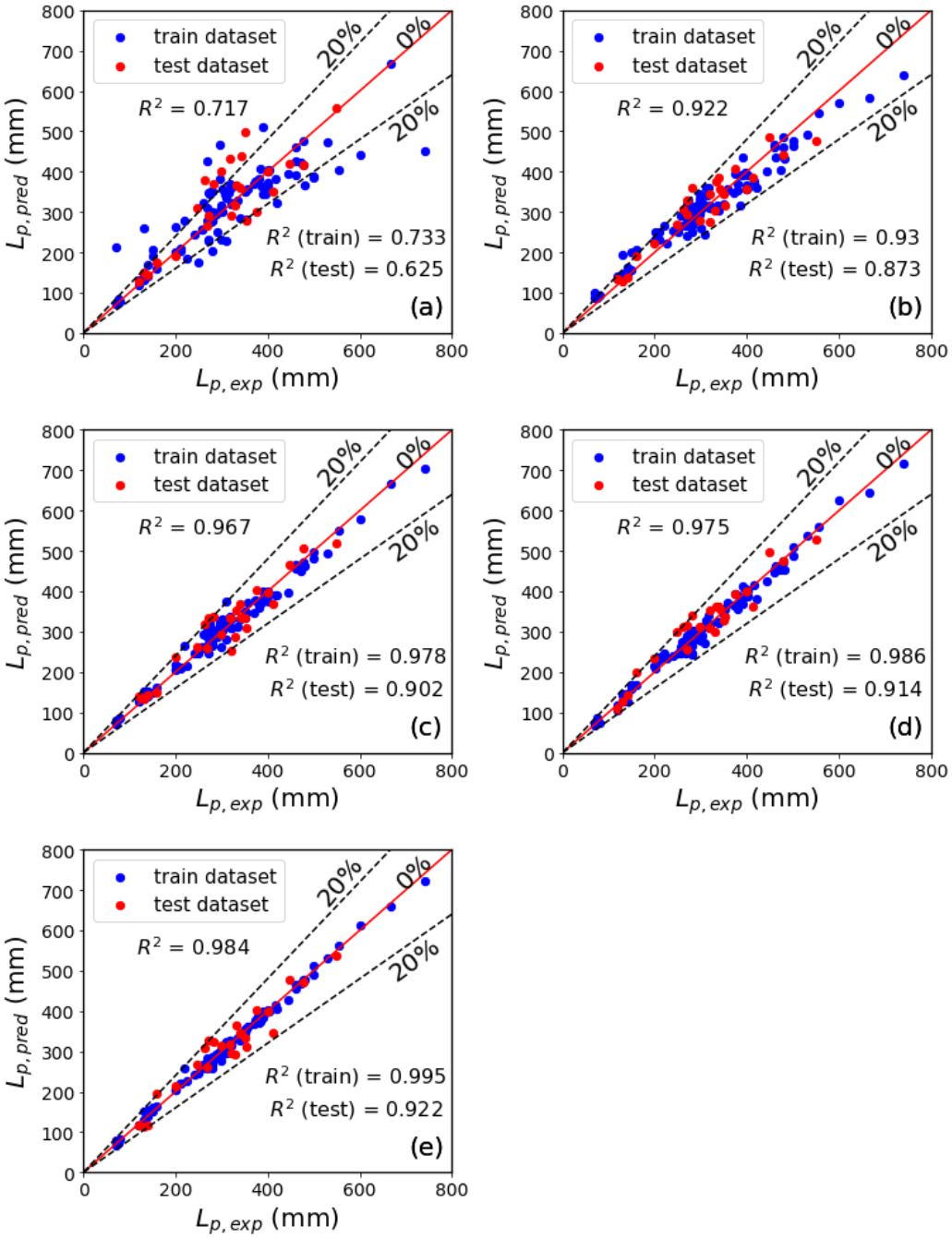

Figure 5.5: Comparison of the PHL predictions based on (a) SVR, (b) RFR, (c) ETR, (d) GBR, and (e) xgBoost.

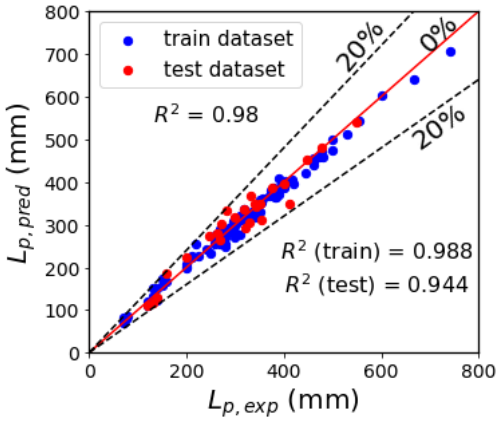

Figure 5.6: Experimentally observed versus predicted PHL based on the proposed stacking ensemble model (with ±20% error bounds).

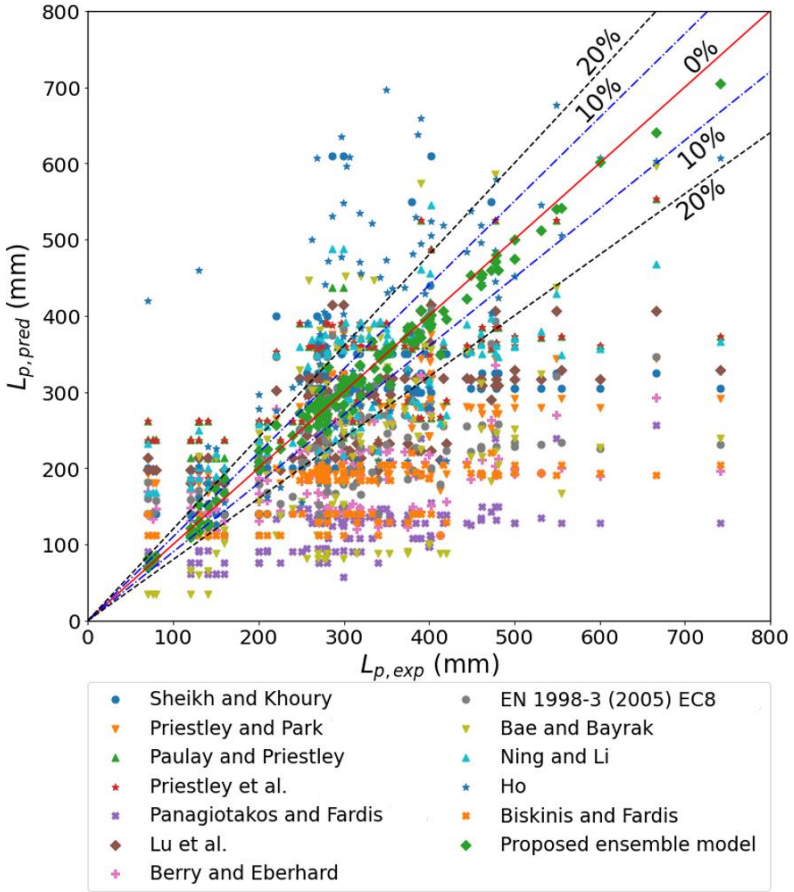

Figure 5.7: Comparisons of predictions based on proposed and existing models with ±10% and ±20% error bounds.

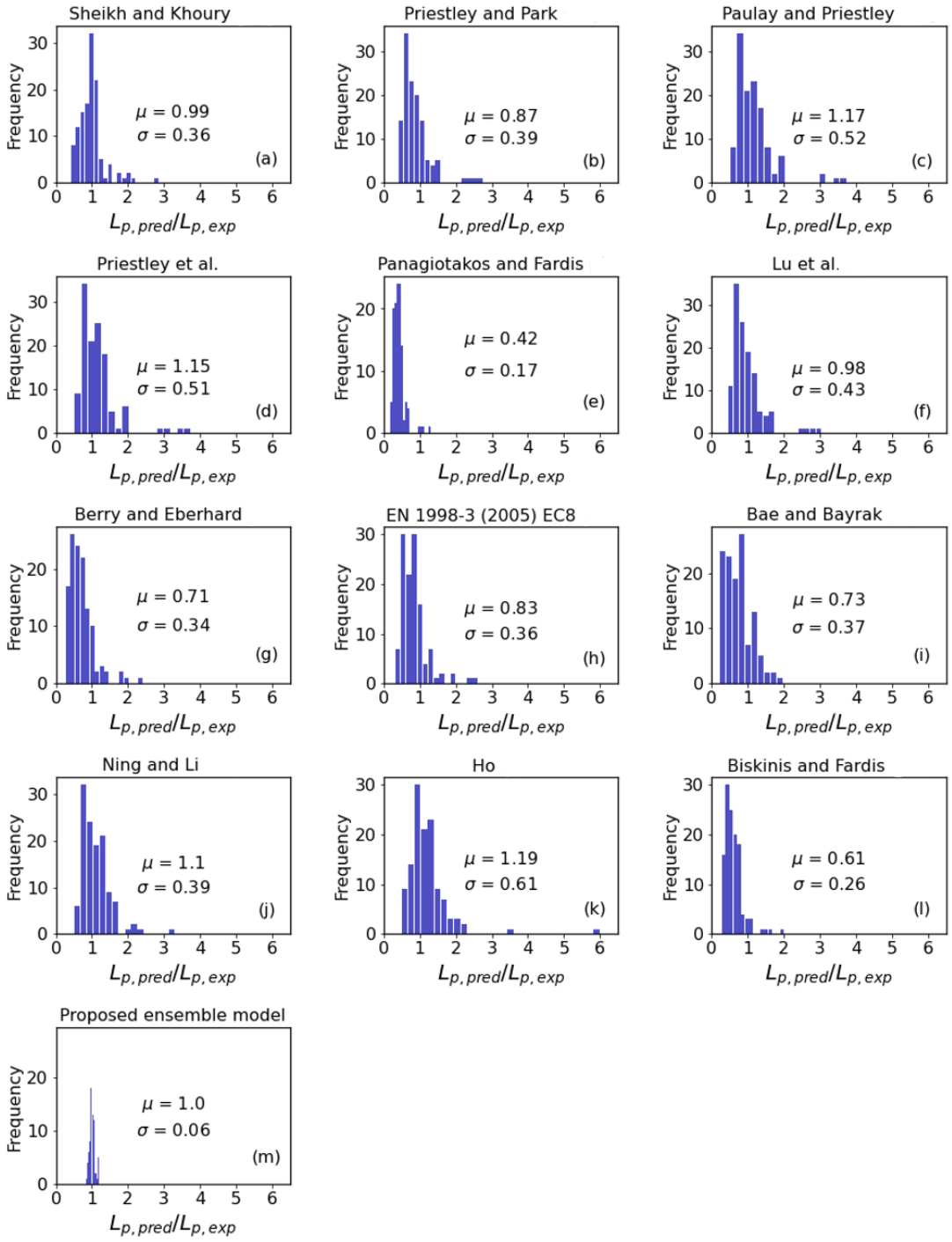

Figure 5.8: Histogram of predicted to experimental PHL ratio.

Figure 5.9 shows the Taylor diagram basis relationship between the standard deviation (STD) and correlation coefficient of the experimental and predicted PHL based on the existing and proposed models. In this figure, the observed data point is

represented by a blue point in the horizontal axis. As shown in Figure 5.9, the proposed stacking ensemble model provided substantially higher prediction capability, with the highest correlation with the experimental PHL. Moreover, the standard deviation for the predicted PHL based on the proposed model is closer to that of the experimental PHL, which confirms the consistency of the proposed model in predicting the PHL for the complete dataset, as shown in Figure 5.9. The correlation coefficients based on the existing models are substantially lower than that of the proposed model. The proposed stacking ensemble model provided the most accurate and robust predictions for PHL. The Ning and Li [80] model provided the best prediction accuracy among the existing models, as shown in Figure 5.9.

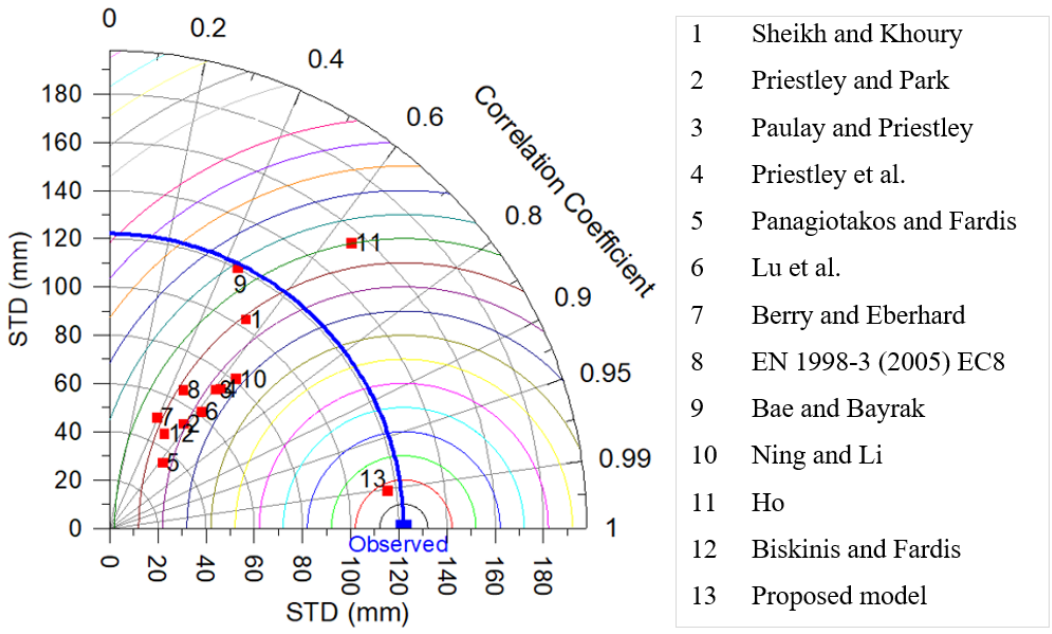

Figure 5.9: Comparison of predictions of existing and proposed models using the Taylor diagram.

5.5.3. Explainability of the ML model and feature importance

The regression process of the PHL for each observation in the database can be explained by the SHAP approach. As discussed earlier, the SHAP value allows the interpretation of each prediction by decomposing it into the sum of the effects of each input feature. In this study, a tree-based SHAP [285] is used to interpret the predictions of the xgBoost model that showed the highest performance. Figure 5.10 shows a typical prediction plot of the PHL based on SHAP values. In this figure, the base value represents the mean of the experimental results, while the length of the bar represents the SHAP value for each input parameter, which shows the degree of significance of the parameter in predicting the PHL. Hence, the prediction of the model is the result of the interpretation function. The figure also shows the direction (positive or negative) of the effect of the input parameters on the predicted PHL. The factors that tend to increase the response are shown in red bars, while blue bars show the factors that tend to lower the response. As can be seen in Figure 5.10, the axial load ratio has the highest positive effect on the predicted PHL.

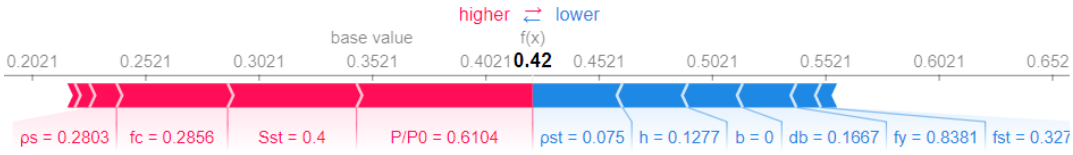

Figure 5.10: Explanation of plastic hinge length for Specimen H60-7.5-C0-2-45 in Barrera et al. [286].

Figure 5.11 shows the summary plot of SHAP values in which the input factors are ordered according to their importance. In this figure, the color represents the factor

value varying from low (blue) to high (red), while the dot points represent the SHAP values of an instance for each factor. As can be seen in *Figure 5.11*, the axial load ratio plays the most critical role in determining the PHL and is the most dominant parameter. The other two most significant factors are f_c' and S_{st}, as shown in Figure 5.11. Moreover, the high level of all parameters except L/H, L, f_{st}, and f_y has a positive influence on the PHL, as shown in Figure 5.11. These results can also be observed in Figure 5.12 which shows the global importance of the input variables which is measured using the mean absolute value of the SHAP values associated with each input variable. The figure also shows the direction of the impact of the input variables using blue and red bars for negative and positive impacts, respectively. Furthermore, the SHAP value can be used to identify the significant interaction between the input factors. The SHAP dependence plots in Figure 5.13a–c reveal the most relevant interaction for the top three significant factors in predicting the PHL. For instance, axial load ratio and S_{st} mostly interact with the diameter of longitudinal reinforcement, as shown in Figure 5.13a and b. Moreover, there exists significant nonlinear interaction between f_c' and ρ_{st} (Figure 5.13c).

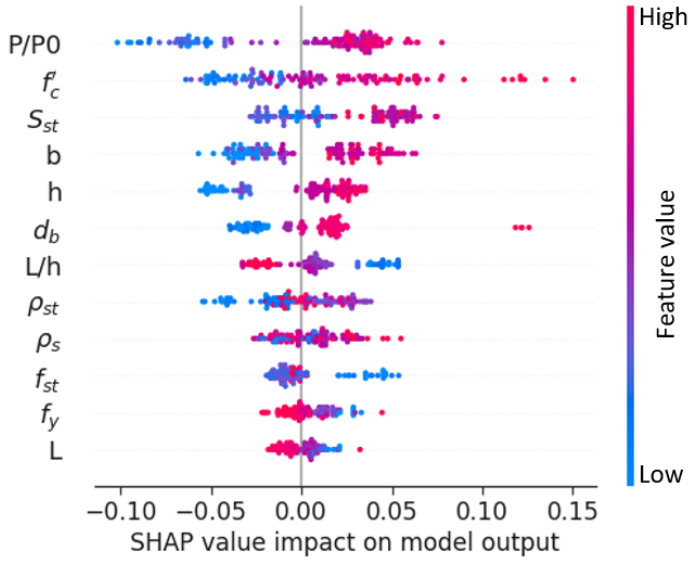

Figure 5.11: SHAP summary plot for the plastic hinge length.

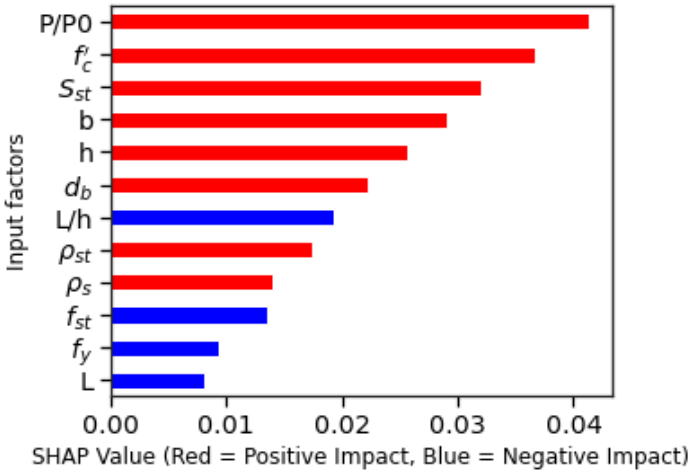

Figure 5.12: Global importance of the input factors based on SHAP approach.

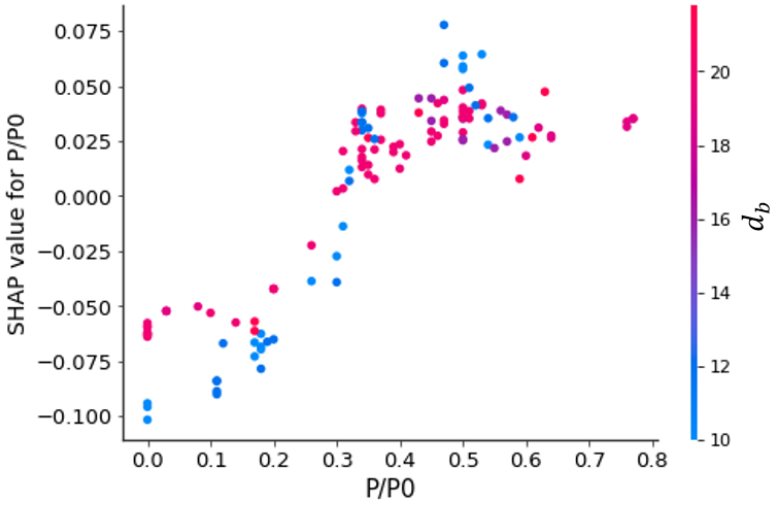

(a)

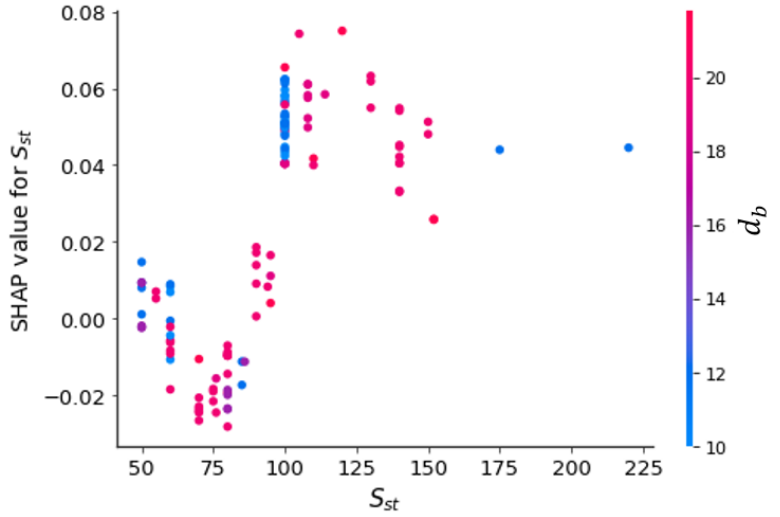

(b)

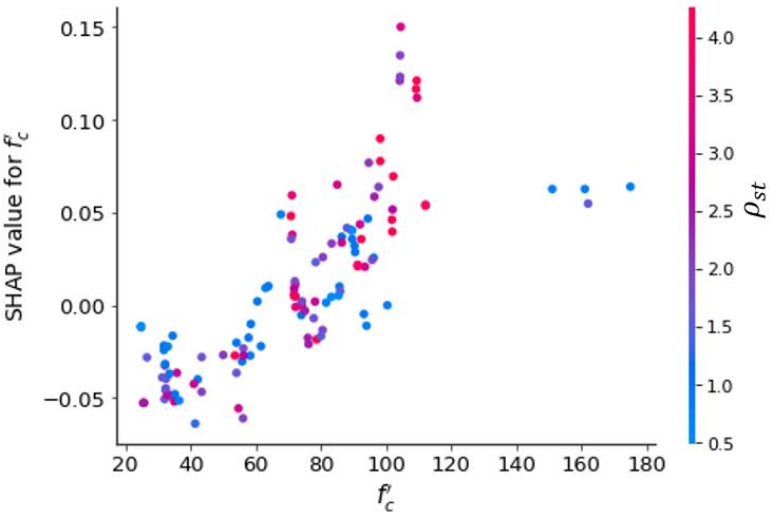

(c)

Figure 5.13: SHAP dependency plots for the plastic hinge length of RC columns.

5.7. Conclusions

The performance of RC columns plays a vital role in the overall performance of structures (e.g., RC bridges and buildings). Identification or proper definition of the plastic hinge region over which the plastic deformation is localized establishes a key step for the seismic performance assessment of RC columns. The extent of the plastic hinge zone can be defined using plastic hinge length. Accurate prediction of the plastic hinge length is thus crucial in assessing the seismic performance of RC members and evaluating their ductility and damage extend. Several formulations have been proposed for predicting the PHL of RC members. However, there exist large discrepancies among the existing formulations and guideline equations for the PHL. To this end, this paper presents a novel ensemble machine learning (ML) model for predicting the PHL of rectangular RC columns. The cross-sectional dimensions of the column (width (b) and depth (h)), shear span (L), aspect ratio (L/h), compressive strength of concrete (f_c'), axial load ratio (P/P_0), diameter of longitudinal bars (d_b), longitudinal reinforcement ratio (ρ_s), yield strength of longitudinal bars (f_y), transverse reinforcement spacing (S_{st}), yield strength of transverse reinforcement (f_{st}), and transverse reinforcement ratio (ρ_{st}) are considered as input parameters for the machine learning models. The efficacy of five ML models including support vector regression, extremely randomized trees, random forest, gradient boosting, and extreme gradient boosting are compared in predicting the PHL. The three best models are stacked via a linear SVR meta-model to improve their predictions. The hyperparameters of each model are optimized using a Grid search with 10-fold cross-validation. The prediction capability of the proposed ensemble model is compared with those of existing formulations and guideline equations for the PHL. Moreover, the SHAP approach is used to interpret the prediction

of the ML model and identify the most significant factors that influence the prediction of the PHL. The following conclusions can be drawn from this study:

- Existing equations for the PHL are mainly empirically developed using a predefined form and are based on a limited number of influential factors. Moreover, there exists a great discrepancy between the existing equations in terms of the significant factors used in determining the PHL. Among the existing models, Ning and Li [80], which is based on a probabilistic approach showed better predictions for the PHL.
- Among the five models, xgBoost showed the highest performance, while support vector regression exhibited the least performance in predicting the PHL. The stacking ensemble model improved the prediction accuracy of the base learners.
- The comparison of the proposed stacking ensemble model against the experimental results for the PHL showed that the proposed procedure is able to yield accurate and stable predictions.
- The comparative results of the proposed model with the existing model and guideline formulae revealed the superior prediction capability of the proposed stacking learner-based ensemble model, with a significantly higher NSE coefficient and index of agreement compared to that for the existing models. In addition, the proposed model showed significantly lower RMSE and MAE. The prediction capability of the existing model is further compared using the Taylor diagram, which confirmed the superior prediction capability of the proposed model.

- The results of the SHAP analysis revealed that the axial load ratio, compressive strength of concrete, and spacing of the transverse reinforcement are the three key parameters governing PHL prediction using xgBoost.
- The high values of all parameters except axial load ratio, yield strength of longitudinal and transverse steel reinforcement, and column shear span increase the PHL prediction using xgBoost.

CHAPTER 6: SUMMARY AND RECOMMENDATION FOR FUTURE WORK

6.1. Summary

In this dissertation, the efficacy of steel reinforced composites for strengthening of RC beams (rectangular and T-section) deficient in shear, as well as seismically deficient RC columns and bridge piers, have been investigated based on experimental, analytical, numerical, and machine learning based studies. An extensive experimental program that comprised a total of thirty-three (33) shear-deficient RC beams was used to investigate the applicability of SRG for strengthening of RC beams. Besides, the effect of different parameters such as steel fabric density, bond scheme, strengthening configuration, amount of internal shear reinforcement within the critical shear span (SRG/stirrups interaction), and shear span-to-depth (*a/d*) ratio was investigated. In addition, the use of the NSE technique for the SRG system was experimentally investigated and its performance was compared with that of the conventional EB technique. In addition, an analytical model based on the simplified modified compression field theory (SMCFT) has been proposed to predict the shear capacity of SRG-strengthened beams. The proposed model considers the effect of different factors such as the strengthening technique and shear span-to-depth ratio.

Moreover, machine learning (ML) based accurate and reliable predictive models were proposed to predict the shear and flexural capacities of RC beams strengthened with different types of inorganic composites for the first time. A reliability analysis is performed to calibrate a resistance reduction factor to achieve a specified target reliability index for the design of both shear and flexural strengthened RC beams based on the proposed ML-based models.

In addition to RC beams, the application of SRC for strengthening of seismically

deficient RC columns and the main/interaction effects of important design parameters on the seismic performance of the strengthened columns was numerically investigated. A proper definition of the plastic hinge region over which the plastic deformation is localized establishes a key step for the seismic performance assessment of RC columns. However, there exist large discrepancies among the existing formulations and guideline equations for the PHL. To this end, this thesis presents a novel ensemble machine learning model for predicting the PHL of rectangular RC columns.

The results of the study support the following conclusions:

- In the first study, the efficacy of SRG for strengthening of shear deficient RC T-beams was investigated. The test parameters were: (a) fabric density (1.57 cords/cm, 3.14 cords/cm), (b) amount of internal shear reinforcement, and (c) bond scheme. Enhancements achieved in the shear capacity ranged from 10% to 71%. The average increase in the shear capacity was 45% and 36% for RC beams strengthened with low-density and high-density SRG fabrics, respectively. On average, the efficacy of the SRG system decreased by 22% because of the change in the bond scheme from U-jacketing to side bonded. The experimental results clearly indicated the SRG/stirrups interaction in terms of the strength gain, as well as the strains developed in the internal shear reinforcement. An analytical procedure was proposed to predict the shear capacity of SRG-strengthened beams and resulted in a safe and accurate prediction capability.
- The second study investigated the behavior of slender and deep RC beams with varying *a/d* ratios (1.60, 2.10, 2.60, and 3.10) and shear strengthened with an externally bonded SRG. The test parameters were *a/d* ratio and fabric density. Overall, the load capacity of the strengthened beams was found to increase by 21–133%, with an average of 78%. The SRG strengthening also delayed the formation

of the first crack. The experimental results demonstrated that the behavior of strengthened RC beams is affected by the *a/d* ratio. The increase in load capacity attributed to the SRG system increased with an increase in *a/d* ratio for deep beams but decreased with increasing *a/d* ratio for slender beams. On average, the increase in the load capacity for slender beams was 108%, whereas this value was only 48% for deep beams. The shear failure of beams strengthened with high-density SRG fabrics was attributed to fiber-matrix interface debonding with delamination of the inner mortar layer, whereas the failure in the low-density SRG strengthened beams occurred by SRG debonding with concrete cover separation. An analytical model for predicting the shear capacity of an SRG-strengthened beam that considers the effect of the shear span-to-depth ratio is proposed.

- In the third study, the use of the NSE technique for the SRG system was experimentally investigated and its performance was compared with that of the conventional EB technique. Moreover, the effects of the fabric density, strengthening scheme, and strengthening amount in a continuous or discontinuous configuration on the strengthening performance of the SRG system were examined. The increase in the shear capacity of the strengthened beams relative to the reference beam ranged from 32 to 132%. The experimental result showed the strength properties of the SRG steel fiber can be better utilized by employing the NSE technique. The failure of the NSE-SRG strengthened beams was mainly characterized by fabric rupture, unlike the EB-SRG beams where failure was attributed to premature SRG debonding. Thus, the former represents a better utilization of the SRG system. An analytical procedure based on the SMCFT was proposed to predict the shear strength of RC beams strengthened with either the NSE-SRG or EB-SRG considering the type of the strengthening technique and

resulted in acceptable prediction accuracy.

- The fourth study presented novel ML-based models for predicting the shear capacity of RC beams strengthened with inorganic composites in shear. The proposed best predictive model provided safe and accurate predictions compared to the available models and guideline equations. The findings of this study showed the successful implementation of machine learning techniques to predict the shear capacity of FRCM-strengthened shear-critical RC beams. In addition, based on the results of the reliability analysis, resistance reduction factors of 0.91 and 0.87 are calibrated to achieve target reliability levels of 3.5 and 4.0, respectively. A design example is provided using $\phi = 0.91$ for $\beta_T = 3.5$.
- The fifth study proposed explainable ML-based model for predicting the flexural and load-carrying capacities of flexural strengthened RC beams using inorganic composites for the first time. In addition, the use of a unified SHAP approach is investigated to explain the predicted response and rank the input features and their interactions for the flexural capacity of FRCM-strengthened beams. Based on the results of SHAP, it is noted that the area of internal tensile steel reinforcement, area of FRCM reinforcement, and width and depth of the beam section have the most significant influences on the flexural capacity of the strengthened beams. A capacity reduction factor $\phi = 0.92$ is calibrated to achieve a reliability index $\beta_T = 3.5$.
- The sixth study investigated the application of SRP for retrofitting of seismically deficient RC columns and bridge piers. Moreover, the main and interaction effects of key design parameters on the performance of SRP-confined columns at different damage limit states, including concrete core crushing, longitudinal reinforcement yielding and buckling, and ductility performance is investigated. Results show that

the lateral load-carrying capacity and ductility performance of SRP-confined RC bridge piers were significantly influenced by the pier aspect ratio, materials properties, and amount of transverse and longitudinal reinforcement. Moreover, the resistance to buckling base shear, and overall ductility increased with increasing number of SRP layers.

- Finally, the seventh study leveraged the power of ensemble learners to predict the PHL of rectangular RC columns. Furthermore, a unified SHAP approach was used to explain the predictions of the developed ML model and identify the important factors and interactions that influence the prediction of the PHL of RC columns for the first time. A comparative study of the prediction of the proposed model with twelve existing models and guideline equations showed the superiority of the proposed model in predicting the PHL.

6.2. Recommendation for Future Work

This study showed the potential application of SRC for strengthening of deficient RC beams as well as confinement of seismically deficient RC columns and bridge piers. To mitigate the premature debonding failure observed in the conventional EB-SRG, an NSE-SRG technique was investigated. Future study is recommended to explore the following:

- Explore the use of other techniques including hybrid NSE/EB technique for SRG strengthened beams, particularly when large number of SRG fabric layers are required.
- Investigate the effect of other factors affecting the shear strengthening performance of the SRG system such as the presence of end anchorage.
- Investigate the application of data-driven ML models to predict the failure mode of

RC beams strengthened in flexure and capacity and failure mode of RC beams strengthened in shear.

- Investigate the efficacy of SRC for strengthening of flexural dominated RC columns and columns with circular cross-section.
- Perform life-cycle analysis of SRG-strengthened RC beams and columns and compare it with other strengthening system.

REFERENCES

[1] Tetta ZC, Bournas D. TRM vs FRP jacketing in shear strengthening of concrete members subjected to high temperatures. Compos Part B Eng 2016;106:190–205. https://doi.org/10.1016/j.compositesb.2016.09.026.

[2] Triantafillou T, Papanicolaou C. Shear strengthening of reinforced concrete members with textile reinforced mortar (TRM) jackets. Mater Struct 2006;39:93–103. https://doi.org/10.1617/s11527-005-9034-3.

[3] Younis A, Ebead U. Bond characteristics of different FRCM systems. Constr Build Mater 2018;175:610–20. https://doi.org/10.1016/j.conbuildmat.2018.04.216.

[4] Blanksvärd T. Strengthening of concrete structures by the use of mineral based composites. vol. Licentiate. 2007.

[5] Koutas L, Tetta ZC, Bournas D, Triantafillou T. Strengthening of concrete structures with Textile Reinforced Mortars : State-of-the-Art Review. J Compos Constr 2019;23:03118001. https://doi.org/10.1061/(ASCE)CC.1943-5614.0000882.

[6] Ebead U, Younis A. Pull-off characterization of FRCM/Concrete interface. Compos Part B Eng 2019;165:545–53. https://doi.org/10.1016/j.compositesb.2019.02.025.

[7] Wakjira TG, Ebead U. Shear behavior of RC beams strengthened with different types of FRCM: Effect of stirrups' configuration. Proc. Tenth Int. Struct. Eng. Constr. Conf., Chicago, Illinois, United States: ISEC Press; 2019, p. SUS-34. https://doi.org/10.14455/ISEC.res.2019.191.

[8] Younis A, Ebead U, Shrestha K. Different FRCM systems for shear-strengthening of reinforced concrete beams. Constr Build Mater 2017;153:514–

26. https://doi.org/10.1016/j.conbuildmat.2017.07.132.

[9] Babaeidarabad S, Loreto G, Nanni A. Flexural strengthening of RC beams with an externally bonded fabric-reinforced cementitious matrix. J Compos Constr 2014;18:1–12. https://doi.org/10.1061/(ASCE)CC.1943-5614.0000473.

[10] Marcinczak D, Trapko T. Shear strengthening of reinforced concrete beams with PBO-FRCM composites with anchorage. Compos Part B Eng 2019;158:149–61. https://doi.org/10.1016/j.compositesb.2018.09.061.

[11] Pellegrino C, D'Antino T. Experimental behaviour of existing precast prestressed reinforced concrete elements strengthened with cementitious composites. Compos Part B Eng 2013;55:31–40. https://doi.org/10.1016/j.compositesb.2013.05.053.

[12] Gonzalez-Libreros JH, Sneed LH, D'Antino T, Pellegrino C. Behavior of RC beams strengthened in shear with FRP and FRCM composites. Eng Struct 2017;150:830–42. https://doi.org/10.1016/j.engstruct.2017.07.084.

[13] Azam R, Soudki K, West J, Noël M. Behavior of shear-critical RC beams strengthened with CFRCM. J Compos Constr 2018;22:04017046. https://doi.org/10.1061/(ASCE)CC.1943-5614.0000829.

[14] Azam R, Soudki K, West J, Noël M. Shear strengthening of RC deep beams with cement-based composites. Eng Struct 2018;172:929–37. https://doi.org/10.1016/j.engstruct.2018.06.085.

[15] Wakjira TG, Afzal MS, Ebead U. Efficacy of FRCM systems in flexural strengthening of RC T-beams. IOP Conf. Ser. Mater. Sci. Eng., vol. 431, 2018. https://doi.org/10.1088/1757-899X/431/7/072007.

[16] Wakjira TG, Ebead U. Internal transverse reinforcement configuration effect of EB/NSE-FRCM shear strengthening of RC deep beams. Compos Part B Eng

2019;166:758–72.
https://doi.org/https://doi.org/10.1016/j.compositesb.2019.03.004.

[17] Wakjira TG, Ebead U. FRCM/internal transverse shear reinforcement interaction in shear strengthened RC beams. Compos Struct 2018;201:326–39. https://doi.org/https://doi.org/10.1016/j.compstruct.2018.06.034.

[18] Wakjira TG, Ebead U. Hybrid NSE/EB technique for shear strengthening of reinforced concrete beams using FRCM: Experimental study. Constr Build Mater 2018;164:164–77. https://doi.org/https://doi.org/10.1016/j.conbuildmat.2017.12.224.

[19] Ebead U, Wakjira TG. Behaviour of RC beams strengthened in shear using near surface embedded FRCM. IOP Conf Ser Mater Sci Eng 2018;431:072001. https://doi.org/10.1088/1757-899X/431/7/072001.

[20] De Santis S, De Felice G, Napoli A, Realfonzo R. Strengthening of structures with Steel Reinforced Polymers: A state-of-the-art review. Compos Part B Eng 2016;104:87–110. https://doi.org/10.1016/j.compositesb.2016.08.025.

[21] Prota A, Tan KY, Nanni A, Pecce M, Manfredi G. Performance of shallow reinforced concrete beams with externally bonded steel-reinforced polymer. ACI Struct J 2006;103:163–70. https://doi.org/10.14359/15173.

[22] Barton B, Wobbe E, Dharani LR, Silva P, Birman V, Nanni A, et al. Characterization of reinforced concrete beams strengthened by steel reinforced polymer and grout (SRP and SRG) composites. Mater Sci Eng A 2005;412:129–36. https://doi.org/10.1016/j.msea.2005.08.151.

[23] Wobbe E, Silva P, Barton BL, Dharani LR, Birman V, Nanni A, et al. Flexural capacity of RC beams externally bonded with SRP and SRG. Proc. Soc. Adv. Mater. Process Eng. Symp., Long Beach, CA, USA: 2004.

[24] Napoli A, Realfonzo R. Reinforced concrete beams strengthened with SRP/SRG systems: Experimental investigation. Constr Build Mater 2015;93:654–77. https://doi.org/10.1016/j.conbuildmat.2015.06.027.

[25] Balsamo A, Nardone F, Iovinella I, Ceroni F, Pecce M. Flexural strengthening of concrete beams with EB-FRP, SRP and SRCM: Experimental investigation. Compos Part B Eng 2013;46:91–101. https://doi.org/10.1016/j.compositesb.2012.10.014.

[26] Sneed L, Verre S, Carloni C, Ombres L. Flexural behavior of RC beams strengthened with steel-FRCM composite. Eng Struct 2016;127:686–99. https://doi.org/10.1016/j.engstruct.2016.09.006.

[27] Thermou GE, Hajirasouliha I. Compressive behaviour of concrete columns confined with steel-reinforced grout jackets. Compos Part B Eng 2018;138:222–31. https://doi.org/10.1016/j.compositesb.2017.11.041.

[28] Thermou GE, Katakalos K, Manos G. Influence of the cross section shape on the behaviour of SRG-confined prismatic concrete specimens. Mater Struct 2016;49:869–87. https://doi.org/10.1617/s11527-015-0545-2.

[29] Thermou GE, Katakalos K, Manos G. Experimental investigation of substandard RC columns confined with SRG jackets under compression. Compos Struct 2018;184:56–65.

[30] De Santis S, Roscini F, de Felice G. Full-scale tests on masonry vaults strengthened with Steel Reinforced Grout. Compos Part B Eng 2018;141:20–36. https://doi.org/10.1016/j.compositesb.2017.12.023.

[31] De Santis S, De Felice G. Steel reinforced grout systems for the strengthening of masonry structures. Compos Struct 2015;134:533–48. https://doi.org/10.1016/j.compstruct.2015.08.094.

[32] Bencardino F, Condello A. Reliability and adaptability of the analytical models proposed for the FRP systems to the steel reinforced polymer and steel reinforced grout strengthening systems. Compos Part B Eng 2015;76:249–59. https://doi.org/10.1016/j.compositesb.2015.02.029.

[33] Bousselham A, Chaallal O. Behavior of reinforced concrete T-beams strengthened in shear with carbon fiber-reinforced polymer — An experimental study. ACI Struct J 2006;103:339–47.

[34] Bousselham A, Chaallal O. Effect of transverse steel and shear span on the performance of RC beams strengthened in shear with CFRP. Compos Part B Eng 2006;37:37–46.

[35] Nguyen-minh L, Vo-le D, Tran-thanh D, Pham T, Ho-huu C. Shear capacity of unbonded post-tensioned concrete T-beams strengthened with CFRP and GFRP U-wraps. Compos Struct 2018;184:1011–29. https://doi.org/10.1016/j.compstruct.2017.10.072.

[36] Dias SJE, Barros JAO. NSM shear strengthening technique with CFRP laminates applied in high T cross section RC beams. Compos Part B Eng 2017;114:256–67. https://doi.org/10.1016/j.compositesb.2017.01.028.

[37] Li W, Leung CK. Y. Shear span-depth ratio effect on behavior of RC beam shear strengthened with full-wrapping FRP strip. J Compos Constr 2016;20:04015067. https://doi.org/10.1061/(ASCE)CC.1943-5614.0000627.

[38] Tetta ZC, Koutas L, Bournas D. Shear strengthening of concrete members with TRM jackets: Effect of shear span-to-depth ratio, material and amount of external reinforcement. Compos Part B Eng 2018;137:184–201. https://doi.org/10.1016/j.compositesb.2017.10.041.

[39] Loreto G, Babaeidarabad S, Leardini L, Nanni A. RC beams shear-strengthened

with fabric-reinforced-cementitious-matrix (FRCM) composite. Int J Adv Struct Eng 2015;7:341–52. https://doi.org/10.1007/s40091-015-0102-9.

[40] Tetta ZC, Koutas L, Bournas D. Textile-reinforced mortar (TRM) versus fiber-reinforced polymers (FRP) in shear strengthening of concrete beams. Compos Part B Eng 2015;77:338–48.

[41] Awani O, El Maaddawy T, Ismail N. Fabric-reinforced cementitious matrix: A promising strengthening technique for concrete structures. Constr Build Mater 2017;132:94–111. https://doi.org/10.1016/j.conbuildmat.2016.11.125.

[42] El-Sherif HE, Wakjira TG, Ebead U. Flexural strengthening of reinforced concrete beams using hybrid near-surface embedded/externally bonded fabric-reinforced cementitious matrix. Constr Build Mater 2020;238:117748. https://doi.org/https://doi.org/10.1016/j.conbuildmat.2019.117748.

[43] Lorenzis L De, Teng JG. Near-surface mounted FRP reinforcement : An emerging technique for strengthening structures. Compos Part B Eng 2007;38:119–43. https://doi.org/10.1016/j.compositesb.2006.08.003.

[44] D'Antino T, Pisani MA. Evaluation of the effectiveness of current guidelines in determining the strength of RC beams retrofitted by means of NSM reinforcement. Compos Struct 2017;167:166–77. https://doi.org/10.1016/j.compstruct.2017.01.070.

[45] Ibrahim M, Wakjira TG, Ebead U. Shear strengthening of reinforced concrete deep beams using near-surface mounted hybrid carbon/glass fibre reinforced polymer strips. Eng Struct 2020;210:110412. https://doi.org/https://doi.org/10.1016/j.engstruct.2020.110412.

[46] Pregnolato M. Bridge safety is not for granted – A novel approach to bridge management. Eng Struct 2019;196:109193.

https://doi.org/10.1016/j.engstruct.2019.05.035.

[47] Abbiati G, Bursi OS, Caperan P, Di Sarno L, Molina FJ, Paolacci F, et al. Hybrid simulation of a multi-span RC viaduct with plain bars and sliding bearings. Earthq Eng Struct Dyn 2015;44:2221–40. https://doi.org/10.1002/eqe.2580.

[48] Cassese P, Ricci P, Verderame GM. Experimental study on the seismic performance of existing reinforced concrete bridge piers with hollow rectangular section. Eng Struct 2017;144:88–106. https://doi.org/10.1016/j.engstruct.2017.04.047.

[49] Reza SM, Alam MS, Tesfamariam S. Lateral load resistance of bridge piers under flexure and shear using factorial analysis. Eng Struct 2014;59:821–35. https://doi.org/10.1016/j.engstruct.2013.12.009.

[50] Priestley MJN, Seible F, Calvi G. Seismic Design and Retrofit of Bridges. New York: Wiley; 1996.

[51] Boys A, Bull DK, Pampanin S. Seismic Performance Assessment Of Inadequately Detailed Reinforced Concrete Columns. Proc New Zeal Soc Earthq Eng 2008.

[52] Calvi GM, Pavese A, Rasulo A, Bolognini D. Experimental and numerical studies on the seismic response of R.C. hollow bridge piers. Bull Earthq Eng 2005;3:267–97. https://doi.org/10.1007/s10518-005-2240-0.

[53] Mostafa K, Sanders D, Saiidi MS. Impact of aspect ratio on two-column bent seismic performance, Center for Civil Engineering Research, Department of Civil Engineering, University of Nevada, Reno, Center for Earthquake Engineering Research Report No. CCEER-05-10, May. 2004.

[54] Yeh YK, Mo YL, Yang CY. Seismic performance of reinforced concrete rectangular hollow bridge columns. J Struct Eng 2002;128:60–8.

https://doi.org/10.6052/j.issn.1000-4750.2013.11.1020.

[55] Lehman D, Moehle J, Mahin S, Calderone A, Henry L. Experimental evaluation of the seismic performance of reinforced concrete bridge columns. J Struct Eng 2004;130:869–79. https://doi.org/10.1061/(ASCE)0733-9445(2004)130:6(869).

[56] Yeh YK, Mo YL, Yang CY. Seismic performance of hollow circular bridge piers. ACI Struct J 2001;98:862–71. https://doi.org/10.14359/10753.

[57] Barcley L, Kowalsky M. Seismic Performance of Circular Concrete Columns Reinforced with High-Strength Steel. J Struct Eng 2020;80:1–11. https://doi.org/10.1061/(ASCE)ST.1943-541X.0002452.

[58] Mo YL, Nien IC. Seismic performance of hollow high-strength concrete bridge columns. J Bridg Eng 2002;7:338–49. https://doi.org/10.1061/(ASCE)1084-0702(2002)7:6(338).

[59] Shao C, Qi Q, Wang M, Xiao Z, Wei W, Hu C, et al. Experimental study on the seismic performance of round-ended hollow piers. Eng Struct 2019;195:309–23. https://doi.org/10.1016/j.engstruct.2019.05.094.

[60] Esmaeily A, Xiao Y. Behavior of reinforced concrete columns under variable axial loads: Analysis. ACI Struct J 2005;102:736–44. https://doi.org/10.14359/14669.

[61] Holub CJ. Interaction of variable axial load and shear effects in RC bridges, Ph.D. thesis, University of Illinois at Urbana-Champaign. 2009.

[62] Goodnight JC, Kowalsky M, Nau JM. Strain Limit States for Circular RC Bridge Columns. Earthq Spectra 2016;32:1627–52. https://doi.org/10.1193/030315EQS036M.

[63] Kusumawardaningsih Y, Hadi MNS. Comparative behaviour of hollow columns confined with FRP composites. Compos Struct 2010;93:198–205.

https://doi.org/10.1016/j.compstruct.2010.05.020.

[64] Parghi A, Alam MS. Seismic behavior of deficient reinforced concrete bridge piers confined with FRP – A fractional factorial analysis. Eng Struct 2016;126:531–46. https://doi.org/10.1016/j.engstruct.2016.08.011.

[65] Elgawady M, Endeshaw M, McLean D, Sack R. Retrofitting of rectangular columns with deficient lap splices. J Compos Constr 2010;14:22–35. https://doi.org/10.1061/(ASCE)CC.1943-5614.0000047.

[66] Bayrak O, Sheikh SA. Plastic Hinge Analysis. J Struct Eng 2001;127:1092–100.

[67] Berry MP, Eberhard MO. Performance Modeling Strategies for Modern Reinforced Concrete Bridge Columns PEER Report 2007/07 Pacific Earthquake Engineering Research Center, College of Engineering, University of California, Berkeley, USA. 2007.

[68] Ho J. Inelastic design of reinforced concrete beams and limited ductile high-strength concrete columns. Ph.D. thesis, University of Hong Kong, 2003.

[69] Thomsen JH, Wallace JW. Lateral load behavior of reinforced concrete columns constructed using high-strength materials. ACI Struct J 1994;91:605–15. https://doi.org/10.14359/4181.

[70] Legeron F, Paultre P. Behavior of high-strength concrete columns under cyclic flexure and constant axial load. ACI Struct J 2000;97:591–601. https://doi.org/10.14359/7425.

[71] Bae S, Bayrak O. Plastic Hinge Length of Reinforced Concrete Columns. ACI Struct J 2008;105:290–300. https://doi.org/10.12989/cac.2012.10.6.663.

[72] Kazaz İ. Analytical Study on Plastic Hinge Length of Structural Walls. J Struct Eng 2013;139:1938–50. https://doi.org/10.1061/(asce)st.1943-541x.0000770.

[73] Mendis P. Plastic hinge lengths of normal and high-strength concrete in flexure.

Adv Struct Eng 2001;4:189–95. https://doi.org/10.1260/136943301320896651.

[74] Billah AHMM, Shahria Alam M. Plastic hinge length of shape memory alloy (SMA) reinforced concrete bridge pier. Eng Struct 2016;117:321–31. https://doi.org/10.1016/j.engstruct.2016.02.050.

[75] Paulay T, Priestley MJN. Seismic design of reinforced concrete and masonry buildings. vol. 25. 1992. https://doi.org/10.5459/bnzsee.25.4.362.

[76] Sakai K, Sheikh SA. What Do We Know about Confinement in Reinforced Concrete Columns? (A Critical Review of Previous Work and Code Provisions). ACI Struct J 1989;21:192–207.

[77] Hines EM, Restrepo JI, Seible F. Force-displacement characterization of well-confined bridge piers. ACI Struct J 2004;101:537–48. https://doi.org/10.14359/13340.

[78] Youssf O, ElGawady MA, Mills JE. Displacement and plastic hinge length of FRP-confined circular reinforced concrete columns. Eng Struct 2015;101:465–76. https://doi.org/10.1016/j.engstruct.2015.07.026.

[79] Priestley MJN, Park R. Strength and ductility of RC bridge columns under seismic loading. Struct J ACI 1987;84:285–336.

[80] Ning C-L, Li B. Probabilistic Approach for Estimating Plastic Hinge Length of Reinforced Concrete Columns. J Struct Eng 2016;142:04015164. https://doi.org/10.1061/(asce)st.1943-541x.0001436.

[81] Sheikh SA, Khoury SS. Confined Concrete Columns with Stubs. ACI Struct J 1993;90:414–31.

[82] Park R, Priestley MJN, Gill WD. Ductility of Square-Confined Concrete Columns. ASCE J Struct Div 1982;108:929–50.

[83] Babazadeh A, Burgueño R, Silva PF. Evaluation of the critical plastic region

length in slender reinforced concrete bridge columns. Eng Struct 2016;125:280–93. https://doi.org/10.1016/j.engstruct.2016.07.021.

[84] Feng D, Cetiner B, Kakavand MRA, Taciroglu E. Data-Driven Approach to Predict the Plastic Hinge Length of Reinforced Concrete Columns and Its Application. J Struct Eng 2021;147:04020332. https://doi.org/10.1061/(ASCE)ST.1943-541X.0002852.

[85] Salehi H, Burgueño R. Emerging artificial intelligence methods in structural engineering. Eng Struct 2018;171:170–89. https://doi.org/10.1016/j.engstruct.2018.05.084.

[86] Demir F. Prediction of elastic modulus of normal and high strength concrete by artificial neural networks. Constr Build Mater 2008;22:1428–35. https://doi.org/10.1016/j.conbuildmat.2007.04.004.

[87] Perera R, Ruiz A, Manzano C. An evolutionary multiobjective framework for structural damage localization and quantification. Eng Struct 2007;29:2540–50. https://doi.org/10.1016/j.engstruct.2007.01.003.

[88] Lee S. Prediction of concrete strength using artificial neural networks. Eng Struct 2003;25:849–57. https://doi.org/10.1016/S0141-0296(03)00004-X.

[89] Chaabene W Ben, Flah M, Nehdi M. Machine learning prediction of mechanical properties of concrete: Critical review. Constr Build Mater 2020;260:119889. https://doi.org/10.1016/j.conbuildmat.2020.119889.

[90] Trocoli A, Dantas A, Leite MB, Nagahama KDJ. Prediction of compressive strength of concrete containing construction and demolition waste using artificial neural networks. Constr Build Mater 2013;38:717–22. https://doi.org/10.1016/j.conbuildmat.2012.09.026.

[91] Inel M. Modeling ultimate deformation capacity of RC columns using artificial

neural networks. Eng Struct 2007;29:329–35. https://doi.org/10.1016/j.engstruct.2006.05.001.

[92] Jiang K, Han Q, Bai Y, Du X. Data-driven ultimate conditions prediction and stress-strain model for FRP-confined concrete. Compos Struct 2020;242:112094. https://doi.org/10.1016/j.compstruct.2020.112094.

[93] Naderpour H, Kheyroddin A, Amiri GG. Prediction of FRP-confined compressive strength of concrete using artificial neural networks. Compos Struct 2010;92:2817–29. https://doi.org/10.1016/j.compstruct.2010.04.008.

[94] Jalal M, Ramezanianpour AA. Strength enhancement modeling of concrete cylinders confined with CFRP composites using artificial neural networks. Compos Part B Eng 2012;43:2990–3000. https://doi.org/10.1016/j.compositesb.2012.05.044.

[95] Elsanadedy HM, Al-Salloum YA, Abbas H, Alsayed SH. Prediction of strength parameters of FRP-confined concrete. Compos Part B Eng 2012;43:228–39. https://doi.org/10.1016/j.compositesb.2011.08.043.

[96] Flood I. Towards the next generation of artificial neural networks for civil engineering. Adv Eng Informatics 2008;22:4–14. https://doi.org/10.1016/j.aei.2007.07.001.

[97] Mangalathu S, Jang H, Hwang S-H, Jeon J-S. Data-driven machine-learning-based seismic failure mode identification of reinforced concrete shear walls. Eng Struct 2020;208:110331. https://doi.org/10.1016/j.engstruct.2020.110331.

[98] Keshtegar B, Nehdi ML, Trung N-T, Kolahchi R. Predicting load capacity of shear walls using SVR-RSM model. Appl Soft Comput 2021;112:107739. https://doi.org/10.1016/j.asoc.2021.107739.

[99] Mansour MY, Dicleli M, Lee JY, Zhang J. Predicting the shear strength of

reinforced concrete beams using artificial neural networks. Eng Struct 2004;26:781–99. https://doi.org/10.1016/j.engstruct.2004.01.011.

[100] Amani J, Moeini R. Prediction of shear strength of reinforced concrete beams using adaptive neuro-fuzzy inference system and artificial neural network. Sci Iran 2012;19:242–8. https://doi.org/10.1016/j.scient.2012.02.009.

[101] Chou JS, Pham TPT, Nguyen TK, Pham AD, Ngo NT. Shear strength prediction of reinforced concrete beams by baseline, ensemble, and hybrid machine learning models. Soft Comput 2020;24:3393–411. https://doi.org/10.1007/s00500-019-04103-2.

[102] Chou J, Ngo N, Pham A. Shear Strength Prediction in Reinforced Concrete Deep Beams Using Nature-Inspired Metaheuristic Support Vector Regression 2012;30:1–9. https://doi.org/10.1061/(ASCE)CP.1943-5487.0000466.

[103] Feng D, Wang WJ, Mangalathu S, Hu G, Wu T. Implementing ensemble learning methods to predict the shear strength of RC deep beams with/without web reinforcements. Eng Struct 2021;235. https://doi.org/10.1016/j.engstruct.2021.111979.

[104] Wakjira T, Ibrahim M, Sajjad B, Ebead U. Shear capacity of reinforced concrete deep beams using genetic algorithm. IOP Conf Ser Mater Sci Eng 2020;910:012002. https://doi.org/10.1088/1757-899X/910/1/012002.

[105] Arslan MH. Predicting of torsional strength of RC beams by using different artificial neural network algorithms and building codes. Adv Eng Softw 2010;41:946–55. https://doi.org/10.1016/j.advengsoft.2010.05.009.

[106] Hwang SH, Mangalathu S, Shin J, Jeon JS. Machine learning-based approaches for seismic demand and collapse of ductile reinforced concrete building frames. J Build Eng 2021;34:101905. https://doi.org/10.1016/j.jobe.2020.101905.

[107] Mangalathu S, Hwang SH, Choi E, Jeon JS. Rapid seismic damage evaluation of bridge portfolios using machine learning techniques. Eng Struct 2019;201. https://doi.org/10.1016/j.engstruct.2019.109785.

[108] Mangalathu S, Sun H, Nweke CC, Yi Z, Burton H V. Classifying earthquake damage to buildings using machine learning. Earthq Spectra 2020;36:183–208. https://doi.org/10.1177/8755293019878137.

[109] Perera R, Arteaga A, Diego A De. Artificial intelligence techniques for prediction of the capacity of RC beams strengthened in shear with external FRP reinforcement. Compos Struct 2010;92:1169–75. https://doi.org/10.1016/j.compstruct.2009.10.027.

[110] Tanarslan HM, Secer M, Kumanlioglu A. An approach for estimating the capacity of RC beams strengthened in shear with FRP reinforcements using artificial neural networks. Constr Build Mater 2012;30:556–68. https://doi.org/10.1016/j.conbuildmat.2011.12.008.

[111] Perera R, Tarazona D, Ruiz A, Martín A. Application of artificial intelligence techniques to predict the performance of RC beams shear strengthened with NSM FRP rods. Formulation of design equations. Compos Part B Eng 2014;66:162–73. https://doi.org/10.1016/j.compositesb.2014.05.001.

[112] Abuodeh OR, Abdalla JA, Hawileh RA. Prediction of shear strength and behavior of RC beams strengthened with externally bonded FRP sheets using machine learning techniques. Compos Struct 2020;234:111698. https://doi.org/10.1016/j.compstruct.2019.111698.

[113] ASTM C39. Standard Test Method for Compressive Strength of Cylindrical Concrete Specimens. ASTM Int 2012:1–7. https://doi.org/10.1520/C0039.

[114] ISE/104 Committee. BS 4449:2005: Steel for the reinforcement of concrete.

Weldable reinforcement steel. Bar, coil and decoiled product, BSI, 2005 n.d.

[115] Kerakoll S.p.A. Kerakoll S.p.A. 2018. http://www.kerakoll.com (accessed December 25, 2018).

[116] Ebead U. Inexpensive strengthening technique for partially loaded reinforced concrete beams : Experimental study. J Mater Civ Eng 2015. https://doi.org/10.1061/(ASCE)MT.1943-5533.0001249.

[117] Chen GM, Teng JG, Chen JF, Rosenboom OA. Interaction between Steel Stirrups and Shear-Strengthening FRP Strips in RC Beams. J Compos Constr 2010;14:498–509. https://doi.org/10.1061/(ASCE)CC.1943-5614.0000120.

[118] Colotti V. Shear interaction effect between transverse reinforcements in FRP-strengthened RC beams. Compos Part B Eng 2013;45:1222–33. https://doi.org/10.1016/j.compositesb.2012.06.009.

[119] Awani O, El Maaddawy T, Refai A. Numerical Simulation and Experimental Testing of Concrete Beams Strengthened in Shear with Fabric-Reinforced Cementitious Matrix. J Compos Constr 2015;20:04016056. https://doi.org/10.1061/(ASCE)CC.1943-5614.0000711.

[120] Ombres L. Structural performances of reinforced concrete beams strengthened in shear with a cement based fiber composite material. Compos Struct 2015;122:316–29.

[121] Ebead U, Wakjira TG. FRCM/stirrups interaction in RC beams strengthened in shear using NSE-FRCM. IOP Conf. Ser. Mater. Sci. Eng., vol. 431, 2018, p. 112001. https://doi.org/10.1088/1757-899X/431/11/112001.

[122] Hu B, Wu YF. Effect of shear span-to-depth ratio on shear strength components of RC beams. Eng Struct 2018;168:770–83. https://doi.org/10.1016/j.engstruct.2018.05.017.

[123] Tan KH, Cheng GH, Zhang N. Experiment to mitigate size effect on deep beams. Mag Concr Res 2008;60:709–23.

[124] Thermou GE, Papanikolaou VK, Lioupis C, Hajirasouliha I. Steel-Reinforced Grout (SRG) strengthening of shear-critical RC beams. Constr Build Mater 2019;216:68–83. https://doi.org/10.1016/j.conbuildmat.2019.04.259.

[125] Baghi H, Barros JAO. New Approach to Predict Shear Capacity of Reinforced Concrete Beams Strengthened with Near-Surface-Mounted Technique. ACI Struct J 2016;114. https://doi.org/10.14359/51689433.

[126] Minelli F, Vecchio FJ. Compression Field Modeling of Fiber-Reinforced Concrete Members Under Shear Loading. ACI Struct J 2006;103:244–52.

[127] Panda SS, Gangolu AR. Study of dowel action in reinforced concrete beam by factorial design of experiment. ACI Struct J 2017;114:1495–505. https://doi.org/10.14359/51700831.

[128] Zhang T, Visintin P, Oehlers DJ. Shear strength of RC beams with steel stirrups. J Struct Eng 2016;142:04015135. https://doi.org/10.1061/(ASCE)ST.1943-541X.0001404.

[129] Esfandiari A, Adebar P. Shear strength evaluation of concrete bridge girders. ACI Struct J 2010;106.

[130] Sadeghian V, Vecchio FJ. The modified compression field theory: Then and now. ACI Spec Publ 2018;328.

[131] Kuo WW, Hsu TTC, Hwang SJ. Shear strength of reinforced concrete beams. ACI Struct J 2014;111:809–18. https://doi.org/10.14359/51686733.

[132] Wakjira TG, Ebead U. A new approach for predicting the shear capacity of FRCM strengthened RC beams in shear. IOP Conf. Ser. Mater. Sci. Eng., vol. 431, 2018. https://doi.org/10.1088/1757-899X/431/11/112006.

[133] Vecchio FJ, Collins MP. The modified compression-field theory for reinforced concrete elements subjected to shear. ACI J Proc 1986;83. https://doi.org/10.14359/10416.

[134] Collins MP, Mitchell D, Adebar P, Vecchio FJ. A general shear design method. ACI Struct J 1996;93:36–45. https://doi.org/10.14359/9838.

[135] Bentz EC, Vecchio FJ, Collins MP. Simplified Compression Field Theory for Calculating Shear Strength of Reinforced Concrete Elements. ACI Struct J 2006;103:614–24. https://doi.org/10.14359/16438.

[136] Chen JF, Teng JG. Shear capacity of FRP-strengthened RC beams: FRP debonding. Constr Build Mater 2003;17:27–41. https://doi.org/10.1016/S0950-0618(02)00091-0.

[137] Tetta ZC, Triantafillou T, Bournas D. On the design of shear-strengthened RC members through the use of textile reinforced mortar overlays. Compos Part B Eng 2018;147:178–96. https://doi.org/10.1016/j.compositesb.2018.04.008.

[138] Wakjira TG, Ebead U. A shear design model for RC beams strengthened with fabric reinforced cementitious matrix. Eng Struct 2019;200:109698. https://doi.org/https://doi.org/10.1016/j.engstruct.2019.109698.

[139] Neto BNM, Barros JAO, Melo GSSA. Model to Simulate the Contribution of Fiber Reinforcement for the Punching Resistance of RC Slabs. J Mater Civ Eng 2014;26:04014020. https://doi.org/10.1061/(ASCE)MT.1943-5533.

[140] Collins MP. Evaluation of shear design procedures for concrete structures. Rep. Prepared for the CSA Technical Committee on Reinforced Concrete Design, Canada: 2001.

[141] Chen JF, Teng JG. Shear Capacity of Fiber-Reinforced Polymer-Strengthened Reinforced Concrete Beams: Fiber Reinforced Polymer Rupture. J Struct Eng

2003;129:615–25. https://doi.org/10.1061/(ASCE)0733-9445(2003)129:5(615).

[142] Joint ACI-ASCE Committee 445. Recent approaches to shear design of structural concrete. J Struct Eng 1998;124:1374–417. https://doi.org/10.1061/(ASCE)0733-9445(1998)124:12(1375).

[143] Yan W, Deng L, Zhang F, Li T, Li S. Probabilistic machine learning approach to bridge fatigue failure analysis due to vehicular overloading. Eng Struct 2019;193:91–9. https://doi.org/10.1016/j.engstruct.2019.05.028.

[144] Weinstein JC, Sanayei M, Asce M, Brenner BR, Asce F. Bridge Damage Identification Using Artificial Neural Networks. J Bridg Eng 2018;23:04018084. https://doi.org/10.1061/(ASCE)BE.1943-5592.0001302.

[145] Fathalla E, Tanaka Y, Maekawa K. Remaining fatigue life assessment of in-service road bridge decks based upon arti fi cial neural networks. Eng Struct 2018;171:602–16. https://doi.org/10.1016/j.engstruct.2018.05.122.

[146] Morfidis K, Kostinakis K. Approaches to the rapid seismic damage prediction of r/c buildings using artificial neural networks. Eng Struct 2018;165:120–41. https://doi.org/10.1016/j.engstruct.2018.03.028.

[147] Feng D, Liu ZT, Wang XD, Chen Y, Chang JQ, Wei DF, et al. Machine learning-based compressive strength prediction for concrete: An adaptive boosting approach. Constr Build Mater 2020;230. https://doi.org/10.1016/j.conbuildmat.2019.117000.

[148] Yu Y, Li W, Li J, Nguyen TN. A novel optimised self-learning method for compressive strength prediction of high performance concrete. Constr Build Mater 2018;184:229–47. https://doi.org/10.1016/j.conbuildmat.2018.06.219.

[149] Mangalathu S, Hwang S, Jeon J. Failure mode and effects analysis of RC members based on machine-learning-based SHapley Additive exPlanations

(SHAP) approach. Eng Struct 2020;219:110927. https://doi.org/10.1016/j.engstruct.2020.110927.

[150] Wakjira TG, Al-Hamrani A, Ebead U, Alnahhal W. Shear capacity prediction of FRP-RC beams using single and ensenble ExPlainable machine learning models. Compos Struct 2022;287:115381. https://doi.org/10.1016/j.compstruct.2022.115381.

[151] Feng D, Liu ZT, Wang XD, Jiang ZM, Liang SX. Failure mode classification and bearing capacity prediction for reinforced concrete columns based on ensemble machine learning algorithm. Adv Eng Informatics 2020;45. https://doi.org/10.1016/j.aei.2020.101126.

[152] Mangalathu S, Jeon J-S. Machine Learning–Based Failure Mode Recognition of Circular Reinforced Concrete Bridge Columns: Comparative Study. J Struct Eng 2019;145:04019104. https://doi.org/10.1061/(asce)st.1943-541x.0002402.

[153] Mangalathu S, Jeon J. Classification of failure mode and prediction of shear strength for reinforced concrete beam-column joints using machine learning techniques. Eng Struct 2018;160:85–94. https://doi.org/10.1016/j.engstruct.2018.01.008.

[154] Feng D-C, Wang W-J, Mangalathu S, Taciroglu E. Interpretable XGBoost-SHAP Machine-Learning Model for Shear Strength Prediction of Squat RC Walls. J Struct Eng 2021;147:04021173. https://doi.org/10.1061/(ASCE)ST.1943-541X.0003115.

[155] Fu B, Feng D. A machine learning-based time-dependent shear strength model for corroded reinforced concrete beams. J Build Eng 2021;36. https://doi.org/10.1016/j.jobe.2020.102118.

[156] Keshtegar B, Nehdi ML, Trung NT, Kolahchi R. Predicting load capacity of

shear walls using SVR–RSM model[Formula presented]. Appl Soft Comput 2021;112. https://doi.org/10.1016/j.asoc.2021.107739.

[157] Almustafa MK, Nehdi ML. Machine learning prediction of structural response for FRP retrofitted RC slabs subjected to blast loading. Eng Struct 2021;244:112752. https://doi.org/10.1016/j.engstruct.2021.112752.

[158] Bashir R, Ashour A. Neural network modelling for shear strength of concrete members reinforced with FRP bars. Compos Part B Eng 2012;43:3198–207. https://doi.org/10.1016/j.compositesb.2012.04.011.

[159] Lee S, Lee C. Prediction of shear strength of FRP-reinforced concrete flexural members without stirrups using artificial neural networks. Eng Struct 2014;61:99–112. https://doi.org/10.1016/j.engstruct.2014.01.001.

[160] Perera R, Barchín M, Arteaga A, Diego A De. Prediction of the ultimate strength of reinforced concrete beams FRP-strengthened in shear using neural networks. Compos Part B Eng 2010;41:287–98. https://doi.org/10.1016/j.compositesb.2010.03.003.

[161] Tanarslan HM, Secer M, Kumanlioglu A. An approach for estimating the capacity of RC beams strengthened in shear with FRP reinforcements using artificial neural networks. Constr Build Mater 2012;30:556–68. https://doi.org/10.1016/j.conbuildmat.2011.12.008.

[162] Breiman L, Friedman JH, Olshen R, Stone C. Classification and regression trees. Wadsworth, Belmont, CA; 1984.

[163] Yan K, Shi C. Prediction of elastic modulus of normal and high strength concrete by support vector machine. Constr Build Mater 2010;24:1479–85. https://doi.org/10.1016/j.conbuildmat.2010.01.006.

[164] Mangalathu S, Shin H, Choi E, Jeon JS. Explainable machine learning models

for punching shear strength estimation of flat slabs without transverse reinforcement. J Build Eng 2021;39:102300. https://doi.org/10.1016/j.jobe.2021.102300.

[165] Rahman J, Ahmed KS, Khan NI, Islam K, Mangalathu S. Data-driven shear strength prediction of steel fiber reinforced concrete beams using machine learning approach. Eng Struct 2021;233. https://doi.org/10.1016/j.engstruct.2020.111743.

[166] Nguyen HD, Truong GT, Shin M. Development of extreme gradient boosting model for prediction of punching shear resistance of r/c interior slabs. Eng Struct 2021;235. https://doi.org/10.1016/j.engstruct.2021.112067.

[167] Wakjira TG, Alam MS, Ebead U. Plastic hinge length of rectangular RC columns using ensemble machine learning model. Eng Struct 2021;244:112808. https://doi.org/10.1016/j.engstruct.2021.112808.

[168] Yu H, Kim S. SVM tutorial-classification, regression and ranking. Handb Nat Comput 2012;1–4:479–506. https://doi.org/10.1007/978-3-540-92910-9_15.

[169] Maalouf M, Homouz D. Kernel ridge regression using truncated newton method. Knowledge-Based Syst 2014;71:339–44. https://doi.org/10.1016/j.knosys.2014.08.012.

[170] Cortes C, Vapnik V. Support-Vector Networks. Mach Learn 1995;20:273–297. https://doi.org/10.1109/64.163674.

[171] Vapnik V. The Nature of Statistical Learning Theory. Springer; 1995.

[172] Chang C, Lin C. LIBSVM: A Library for support vector machines. ACM Trans Intell Syst Technol 2011;2:1–27. https://doi.org/https://doi.org/10.1145/1961189.1961199.

[173] Theodoridis S. Learning in Reproducing Kernel Hilbert Spaces. 2015.

https://doi.org/10.1016/b978-0-12-801522-3.00011-2.

[174] Mitchell TM. Machine Learning and Data Mining. vol. 42. 1999. https://doi.org/10.1145/319382.319388.

[175] Cherkassky V, Ma Y. Practical selection of SVM parameters and noise estimation for SVM regression. Neural Networks 2004;17:113–26. https://doi.org/10.1016/S0893-6080(03)00169-2.

[176] Sutton CD. Classification and Regression Trees, Bagging, and Boosting. Handb Stat 2005;24:303–29. https://doi.org/10.1016/S0169-7161(04)24011-1.

[177] Breiman L. Random Forests. Mach Learn 2001;45:5–32.

[178] Svetnik V, Liaw A, Tong C, Christopher Culberson J, Sheridan RP, Feuston BP. Random Forest: A Classification and Regression Tool for Compound Classification and QSAR Modeling. J Chem Inf Comput Sci 2003;43:1947–58. https://doi.org/10.1021/ci034160g.

[179] Geurts P, Ernst D, Wehenkel L. Extremely randomized trees. Mach Learn 2006;63:3–42. https://doi.org/10.1007/s10994-006-6226-1.

[180] Friedman JH. Greedy Function Approximation: A Gradient Boosting Machine. Ann Stat 2001:1189–232. https://doi.org/10.1214/aos/1013203451.

[181] Chen T, Guestrin C. Xgboost: A scalable tree boosting system. In 22nd SIGKDD Conference on Knowledge Discovery and Data Mining 2016.

[182] Yang L, Shami A. On hyperparameter optimization of machine learning algorithms: Theory and practice. Neurocomputing 2020;415:295–316. https://doi.org/10.1016/j.neucom.2020.07.061.

[183] Lundberg SM, Lee S. A Unified Approach to Interpreting Model Predictions. 31st Conf. neural Inf. Process. Syst. (NIPS 2017), Long Beach, CA, USA: 2017, p. 1–10.

[184] Gao X, Lin C. Prediction model of the failure mode of beam-column joints using machine learning methods. Eng Fail Anal 2021;120:105072. https://doi.org/10.1016/j.engfailanal.2020.105072.

[185] Blanksvärd T, Täljsten B, Carolin A. Shear strengthening of concrete structures with the use of mineral-based composites. J Compos Constr 2009;13:25–34. https://doi.org/10.1061/(ASCE)1090-0268(2009)13:1(25).

[186] Al-Salloum Y, Elsanadedy H, Alsayed S, Iqbal R. Experimental and numerical study for the shear strengthening of reinforced concrete beams using textile-reinforced mortar. J Compos Constr 2012;16:74–90. https://doi.org/10.1061/(ASCE)CC.1943-5614.0000239.

[187] Azam R, Soudki K. FRCM strengthening of shear-critical RC beams. J Compos Constr 2014;18:1–9.

[188] Escrig C, Gil L, Bernat-Maso E, Puigvert F. Experimental and analytical study of reinforced concrete beams shear strengthened with different types of textile-reinforced mortar. Constr Build Mater 2015;83:248–60.

[189] Tetta ZC, Koutas L, Bournas D. Shear strengthening of full-scale RC T-beams using textile-reinforced mortar and textile-based anchors. Compos Part B Eng 2016;95:225–39.

[190] Brückner A, Ortlepp R, Curbach M. Textile reinforced concrete for strengthening in bending and shear. Mater Struct 2006;39:741–8. https://doi.org/10.1617/s11527-005-9027-2.

[191] Azam R, Soudki K, West J, Noël M. Strengthening of shear-critical RC beams: Alternatives to externally bonded CFRP sheets. Constr Build Mater 2017;151:494–503.

[192] Brückner A, Ortlepp R, Curbach M. Anchoring of shear strengthening for T-

beams made of textile reinforced concrete (TRC). Mater Struct 2008;41:407–18. https://doi.org/10.1617/s11527-007-9254-9.

[193] Contamine R, Si Larbi A, Hamelin P. Identifying the contributing mechanisms of textile reinforced concrete (TRC) in the case of shear repairing damaged and reinforced concrete beams. Eng Struct 2013;46:447–58. https://doi.org/10.1016/j.engstruct.2012.07.024.

[194] Tzoura E, Triantafillou TC. Shear strengthening of reinforced concrete T-beams under cyclic loading with TRM or FRP jackets. Mater Struct 2016;49:17–28. https://doi.org/10.1617/s11527-014-0470-9.

[195] Jung K, Hong K, Han S, Park J, Kim J. Shear Strengthening Performance of Hybrid FRP-FRCM. Adv Mater Sci Eng 2015;2015. https://doi.org/10.1155/2015/564876.

[196] Wakjira TG, Ebead U. Experimental and analytical study on strengthening of reinforced concrete T-beams in shear using steel reinforced grout (SRG). Compos Part B Eng 2019;177:107368. https://doi.org/10.1016/j.compositesb.2019.107368.

[197] Wakjira TG, Ebead U. Shear span-to-depth ratio effect on steel reinforced grout strengthened reinforced concrete beams. Eng Struct 2020;216:110737. https://doi.org/10.1016/j.engstruct.2020.110737.

[198] Wakjira TG, Ebead U. Strengthening of reinforced concrete beams in shear using different steel reinforced grout techniques. Struct Concr 2021;22:1113–27. https://doi.org/10.1002/suco.202000354.

[199] Hashemi S, Al-Mahaidi R. Experimental and finite element analysis of flexural behavior of FRP-strengthened RC beams using cement-based adhesives. Constr Build Mater 2012;26:268–73.

https://doi.org/10.1016/j.conbuildmat.2011.06.021.

[200] Bencardino F, Condello A. Structural behaviour of RC beams externally strengthened in flexure with SRG and SRP systems. Int J Struct Eng 2014;5:346–68. https://doi.org/10.1504/IJSTRUCTE.2014.065928.

[201] D'Ambrisi A, Focacci F. Flexural Strengthening of RC Beams with Cement-Based Composites. J Compos Constr 2011;15:707–20. https://doi.org/10.1061/(ASCE)CC.1943-5614.0000218.

[202] Hashemi S, Al-Mahaidi R. Investigation of Flexural Performance of RC Beams Strengthened with CFRP Textile and Cement Based Adhesives. Proc. The 3rd asia-pacific conference on FRP in structures, APFIS, Hokkaido, Japan, 2012.

[203] Elsanadedy H, Almusallam T, Alsayed S, Al-Salloum Y. Flexural strengthening of RC beams using textile reinforced mortar - Experimental and numerical study. Compos Struct 2013;97:40–55. https://doi.org/10.1016/j.compstruct.2012.09.053.

[204] Ombres L. Flexural analysis of reinforced concrete beams strengthened with a cement based high strength composite material. Compos Struct 2011;94:143–55. https://doi.org/10.1016/j.compstruct.2011.07.008.

[205] Escrig C, Gil L, Bernat-maso E. Experimental comparison of reinforced concrete beams strengthened against bending with different types of cementitious-matrix composite materials. Constr Build Mater 2017;137:317–29.

[206] Ebead U, Shrestha K, Afzal MS, El Refai A, Nanni A. Effectiveness of fabric-reinforced cementitious matrix in strengthening reinforced concrete beams. J Compos Constr 2017;21:04016084. https://doi.org/10.1061/(ASCE)CC.1943-5614.0000741.

[207] Ebead U, El Refai A, Shrestha K, Nanni A. Soffit and U-wrap fabric-reinforced

cementitious matrix strengthening for reinforced concrete beams. ACI Struct J 2019;116:267–78. https://doi.org/doi: 10.14359/51713292.

[208] Loreto G, Leardini L, Arboleda D, Nanni A. Performance of RC slab-type elements strengthened with fabric-reinforced cementitious-matrix composites. J Compos Constr 2013;18:A4013003. https://doi.org/10.1061/(ASCE)CC.1943-5614.0000415.

[209] ACI Committee 549. Guide to Design and Construction of Externally Bonded Fabric- Reinforced Cementitious Matrix (FRCM) Systems for Repair and Strengthening Concrete and Masonry Structures (ACI 549.4R-13). Farmington Hills, MI, USA: American Concrete Institute; 2013.

[210] Wakjira TG, Ebead U. Simplified Compression Field Theory-Based Model for Shear Strength of Fabric-Reinforced Cementitious Matrix- Strengthened Reinforced Concrete Beams. ACI Struct J 2020;117:91–104. https://doi.org/10.14359/51721366.

[211] Jung K, Hong K, Han S, Park J, Kim J. Prediction of Flexural Capacity of RC Beams Strengthened in Flexure with FRP Fabric and Cementitious Matrix. Int J Polym Sci 2015;2015. https://doi.org/10.1155/2015/868541.

[212] Bencardino F, Carloni C, Condello A, Focacci F, Napoli A, Realfonzo R. Flexural behaviour of RC members strengthened with FRCM: State-of-the-art and predictive formulas. Compos Part B Eng 2018;148:132–48. https://doi.org/10.1016/j.compositesb.2018.04.051.

[213] Teng JG, Smith ST, Yao J, Chen JF. Intermediate crack-induced debonding in RC beams and slabs. Constr Build Mater 2003;17:447–62. https://doi.org/10.1016/S0950-0618(03)00043-6.

[214] Ceroni F, Salzano P. Design provisions for FRCM systems bonded to concrete

and masonry elements. Compos Part B Eng 2018;143:230–42. https://doi.org/10.1016/j.compositesb.2018.01.033.

[215] Mandor A, Refai A El. Assessment and modeling of the debonding failure of fabric-reinforced cementitious matrix (FRCM) systems. Compos Struct 2021;275:114394. https://doi.org/10.1016/j.compstruct.2021.114394.

[216] ACI Committee 549. ACI 549.4R-20 Guide to design and construction of externally bonded fabric-reinforced cementitious matrix and steel-reinforced grout systems for repair and strengthening of concrete structures. 2020.

[217] Said H, Wu Z. Evaluating and Proposing Models of Predicting IC Debonding Failure. J Compos Constr 2008;12:284–99. https://doi.org/10.1061/(ASCE)1090-0268(2008)12:3(284).

[218] Lu XZ, Teng JG, Ye LP, Jiang JJ. Intermediate Crack Debonding in FRP-Strengthened RC Beams: FE Analysis and Strength Model. J Compos Constr 2007;11:161–74. https://doi.org/10.1061/(asce)1090-0268(2007)11:2(161).

[219] CNR-DT200 R1/2012. Guide for design and construction of externally bonded FRP systems for strengthening existing structures : materials, RC and PC structures, masonry structures. 2006.

[220] ACI Committee 318, American Concrete Institute. Building code requirements for structural concrete (ACI 318-14): an ACI standard : commentary on building code requirements for structural concrete (ACI 318R-14), an ACI report. 2014.

[221] Szerszen MM, Nowak AS. Calibration of design code for buildings (ACI 318): Part 2 - Reliability analysis and resistance factors. ACI Struct J 2003;100:383–91. https://doi.org/10.14359/12614.

[222] Wight JK. Reinforced concrete mechanics and design (7th edition), Pearson Education Inc, Hoboken, New Jersey. 2016.

[223] Kerakoll - The GreenBuilding Company n.d. www.kerakoll.com (accessed December 25, 2018).

[224] Su J, Wang J, Li Z, Liang X. Effect of reinforcement grade and concrete strength on seismic performance of reinforced concrete bridge piers. Eng Struct 2019;198:109512. https://doi.org/10.1016/j.engstruct.2019.109512.

[225] Memon MS, Sheikh SA. Seismic resistance of square concrete columns retrofitted with glass fiber-reinforced polymer. ACI Struct J 2005;102:774–83. https://doi.org/10.14359/14673.

[226] Pantelides CP, Gergely J. Carbon-fiber-reinforced polymer seismic retrofit of RC bridge bent: Design and in situ validation. J Compos Constr 2002;6:52–60. https://doi.org/10.1061/(ASCE)1090-0268(2002)6:1(52).

[227] Chen G, Yuan W, Yang X, Fan L. Seismic Performance Assessment and Retrofit of Rectangular Bridge Piers With Externally Encased Circular Steel Jackets. Proc 12th World Conf Earthq Eng Auckland, New Zeal 2000;Paper No.:2–7.

[228] Endeshaw M, ElGawady M, Sack RL, McLean DI. Retrofit of Rectangular Bridge Columns using CFRP Wrapping Rep. No. WA-RD 716.1, Dept. of Civil and Environmental Engineering, Washington State Univ., Pullman, WA. 2008.

[229] Parghi A, Alam MS. Seismic collapse assessment of non-seismically designed circular RC bridge piers retrofitted with FRP composites. Compos Struct 2017;160:901–16. https://doi.org/10.1016/j.compstruct.2016.10.094.

[230] Rutledge S, Kowalsky M, Seracino R, Nau J. Repair of Reinforced Concrete Bridge Columns Containing Buckled and Fractured Reinforcement by Plastic Hinge Relocation. J Bridg Eng 2014;19:A4013001. https://doi.org/10.1061/(ASCE)BE.1943-5592.0000492.

[231] Pavese A, Bolognini D, Peloso S. FRP seismic retrofit of RC square hollow

section bridge piers. J Bridg Eng 2004;8:225–50. https://doi.org/10.1080/13632460409350526.

[232] Monti G, Nisticò N, Santini S. Design of FRP jackets for upgrade of circular bridge piers. J Compos Constr 2001;5:94–101. https://doi.org/10.1061/(ASCE)1090-0268(2001)5:2(94).

[233] Huang X, Birman V, Nanni A, Tunis G. Properties and potential for application of steel reinforced polymer and steel reinforced grout composites. Compos Part B Eng 2005;36:73–82. https://doi.org/10.1016/S1359-8368(03)00080-5.

[234] Lopez A, Galati N, Alkhrdaji T, Nanni A. Strengthening of a reinforced concrete bridge with externally bonded steel reinforced polymer (SRP). Compos Part B Eng 2007;38:429–36. https://doi.org/10.1016/j.compositesb.2006.09.003.

[235] Cao R, Agrawal AK, El-Tawil S, Xu X, Wong W. Performance-Based Design Framework for Bridge Piers Subjected to Truck Collision. J Bridg Eng 2019;24:1–11. https://doi.org/10.1061/(ASCE)BE.1943-5592.0001423.

[236] Zhu L, Elwood KJ, Haukaas T. Classification and seismic safety evaluation of existing reinforced concrete columns. J Struct Eng 2007;133:1316–30. https://doi.org/10.1061/(ASCE)0733-9445(2007)133:9(1316).

[237] Ouyang LJ, Gao WY, Zhen B, Lu ZD. Seismic retrofit of square reinforced concrete columns using basalt and carbon fiber-reinforced polymer sheets: A comparative study. Compos Struct 2017;162:294–307. https://doi.org/10.1016/j.compstruct.2016.12.016.

[238] Galal K, Arafa A, Ghobarah A. Retrofit of RC square short columns. Eng Struct 2005;27:801–13. https://doi.org/10.1016/j.engstruct.2005.01.003.

[239] Ma R, Xiao Y, Li KN. Full-scale testing of a parking structure column retrofitted with carbon fiber reinforced composites. Constr Build Mater 2000;14:63–71.

https://doi.org/10.1016/S0950-0618(00)00008-8.

[240] Nigel Priestley MJ, Seible F, Xiao Y, Verma R. Steel jacket retrofitting of reinforced concrete bridge columns for enhanced shear strength. Part 2: Test results and comparison with theory. ACI Mater J 1994;91:537–51. https://doi.org/10.14359/4168.

[241] Wei H, Wu Z, Guo X, Yi F. Experimental study on partially deteriorated strength concrete columns confined with CFRP. Eng Struct 2009;31:2495–505. https://doi.org/10.1016/j.engstruct.2009.05.006.

[242] Saljoughian A, Mostofinejad D. Axial-flexural interaction in square RC columns confined by intermittent CFRP wraps. Compos Part B Eng 2016;89:85–95. https://doi.org/10.1016/j.compositesb.2015.10.047.

[243] Zeng JJ, Guo YC, Gao WY, Li JZ, Xie JH. Behavior of partially and fully FRP-confined circularized square columns under axial compression. Constr Build Mater 2017;152:319–32. https://doi.org/10.1016/j.conbuildmat.2017.06.152.

[244] Taucer FF, Spacone E, Filippou FC. A Fiber Beam-Column Element for Seismic Response Analysis of Reinforced Concrete Structures, Report No. UCB/EERC-91/17: Earthquake Engineering Research Center College of Engineering University of California, Berkeley. 1991.

[245] Spacone E, Filippou FC, Taucer FF. Fibre beam-column model for non-linear analysis of R/C frames: Part I. Formulation. Earthq Eng Struct Dyn 1996;25:711–25. https://doi.org/10.1002/(SICI)1096-9845(199607)25:7<711::AID-EQE576>3.0.CO;2-9.

[246] Abbiati G, Cazzador E, Lanese I, Azam SE, Bursi OS, Pavese A. Recent advances on the hybrid simulation of bridges base on partitioned time integration, dynamic identification and model updating, International

Conference on Advances in Experimental Structural Engineering, University of Illinois Urbana-Champaign; United States: 2015.

[247] Su J, Dhakal RP, Junjie Wang. Fiber-based damage analysis of reinforced concrete bridge piers. Soil Dyn Earthq Eng 2017;96:13–34. https://doi.org/10.1016/j.soildyn.2017.01.029.

[248] Feng Y, Kowalsky M, Nau JM. Fiber-Based Modeling of Circular Reinforced Concrete Bridge Columns Fiber-Based Modeling of Circular Reinforced. J Earthq Eng 2014;18:714–34. https://doi.org/10.1080/13632469.2014.904254.

[249] Seismosoft [2020]. SeismoStruct 2020 – A computer program for static and dynamic nonlinear analysis of framed structures n.d. https://seismosoft.com/.

[250] Pinho R, Casarotti C, Antoniou S. A comparison of single-run pushover analysis techniques for seismic assessment of bridges. Earthq Eng Struct Dyn 2007;36:1347–62. https://doi.org/10.1002/eqe.684.

[251] Casarotti C, Pinho R. Seismic response of continuous span bridges through fiber-based finite element analysis. Earthq Eng Eng Vib 2006;5:119–31. https://doi.org/10.1007/s11803-006-0631-0.

[252] Alam MS, Youssef MA, Nehdi M. Analytical prediction of the seismic behaviour of superelastic shape memory alloy reinforced concrete elements. Eng Struct 2008;30:3399–411. https://doi.org/10.1016/j.engstruct.2008.05.025.

[253] Mander JB, Priestley MJN, Park R. Theoretical Stress-Strain Model for Confined Concrete. J Struct Eng 1989;114:1804–26.

[254] Martínez-Rueda JE, Elnashai AS. Confined concrete model under cyclic load. Mater Struct 1997;30:139–47. https://doi.org/10.1007/bf02486385.

[255] Ferracuti B, Savoia M. Cyclic behavior of FRP-wrapped columns under axial and flexural loadings. Proceedings of the International Conference on Fracture,

Turin, Italy 2005.

[256] Spoelstra MR, Monti G. FRP-Confined Concrete Model. J Compos Constr 1999;3:143–50. https://doi.org/10.1061/(asce)1090-0268(2001)5:1(62).

[257] Yankelevsky DZ, Reinhardt HW. Uniaxial behavior of concrete in cyclic tension. J Struct Eng (United States) 1989;115:166–82. https://doi.org/10.1061/(ASCE)0733-9445(1989)115:1(166).

[258] Menegotto M, Pinto PE. Method of Analysis for Cyclically Loaded R. C. Plane Frames Including Changes in Geometry and Non-Elastic Behavior of Elements under Combined Normal Force and Bending. Proc IABSE Symp Resist Ultim Deform Struct Acted by Well Defin Loads 1973:15–22. https://doi.org/http://dx.doi.org/10.5169/seals-13741.

[259] Filippou FC, Popov EP, Bertero V V. Modeling of R/C joints under cyclic excitations. J Struct Eng (United States) 1983;110. https://doi.org/10.1061/(ASCE)0733-9445(1984)110:12(3068).

[260] Montgomery DC. Design and Analysis of Experiments. 8th ed. Hoboken, New Jersey, USA: John Wiley & Sons Inc; 2013.

[261] ACI Committee 318. Building Code Requirements for Structural Concrete and commentary (ACI 318–14). Am Concr Institute, Farmingt Hills, MI 2011:524.

[262] Goodnight JC, Kowalsky M, Nau JM. Effect of Load History on Performance Limit States of Circular Bridge Columns. J Bridg Eng 2013;18:1383–96. https://doi.org/10.1061/(ASCE)BE.1943-5592.0000495.

[263] Muntasir Billah AHM, Shahria Alam M. Seismic fragility assessment of concrete bridge pier reinforced with superelastic shape memory alloy. Earthq Spectra 2015;31:1515–41. https://doi.org/10.1193/112512EQS337M.

[264] Kowalsky M. Deformation limit states for circular reinforced concrete bridge

columns. J Struct Eng 2000;126:869–78. https://doi.org/10.1061/(ASCE)0733-9445(2000)126:8(869).

[265] Lam L, Teng J. G. Design-oriented stress – strain model for FRP-confined concrete. Constr Build Mater 2003;17:471–89. https://doi.org/10.1016/S0950-0618(03)00045-X.

[266] Teng JG, Huang YL, Lam L, Ye LP. Theoretical Model for Fiber-Reinforced Polymer-Confined Concrete. J Compos Constr 2007;11:201–10. https://doi.org/10.1061/(ASCE)1090-0268(2007)11.

[267] Jiang T, Teng JG. Analysis-oriented stress – strain models for FRP – confined concrete. Eng Struct 2007;29:2968–86. https://doi.org/10.1016/j.engstruct.2007.01.010.

[268] Teng JG, Lin G, Yu T. Analysis-Oriented Stress-Strain Model for Concrete under Combined FRP-Steel Confinement. J Compos Constr 2015;19:04014084. https://doi.org/10.1061/(ASCE)CC.1943-5614.0000549.

[269] Lin G, Yu T, Teng JG. Design-Oriented Stress – Strain Model for Concrete under Combined FRP-Steel Confinement. J Compos Constr 2016;20:04015084. https://doi.org/10.1061/(ASCE)CC.1943-5614.0000651.

[270] Teng JG, Jiang T, Lam L, Luo Y. Z. Refinement of a Design-Oriented Stress – Strain Model for FRP-Confined Concrete. J Compos Constr 2009;13:269–78. https://doi.org/10.1061/(ASCE)CC.1943-5614.0000012.

[271] ACI 440.2R-08, ACI committee 440. Guide for the design and construction of externally bonded FRP systems for strengthening existing structures. vol. 440. 2008.

[272] Berry MP, Eberhard MO. Practical performance model for bar buckling. J Struct Eng 2005;131:1060–70. https://doi.org/10.1061/(ASCE)0733-9445(2005)131.

[273] Feng Y, Kowalsky M, Nau JM. Effect of Seismic Load History on Deformation Limit States for Longitudinal Bar Buckling in RC Circular Columns. J Struct Eng 2015;141:1–13. https://doi.org/10.1061/(ASCE)ST.1943-541X.0001153.

[274] Bournas DA, Triantafillou TC, Asce M. Bar Buckling in RC Columns Confined with Composite Materials. J Compos Constr 2011;15:393–403. https://doi.org/10.1061/(ASCE)CC.1943-5614.0000180.

[275] Lu Y, Gu X, Guan J. Probabilistic Drift Limits and Performance Evaluation of Reinforced Concrete Columns. J Struct Eng 2005;131:966–78. https://doi.org/10.1061/(asce)0733-9445(2005)131:6(966).

[276] Panagiotakos TB, Fardis MN. Deformations of Reinforced Concrete Members at Yielding and Ultimate. ACI Struct J 2001;98:135–48.

[277] EN 1998-3:2005. Eurocode 8: Design of structures for earthquake resistance - Part 3: Assessment and retrofitting of buildings. vol. 1. 2005.

[278] Biskinis D, Fardis MN. Flexure-controlled ultimate deformations of members with continuous or lap-spliced bars. Struct Concr 2010;11:93–108.

[279] fédération internationale du béton/International Federation for Structural Concrete (fib). fib Model Code for Concrete Structures 2010 2010.

[280] Wolpert D. Stacked Generalization. Neural Networks 1992;5:241–59.

[281] Zhou H, Huang G Bin, Lin Z, Wang H, Soh YC. Stacked extreme learning machines. IEEE Trans Cybern 2015;45:2013–25. https://doi.org/10.1109/TCYB.2014.2363492.

[282] Breiman L. Stacked regressions. Mach Learn 1996;24:49–64. https://doi.org/10.1023/A:1018046112532.

[283] Willmott Cort J. On the validation of models. Phys Geogr 1981;2:184–94.

[284] Pedregosa F, Varoquaux G, Gramfort A, Michel V, Thirion B, Grisel O, et al.

Scikit-learn: Machine Learning in Python. J Mach Learn Res 2011;12:2825–30.

[285] Lundberg SM, Erion GG, Lee SI. Consistent individualized feature attribution for tree ensembles. ArXiv:180203888 2018.

[286] Barrera AC, Bonet JL, Romero ML, Miguel PF. Experimental tests of slender reinforced concrete columns under combined axial load and lateral force. Eng Struct 2011;33:3676–89. https://doi.org/10.1016/j.engstruct.2011.08.003.

APPENDIX

Appendix A: List of Publications

This thesis was written based on the following journal publications:

Wakjira TG, Ebead U. Experimental and analytical study on strengthening of reinforced concrete T-beams in shear using steel reinforced grout (SRG). *Composites Part B: Engineering* 2019;177:107368. https://doi.org/10.1016/j.compositesb.2019.107368.

Wakjira TG, Ebead U. Shear span-to-depth ratio effect on steel reinforced grout strengthened reinforced concrete beams. *Engineering Structures* 2020;216:110737. https://doi.org/10.1016/j.engstruct.2020.110737.

Wakjira TG, Ebead U. Strengthening of reinforced concrete beams in shear using different steel reinforced grout techniques. *Structural Concrete* 2021;22:1113–27. https://doi.org/10.1002/suco.202000354.

Wakjira TG, Ebead U, Alam MS. Machine Learning-Based Shear Capacity Prediction and Reliability Analysis of Shear-Critical RC Beams Strengthened with Inorganic Composites. Case Studies in Construction Materials 2022; 16: e01008. https://doi.org/10.1016/j.cscm.2022.e01008.

Wakjira TG, Ibrahim M, Ebead U, Alam MS. Explainable machine learning model and reliability analysis for flexural capacity prediction of RC beams strengthened in flexure with FRCM. *Engineering Structures* 2022;255. https://doi.org/10.1016/j.engstruct.2022.113903.

Wakjira TG, Nehdi ML, Ebead U. Fractional factorial design model for seismic performance of RC bridge piers retrofitted with steel-reinforced polymer composites. *Engineering Structures* 2020;221:111100. https://doi.org/10.1016/j.engstruct.2020.111100.

Wakjira TG, Alam MS, Ebead U. Plastic hinge length of rectangular RC columns using ensemble machine learning model. *Engineering Structures* 2021;244:112808. https://doi.org/10.1016/j.engstruct.2021.112808.